GENESIS OF THE BLACKBUSH URANIUM DEPOSIT, SOUTH AUSTRALIA

Urs Domnick

This thesis is submitted for the degree of Doctor of Philosophy

in the

School of Chemical Engineering and Advanced Materials,

Faculty of Engineering, Computer and Mathematical Sciences

at

The University of Adelaide

November 2019

TABLE OF CONTENTS

ABSTRACT

The Blackbush deposit, northern Eyre Peninsula, South Australia is a recently discovered sediment-hosted U deposit. The resource is mainly hosted at the unconformity between Eocene sandstone (Kanaka Beds) and a massive saprolite derived from subjacent ~1585 Ma granites, affiliated with the Samphire Pluton. Three distinct granitoids are recognised in basement underlying the deposit. The southern part of the pluton features a characteristic green-coloured granite (B) whereas the northern part (granite C), immediately underlying the Blackbush deposit, is characterised by reddened feldspars. These two granites are separated by an arcuate domain of a yellowish granite (A), which is significantly less evolved than the other two, as indicated by higher Ca, and lower U. All three granites show complex alteration overprints and textures, as well as crosscutting veins. Alkali feldspar is replaced by porous K-feldspar and albite, and plagioclase is overprinted by an assemblage of porous albite + sericite ± calc-silicates. In granites A and B, igneous biotite is replaced by calc-silicate minerals, the products of Ca-metasomatism, sourced from the anorthite component of altered plagioclase. Vein assemblages include quartz, hematite, coffinite, fluorite and clay minerals.

The geological evolution of the Blackbush deposit is constrained by new SHRIMP U-Pb zircon data from the three granites and microprobe U-Pb ages for coffinite and uraninite in veins within granite, saprolite and overlying sandstone. The new geochronological data for the granites: 1585 ± 9 Ma (Granite B), 1579 ± 9 Ma (Granite C), and 1588 ± 9 Ma (Granite A) show statistical overlap. Their distinct appearance and geochemistry may be attributed, in part, to fractionation within a single magmatic event. Granite C, immediately beneath the deposit, is significantly more altered than the other granites. Anomalously high U contents (10-81 ppm), as well as highly variable Th/U ratios, and the presence of hydrothermal uranothorite and coffinite are clear evidence for U mobility facilitated by porosity created during feldspar

alteration, and strongly indicate that the granite is the most probable source rock for the uranium. Pervasive alteration is also expressed in the modified chemistry and textures displayed by contained zircons from Granite C, which have been examined and chemically mapped down to the nanoscale.

In the deposit, uranium is present as coffinite and is hosted mainly in the sandstone, along the unconformity, as well as within a roll front downstream, and to a minor degree also in saprolite. Coffinite in the sandstone and saprolite occurs intergrown with framboidal Fe-sulphides and lignite grains, as well as coatings around grains of quartz. It is poor in trace elements such as REE or Th. In contrast, coffinite within the granite-hosted veins contains a significant Y (11 wt.%) and HREE. Minor U also occurs absorbed in lignite. Chemical U-Pb dating (608 spot analyses) of coffinite in sandstone, saprolite and veins gives a normal distribution with a mean age of 17 ± 1.6 Ma. Uraninite in the granite-hosted vein yielded a significantly older age (41 ± 2 Ma).

Coffinite ages are interpreted as evidence for a single ore-forming event during the Miocene. Such an event likely coincided with tectonic movement, indicated by horst and graben structures in the early Miocene Melton Limestone. The latter unit overlies the Eocene sandstone, and is, in turn, overlain by Pliocene Gibbon Beds that show no evidence of tectonism. The significantly older age of granite-vein uraninite indicates this predates Eocene sedimentation, and likely indicates transport and redeposition of uranium by oxidising fluids within the exposed granite. Combined, the new ages for hydrothermal minerals indicate that uraninite formed in granite veins and was subsequently dissolved and reprecipitated as coffinite in younger sediments during Tertiary tectonic events.

DECLARATION

I certify that this work contains no material which has been accepted for the award of any other degree or diploma in my name, in any university or other tertiary institution and, to the best of my knowledge and belief, contains no material previously published or written by another person, except where due reference has been made in the text. In addition, I certify that no part of this work will, in the future, be used in a submission in my name, for any other degree or diploma in any university or other tertiary institution without the prior approval of the University of Adelaide and where applicable, any partner institution responsible for the joint-award of this degree.

I acknowledge that copyright of published works contained within this thesis resides with the copyright holder(s) of those works.

I also give permission for the digital version of my thesis to be made available on the web, via the University's digital research repository, the Library Search and also through web search engines, unless permission has been granted by the University to restrict access for a period of time.

Signed Date 15/11/2019

ACKNOWLEDGEMENTS

I would like to thank my principal supervisor Professor Nigel J. Cook, whose ongoing support has been invaluable for me and the progress of this thesis over the last four years. His incredible patience and dedication to his students were a constant motivation in hard times.

I would like to acknowledge my co-supervisor Dr. Cristiana L. Ciobanu for opening my eyes more than once with her honesty. Her energy and enthusiasm were always a welcome remedy for my lethargy.

I would like to thank my co-supervisor Russel Bluck for having great confidence in me and entrusting me with the research on his brainchild, the Blackbush deposit. His unconventional approach and unique perspective have been highly insightful.

Special thanks to my colleagues Liam Courtney-Davies, Marija Dmitrijeva, Max R. Verdugo-Ihl, Dr. William Keyser, and Jing Xu. I could not have finished this thesis without their tremendous selfless contribution, in a time when they were struggling with their own projects.

Dr. Benjamin P. Wade, Dr. Sarah E. Gilbert and the staff or Adelaide Microscopy are thanked for their time, effort, and patience during analytical sessions.

I want to thank my family for their continuous support.

Thank you, Dawn, for putting up with me.

PREFACE

This thesis comprises of a portfolio of articles and manuscripts which are either published or under review in international peer-reviewed journals, The journals in which these papers are published or have been submitted to are *'Lithos'* (Chapter 2, published), *'Precambrian Research'* (Chapter 3, submitted) and *'Minerals'* (Chapter 4, submitted). All chapters are closely related and summarize key findings and interpretations, to be read as standalone contributions. Recommendations have been made in Chapter 5, as a direct result of the key findings of this research.

The one published article and two submitted manuscripts which form the basis of this thesis are:

1. Domnick, U, Cook, N.J., Bluck, R., Brown, C., Ciobanu, C.L., 2018. Petrography of granitoids from the Samphire Pluton, South Australia: implications for uranium mineralisation in overlying sediments. Lithos 300–301, 1–19.
2. Domnick, U., Cook, N.J., Ciobanu, C.L., Courtney-Davies, L., Dmitrijeva, M., Verdugo-Ihl, M.R., Xu, J., Keyser, W., Slattery, A., Kennedy, A.K., Bluck, R., in review. Micron- to nanoscale characterisation and U-Pb geochronology of zircon from granites of the samphire pluton, South Australia. Precambrian Research.
3. Domnick, U., Cook, N.J., Ciobanu, C.L., Wade, BP., Bluck, R., 2020. A Mineralisation Age for the Sediment-Hosted Blackbush uranium Prospect, North-Eastern Eyre Peninsula, South Australia. Minerals, 10, 191.

Chapter 6 contains supplementary material for all chapters outlined above, as well as co-authored publication abstracts and conference abstracts that have been generated during PhD candidature.

The additional material is as follows:

A. Supplementary material for Chapter 2 (Lithos).

B. Supplementary material for Chapter 3 (Precambrian Research).

C. Supplementary material for Chapter 4 (Minerals).

Co-authored article abstract

D. Courtney-Davies, L., Ciobanu, C.L., Verdugo-Ihl, M.R., Slattery, A., Cook, N.J., Dmitrijeva, M., Keyser, W., Wade, B.P., **Domnick, U.**, Ehrig, K., Xu, J., Kontonikas-Charos, A., 2019. Zircon at the nanoscale records metasomatic processes leading to large magmatic-hydrothermal ore systems. Minerals, 9, 364.

First author conference abstracts and conference poster

E. **Domnick, U**., Cook, N.J., Bluck, R., Brown, Callan., Ciobanu, C.L., 2017. Petrography and Hydrothermal Alteration of Granitoids from the Samphire Magmatic Complex, South Australia, and Implications for Uranium Mineralisation in Overlying Sediments. AusIMM Uranium Conference 2017, Adelaide, Australia,

F. **Domnick, U**., Cook, N.J., Bluck, R., Brown, Callan., Ciobanu, C.L., Wade, B.P., 2018. Coffinite Ages In the Blackbush Uranium Deposit, South Australia: Uranium Transport Induced By Tectonic Events. AusIMM Uranium Conference 2018, Adelaide, Australia,

G. **Domnick, U**., Cook, N.J., Ciobanu, C.L., Wade, B.P., Bluck, R., Brown, Kennedy, A.K., 2018. Uranium Transport from Mesoproterozoic Bedrock Granite Induced

Tectonism: The Blackbush Uranium Deposit, South Australia. 15th Quadrennial IAGOD Symposium, Salta, Argentina.

The final chapter of this thesis consists of a complete reference list of all publications cited within any of the manuscripts, chapters, supplementary and additional material submitted as a component of this thesis

CHAPTER 1

INTRODUCTION

1 INTRODUCTION

Australia has some of the largest uranium resources in the world, with at least 80% contained in deposits within the state of South Australia (23% of the global total; Government of South Australia 2019). The largest part of this uranium is contained within Mesoproterozoic deposits of iron-oxide copper-gold (IOCG) deposit type in the Olympic Cu-Au Province (Skirrow et al. 2007; Reid 2019), notably at Olympic Dam (Ehrig et al. 2012). Several other deposit types exist in South Australia, including 'classic' roll-front deposits of the Lake Frome Basin (Skirrow 2009; Ingham et al. 2014). More recently, exploration has revealed other styles of uranium mineralization in South Australia that have proven somewhat more enigmatic. The latter group includes unconformity-related, sediment-hosted uranium mineralization at the Samphire prospect located in the Pirie basin on the eastern Eyre Peninsula, 20 km southwest of the town of Whyalla. The prospect, the subject of this thesis, overlies ~1585 Ma granites belonging to the Hiltaba Intrusive Suite – like the host rock to the Olympic Dam deposit.

The Samphire prospect comprises two deposits: Blackbush, the larger of the two, has a JORC inferred resource of 64.5 Mt. ore at an average bulk grade of 200 ppm U (85 ppm U cut-off). The smaller deposit (Plumbush) has a JORC inferred resource of 21.8 Mt. ore at an average grade of 250 ppm U (85 ppm U cut-off). Together, the two deposits are estimated as 12,700 and 5,400 tonnes U, respectively (Samphire Uranium 2019). These prospects were initially discovered in 2007 (UraniumSA 2007) and are currently the only sediment-hosted uranium systems in the Gawler Craton that have been investigated in any detail, even though sediment-hosted U is widespread (Hou et al. 2007, 2017).

Development of the prospect by current owner Samphire Uranium Limited (http://www.samphireuranium.com.au/) and exploration for additional resources within the region are, in part, dependent on a genetic model for the deposit based around accurate information on the mineralogy, petrography and geochemistry of mineralization, and the temporal-spatial relationships between mineralization and host rocks. These knowledge gaps provided the basis for the present thesis.

The first part of Chapter 1 will provide background information on (1) uranium geology, geochemistry, mineralogy, ore deposits and ore genesis, (2) regional bedrock and cover sequence geology, with emphasis on the area around the Samphire deposit, and (3) the Blackbush deposit, with a short review of previous work, interpretations of geological setting and ore genesis. Coverage of these topics represents a context for the research focus of this thesis and the published papers and manuscripts contained within it.

1.1 BACKGROUND

1.1.1 Uranium geology, geochemistry, mineralogy, ore deposits and ore genesis

Uranium is the primordial element with the highest atomic weight and contains 92 protons. It is the 50th most abundant element in earth crust with an average concentration of ~2.7 ppm (Taylor 1964). Several natural uranium isotopes exist, of which ^{238}U is the most common with ~99.2745 atom.%, followed by ^{235}U with ~0.7200 atom.% and 0.0055 atom.% ^{234}U (IUPAC 1998). All U isotopes are radioactive. The main use of U is the release of energy through nuclear fission, either continuously in one of the 449 currently operational reactors (IAEA 2019) or instantaneously through ~14,000 nuclear warheads (Kristensen and Korda 2019).

The two main ionic forms of U relevant for geological processes are U^{4+} and U^{6+}. U^{4+} dominates in rather reducing conditions, including most melts, whereas U^{6+} is more abundant in highly oxidizing conditions, usually in balance with the atmosphere (Murphy and Shock 1999). A wide range of U^{4+} and U^{6+}-bearing minerals exist, which can be grouped as relatively U ore minerals, complex U minerals, and accessory minerals (Dahlkamp 1993).

The first group, uranium ore minerals containing essential U, includes uraninite (UO_{2+x}), coffinite ($USiO_4 \bullet nH_2O$), and brannerite (UTi_2O_6), and a variety of U^{6+} minerals, mostly compounds of uranyl (UO_2^{2+}) and diverse oxyanions, e.g., carbonates, phosphates, or vanadates (Dahlkamp 1993). One such mineral is carnotite $K_2(UO_2)_2(VO_4)_2 \cdot 3H_2O$.

The designation of complex U minerals is not based on crystal structure but rather on the incorporation of U and other elements via multiple substitution mechanisms giving rise to extensive solid solution series. Whereas the theoretical formula may be simple, e.g., AB_2O_6, the practical implementation is complex, e.g., $(REE,Y,Ca,Ce^{4+},U,Th)(Nb,Ta,Ti)_2O_6$ (euxenite). This group includes all U-bearing titanates, niobates, and tantalates, except for brannerite, as well as a wide range of U-bearing silicates, e.g., steenstrupine $Na_{14}Ce_6Mn_2Fe_2(Zr,Th,U)(Si_6O_{18})_2 (PO_4)_7 \bullet 3(H_2O)$. Most complex U minerals are refractory, they are resistant to weathering and alteration, and consequently to also to hydrometallurgical processing and U extraction (Dahlkamp 1993).

The third group, accessory minerals, comprises minerals that contain U as a minor or trace component (<1 wt.%), substituting for other elements (Dahlkamp 1993). Major rock-forming minerals like quartz or feldspar do not incorporate U at any significant concentration, and U is always found in accessory minerals in igneous rocks, hence the name of this group

(Cuney 2014). U^{4+} can substitute and be substituted by elements of similar charge and ionic radius, e.g., Th^{4+}, Zr^{4+}, Ce^{4+}, and with slightly more complex substitutions REY^{3+} or Ca^{2+}. As a result, most accessory minerals contain some U, notably REE-minerals such as allanite, monazite, and xenotime, Ca-essential minerals like apatite, titanite, and fluorite, and the zircon group of minerals (Dahlkamp 1993).

The zircon group comprises all tetragonal minerals with the formula $ASiO_4$, where A is a tetravalent ion, e.g., Zr (zircon), Hf (hafnon), Th (thorite), Ce^{4+}, or U^{4+}. They form continuous solid solutions. Uranium rich thorite is called *uranothorite* and an accessory mineral of major importance for U. Zircon group minerals can contain significant amounts of REY and P, and xenotime, $(Y,HREE)PO_4$, is part of this tetragonal solid solution series. Although REY and P should, theoretically, be coupled to achieve charge balance, i.e., $REY^{3+} + P^{5+} \leftrightarrow U^{4+} + Si^{4+}$, both elements rarely perfectly correlate. Heavy rare earth substitute tetravalent ions more easily than P substitutes for Si, and the incorporation of HREE facilitates the incorporation of P, as a result, zircon group minerals usually contain more HREE than P, and P substitution correlates with the whole-rock HREE content (Finch and Hanchar 2003). The exact mechanism to achieve charge balance are still discussed and may be complicated by the presence of even lesser charged ions, e.g., Ca^{2+}.

It should be mentioned that the U endmember of the zircon group, $USiO_4$, is apparently not stable, and $UO_2 + SiO_2$ is always preferred in melts. The U silicate coffinite, $USiO_4 \bullet nH_2O$ $0<n<2$, contains significant amounts of water, which is presumably essential for the stability of the mineral (Guo et al. 2015).

As a high field strength element (HFSE), U is incompatible in melts and its content is higher in felsic than mafic melts. At the same time the solubility of U (and other HFSE) is reversely correlated with the degree of polymerization in a melt, which increases with differentiation and fractionation (Peiffert et al. 1996). As a result, U tends to leave the melt early, either as dedicated U-mineral, or as minor element in other minerals.

Several elements can lower polymerization, namely halogens (F and Cl), and alkalis, e.g., K and Na. Peralkaline igneous rocks (whole-rock $Al/(Na+K) < 1$; Shand 1943) have high HFSE solubility and hence high U content (Cuney 2014). In these rocks, U is usually incorporated into complex minerals together with other HFSE (Cuney 2014). The resulting deposits can be of large size, up to 100,000 tonnes contained U, but are always low grade (<250

ppm) (IAEA 2018). In addition, U is trapped in complex refractory minerals with high extraction costs (Dahlkamp 1993, Skirrow 2009).

In contrast, peraluminous igneous rocks (Al/(Na+K+2Ca)>1) have high polymerization and low solubilities, but U seems to be slightly less affected by low solubility than other HFSE. This results in melts with low U content but high U/HFSE ratios, which allows the formation of minerals containing essential U, notably uraninite (Cuney and Friedrich 1987). In metaluminous melts where Al/(Na+K)>1 and Al/(Na+K+2Ca)<1, the U-content can increase, decrease, or stay constant, depending on slight differences in the whole-rock geochemistry and the halogen content (Cuney 2014). The ratio of U to Th and other HFSE will define the expected minerals (Cuney 2014). A low (U+Th)/REE ratio will result in the incorporation of U and Th as minor elements into REE-minerals, e.g., allanite or xenotime. High (U+Th)/REE will lead to the formation of *uranothorite* where Th/U is high, and uraninite whenever Th/U is low. Rarely high HFSE/(U+Th) ratios will force U and Th into minerals of those elements, e.g., high Nb/(U+Th) will form euxenite with significant U and Th content. The resulting met- to peraluminous granites are always very low grade (tens of ppm U).

This dependence of solubility and expected mineral species on whole-rock geochemistry infers that intrusive igneous rocks are never economic U deposits. The only exceptions are seen in case with low degrees of partial melting of a U-rich protolith, where the processes described above are not in full effect (Cuney 2014). One such example is the Rössing deposit (Namibia). Deposits of this type can be very large (~250,000 tonnes U) but are always low grade (<400 ppm U). In volcanic rocks, some of these disadvantages can be bypassed; very quick cooling will prevent formation of complex minerals and U is part of the glassy matrix, but even then, economic deposits never form (Cuney 2014).

Uranium deposits display an extraordinarily diverse range of mineralization styles (e.g., Cuney 2009, 2010). Almost all granite-related U deposits (e.g., Cerny et al. 2005) are the result of the deposition of U from a U bearing fluid. This fluid can be of magmatic, metamorphic, or have a surficial/basinal origin. The fluid-melt partition coefficient of U is dependent on the whole-rock geochemistry, and basically reversely proportional to the U solubility (Skirrow 2009). Peralkaline melts are associated with magmatic fluids containing less U than the melt, fluids associated with peraluminous melts have usually higher than melt U. Metaluminous melts may behave one way or the other, but usually the partition coefficient prefers fluid over melt (Cuney 2014). This leads to a variety of magmatic, fluid-derived deposits; hand veins and stockworks in plutons or volcanic rocks, or in the host rock of intrusions. Deposits are highly

variable in size and grade but can reach up to 95,000 tonnes U at grades of ~1 wt.%. Iron-oxide copper gold (IOCG) deposits typically contain anomalous U but only Olympic Dam contains a sufficiently high U grade for extraction to be economic. Olympic Dam is the world's largest U deposit (containing ~2 Mt U), some of the U is likely sourced from magmatic fluids, but the sheer size compels the presence of other sources and/or concentration processes.

Metamorphic fluids, e.g., those released through dehydration reactions, can mobilize U and transport it upwards, resulting in metamorphic U veins or stockworks (Dahlkamp 1993). The characterization of a fluid or deposit as magmatic or metamorphic may therefore often be ambiguous. Some U deposits are associated with metasomatic reactions, e.g., in albitites or skarns. This metasomatism can be associated with intrusions (contact metamorphism), or regional metamorphism. Deposits are highly variable in size and grade and can reach up to 100,000 tonnes at U concentrations of ~5,000 ppm (IAEA 2018).

Surface and basin fluids can transport U only in significant concentrations (>0.01ppm) as U^{6+}, or precisely as uranyl ion (UO^{2+}). Precipitation of U from these fluids can be achieved by four principle mechanisms:

1. Substitution of elements in precipitating minerals, mainly Ca in apatite.

   This process leads to the occurrence of U within phosphate deposits, albeit at low grades, usually <150 ppm, but the high prevalence of phosphorite results in millions of tonnes of U (e.g., Guzman et al. 1995). Currently phosphates host ~25% of the known U resources worldwide.
2. Adsorption of uranyl on organic matter, clay, or secondary oxides, e.g., limonite.

   Adsorption is the main mechanism for the enrichment of U in black shales, which can contain up to 200 ppm U, but minerals containing essential U are absent. Black shales are so common that despite their low grade they account for roughly one third of world's U resources (IAEA 2018).
3. Precipitation of insoluble U^{6+} bearing minerals, mostly uranyl oxyanion compounds.

   The precipitation of these minerals is supported by evaporation of water and thus increasing concentrations of solved ions. As a result, deposits are formed in arid environments and associated with duricrust sediments, either in paleochannels or playas. The main mineral is usually carnotite. These deposits can be economical with up to 50,000 tonnes contained U and grades of up to 1 wt.% U (IAEA 2018). Typical carnotite deposits can be found in Western Australia, where the arid climate and the deep weathering of the U-rich Yilgarn Craton provide excellent conditions.

4. Reduction of U to the tetravalent state and subsequent precipitation, mostly as uraninite or coffinite.

   Reduction of U needs a reductive agent, this can be organic matter, graphite, sulphides, gases like methane, or Fe^{2+}. As a result, the deposits vary widely in morphology, size, and grade. The host rock is always a sediment, as permeability is essential for the precipitation of significant amounts of U. In most cases this is a medium- to coarse grained sandstone, but carbonate hosted U is not unusual. Three basic morphologies can be differentiated, concordant/stratabound, discordant, and roll front. Concordant U deposits occur in sediments which contain the reductant, e.g., organic or pyrite-rich sandstone. Uranium forms tabular to lenticular orebodies, parallel to the sedimentation. Discordant sediment-hosted orebodies usually use an external reductant, e.g., hydrocarbons rising along fractures or rarely mafic dykes crossing the sediment. Roll-front deposits occur if U-bearing oxidising fluids continuously move through a reductant rich sandstone. Upstream the sandstone is oxidised, free of reductant, and all U goes into solution. At contact with the reducing sediment downstream U precipitates as uraninite or coffinite. The resulting roll-front is convex in downstream direction and perpendicular to the direction of flow. The contact to the oxidised sandstone is sharp, to the reducing sandstone diffuse.

A unique subtype of U deposit, associated with diagenetic fluids, are unconformity-related deposits (Cuney 2005). Uranium is deposited directly at the contact between >1.6 Ma crystalline basement and <1.6 Ma (meta)sediments, often reaching several meters into the basement or the overlying metasediment. These deposits can contain up to 200,000 tonnes U and are unique in their particularly high grades (up to 20 wt.% U, IAEA 2018).

Almost all U deposits are thus formed by fluids and most of those deposits are secondary, U is remobilized from a low-grade source rock and deposited at a higher grade. Several factors control the development of a U deposit, they can be split in three groups: source, host, and fluid (Skirrow 2009). Important source parameters are U content and leachability, the ability of a fluid to reach the mineral and to dissolve U from this mineral (Skirrow 2009). The contribution of the host is basically the ability to precipitate U from the transporting fluid, either by providing sufficient amounts of reductant, or by significantly changing the properties of the transporting fluid, e.g., through pressure or temperature change, including evaporation (Skirrow 2009). It should be noted that these factors do not necessarily come from the host itself, a rock can be an excellent host due to reductant-rich water circulating through it.

Fluid parameters can be divided into three subgroups, chemistry, flow, and flow drivers (Skirrow 2009). Chemical parameters are oxidation state (fO_2) and ligand availability. Flow parameters are the volume of the transporting fluid and the time frame during which the fluid is present. Flow drivers enable the fluid to access rocks, e.g., by alteration or faulting, and they allow the fluid to move against gravity, e.g., through a steep geothermal gradient (Skirrow 2009).

Normal groundwater is capable of transporting U, it has the right oxidation state and usually contains carbonate and sulphate enhancing the transport of U. Volume and duration of flow of groundwater are usually excellent. As a result, the two most important factors for the formation of a sediment-hosted deposit are the source and the host.

1.1.2 Solid geology of South Australia

The crust underlying South Australia comprises three major crustal provinces, the Gawler Craton, the Curnamona Province, and the Musgrave Province (Fig. 1). The Proterozoic Gawler Craton (Hand et al. 2007) dominates the geology of South Australia spanning roughly 1,000 km from Kangaroo Island in the south to Oodnadatta in the north, and ~700 km from the Flinders Ranges in the east to the Nullarbor Plain in the west. The southern boundary of the Gawler Craton is the continental shelf, to the east the craton is separated from Curnamona Province by (meta)sediments of the Adelaide Geosyncline. To the northeast, the Craton is attached to the Lake Eyre basin, and to the northwest the craton is separated from the Musgrave Province by the Officer Basin, which extends southwards, and together with the Coompana Block, marks the western boundary of the craton. Relatively little is known about the crystalline basement outside the three major provinces, e.g., under the Officer or Lake Eyre basins.

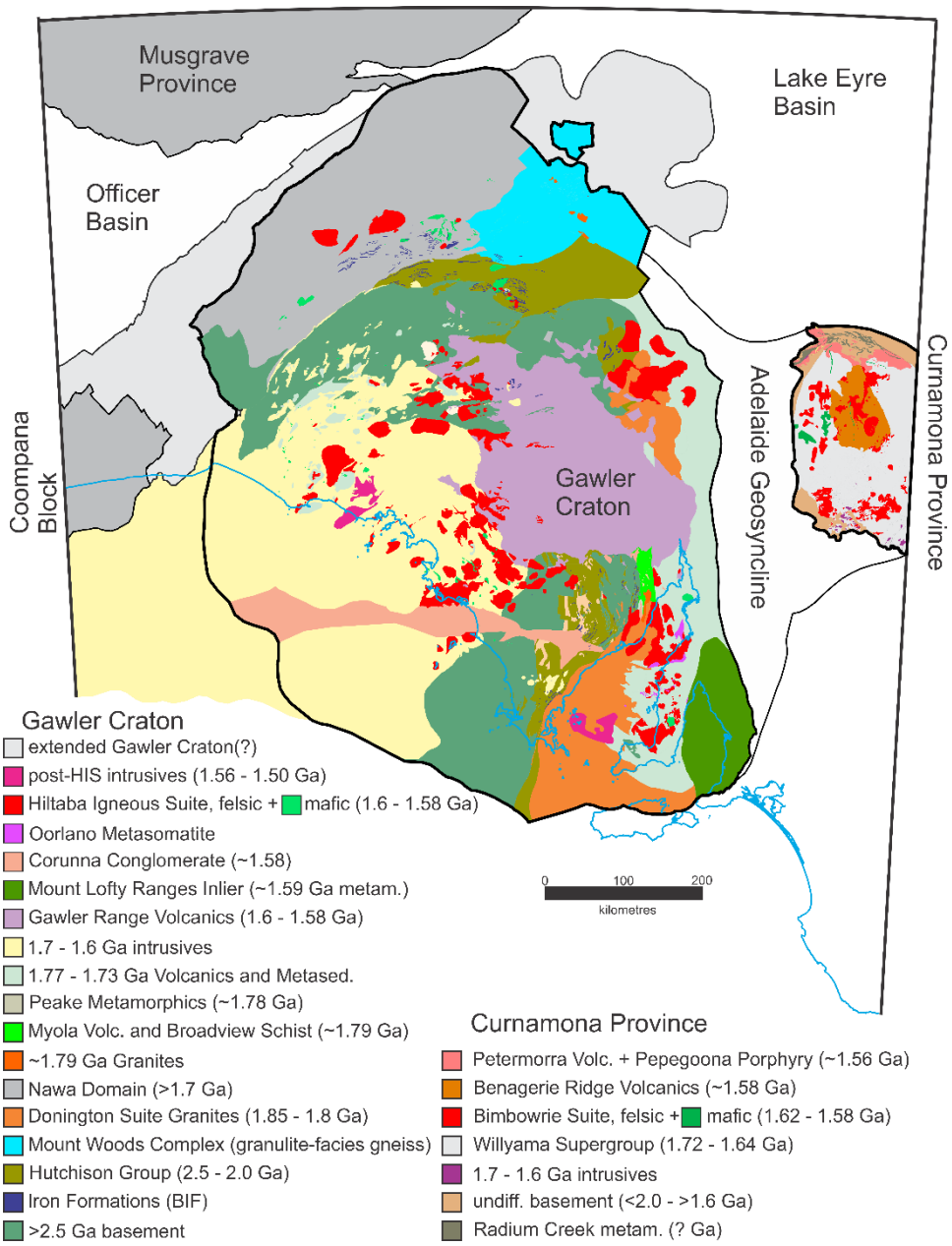

Figure 1. Archean to Mesoproterozoic solid geology of South Australia and geological provinces (adapted from SARIG 2019).

The Gawler Craton has experienced a complex magmatic and metamorphic evolution (e.g., Reid and Hand 2012 and references therein). Of major importance for U and its deposits is the fact that the Gawler Craton consists of two fused terranes, which separates the craton into two areas with substantially different basement geology: the eastern and western Gawler Craton. The palaeosuture of these terranes is the Kalinjala Mylonite Zone and its northern extension, the Roopena Fault, on the eastern edge of the Eyre Peninsula (Curtis and Thiel 2019). The northern continuation of this lithospheric boundary is covered by younger rocks but assumed to turn northwest. It remains unclear when the two terranes merged. After ~1750 Ma

the same igneous rocks can be found on both sides of the Gawler Craton, but older rocks, e.g., the ~1850 Ma Donington Suite granites do not fit the magmatism expected on convergent plate margins (Curtis and Thiel 2019). The fact that the Donington granites are confined to the eastern craton does not necessarily imply that the terranes were not fused, instead the palaeosuture could have controlled the placement.

At around ~1590 Ma, the Gawler Craton was intruded by bimodal rocks of the Hiltaba Suite (HS), which together with the contemporaneous Gawler Range Volcanics (GRV) form the Gawler Silicic Large Igneous Province (Allen et al. 2008). Intrusive rocks are dominantly felsic, although gabbros are also present (Daly et al. 1998; Allen et al. 2008). HS granitoids show significant differences depending on the basement they intrude (Stewart and Foden 2003, Budd 2006). In the eastern Gawler Craton, HS granitoids have, on average, higher contents of U and Th, but lower Mn, and are associated with IOCG deposits. The western HS granitoids have lower U and IOCG deposits are conspicuously absent, although Au, as well as base metal deposits have been discovered. In broad terms, the eastern and western Gawler Craton are equivalent to the Olympic Cu-Au province and the Central Gawler gold province (Budd and Skirrow 2007), showing the significant impact on metallogeny which different basements can have.

The South Australian Heat Flow Anomaly (SAHFA) covers a large part of South Australia, including the Curnamona Province, the Lake Eyre Basin, and the eastern Gawler Craton, but terminates at the palaeosuture (e.g., Neumann et al. 2000). This indicates significant differences in the U content in rocks of the eastern and western Gawler Craton and can readily explain the differences in U content seen in HIS granites.

The HS-affiliated Roxby Downs Granite hosts the supergiant Olympic Dam deposit, the World's largest U deposit with an estimated resource of ~2 Mt U, yet U is only a by-product of Cu mining. The genesis of the deposit is interpreted in terms of a magmatic-hydrothermal model (Ehrig et al. 2012, 2017; Verdugo-Ihl et al. in press; Courtney-Davies et al. in review) but remains hotly debated. The main U minerals are uraninite, coffinite, and brannerite (Macmillan et al. 2016, 2017). Hematite within the Olympic Dam deposit contains modest concentrations of U (Ciobanu et al. 2013; Verdugo-Ihl et al. 2017) but considering the abundance of hematite contributes a significant amount of the total U. Dating of uraninite yields a wide variety of ages, including the age of formation (Apukhtina et al. 2017) but also reflecting subsequent overprinting during later tectonothermal events. Based on these ages and the distinct textural types of uraninite recognised (Macmillan et al. 2016), U mineralisation can be divided into that deposited during an initial mineralisation event at ~1590 Ma almost

contemporaneous with emplacement of the granite (Courtney-Davies et al. in review) - likely from a hydrothermal fluid derived from the granite, and secondly, recrystallised and isotopically-reset mineralization relating to the Musgravian (~1300 Ma) and Delamerian (~520 Ma) Orogenies and emplacement of the Gairdner Dyke Swarm (~820 Ma), among others. Olympic Dam could thus be interpreted as a hybrid-type uranium deposit of mixed magmatic-hydrothermal-metamorphic origin (Skirrow 2009).

In the Curnamona Province to the East, the Ninnerie Supersuite (Wade 2011) appears synchronous with the GRV and HS. It consists of largely felsic volcanic and intrusive rocks and is likely analogous with the 'Hiltaba-Event' (Wade et al. 2012). Granites of the Ninnerie Supersuite are more diverse than the HIS and include S-, I-, and A-type granites. Several granites are highly anomalous with respect to U, e.g., Crocker Well Suite granites in the southern Curnamona province (Schofield 2011), and the Pepegoona Porphry in the Mount Painter Inlier, which likely sourced roll-front U deposits in the western Frome basin (Wülser et al. 2015). As mentioned, the SAHFA covers the Curnamona province and it is likely that the U enrichment of these rocks is the result of U-rich basement.

Although large-scale magmatism and metamorphism in the Gawler Craton and the Curnamona Province ceased around 1450 Ma and the cratons became stable, geological change was caused by development of basins, sedimentations and erosion.

1.1.3 Cainozoic basins

Even though several basins formed in what is now South Australia during the Proterozoic, Palaeozoic, and Mesozoic, they do not seem to have significance for U. Currently the oldest sediment unit hosting U in South Australia is the Cretaceous Bulldog Shale of the Lake Eyre Basin.

During the Cainozoic several basins formed, the three largest and most important are introduced here. The Eucla Basin overlies the western Gawler Craton and extends westwards far into Western Australia, where the basin is in contact with the Yilgarn Craton. The Lake Eyre Basin covers a large part of north-eastern South Australia outside the Gawler Craton. It later separated into several sub-basins of which the southern Callabonna sub-basin (overlying the Curnamona Province), is of major importance. The Pirie Basin, within which the Blackbush deposit is located, is confined to what is today the Spencer Gulf and its coast.

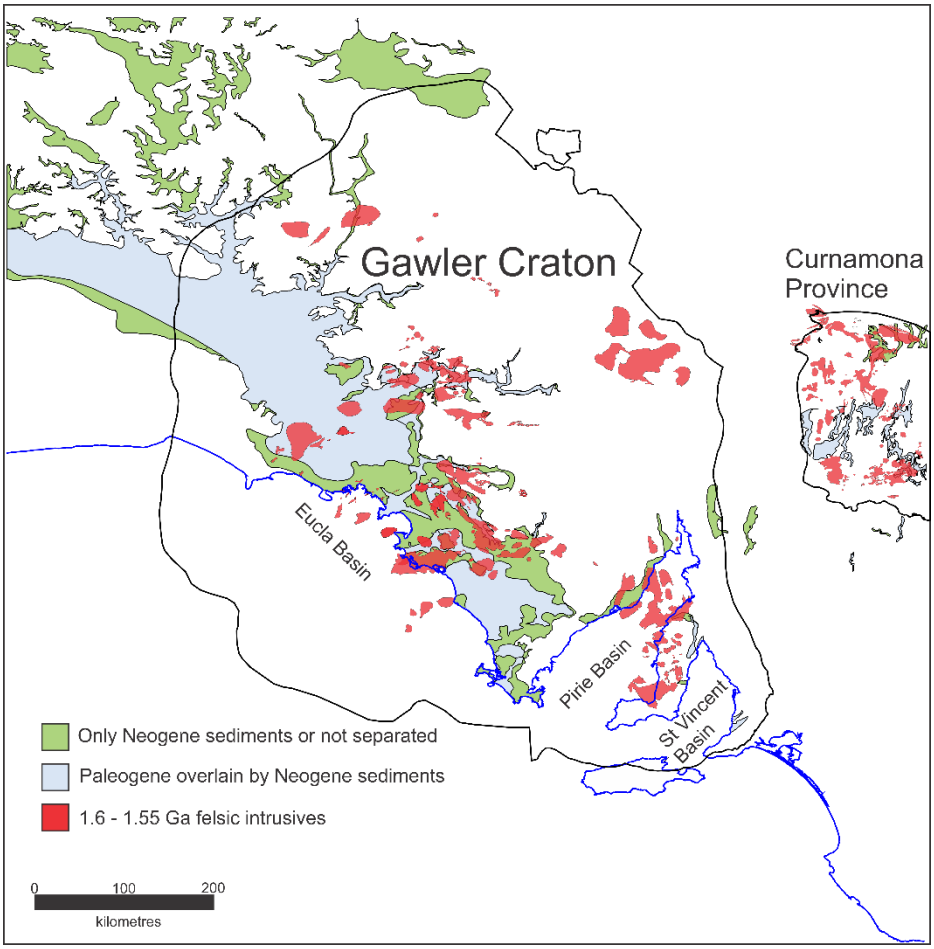

Figure 2. Cainozoic sediments in South Australia, and the most important source rocks of U, Mesoproterozoic intrusives. With data from SARIG (2019).

South Australia is a relatively flat continent and sea level changes affect large areas and can move the coastline up to several hundred kilometres inland. This is easily recognizable today by areas of South Australia that lie under sea level, notably the ephemeral lakes of Lake Eyre, Lake Torrens, Lake Frome, and their corresponding salt pans. In the Cainozoic, Australia was dominated by warm and often wet climates, delivering ideal conditions for flora and fauna (McGowran and Hill 2015). Combined, this leads to extended shallow marine to lacustrine sediments in the basins of South Australia. The restricted water depth limits water exchange and together with the high influx of organic matter leads to anoxic conditions in these sediments. The stratigraphy in the basins is similar and can roughly be divided in three timeframes, late Palaeocene-Eocene-early Oligocene, late Oligocene-Miocene, and Pliocene to today (Alley et al. 1999).

During the Eocene, the basins receive largely siliciclastic sediments, often organic-rich. In the Eucla basin, the Maralinga Member was deposited, consisting of marine, fluviatile, or aeolian sandstone and minor limestone. One unit of the Maralinga Member contains organic-

rich sandstones and lignites. The unit reaches 40 to 50 m in thickness, the lignite up to 20 m. In the southern Callabonna Basin, the Eyre Formation contains, often organic-rich, siliciclastic sediments, locally reaching a thickness of 20 m. In the Pirie Basin, organic-rich sediments and lignites of the Kanaka Beds were deposited (Alley et al. 1999). The Kanaka Beds are always carbonaceous and reduced.

Sedimentation was variable in the Oligocene-Miocene, but with similar patterns in each basin. All three basins start the beginning of sedimentation with siliciclastic sediments, often fining upward, followed by limestones and dolomites. The limestones are often interrupted by (organic-rich) clays and lignites (Alley et al. 1999). In the Pirie Basin, all limestones and oxidised siliciclastic sediments between the underlying reduced Kanaka Beds and the overlying Pliocene Gibbon Beds clays are pooled together and called Melton Limestone. The age of the Melton Limestone unit is debated. Hou et al. (2012) mention an age of late Eocene to early Miocene, while McAvaney et al. (2014) give a range from Late Oligocene to Middle Miocene. In addition, reduced carbonaceous layers interspersed within the Melton Limestone are either 'unnamed' (Hou et al. 2012), or added to the Kanaka Beds (McAvaney et al. 2014), which is used as collective term for reduced Tertiary sediments in the Pirie Basin. Following the naming scheme of Hou et al. (2012) and as used by UraniumSA (e.g. UraniumSA 2013), the Kanaka Beds are defined as reduced **Eocene** sediments in this thesis. Despite this, the ages given by McAvaney et al. (2014) are likely a much better estimate for the age of the Melton unit.

The third phase is largely siliciclastic again with dune sands in the Eucla Basin, the Gibbon Bed clays in the Pirie Basin, and fine-grained lacustrine sediments in the southern Callabonna, showing its disconnection from the ocean (Alley et al. 1999).

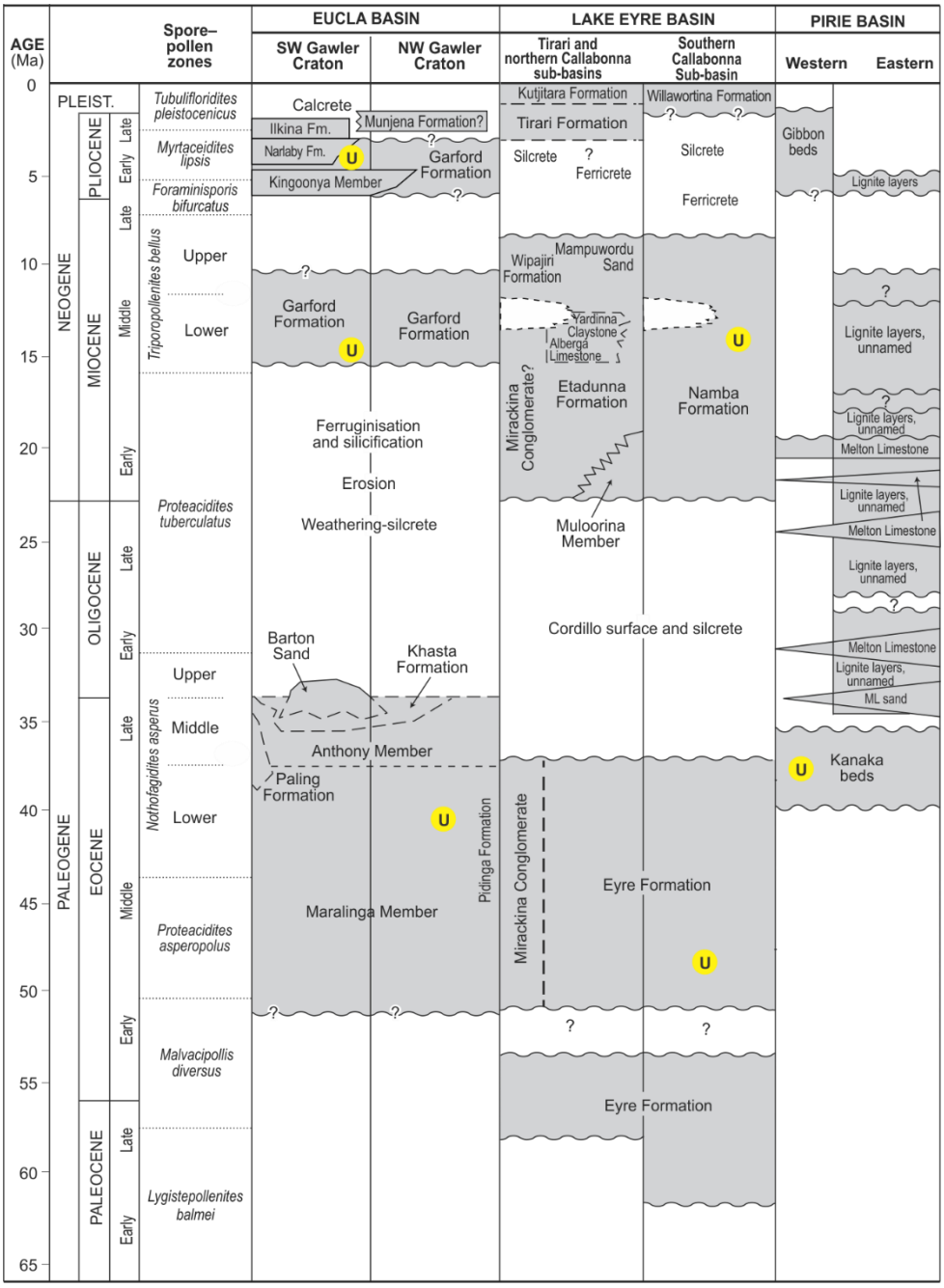

Figure 3. Cainozoic stratigraphy of selected South Australian basins. (after Hou et al. 2012).

1.1.4 Uranium deposits in South Australia

South Australia is recognized as U-rich and hosts a wide variety of magmatic, metamorphic, and/or surface/basin derived deposits. Currently, only the hybrid-type IOCG deposits and sediment hosted U deposits are of economic importance. Three mines are in operation: Olympic Dam in the Gawler Craton; as well as Four Mile and Beverley in the northern Curnamona Province. The Honeymoon mine, southern Curnamona Province, is

approved and could be operational, but is currently on care and maintenance due to low U prices.

As given above, South Australia offers a variety of U-rich igneous rocks and suitable organic-rich host rocks. At Beverley, U is hosted in tabular and lenticular bodies in organic-rich units of the Miocene Namba Formation and likely sourced from U-rich granites of the Mount Painter Inlier ~12 km upstream (Wülser et al. 2011). The Four Mile deposit also sources its U from the Mount Painter Inlier, but the host are sands of the Eocene Eyre Formation (Wilson 2015).

The Honeymoon deposit is a classic roll-front deposit sourced from the U-rich Honeymoon granite of the Ninnerie Supersuite. It is hosted in organic-rich Eyre Formation (Wilson 2015).

1.1.5 The Blackbush deposit

The first indication of U mineralization in the organic-rich sediments of the Kanaka Beds was a 'redox' signature in a gamma ray log produced by BHP in the 1980s, drilling for lignite in the Pirie Basin (BHP 1982). This signature is characteristic for an intercepted roll front. In 2006, driven by this signature, UraniumSA, a junior exploration company, recognized the Kanaka Beds as highly prospective for U and significant effort was undertaken for a thorough exploration. The first drill hole intersected a roll front, which culminated in the discovery of the Blackbush deposit in 2007 (UraniumSA 2007), and shortly after the discovery of the geologically similar Plumbush deposit. The U is mainly hosted in organic-rich sediments of Kanaka Beds affiliation, unconformably overlying clay-altered granite.

1.1.5.1 Stratigraphy

1.1.5.1.1 Sediments

A palynological study of the mineralised sediments identified the spore-pollen zone of *Middle Nothofagidites asperus*, which denotes an age of middle to late Eocene and identifies the sediment as Kanaka Beds (Stoian 2009). The Kanaka Beds comprise all siliciclastic sediments of Eocene age in the Pirie basin, their depositional environment is mainly lacustrine to lagoonal-estuarine. In and around the Blackbush deposit, located on the western edge of Pirie Basin, there is significant fluviatile influence and the Kanaka Beds are confined to a paleochannel (Fig. 4).

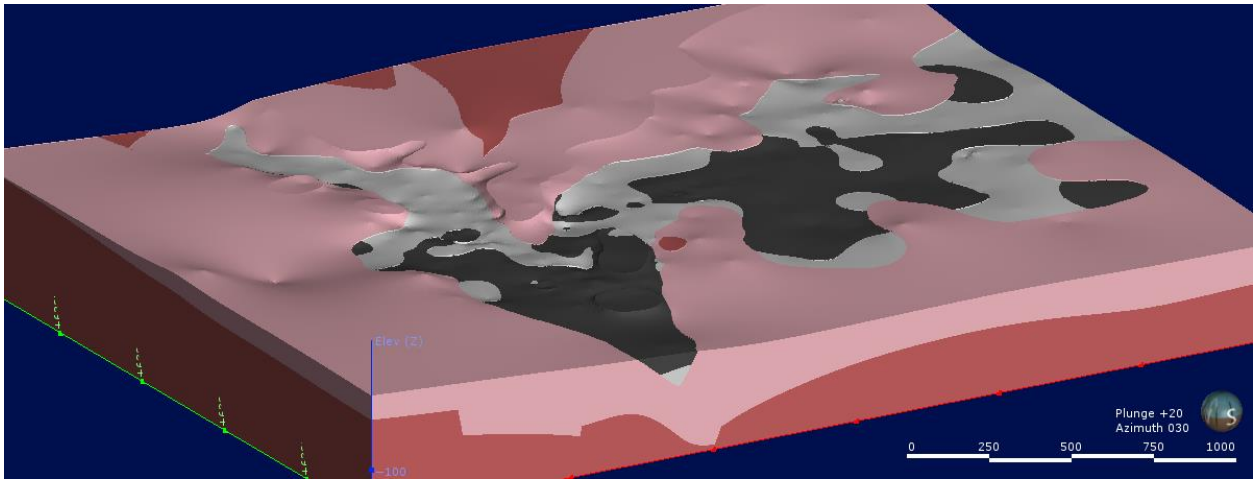

Figure 4. three-dimensional model of palaeochannel, including Kanaka Beds (black+white) and underlying granite (red). Provided by UraniumSA.

UraniumSA (2013) defined five units named A to E from oldest to youngest, based on drill cores. Unit A and B are interpreted as fluviatile sediments of braided and anastomosing rivers, C and D are (marine) delta sediments, lagoonal-estuarine sediments form unit E (UraniumSA 2013). All units consist of usually well-sorted upward-fining or upward-coarsening cycles. The grain size varies widely from clay to pebbles. Organic content is negatively correlated with grain size, meaning finer sediments usually have more organic material, several upward-fining cycles are topped by lignite. All units are separated by erosive horizons, and sediments over the horizon often contain reworked material from below the horizon, e.g., clay-clasts or lignite fragments. The colour of these five units is brown-grey to black illustrating their highly reduced nature.

These five units are followed by a sixth unit F, a limonitic, fossiliferous coarse-grained sand, which does not contain organic material, interpreted as barrier bar (UraniumSA 2013). This clearly more oxidised unit is separated from the underlying unit E by an erosive horizon. Based on drill logs from UraniumSA, it appears that the redox boundary and the erosive horizon are congruent, supporting the idea that the redox states of the units are defined by their organic content and are likely unchanged after sedimentation, e.g. by later oxidising fluids. As mentioned above the Kanaka Beds are reduced, and oxidised sediments are part of the Melton Limestone. In documents of UraniumSA unit F is informally called ‘Melton Sand’ to avoid confusion resulting from the mismatch of unit name ‘Limestone’ and observed lithology. An Eocene-Miocene unconformity is postulated between units E and F (UraniumSA 2013), likely based on an earlier report (BHP 1982) which documented the age-dating of limonitic, fossiliferous coarse-grain sand, resembling unit F, and which yielded a Miocene age. Even

though most publications assume an earlier start of oxidised sedimentation in the Pirie Basin (see section 1.1.3).

The 'Melton Sand' is overlain other units of the Melton Limestone, which comprises, besides the name-giving limestones, limonitic, fossiliferous sands(tones) and clays (McAvaney et al. 2014). The top of the Melton Limestone unit is weathered and eroded (Hou et al. 2012). The Pliocene clays of the Gibbon beds cover everything in the Pirie Basin and are the base of all quaternary soils (Hou et al. 2012).

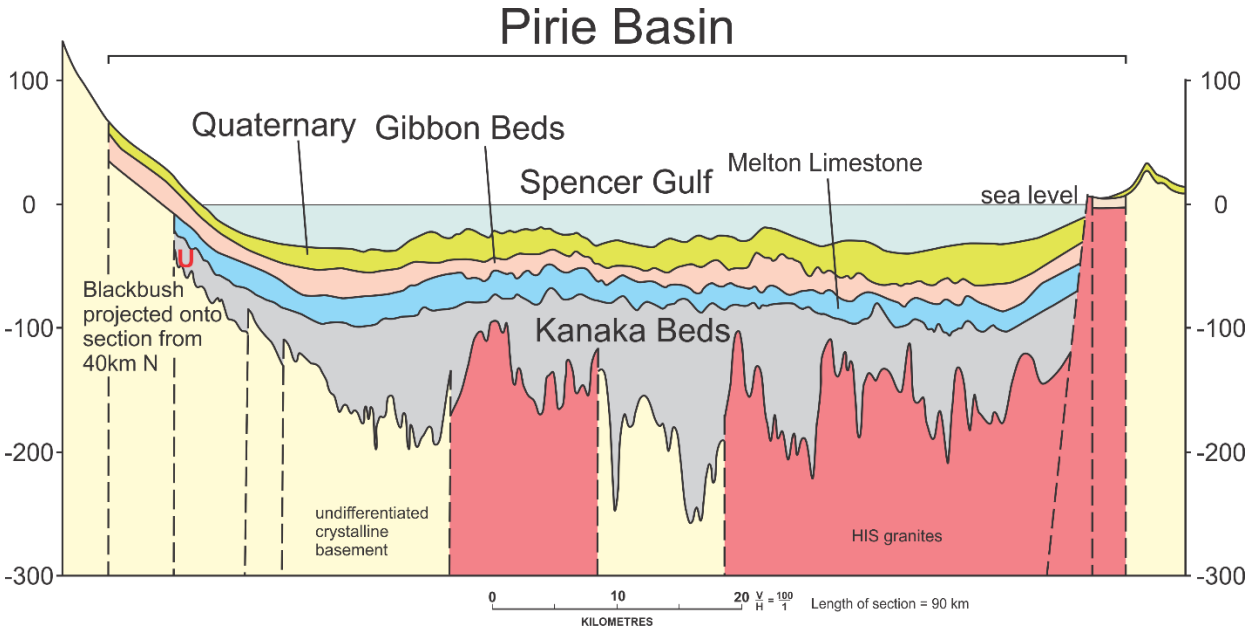

Figure 5. Profile of the Pirie Basin (after Hou et al. 2012). Vertical scale (in metres) is exaggerated.

It should be noted that all units, including the crystalline basement, are affected by later tectonic movement, likely starting in the late Miocene (~10 Ma) and still active today. It appears the Pirie Basin, as a whole, is subsiding, possibly in a slightly extensional setting, and areas in the centre are more strongly affected than the edges, but this is not uniformly the case. The area of the Blackbush deposit is crossed by faults with several meters offset along these faults (Fig. 6). The shape of the paleochannel is largely the result of water following faults (compare Fig. 4 and Fig. 6). In addition to the smaller relative movement within the deposit the larger area apparently dropped several tens of meters. Today the Blackbush deposit lies under sea level (Fig. 5) and the groundwater is of normal marine salinity (UraniumSA 2013).

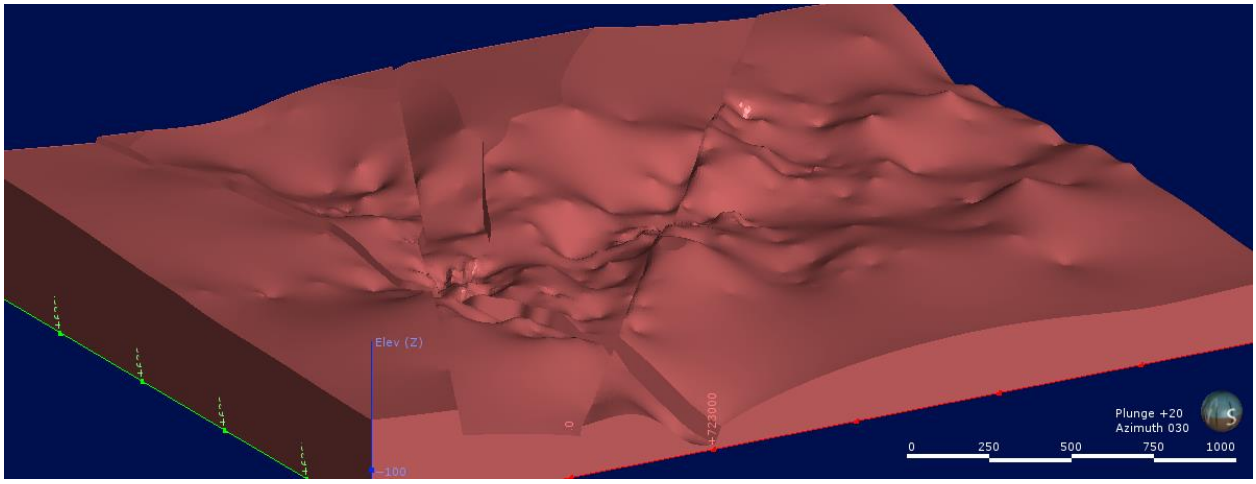

Figure 6. three-dimensional model of underlying granite (without saprolite), same area as Fig. 4. Provided by UraniumSA.

1.1.5.1.2 Crystalline basement

The Kanaka Beds overlie a Hiltaba-age granite, resulting in an unconformity with a more than 1.5 Ga age gap. In the larger area around the deposit UraniumSA identified (at least) three different granitic domains, based on different reactions in total magnetic intensity geophysical imaging (a summary of UraniumSA's interpretations of the different domains is given in Bluck and Brown 2017). In 2011, the three most prominent domains were targeted by government funded drilling to acquire material for geochemistry and geochronology. Based on this material Anthony Reid proposed in 2013 the separation of the pluton into two granites, a coarse-grained red granite under the deposit, and a green granite in the centre of the pluton (published in Reid et al. 2017). The third domain, arc shaped and wedged between the other two, was interpreted as altered green granite (Reid et al. 2017). Therefore, only red and green granite were dated (SHRIMP U-Pb on zircons), the ages are basically identical within error, red granite 1586±6 Ma, green granite 1584±4 Ma (Reid et al. 2017). Samples of all three domains are geochemically and mineralogically similar, the main mineral components are perthitic feldspar, quartz, plagioclase, biotite, and accessories (Reid et al. 2017). The age, geochemistry, and appearance identify them as belonging to the Hiltaba Igneous Suite (Reid et al. 2017). More precisely, the anomalously high U, Nb, and Rb indicates a Hiltaba granite belonging to the Roxby Downs Group (Budd et al. 1998).

The red granite under the deposit is weakly fractured, crosscut by various veins, and contains several zones of alteration, e.g., 'fluorite flooding' (Reid et al. 2017, UraniumSA 2015).

The upper 10 to 25 meters of the granite are heavily clay-altered, feldspar is replaced by kaolinite ± illite, this unit is informally called saprolite (UraniumSA 2014). The exact mechanism of clay-alteration is debated. It is largely the result of weathering, but UraniumSA postulates a partly hydrothermal origin of the clay, based on observations of undisturbed magmatic REE patterns in several samples of clay-altered granite (R. Bluck, pers. comm. 2019), but this might be explained by REE being trapped in refractory minerals. The presence of monazite and xenotime in the saprolite and sediment indicates that they are not attacked by fluids in the system (Reid et al. 2017). The saprolite can be divided into three units, the lowest unit is red of dispersed hematite, the middle unit is yellow and contains limonite, the highest unit in contact with the Kanaka Beds is reduced, of white to grey colour and contains pyrite (Russel Bluck, pers. comm. 2019).

The Blackbush deposit can be separated into an eastern and western mineralised zone (UraniumSA 2013). The western zone is upstream, the U here is mainly concentrated along the unconformity between the Kanaka Beds and the saprolite, largely hosted in the sediment, to a minor degree in the saprolite (UraniumSA 2014). The U mineralisation extends along fractures into the saprolite (UraniumSA 2014). In addition, U is enriched in tabular to lenticular bodies associated with zones of higher organic material, including lignite layers. In the eastern zone the unconformity and the lowest 5-10 m interval of the Kanaka Beds are not mineralised, the U is present as tabular to lenticular bodies, and to a smaller part as a roll-front (UraniumSA 2014). The eastern mineralised zone is interpreted as remobilized and redeposited U of the western zone (UraniumSA 2014). It should be noted that the 'ore bodies' do not have sharp boundaries. The cores have high concentrations up to several thousand ppm, with increasing distance from the core the grades drop until they reach background/uneconomic levels. If the cut-off grade of U is chosen low enough (~50 ppm) the whole paleochannel appears as one large deposit.

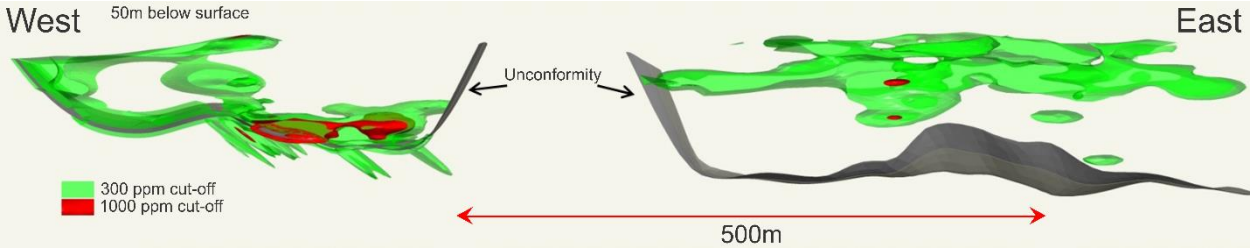

Figure 7. NW-SE profile through the Blackbush deposit, depicting the unconformity and U mineralization (adapted from UraniumSA 2013)

At a cut-off of 100 ppm U, UraniumSA estimates ~56.5% of the U is hosted in sand of the Kanaka Beds (stratabound bodies), ~11.5% in sediments finer than sand, and lignite, ~6.5% at the unconformity, ~2.5% in Unit F ('Melton Sand'), and ~23.0% in the saprolite (UraniumSA 2013).

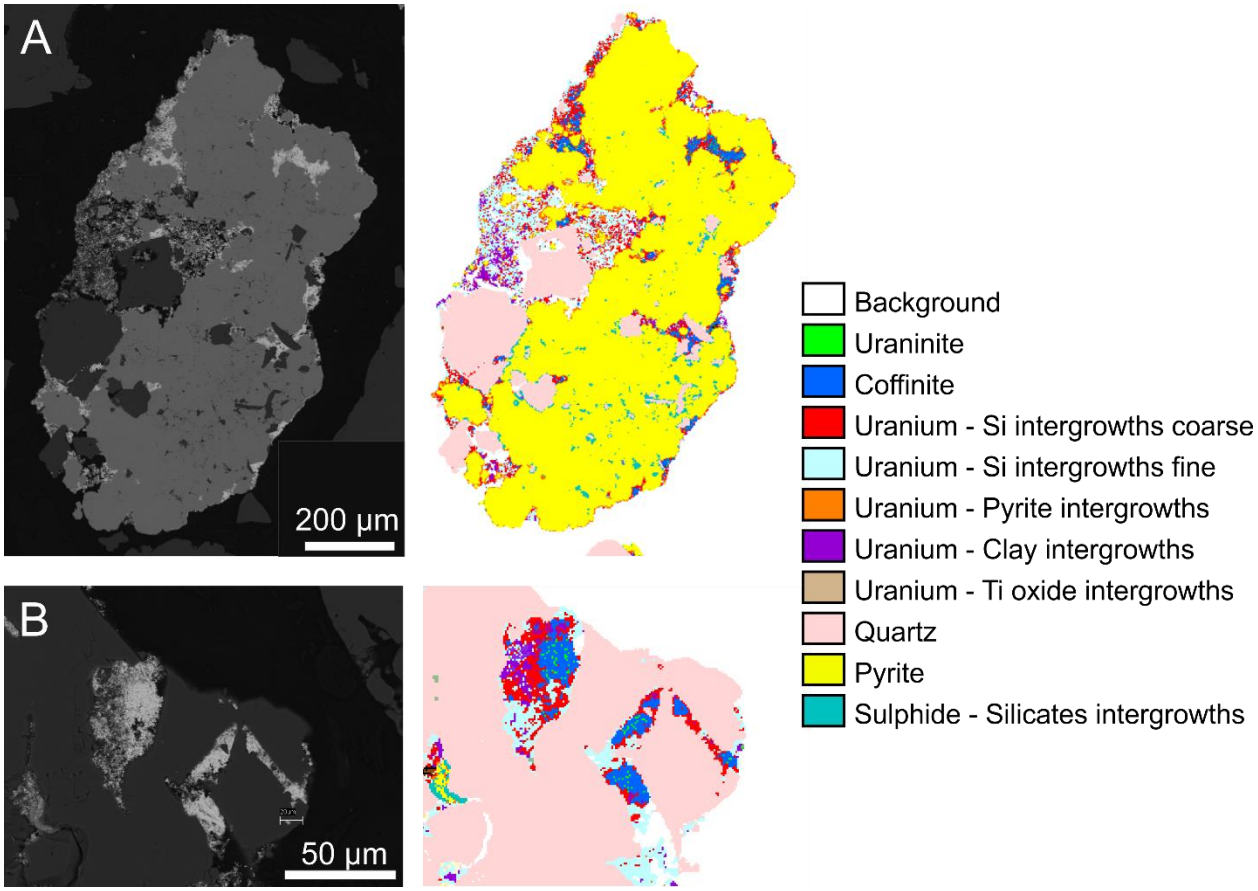

Figure 8. Backscatter electron and QEMSCAN images of selected grains. A: pyrite nodule; B: coffinite and clay along fractures in quartz. Provided by UraniumSA.

The main U mineral is coffinite, it is often associated with framboidal pyrite, or present as fine grained coffinite-pyrite or coffinite-clay intergrowth, in addition coffinite can be associated with lignite fragments (UraniumSA 2010). These intergrowths can mostly be found along fractures in quartz grains, but it remains unclear if this concentration of U along fractures has any significance or is an artefact (UraniumSA 2010). The U minerals are very delicate and easily removed during sample processing, e.g., during drying of samples. To the authors knowledge estimates of the prevalence of U^{6+} absorbed onto organic matter do not exist.

Exploration work to date by UraniumSA and Samphire Uranium comprises a total of 791 drillholes. These have largely targeted the sediment-hosted uranium mineralization and saprolite. Only nine diamond drillholes have intersected granitic basement.

1.2 RESEARCH OBJECTIVES

The objectives of the research presented in this thesis are firstly to acquire a comprehensive understanding of the petrography, mineralogy and geochronology of bedrock granites in the Samphire area. Emphasis is placed on identifying alteration and differences between the macroscopically distinct types of granite present. Secondly, the research aims to provide a characterization of the sediment-hosted mineralization and an understanding of the spatial-temporal relationships between this and the underlying granites. The overarching aim is to provide a genetic model for the mineralization that is supported by a variety of data. The fundamental knowledge gained through this study also contributes to an understanding of bedrock uranium throughout the eastern Gawler Craton, and its distribution in deposits of different types.

Samples used for this project were exclusively from drillcore. Twenty-seven granite samples were acquired from nine different drill holes, including representative 'fresh' granite, veins, and alterations. One drill core provided all 17 saprolite samples, including ten samples of reduced saprolite, two samples of limonitic, and five samples of hematite-bearing saprolite. Fourteen samples of sand were mounted in one-inch blocks, two per each of seven drill holes. In addition, UraniumSA provided twelve high-U samples, consisting of pyrite nodules and lignite fragments. These samples were chosen purely based on their U content and are likely from various depths and units within in the Kanaka Beds.

Following preparation, samples were analysed using a range of complimentary qualitative and quantitative microanalytical techniques capable of characterization at different scales of observation, including microscopy (optical, scanning electron), chemical analysis (electron probe microanalysis, and laser-ablation inductively coupled plasma mass spectrometry), and U-Pb zircon geochronology (SHRIMP).

Each of the three main chapters in this thesis is written as an independent published or submitted manuscript, and therefore further details on methodology and sampling are included within each chapter.

1.3 THESIS STRUCTURE

One of the fundamental knowledge gaps explored in research reported in this thesis is the petrography and mineralogy of granites underlying the Blackbush deposit. **Chapter 2** (Domnick et al. 2018) constrains the mineralogy and geochemistry and primary igneous

relationships between three different granitoids within the Samphire Pluton and their alteration overprints.

Chapter 3 (Domnick et al. in review) firstly addresses the geochronology of the three granites and assess the implications these data have for mineralization. This chapter also contains a critical evaluation of the ages obtained and closed/open-system behaviour in light of micron- to nanoscale characterization of contained zircons. The results of these studies permit insights into the evolution of the Samphire Pluton in space and time and carry implications for U-Pb zircon geochronology across the Eastern Gawler Craton.

Chapter 4 (Domnick et al. 2020) addresses uranium mineralization within the cover sequence and within saprolite. This chapter includes a detailed mineralogical characterization of sediment-hosted mineralization and provides valuable new constraints on the timing of coffinite mineralization.

Chapter 5 provides a summary of key findings and implications of this research, as well as identifying several areas for future investigation. Supplemental and appendix material for each chapter are all included within **Chapter 6**, as well as additional materials (co-authored publications and conference contributions). A complete set of references cited is given in **Chapter 7**,

2 REFERENCES

Allen, S.R., McPhie, J., Ferris, G., Simpson, C., 2008. Evolution and architecture of a large felsic Igneous Province in western Laurentia: The 1.6 Ga Gawler Range Volcanics, South Australia. Journal of Volcanology and Geothermal Research 172, 132–147.

Alley, N.F., Clarke, J.D.A., MacPhail, M., Truswell, E.M., 1999. Sedimentary infillings and development of major Tertiary palaeodrainage systems of south-central Australia. In: Thiry, M., Simon-Coinçon, R. (Eds), Palaeoweathering, Palaeosurface and Related Continental Deposits, Special Publication No. 27, International Association of Sedimentologists, Blackwell Science, 337-367.

Apukhtina, O.B., Kamenetsky, V.S., Ehrig, K., Kamenetsky, M.B., Maas, R., Thompson, J., McPhie, J., Ciobanu, C.L., Cook, N.J., 2017. Early, deep magnetite-fluorapatite mineralization at the Olympic Dam Cu-U-Au-Ag deposit, South Australia. Economic Geology 112, 1531-1542.

BHP, 1982. Open File Envelope No. 4124, EL 766 Mullaquana, Progress and final reports for the period 8/12/80 to 7/12/82.

Bluck, R., Brown, C., 2017. Characterisation of the Samphire granite, Hiltaba Suite, northeastern Eyre Peninsula. MESA Journal 85, 31-40.

Budd, A.R., 2006. A- and I-type subdivision of the Gawler Ranges-Hiltaba Volcano-Plutonic Association. Presentation at Goldschmidt Conference 2006.

Budd, A.R., Skirrow, R.G., 2007. The nature and origin of gold deposits of the Tarcoola goldfield and implications for the central Gawler gold province, South Australia. Economic Geology 102, 1541–1563.

Budd, A.R., Wyborn, L., Bastrakova, I., 1998. Exploration significance of the Hiltaba Suite, South Australia. AGSO Research Newsletter 29, 1-4.

Cerny, P., Blevin, P.L., Cuney, M., London, D., 2005. Granite-related ore deposits. Economic Geology 100th Anniversary Volume, 337-370.

Ciobanu, C.L., Wade, B.P., Cook, N.J., Schmidt Mumm, A., Giles, D., 2013. Uranium-bearing hematite from the Olympic Dam Cu-U-Au deposit, South Australia: a geochemical tracer and reconnaissance Pb-Pb geochronometer. Precambrian Research 238, 129-147.

Courtney-Davies, L., Ciobanu, C.L., Tapster, S.R., Cook, N.J., Ehrig, K., Crowley, J.L., Verdugo-Ihl, M.R., Wade, B.P., Condon, D.J., in review. Opening the Magmatic-Hydrothermal Window: High-Precision U-Pb Geochronology of the Mesoproterozoic Olympic Dam Cu-U-Au-Ag Deposit, South Australia. Economic Geology.

Cuney, M., Friedrich, M., 1987. Physicochemical and crystal-chemical controls on accessory mineral paragenesis in granitoids. Implications on uranium metallogenesis. Bulletin de mineralogie 110, 235-247.

Cuney, M., 2005. World-class unconformity-related uranium deposits: Key factors for their genesis. In: Mao J., Bierlein F.P. (Eds), Mineral Deposit Research: Meeting the Global Challenge. Springer, Berlin, Heidelberg.

Cuney, M., 2009. The extreme diversity of uranium deposits. Mineralium Deposita 44, 3-9

Cuney, M., 2010. Evolution of uranium fractionation processes through time: driving the secular variation of uranium deposit types. Economic Geology 105, 553-569

Cuney, M., 2014. Felsic magmatism and uranium deposits. Bulletin de la Société Géologique de France 185, 75-92.

Curtis, S., Thiel. S., 2019. Identifying lithospheric boundaries using magnetotellurics and Nd isotope geochemistry: An example from the Gawler Craton, Australia. Precambrian Research 320, 403-423.

Dahlkamp, F.J., 1993. Uranium Ore Deposits. Springer.

Daly, S.J., Fanning, C.M., Fairclough, M.C., 1998. Tectonic evolution and exploration potential for the Gawler Craton, South Australia. AGSO Journal of Australian Geology and Geophysics 17, 145–168.

Domnick, U, Cook, N.J., Bluck, R., Brown, C., Ciobanu, C.L., 2018. Petrography of granitoids from the Samphire Pluton, South Australia: implications for uranium mineralisation in overlying sediments. Lithos 300–301, 1–19.

Domnick, U., Cook, N.J., Ciobanu, C.L., Courtney-Davies, L., Dmitrijeva, M., Verdugo-Ihl, M.R., Xu, J., Keyser, W., Slattery, A., Kennedy, A.K., Bluck, R., in review. Micron- to nanoscale characterisation and U-Pb geochronology of zircon from granites of the Samphire Pluton, South Australia. Precambrian Research.

Domnick, U., Cook, N.J., Ciobanu, C.L., Wade, B.P., Courtney-Davies, L., Bluck, R., 2020. A Mineralisation Age for the Sediment-Hosted Blackbush Uranium Prospect, North-Eastern Eyre Peninsula, South Australia. Minerals 10, 191; doi:10.3390/min10020191

Ehrig, K., McPhie, J., Kamenetsky, V., 2012. Geology and mineralogical zonation of the

Olympic Dam iron oxide Cu-U-Au-Ag deposit, South Australia. In: Hedenquist, J.W., Harris, M., Camus, F. (Eds), Geology and Genesis of Major Copper Deposits and Districts of the World, a Tribute to Richard Sillitoe. SEG Special Publication 16, 237-268.

Ehrig, K., Kamenetsky, V., Mc`Phie, J., Cook, N.J., Ciobanu, C.L., 2017. Olympic Dam iron-oxide Cu-U-Au-Ag deposit. In: G.N. Phillips, ed., Australian Ore Deposits. AusIMM, Melbourne, p. 601-610.

Finch, R.J., Hanchar, J.M., 2003. Structure and chemistry of zircon and zircon-group minerals. Reviews in Mineralogy and Geochemistry 53, 1–25.

Government of South Australia (Department for Energy and Mining) (2019). Uranium. http://www.energymining.sa.gov.au/minerals/invest/mineral_commodities/uranium

Guo, X.F., Szenknect, S., Mesbah, A., Labs, S., Clavier, N., Poinssot, C., Ushakov, S.V., Curtius, H., Bosbach, D., Ewing, R.C., Burns, P.C., Dacheux, N., Navrotsky, A., 2015. Thermodynamics of formation of coffinite, $USiO_4$. PNAS 112, 6551-6555.

Guzman, E.R., Solache, M., Iturbe-García, J.L., Ordonez-Regil, E., 1995. Uranium in phosphate rock and derivates. Journal of Radioanalytical and Nuclear Chemistry 189, 301-306.

Hand, M., Reid, A., Jagodzinski, L., 2007. Tectonic Framework and Evolution of the Gawler Craton, Southern Australia. Economic Geology 102, 1377–1395.

Hou, B., Fabris, A.J., Keeling, J.L., Fairclough, M.C., 2007. Cainozoic palaeochannel hosted uranium and current exploration methods, South Australia. MESA Journal 46, 34–39.

Hou, B., Fabris, A.J., Michaelsen, B.H., Katona, L.F., Keeling, J.L., Stoian, L., Wilson, T.C., Fairclough, M.C., Cowley, W.M., 2012. Paleodrainage and Cenozoic costal barriers of South Australia: a new map and GIS dataset. MESA Journal 66, 26–32.

Hou, B., Keeling, J., Li, Z., 2017. Paleovalley-related uranium deposits in Australia and China: a review of geological and exploration models and methods. Ore Geology Reviews 88, 201–234.

IAEA, 2018. Geological Classification of Uranium Deposits and Description of Selected Examples. IAEA TECDOC No. 1842. Vienna: International Atomic Energy Agency, 2018.

IAEA, 2019. PRIS Power Reactor Information System. https://pris.iaea.org/pris/, accessed 11/11/19.

Ingham, E.S., Cook, N.J., Cliff, J., Ciobanu, C.L., Huddleston, A., 2014. A combined chemical, isotopic and microstructural study of pyrite from roll-front uranium deposits, Lake Eyre Basin, South Australia. Geochimica et Cosmochimica Acta 125, 440-465.

IUPAC, 1998. Isotopic compositions of the elements 1997. Pure & Appl. Chem 70, 1, 217-235.

Kristensen, H.M., Korda, M., 2019. Tactical Nuclear Weapons 2019. Bulletin of the Atomic Scientists, 75:5, 252-261.

Macmillan, E., Cook, N.J., Ehrig, K., Ciobanu, C.L., Pring, A., 2016. Uraninite from the Olympic Dam IOCG-U-Ag deposit: linking textural and compositional variation to temporal evolution. American Mineralogist 101, 1295–1320.

McAvaney, S.O., Thiel, S., Wade, C.E., 2016. The Kalinjala Shear Zone - intracontinental

shear zone or palaeosuture? Paper Presented at the Australian Earth Science Convention, Adelaide.

McGowran, B., Hill, R.S., 2015. Cenozoic climatic shifts in southern Australia. Transactions of the Royal Society of South Australia 139, 1, 19-37.

Murphy, W.M., Shock, E.L., 1999. Environmental aqueous geochemistry of actinides. In: Burns, P.C., Finch, R. (Eds), Uranium: Mineralogy, Geochemistry and the Environment. Reviews in Mineralogy and Geochemistry 38, 221–254.

Neumann, N., Sandiford, M., Foden, J., 2000. Regional geochemistry and continental heat flow: Implications for the origin of the South Australian heat flow anomaly. Earth and Planetary Science Letters 183, 107-120.

Peiffert, C., Nguyen-Trung, C., Cuney, M., 1996. Uranium in granitic magmas. Part 2: Experimental determination of uranium solubility and fluid-melt partition coefficients in the uranium oxide-haplogranite-H_2O-NaX (X=Cl,F) system at 770°C 2 kbar. Geochimica et Cosmochimica Acta 60, 1515-1529.

Reid, A., 2019. The Olympic Cu-Au Province, Gawler Craton: A Review of the Lithospheric Architecture, Geodynamic Setting, Alteration Systems, Cover Successions and Prospectivity. Minerals 9(6), 371.

Reid, A.J., Hand, M., 2012. Mesoarchean to Mesoproterozoic evolution of the southern Gawler Craton, South Australia. Episodes 35, 216–225.

Reid, A., Jagodzinski, E., Gerhard, F., 2017. Project PGC03-01: Geochronology from the Samphire Uranium Project. In: Jagodzinski, E.A., Reid, A.J. (Eds), PACE Geochronology: Results of collaborative geochronology projects 2013–2015, Report Book 2015/00003. Department of the Premier and Cabinet, South Australia, Adelaide, 10–28.

Samphire Uranium, 2019. http://www.samphireuranium.com.au/.

Schofield, A., 2011. Uranium systems processes in the Crocker Well Suite, South Australia. Geoscience Australia. Record 2011/45.

Shand, S.J., 1943. Eruptive rocks. Their genesis, composition, classification, and their relation to ore-deposits with a chapter on meteorite. John Wiley & Sons, New York.

Skirrow, R., Bastrakov, E.N., Barovich, K., Fraser, G.L., Creaser, R.A., Fanning, C.M., Raymond, O.L. & Davidson, G.J., 2007. Timing of Iron Oxide Copper-Gold Hydrothermal Activity and Nd Isotope Constraints on Metal Sources in the Gawler Craton, South Australia. Economic Geology 102, 1441–1470.

Skirrow, R.G. (Ed), 2009. Uranium ore-forming systems of the Lake Frome region, South Australia: Regional spatial controls and exploration criteria. Geoscience Australia Record 2009/40.

Stewart, K.P., Foden, J., 2003. Mesoproterozoic granites of South Australia. South Australia. Department of Primary Industries and Resources. Report Book 2003/15.

Stoian, L.M., 2009. Palynological analysis of samples 2490100, and 2490112. South Australian Resources Information Gateway. minerals.sarig.sa.gov.au, accessed 05/11/19.

Taylor, S.R., 1964. Abundance of chemical elements in the continental crust; a new table. Geochimica et Cosmochimica Acta 28, 1273-1285.

UraniumSA, 2007. Uranium discovery. ASX RELEASE 12 December 2007. 1–4 pp,

http://www.asx.com.au/asx/statistics/displayAnnouncement.do?display=pdf&idsId=00794394.

UraniumSA, 2010. The Mullaquana Uranium Project. South Australian Explorers' Conference, 26 November 2010.

UraniumSA, 2013. SAMPHIRE PROJECT UPDATE. ASX RELEASE 27 September 2013. 1–27 pp. http://www.asx.com.au/asx/statistics/displayAnnouncement.do?display=pdf&idsId=01448164.

UraniumSA, 2014. Significant upside targeting high grade unconformity uranium mineralisation Blackbush deposit, Samphire Project. ASX RELEASE 25 July 2014. 1–8 pp. http://www.asx.com.au/asx/statistics/displayAnnouncement.do?display=pdf&idsId=01536222.

UraniumSA, 2015. Samphire Uranium Project – April 2015. Presentation at South Australian Resources and Energy Investment Conference 2015.

Verdugo-Ihl, M.R., Ciobanu, C.L., Cook, N.J., Ehrig, K., Courtney-Davies, L., 2019. Defining early stages of IOCG systems: Evidence from iron oxides in the outer shell of the Olympic Dam deposit, South Australia. Mineralium Deposita, 1-24.

Wade, C.E., 2011, Definition of the Mesoproterozoic Ninnerie Supersuite, Curnamona Province, South Australia, MESA Journal, 62, 25-42.

Wade, C.E., Reid, A.J., Wingate, M.T.D., Jagodzinski, E.A., Barovich, K., 2012. Geochemistry and geochronology of the c. 1585 Ma Benagerie Volcanic Suite, southern Australia: Relationship to the Gawler Range Volcanics and implications for the petrogenesis of a Mesoproterozoic silicic large igneous province. Precambrian Research 206, 17–35.

Wilson, T., 2015. Uranium and uranium mineral systems in South Australia, 3rd edition. Report Book 2015/00011, Geological Survey of South Australia, Mineral and Energy Resources Group.

Wülser P.A., Brugger J., Foden J., Pfeifer H.R., 2011. The sandstone-hosted Beverley uranium deposit, Lake Frome Basin, South Australia: mineralogy, geochemistry, and a time constrained model for its genesis. Economic Geology 106, 835–867.

CHAPTER 2

PETROGRAPHY AND GEOCHEMISTRY OF GRANITOIDS FROM THE SAMPHIRE PLUTON, SOUTH AUSTRALIA: IMPLICATIONS FOR URANIUM MINERALISATION IN OVERLYING SEDIMENTS

Urs Domnick[1], Nigel J. Cook[1], Russel Bluck[2], Callan Brown[2], Cristiana L. Ciobanu[1], Benjamin P. Wade[3]

[1]*School of Chemical Engineering and Advanced Materials, The University of Adelaide, Adelaide, SA 5005, Australia*

[2]*Samphire Uranium, 28 Greenhill Road, Wayville, SA 5034, Australia*

[3]*Adelaide Microscopy, The University of Adelaide, Adelaide, SA 5005, Australia*

Article published in Lithos (2018), 300-301, 1-19.

Statement of Authorship

Title of Paper	Petrography and Geochemistry of Granitoids From The Samphire Pluton, South Australia: Implications for Uranium Mineralisation in Overlying Sediments
Publication Status	☑ Published ☐ Accepted for Publication ☐ Submitted for Publication ☐ Unpublished and Unsubmitted work written in manuscript style
Publication Details	Domnick, U, Cook, N.J., Bluck, R., Brown, C., Ciobanu, C.L., 2018. Petrography of granitoids from the Samphire Pluton, South Australia: implications for uranium mineralisation in overlying sediments. Lithos 300–301, 1–19.

Principal Author

Name of Principal Author (Candidate)	Urs Domnick		
Contribution to the Paper	petrography, analytical work, data processing, interpretation, manuscript, revisions		
Overall percentage (%)	60		
Certification:	This paper reports on original research I conducted during the period of my Higher Degree by Research candidature and is not subject to any obligations or contractual agreements with a third party that would constrain its inclusion in this thesis. I am the primary author of this paper.		
Signature		Date	14/11/2019

Co-Author Contributions

By signing the Statement of Authorship, each author certifies that:

i. the candidate's stated contribution to the publication is accurate (as detailed above);
ii. permission is granted for the candidate in include the publication in the thesis; and
iii. the sum of all co-author contributions is equal to 100% less the candidate's stated contribution.

Name of Co-Author	Nigel J. Cook
Contribution to the Paper	supervised work, assisted with interpretation, manuscript, and revisions
Overall percentage (%)	20

Signature		Date	14/11/2019

Name of Co-Author	Russel Bluck		
Contribution to the Paper	provided samples, evaluation of manuscript		
Overall percentage (%)	5		
Signature	(in absence, signed by Nigel Cook)	Date	14/11/2019

Name of Co-Author	Callan Brown		
Contribution to the Paper	Assisted with sample collection, evaluation of manuscript		
Overall percentage (%)	5		
Signature	(in absence, signed by Nigel Cook)	Date	14/11/2019

Name of Co-Author	Cristiana L. Ciobanu		
Contribution to the Paper	evaluation of manuscript		
Overall percentage (%)	5		
Signature		Date	14/11/2019

Name of Co-Author	Benjamin P. Wade		
Contribution to the Paper	assisted with analytical work, data processing, evaluation of manuscript		
Overall percentage (%)	5		
Signature		Date	14/11/2019

Lithos 300–301 (2018) 1–19

Contents lists available at ScienceDirect

Lithos

journal homepage: www.elsevier.com/locate/lithos

Petrography and geochemistry of granitoids from the Samphire Pluton, South Australia: Implications for uranium mineralisation in overlying sediments

Urs Domnick [a,*], Nigel J. Cook [a], Russel Bluck [b], Callan Brown [b], Cristiana L. Ciobanu [a]

[a] School of Chemical Engineering, The University of Adelaide, Adelaide, SA 5005, Australia
[b] Samphire Uranium Pty Ltd., 28 Greenhill Road, Wayville, SA 5034, Australia

ARTICLE INFO

Article history:
Received 14 June 2017
Accepted 28 November 2017
Available online 02 December 2017

Keywords:
Uranium
Granites
Hydrothermal alteration
Hiltaba intrusive suite
Samphire
Remobilisation

ABSTRACT

The Blackbush uranium deposit (JORC Inferred Resource: 12,580 tonnes U), located on the north-eastern Eyre Peninsula, is currently the only sediment-hosted U deposit investigated in detail in the Gawler Craton. Uranium is hosted within Eocene sandstone of the Kanaka Beds, overlying Mesoproterozoic granites of the Samphire pluton, affiliated with the Hiltaba Intrusive Suite (~1.6 Ga). These are considered the most probable source rocks for uranium mineralisation. By constraining the petrography and mineralogy of the granites, insights into the post-emplacement evolution can be gained, which may provide an exploration indicator for other sediment-hosted uranium systems. Three geochemically distinct granite types were identified in the Samphire Pluton and correspond to domains interpreted from geophysical data. All granites show complex alteration overprints and textures with increasing intensity closer to the deposit, as well as crosscutting veining. Alkali feldspar has been replaced by porous K-feldspar and albite, and plagioclase is overprinted by an assemblage of porous albite + sericite ± calc-silicates (prehnite, pumpellyite and epidote). This style of feldspar alteration is regionally widespread and known from Hiltaba-aged granites associated with iron-oxide copper gold mineralisation at Olympic Dam and in the Moonta-Wallaroo region. In two granite types biotite is replaced by calcic garnet. Calc-silicates are indicative of Ca-metasomatism, sourced from the anorthite component of altered plagioclase. Minor clay alteration of feldspars is present in all samples. Mineral assemblages in veins include quartz + hematite, hematite + coffinite, fluorite + quartz, and clay minerals. Minor chlorite and sericite are found in all vein types. All granite types are anomalously rich in U (concentrations between 10 and 81 ppm). Highly variable Th/U ratios, as well as hydrothermal U minerals (mostly coffinite) in granites and veins, are clear evidence for U mobility. Uranium may have been preconcentrated in veins in the upper parts of the pluton, and was subsequently leached after deposition of the sediment.

1. Introduction

Mesoproterozoic granites of the Hiltaba Intrusive Suite (HIS) have long been suggested as the most probable source for uranium (U) in iron-oxide copper gold (IOCG) deposits of the Olympic Cu-Au Province, eastern Gawler Craton, South Australia (Hitzman and Valenta, 2005). South Australian IOCG deposits have some of the highest U grades among this deposit type, but so far, Olympic Dam is the only mining operation economically producing by-product uranium (Ehrig et al., 2012). HIS granites contain an average of 14 ppm U (Neumann et al., 2000), more than five times the average of the upper crust (2.8 ppm; Rudnick and Gao, 2003). Therefore, such U enrichment in the South Australian IOCG deposits may be correlated with anomalous U content of HIS granites since they are considered genetically related to the IOCG mineralisation event at ~1.6 Ga (e.g., Skirrow et al., 2007).

In this contribution, we report on the mineralogy and geochemistry of a ~1585 Ma pluton (Reid et al., 2017) comprising variably altered HIS granites, which underlies the unconformity-related, sediment-hosted Blackbush uranium deposit (UraniumSA, 2013). This recently discovered deposit, on the eastern Eyre Peninsula, 20 km southwest of Whyalla (Fig. 1), is currently the only sediment-hosted U deposit in the Gawler Craton that has been investigated in any detail, even though sediment-hosted U might be widespread considering the abundance of U-rich source rocks and suitable host rocks (Hou et al., 2007).

By constraining the mineralogy and geochemistry, with emphasis on recognising primary igneous relationships between different granitoids, as well as the alteration overprint, insights can be gained into the post-emplacement evolution of these rocks. Furthermore, the distribution and migration of uranium in HIS granites and the significance which this carries for the formation of unconformity-related uranium deposits

* Corresponding author.
E-mail address: urs.domnick@adelaide.edu.au (U. Domnick).

https://doi.org/10.1016/j.lithos.2017.11.031
0024-4937/

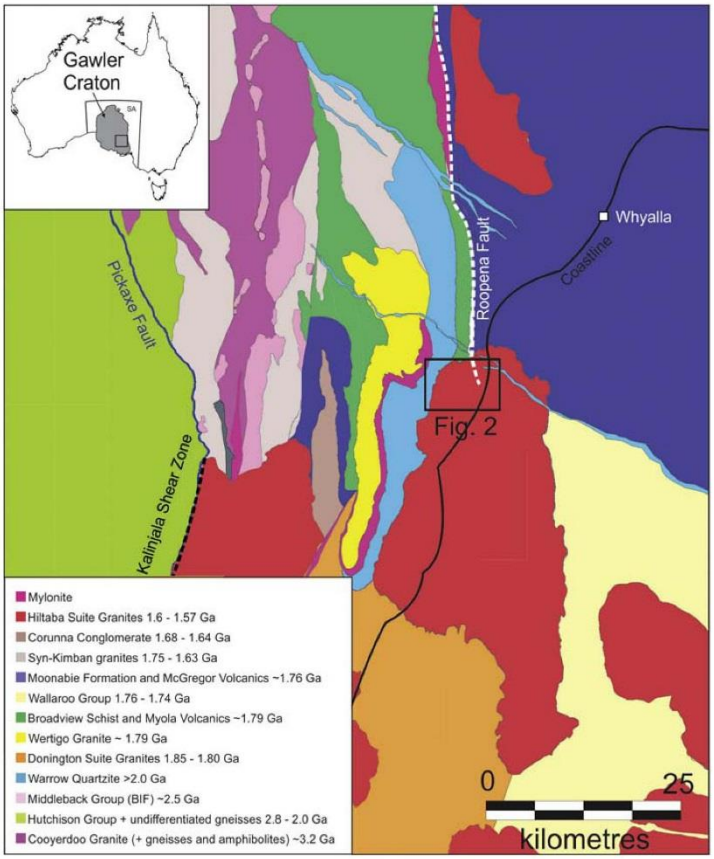

Fig. 1. Geological map of the Eastern Eyre Peninsula and the Spencer Gulf (based on unpublished work of SUL). The Kalinjala Shear Zone (KSZ) and the Roopena Fault (RF) form together as palaeosutures between the eastern and western Gawler Craton.

will be discussed. This information may, in-turn, provide an exploration indicator enabling location of undiscovered sediment-hosted uranium systems in the Gawler Craton.

2. Geological setting

2.1. Regional geology

In 2007 UraniumSA Limited, a junior exploration company, discovered the Samphire uranium deposits (UraniumSA, 2007), which are now owned by Samphire Uranium Pty Ltd. (SUL). These discoveries were made on the western margin of the Pirie Basin, on the eastern Eyre Peninsula, within a region of the Gawler Craton better known for the Banded Iron Formations (BIF) derived iron deposits of the Middleback Ranges (Yeates, 1990; Fig. 1).

The Gawler Craton is a major Proterozoic crustal province that has experienced a complex magmatic and metamorphic evolution (see Reid and Hand, 2012 and references therein). The Samphire uranium deposits are located on the easternmost part of the Eyre Peninsula. This part of the Gawler Craton is characterised by the ~1.85 Ga Donington Suite, comprising granites and charnockites associated with the Cornian orogeny (Reid and Hand, 2012), in the northwest by ~3.2 Ga granites, gneisses, and amphibolites (Fraser et al., 2010; Goodwin, 2010), the ~2.5 Ga Middleback Group, and the >2.0 Ga Warrow Quartzite (Szpunar et al., 2011); and in the northeast by 1.8–1.75 Ga magmatic and metasedimentary rocks (Parker and Fanning, 1998). Although geologically resembling the Olympic Cu-Au province, a >500 km-long Mesoproterozoic metallogenic belt running along the eastern margin of the Gawler Craton (Skirrow et al., 2007), no significant IOCG deposits have been found so far in this region (Ferris et al., 2002).

The Kalinjala Shear Zone (KSZ; Parker, 1980) and the Roopena Fault (RF; Ferris et al., 2002) are the two dominating structural features on the eastern Eyre Peninsula (Fig. 1). New geophysical data (McAvaney et al., 2016) indicates that both faults form a single palaeosuture between two different terranes (Howard et al., 2006), separating the Archean to Paleoproterozoic rocks in the north west from the ~1.85 Ga Donington Suite in the south east, and on a broader scale, separating the western and eastern Gawler Craton into two provinces. A comparison of the Central Au and Olympic Cu-Au provinces is provided by Budd et al. (2002) and Skirrow et al. (2002). This palaeosuture closed during the 1.75–1.69 Ga Kimban orogeny, which exposed the rocks on the northern Eyre Peninsula to regional metamorphism at lower amphibolite facies conditions (5–7 kbar; ~600 °C; Parker, 1993). SUL interpret a complex history of repetitive movement along the KSZ and RF, as indicated by extensive mylonite along these

shear zones and magnetic destructive alteration in rocks younger than the ~1.7 Ga closing time of the palaeosuture.

The older Archean to Paleoproterozoic units are intruded by HIS granites, namely the Charleston granite (1585 ± 2 Ma; Creaser and Fanning, 1993) in the west, and the pluton focused on in this study in the east, informally called the Samphire or Mullaquana pluton (Reid et al., 2017). The 1600–1570 Ma (Reid and Hand, 2012) HIS intrusives are dominantly felsic, although gabbros are also present (Daly et al., 1998; Allen et al., 2003) and, together with the contemporaneous Gawler Range Volcanics, are interpreted to form part of the Gawler Silicic Large Igneous Province (SLIP; Allen et al., 2008). The bimodal character of magmatism indicates widespread crustal melting was associated with mantle melting. Hiltaba Suite granites occur in the southern, central and north-eastern Gawler Craton and are interpreted to be important sources of heat, and metals necessary for generation of IOCG mineral systems; see Budd et al. (2002) and references therein. The broadly contemporaneous Kararan orogeny (1.6–1.55 Ga), characterised by deformation and greenschist facies metamorphism, overprinted Kimban-aged fabrics on the Eyre Peninsula (Reid and Hand, 2012).

The basement of the eastern Eyre Peninsula is unconformably overlain by Tertiary and Quaternary sediments, with a thickness of 60 to 150 m over the Samphire pluton, which obscure all bedrock outcrop of HIS granites on the Samphire area. The pluton is, however, constrained by different geophysical methods, and is particularly well configured on the Total Magmatic Intensity (TMI) geophysical maps (Fig. 2). These data are supplemented by several hundred end-of-hole rotary mud samples intersecting the basement. The pluton is part of a larger batholith that includes the HIS granites on the Yorke Peninsula, e.g., north of Wallaroo, as shown by geophysical methods.

The Samphire pluton intruded into several older rocks, to the north the 1792 ± 5 Ma felsic Myola Volcanics (Fraser and Neumann, 2010), and the associated Broadview Schist are in direct contact with the intrusion (Parker and Fanning, 1998). To the west, the pluton abuts to the Warrow Quartzite, with a maximum depositional age of 2005 Ma (Szpunar et al., 2011). Donington Suite (~1.85 Ga) granites probably constitute the larger part of the basement to the south and east of the pluton as indicated by geophysics. This assumption is supported by N-S trending faults, which are an extension of the Roopena Fault, indicating a change of basement across the faults. Two inherited zircons, found during dating of the HIS intrusion (Reid et al., 2017), show Pb-Pb ages of ~1770 and ~1800 Ma, and most probably originate from igneous rocks with these ages, indicating crustal assimilation. Gairdner dolerites (~827 Ma; Wingate et al., 1998) represent the most recent magmatic event on the Eyre Peninsula.

2.2. The Samphire uranium deposits

The larger of the two deposits, Blackbush, has a JORC Inferred Resource of 64.5 Mt. ore at an average grade of 195 ppm U (85 ppm cut-off). The smaller deposit, Plumbush, has a JORC Inferred Resource of 21.9 Mt. ore at an average grade of 248 ppm U (85 ppm cut-off) (UraniumSA, 2013). Together these deposits are estimated as 12,580 and 5420 tonnes U, respectively (UraniumSA, 2013).

The deposits are located 400–800 m inside the north-western margin of the Samphire pluton, in an arcuate domain of moderate-low amplitude/frequency magnetics, easily identifiable on the TMI geophysical map (Fig. 2). It is surrounded by areas of higher magnetic intensity, to the north interpreted as Myola Volcanics and Broadview schist, to the northwest as Warrow Quartzite, and to the south as high magnetic domain of the same pluton. This domain can be further divided into a higher magnetic arcuate rim and a lower magnetic core. Two different granitoids, a 'green' magnetite-bearing granite in the high magnetic domain, and a 'red' hematite-rich granite, in the low magnetic domain under the deposits, have been identified in the pluton. These have been dated by SHRIMP U-Pb zircon methods,

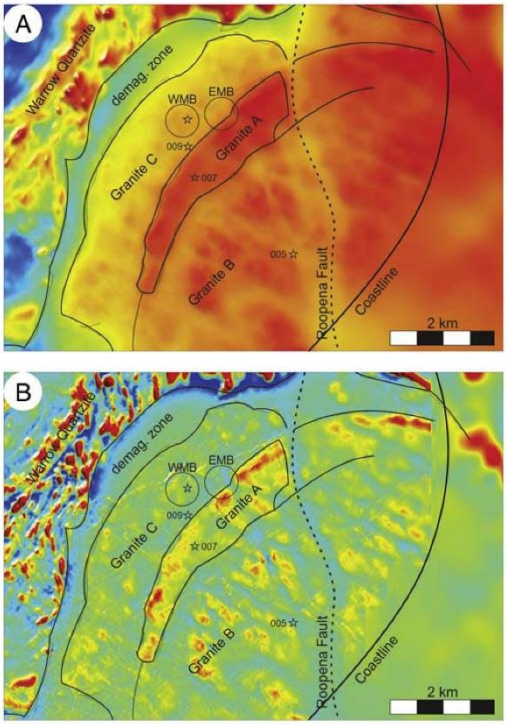

Fig. 2. Geophysical maps (based on publicly-available geophysical data (SARIG, https://map.sarig.sa.gov.au) and data of UraniumSA of the north-western edge of the Samphire Pluton; the two circles mark the Blackbush Palaeochannel comprising the Western Mineralised Zone (WMB) and the Eastern Mineralised Zone (EMB); stars mark drillholes; the spot in the WMB comprises all drillholes numbered 7xx and 8xx; three different magnetic domains correspond with the three granites: (A) geophysical map of the total magnetic intensity (TMI) reduced to the pole (RTP); and (B) TMI RTP first vertical derivative (1vd), slightly emphasizing the difference between Granites A and B.

yielding ages of 1583 ± 4 Ma for the green, and 1585 ± 7 Ma for the red granite (Reid et al., 2017). This age overlap for granites of distinct appearance indicates differences in magmatic and/or hydrothermal history.

The uranium mineralisation is hosted in Eocene sandstone of the Kanaka Beds of the Western Pirie Basin (Hou et al., 2012, 2017) and within clay-altered HIS granite (UraniumSA, 2013). The organic-rich sandstone fills a palaeochannel, incised into the granite (Fig. 3; UraniumSA, 2013).

The uppermost 10 to 25 m of the granite are heavily clay altered to illite- and kaolinite-group minerals and informally called saprolite, although the process of alteration is unknown, but suspected to be at least partially hydrothermal (UraniumSA, 2013). The uranium minerals are coffinite and minor uraninite, present as coating around quartz grains, intergrowth with pyrite, or as lenses in lignite.

Exploration work to date by UraniumSA comprises a total of 791 drillholes. These have largely targeted the sediment-hosted uranium mineralisation and saprolite; only nine diamond drillholes have intersected granitic basement. The cover is typically 60–155 m thick, with drillholes reaching depths between 61.6 and 162.5 m (Fig. 3, UraniumSA, 2014).

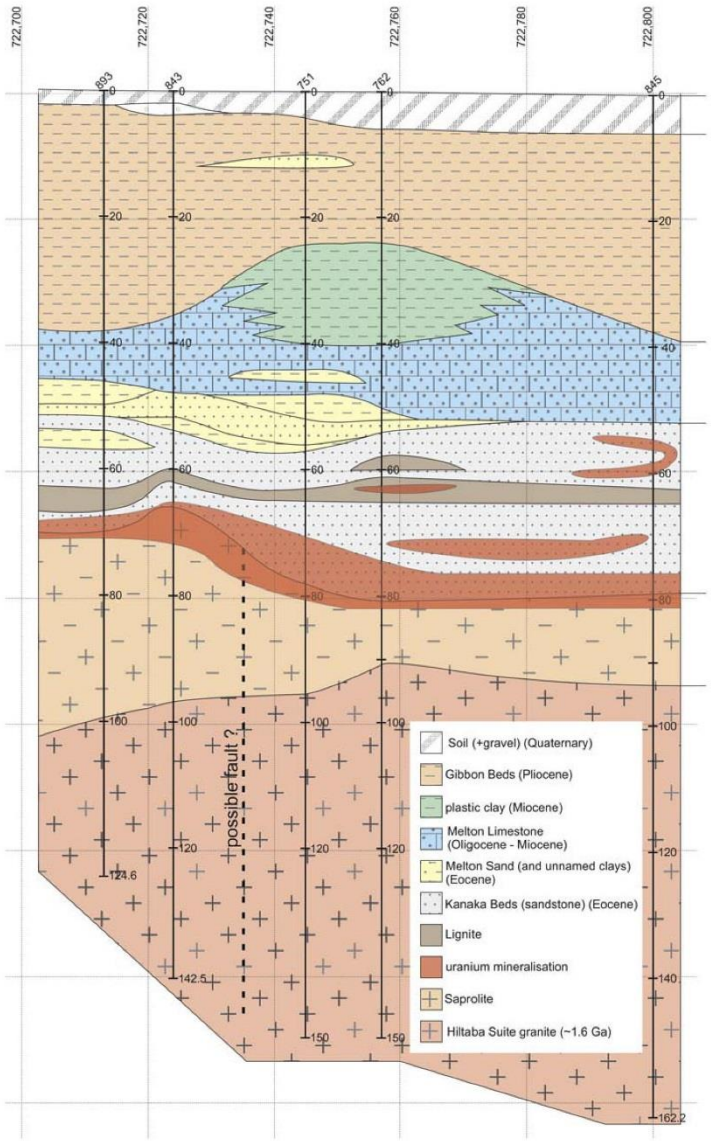

Fig. 3. Cross-section of the area sampled by the MRM7xx and MRM8xx drillholes. Vertical scale (on drillholes) in metres. Uranium mineralisation is symbolic and does not represent information from the drillcores; the mineralisation is multiform, including unconformity-related within saprolite and cover sediments, tabular sediment-hosted in sandstone, as well as lignite, and roll-front mineralisation in the sediment.

3. Sampling and methodology

3.1. Sample suite

Thirty-five core samples were selected from the nine available drillholes provided by UraniumSA. Three drillholes (MRC005, MRC007, MRC009) span ~4 km northwest to southeast, and were located to test geophysically distinct areas of the pluton. These holes were drilled with the assistance of a 2010 South Australian PACE grant. The remaining samples are from core-tails of rotary mud drill holes investigating a ~300 m diameter area within the Western Mineralised Zone of the Blackbush palaeochannel (Fig. 2), with core-tails drilled into granite underlying well mineralised sediments. This suite, comprising bedrock within a 20 km^2 area, was designed to be representative of the primary magmatic rocks, but also different degrees of superimposed hydrothermal alteration. The sample suite includes two samples of the green

granitic phase to the centre of the pluton (drillhole MRC005), four samples of granite from drillhole MRC007, inside an arcuate, linearly textured, domain of the pluton with high amplitude/frequency magnetic response, 24 samples of the reddish granitic phase, divided into two samples from drillhole MRC009 without overlying U mineralisation, and 22 samples from core-tails of drillholes MRM751, MRM762, MRM843, MRM845, MRM873, and MRM893 under high U-grade parts of the sediment-hosted deposit. The sample suite is completed by two samples of aplite, found in the drillholes MRC009 and MRM873, and three samples of a metasomatite (drillholes MRM751 and MRM762). Each drillcore has been analysed using hand-held XRF by UraniumSA, and several samples have been picked based on anomalous readings, e.g., samples 762-4 and 845-4 with U-bearing veins, and sample 762-5 with ~700 ppm Cu (Table 1). The sample suite contains one sample of drillcore MRM762 collected by Goldsmith (2014).

3.2. Analytical methodology

Whole rock geochemical data were determined by Genalysis-Intertek (Adelaide). Methodologies and minimum detection limits (mdl) are given in Electronic Appendix A.

Mineral identification and sample characterisation was made on one-inch polished blocks by optical microscope and by scanning electron microscope (SEM) using a FEI Quanta 450 SEM housed at Adelaide Microscopy, The University of Adelaide. SEM work was carried out in back-scatter electron (BSE) imaging mode at an accelerating voltage of 20 kV, a beam current of 10 nA, and spot size 4 μm.

Quantitative compositions of selected minerals within representative samples were determined using a Cameca SX-Five electron probe microanalyser (EPMA). Details of EPMA methodology, including standards, wavelengths measured, count times and minimum detection limits (mdl) are given in Electronic Appendix B.

Laser-ablation inductively-coupled mass spectrometry (LA-ICP-MS) was used on selected samples to provide trace element data for K-feldspar, plagioclase, and albite, as well as fluorite, titanite, garnet, and prehnite, using a Resonetics M-50-LR 193 nm Excimer laser microprobe, coupled to an Agilent 7900 Quadrupole ICP-MS at Adelaide Microscopy, University of Adelaide. Details of LA-ICP-MS methodology, including measured isotopes, standards, and detection limits are given in Electronic Appendix C.

Table 1
List of samples; they are referred in the text through their drillcore and sample numbers.

Drillhole	Depth (m)	Sample#	Granite type	Description/lithology
MRC005	59.65–59.83	1	B	Least-altered
		2	B	Least-altered
MRC007	156.14–156.22	4	A	Altered + veins
	157.39–157.55	1	A	Least-altered
	158.82–158.96	2	A	Least-altered
	158.30–158.50	3	A	Mafic enclave
MRC009	94.63–94.72	1	Aplite	Altered
	95.94–96.04	2	C	Least-altered
	98.52–98.72	3	C	Altered + veins
MRM751	114.30–114.52	5	C	Altered + veins
	119.28–119.40	2	Metasomatite	Altered
	126.61–126.81	4	C	Altered + veins
	133.19–133.26	1	C	Least-altered
MRM762	118.69–118.88	1	C	Altered
	114.57–114.62	5	C	Vein (Cu-rich)
	<115.37	6	C	Vein
	119.43–119.50	2A	Metasomatite	Altered
	119.50–119.57	2B	Metasomatite	Altered
	119.57–119.66	3	C	Mafic enclave
	149.96–150.08	4	C	Vein (U-rich)
MRM843	123.71–123.81	1	C	Least-altered
	132.08–132.23	2	C	Altered
	139.12–139.32	3	C	Altered + vein
MRM845	113.54–113.74	3	C	Altered + vein
	118.06–118.16	2	C	Altered
	134.18–134.37	5	C	Altered
	150.43–150.49	4	C	Vein (U-rich)
	154.27–154.35	1	C	Least-altered
MRM873	91.50–91.68	3	Aplite	Altered
	111.64–111.82	4	C	Altered
	119.01–119.11	1	C	? least-altered, dark coloured
	122.02–122.09	2	C	? least-altered, light coloured
	125.70–125.76	5	C	Altered
MRM893	111.19–111.25	2	C	Fluorite + quartz vein
	124.37–124.55	3	C	Vein

4. Results

Differences in colour, grain size, whole-rock geochemistry, mineral assemblage and relative proportions of constituent minerals allow five different granitoid facies to be recognised. The three major granite types are hereafter termed Granite A (yellow), Granite B (green), and Granite C (red), named in order of their degree of fractionation (see below). They correlate with domains of different total magnetic intensity. Whereas Granite A (yellow) and Granite B (green) have a fresh appearance and are very coarse (Fig. 4A, B), Granite C is intensively altered with red-stained feldspars and a generally smaller grain size (Fig. 4C, D); all granites include areas with a high concentration of mafic minerals and accessories that may be considered mafic enclaves (Fig. 5A). Two minor granitoid phases, aplite and metasomatite, occur as small dykes and sills of not >40 cm width within Granite C (Fig. 4E, F).

4.1. Petrography and mineral composition

4.1.1. Granite a (yellow) + Granite B (green)

The coarse-grained Granite A (yellow), exemplified in drillhole MRC007, and Granites B (green), as observed in drillhole MRC005, are very similar in terms of their petrography, mineralogy, and mineral composition, and can thus be described together (Table 2). Differences in colour and whole rock geochemistry (see below) nevertheless allow two different intrusions to be distinguished.

The primary igneous assemblage comprises alkali feldspar, plagioclase, quartz, mafic minerals, and accessories. This paragenesis is incompletely preserved, e.g., no igneous alkali feldspar can be observed, but can nevertheless be strongly implied by alteration products (see below). Feldspar phenocrysts range in size from 0.3 to 3 cm, the crystal shape is usually subhedral to anhedral, rarely euhedral crystals are found. (Former) alkali feldspar grains are reddish grey to light pink in Granite B (green), and stronger coloured from reddish grey to orange in Granite A. The colour of plagioclase grains ranges from white through grey to yellowish green in both granites. Both feldspars appear patchy, due to the presence of abundant inclusions, and may display domains of different colours within a single grain. Rarely, feldspars with rapakivi texture are observed (Fig. 5B), a finding consistent with other HIS granites (Kontonikas-Charos et al., 2017). The greenish colour of plagioclase, indicating sericitic alteration, is responsible for the overall impression of Granite B being green-coloured, whereas the colour of Granite A is dominated by the strong reddening of alkali feldspar grains.

Veins, up to 2 mm-wide, containing prehnite, as well as minor chlorite and epidote, crosscut Granite A. Alkali feldspar grains within 2 cm from the vein are characteristically yellow to orange in colour, displaying a transition to the usual reddish colour in this granite (Fig. 5C). Rarely matt white 'grains' are observed in Granite A, which, on closer examination (see below), comprise titanite, rutile, and calcite.

The plagioclase is andesine-oligoclase. In Granite A (yellow), plagioclase is more Ca-rich than in Granite B (green) (An_{28} compared to An_{18}; Table 3; Fig. 6A). The REY content is low, between 20 and 48 ppm. The REY pattern is characteristic for plagioclase with LREE being more

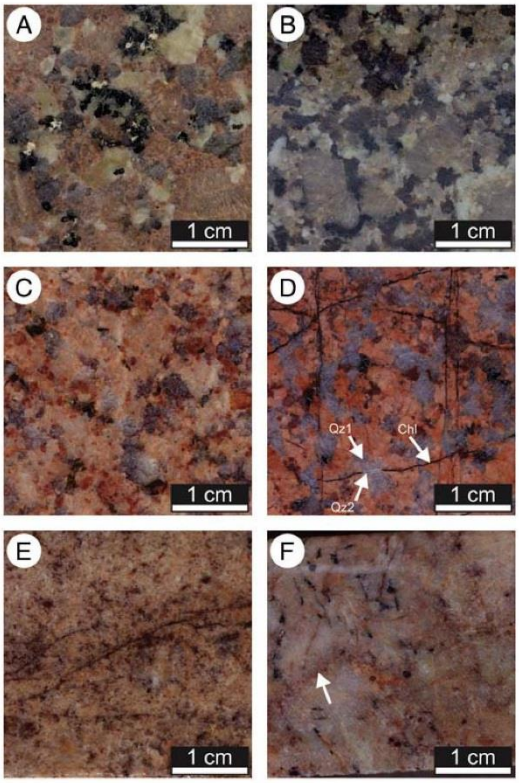

Fig. 4. Photos of hand specimen of granite types. A) Yellowish Granite A; red alkali feldspar, greenish plagioclase, grey quartz, black biotite and amphibole; the white grains are an aggregate of titanite, rutile, and calcite; 007-1. B) Green Granite B; red-brown alkali feldspar, white to yellowish green plagioclase, dark grey quartz, black mafic minerals, including biotite and ferro-edenite; rapakivi feldspar in the lower right corner; 005-1. C) Red Granite C; strongly reddened alkali feldspar and plagioclase; minor biotite; 009-2. D) Red Granite C + chlorite (Chl) veins; the veins are randomly distributed (stockwork); secondary quartz (Qz2) grows syntaxially on igneous quartz (Qz1); the feldspars are more strongly reddened compared to photo C. E) Aplite; fine-grained intergrowth of reddened feldspar and quartz; minor biotite; 009-1. F) Metasomatite; fine-grained micrographic intergrowth of feldspar and quartz; minor biotite; the red ghost structure (arrowed) may be a former grain boundary, indicating complete recrystallisation of the rock; 762-2B. (For interpretation of the references to colour in this figure legend, the reader is referred to the web version of this article.)

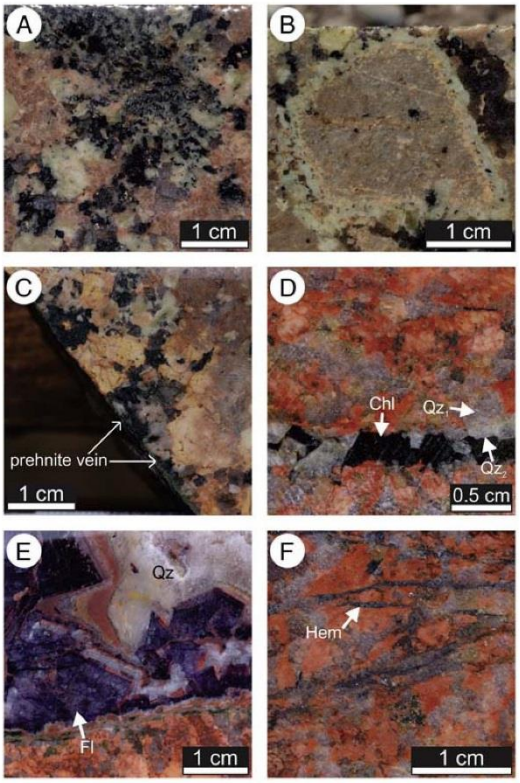

Fig. 5. A) Granite A; mafic enclave, containing biotite, magnetite, amphibole, titanite, and minor ilmenite; 007-3. B) Granite B; rapakivi feldspar; both feldspars have been altered and replaced; 005-1. C) Granite A; prehnite vein; the vein contains prehnite, as well as minor epidote and chlorite; the feldspar is orange within 2 cm around the vein; 007-4. D) Granite C; chlorite (Chl) + sericite + fluorite + quartz vein; chlorite and sericite have partially replaced fluorite; secondary quartz (Qz2) grows syntaxially on igneous quartz (Qz1); 751-5. E) Granite C; fluorite + quartz + minor hematite vein; euhedral purple fluorite (Fl) is followed by clear white quartz, and hematite inclusion rich brown quartz; 893-2. F) Granite C; veins of specular hematite (Hem) + quartz; quartz grows syntaxially on quartz of the surrounding rock, leaving the impression of hematite only occurring in feldspar grains; 762-4. (For interpretation of the references to colour in this figure legend, the reader is referred to the web version of this article.)

enriched than HREE, and a strongly positive Eu-anomaly, as generally observed in plagioclase (Kontonikas-Charos et al., 2018).

Mafic minerals, represented by biotite and amphibole, are slightly more abundant in Granite A. The composition of biotite is closer to the annite end-member, and slightly richer in Fe in Granite B (green) compared to Granite A ($annite_{68}$ to $annite_{53}$; Table 3). Ferro-edenite, a Na-Ca-amphibole, is found in both granites (Table 3).

Accessory minerals include allanite, zircon, fluorapatite, magnetite, ilmenite, titanite, *uranothorite* (U-rich thorite), and trace amounts of sulphides, including pyrite, galena, and molybdenite. Allanite is euhedral, and typically around 400 μm in size. It displays strong compositional zonation (Fig. 7A). Zircon, fluorapatite, magnetite, ilmenite, and *uranothorite* occur as single grains or as mineral aggregates. Zircon crystals are subhedral, and show areas of varying composition. Rarely, zircon grains seem to be corroded, leaving skeletal remnants behind. The main U mineral is subhedral to anhedral *uranothorite*, which is spatially correlated with pyrite, which occurs either as starlet inclusions or as rims around *uranothorite* (Fig. 7B).

Mineral aggregates, not >1 mm in size, contain most of the magnetite, ilmenite, and fluorapatite, which rarely occur as single grains interstitial between silicates (Fig. 7B). These aggregates often have a larger crystal (>250 μm) in the centre, which may be zircon or allanite, surrounded by the main component of the intergrowths, subhedral magnetite grains of varying size (50 to 400 μm). Fluorapatite occurs as small grains of <100 μm size. Ilmenite is anhedral and occurs mainly along grain boundaries. *Uranothorite* occurs along grain boundaries or attached to the edge of the aggregate (Fig. 7B). Rarely, minor titanite is observed along grain boundaries. This titanite is strongly enriched in REY (Fig. 8A), Zr, U, and Nb (Table 4). Xenotime was only observed in smallest traces and titanite might be the main host for HREE + Y in these granites. In general, the accessory phases tend to clump together, e.g., zircon grains attached to decomposed or altered allanite (Fig. 7C).

Mafic enclaves, up to 5 cm in size, are common in the both granites. They contain higher concentrations of magnetite, ilmenite, titanite,

Table 2
Texture and mineralogy of all granitoids.

Lithology	Drillholes	Texture	Primary magmatic minerals	Secondary (hydrothermal) minerals + vein minerals
Granite A	MRC007	Coarse-grained, granitic	35 vol% alkali feldspar, 30 vol% quartz, 20 vol% plagioclase, 15 vol% mafic minerals and accessories, including amphibole, biotite, magnetite, ilmenite, titanite, *uranothorite*, zircon, fluorapatite, pyrite, galena, allanite	Chlorite, rutile, synchysite-(Ce), clay minerals (illite + montmorillonite), prehnite, pumpellyite, epidote, garnet, rutile, titanite, hematite, sericite, calcite
Granite B	MRC005	Coarse-grained, granitic	40 vol% alkali feldspar, 30 vol% quartz, 20 vol% plagioclase, 10 vol% mafic minerals and accessories, including amphibole, biotite, magnetite, ilmenite, titanite, *uranothorite*, zircon, fluorapatite, pyrite, galena, allanite, fluorite, molybdenite	Chlorite, rutile, synchysite-(Ce), clay minerals (illite + montmorillonite), prehnite, pumpellyite, epidote, garnet, titanite, hematite, sericite, calcite
Granite C	MRC009, MRM751, MRM762, MRM843, MRM845, MRM873, MRM893	Coarse-grained, granitic, equigranular, weakly-fractured	50 vol% alkali feldspar, 30 vol% quartz, 15 vol% plagioclase, 5 vol% mafic minerals and accessories, including biotite, magnetite, ilmenite, titanite, *uranothorite*, zircon, pyrite, galena, synchysite-(Ce), fluorite, fluorapatite	Chlorite, rutile, synchysite-(Ce), clay minerals (illite + montmorillonite), hematite, pseudorutile, monazite, coffinite, uraninite, pyrite, fluorite
Aplite	MRC009, MRM873, MRM845 (?)	Fine-grained	40 vol% alkali feldspar, 30 vol% quartz, 20 vol% plagioclase, 10 vol% mafic minerals and accessories, including biotite, *uranothorite*, uraninite, euxenite-(Y), zircon	Hematite
Metasomatite	MRM751, MRM762	Fine grained, micrographic to granophyric intergrowth	40 vol% alkali feldspar, 30 vol% quartz, 20 vol% plagioclase, 10 vol% mafic minerals and accessories, including biotite, *uranothorite*, zircon	Hematite; euxenite-(Y)

Table 3
Mean Electron Microprobe microanalytical data for biotite, amphibole, plagioclase, and chlorite.

Biotite				Amphibole		Plagioclase				Chlorite			
Granite	B ($n = 5$)	A ($n = 8$)	C ($n = 19$)	Granite	A + B ($n = 30$)	Granite	B ($n = 28$)	A ($n = 18$)	C ($n = 22$)	Granite	B ($n = 2$)	A (007-3; $n = 18$)	A (007-4; $n = 6$)
CaO	1.64	0.04	0.18	CaO	10.94	CaO	3.96	5.88	2.87	CaO	0.37	0.27	0.11
MgO	6.33	10.01	8.01	MgO	6.61	MgO	0.01	0.01	<mdl	MgO	7.76	22.39	10.96
TiO_2	2.76	3.20	0.43	TiO_2	1.18	TiO_2	0.01	0.02	0.01	TiO_2	0.73	0.05	0.11
SiO_2	30.78	36.11	34.71	SiO_2	41.22	SiO_2	61.64	59.39	62.96	SiO_2	28.16	33.04	26.09
Al_2O_3	13.52	12.08	13.10	Al_2O_3	8.55	Al_2O_3	23.13	24.36	21.99	Al_2O_3	14.79	13.46	17.35
FeO	31.31	24.34	26.65	FeO	24.24	FeO	0.11	0.16	0.07	Fe_2O_3	39.06	19.24	35.21
MnO	0.22	0.34	0.06	MnO	0.60	MnO	<mdl	<mdl	<mdl	MnO	0.40	0.34	0.58
Cl	0.25	0.24	0.15	Cl	0.42	Cl	0.05	0.01	0.01	Cl	0.05	0.13	0.01
F	0.15	0.93	0.41	FeO	0.97	F	0.11	0.16	0.07	F	0.05	0.30	0.08
K_2O	4.44	8.62	5.58	K_2O	1.47	K_2O	0.34	0.36	0.28	K_2O	0.43	0.03	<mdl
P_2O_5	0.01	<mdl	<mdl	P_2O_5	0.01	P_2O_5	<mdl	0.01	<mdl	P_2O_5	<mdl	<mdl	0.03
Na_2O	0.07	0.10	0.22	Na_2O	1.81	Na_2O	9.53	8.27	10.25	Na_2O	0.05	1.38	0.08
SrO	0.03	0.18	0.15	SrO	0.03	SrO	<mdl	0.04	<mdl	SrO	0.09	0.13	0.08
BaO	0.03	0.14	0.03	BaO	0.01	BaO	<mdl	0.02	<mdl	BaO	<mdl	<mdl	<mdl
Total	91.52	95.90	89.47	Total	97.69	Total	98.78	98.51	98.44	Total	87.99	88.69	87.15

Calculated formula (11 O atoms)				Calculated formula (23 O atoms)		Calculated formula (8 O atoms)				Calculated formula (14 O atoms)			
$AB_3C_4O_{10}(OH)_2$				$AB_2C_5D_8O_{22}(OH)_2$		$AB_{1-2}C_{2-3}O_8$				$A_{5-6}B_4O_{10}(OH)_8$			
Ca	0.15	<mdl	0.02	K	0.30	Ca	0.19	0.29	0.14	Ca	0.04	0.03	0.01
K	0.48	0.86	0.59	Na	0.56	Mg	0.001	0.001	0.001	K	0.06	0.001	–
Na	0.01	0.02	0.04	Ca	0.06	K	0.02	0.02	0.02	Na	0.01	0.27	0.02
Sr	0.001	0.01	0.01	Total	0.93	Na	0.83	0.73	0.89	Sr	0.01	0.01	0.01
Ba	0.001 l	0.01	0.001			Mn	–	–	–	Ba	–	–	–
Total	0.64	0.90	0.65	Ca	1.81	Ba	–	0.001	–	Total	0.12	0.31	0.04
				Mg	0.19	Total	1.04	1.03	1.05				
Ti	0.18	0.19	0.03	Total	2.00					Mg	1.29	3.34	1.81
Mg	0.80	1.17	0.99			Al	1.23	1.30	1.16	Fe	3.28	1.45	2.93
Fe	2.15	1.56	1.85	Mg	1.38	Fe^{2+}	0.001	0.01	0.001	Mn	0.04	0.03	0.05
Mn	0.02	0.02	0.001	Fe	3.23	Total	1.23	1.31	1.17	Al	1.14	0.90	1.16
Al	0.01	0.001	0.23	Mn	0.08					Total	5.74	5.72	5.95
Total	3.15	2.95	3.10	Al	0.31	Si	2.77	2.69	2.83				
				Total	5.00	Ti	0.001	0.001	0.001	Ti	0.06	0.001	0.01
Fe	0.06	0.04	0.05			P	–	0.001	–	Al	0.80	0.69	1.10
Al	1.34	1.12	1.06	Ti	0.14	Total	2.77	2.69	2.83	Si	3.14	3.31	2.88
Si	2.60	2.84	2.89	Si	6.57					P	–	–	0.001
P	0.001	–	–	Al	1.29	%An	18.3	27.6	13.3	Total	4.00	4.00	4.00
Total	4.00	4.00	4.00	P	0.001								
				Total	8.00					Cl	0.01	0.02	0.001
Annite	68%	53%	60%							F	0.02	0.10	0.03
				Cl	0.11					Total	0.02	0.12	0.03
				F	0.49								
				OH	1.40								
				Total	2.00								

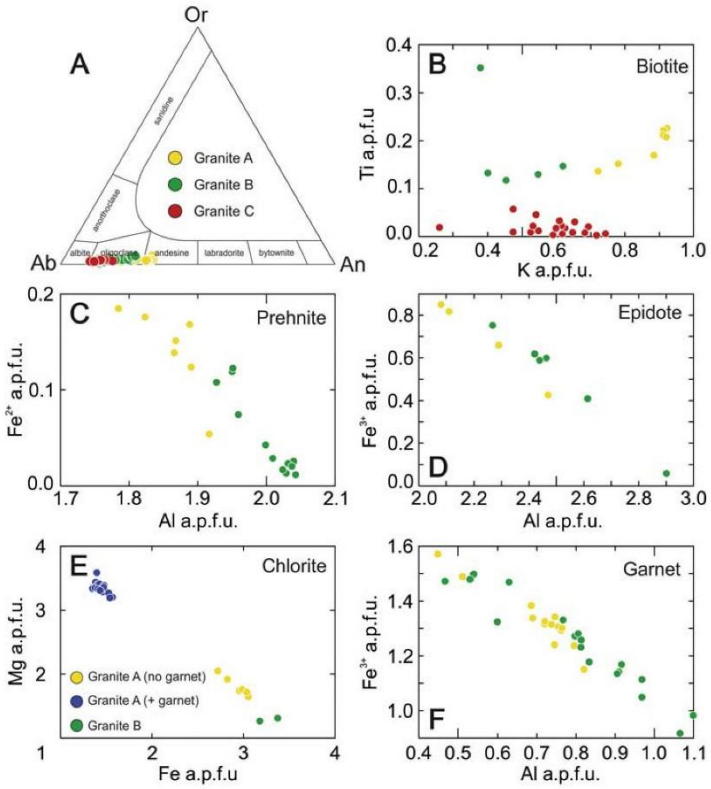

Fig. 6. A) Composition of plagioclase grains in all three granites plotted on an albite–anorthite–orthoclase diagram. B) K atoms-per-formula unit (apfu) vs. Ti apfu; smaller K values indicate a loss of K and higher degree of alteration; the lower Ti contents in biotite in Granite C might be the result of a lower crystallisation temperature. C) Al apfu vs. Fe apfu in prehnite; the prehnite in Granite A is richer in Fe. D) Al apfu vs. Fe apfu in epidote; grains show the whole compositional spectrum between the epidote and clinozoisite endmember; grains in Granite A have slightly more Fe on average. E) Fe apfu vs. Mg apfu in chlorite; chlorite is richer in Mg in Granite A compared to Granite B, due to the higher Mg content of the rock; in the presence of garnet chlorite is strongly Mg-rich, Fe is partitioned into coexisting garnet. F) Al apfu vs. Fe apfu in garnet; showing a large spectrum of compositions.

amphibole, and biotite than the average granite (Fig. 7D). Minerals in these enclaves are generally more mafic, e.g., more Mg and less Fe in biotite compared to the average granite.

Alteration in the two granites has impacted on the feldspars, which display several different textural and chemical overprints. Alkali feldspar is completely replaced by highly porous, near-end-member albite ($Ab_{>95}$) and K-feldspar ($Or_{>95}$). Potassium feldspar is the main component (ca. 90%). Albite occurs as inclusions within K-feldspar, and is either randomly distributed or elongated along inherited cleavage planes (Fig. 7E). Considering the ratio of K-feldspar and albite an originally perthitic composition of alkali feldspar can be assumed.

Most plagioclase is extensively altered and shows complex overprinting textures. The cores of plagioclase grains have been altered and replaced by highly porous albite, containing inclusions of sericite and various Ca-bearing minerals (mainly calc-silicates but also minor fluorite and calcite) (Fig. 7E). Sericite grains reach between 5 and 30 μm, and calc-silicates 5 to 20 μm (Fig. 7F). The pores are between 1 and 10 μm in size, and almost always have a circular shape in cross-section, strongly suggesting that the pores are not interconnected (Fig. 7F).

These calc-silicates include prehnite, epidote, and minor pumpellyite. A differentiation into pumpellyite-Al and pumpellyite-Fe does not seem to be useful, as the composition of pumpellyite is always around a Fe/Al ratio of 1 (Table 5). The calc-silicates are slightly iron-richer in Granite A (yellow) compared to Granite B (green), highlighting subtle differences between the two granites (Fig. 6C, D). Inclusions of calcite and fluorite are rare and may have an igneous origin, as has been described from other HIS granites at Olympic Dam (Kontonikas-Charos et al., 2017).

Plagioclase has sometimes been replaced by an aggregate of clay minerals and synchysite-(Ce) (Fig. 9A). These aggregates can also occur inside the highly porous albite. In addition, a narrow rim of albite is observed between plagioclase and K-feldspar grains. This albite is less porous than the replacive albite inside the plagioclase grains (Fig. 9B), and may be sourced from perthitic intergrowth in a pre-existing alkali feldspar. Plagioclase lost almost all REY during alteration. The REY content drops from up to 48 ppm to ~0 (values for all REY below minimum detection limits). The REY patterns of prehnite are irregular, but some grains reflect the REY patterns of plagioclase (Fig. 8B).

Biotite shows different replacement reactions. It is partially replaced by chlorite and either rutile and/or titanite, but can also be replaced by calcic garnet (Fig. 9C). This garnet shows varying composition from grossular- to andradite-dominant (Fig. 6F). On average, the garnet is andradite dominant, but slightly Al-richer in Granite B ($An_{61}Gr_{39}$ in Granite B, $An_{65}Gr_{35}$ in Granite A, Table 4, Fig. 6F). Low analytical totals obtained by EPMA (averaging 93.7% in Granite B), as well as the high F

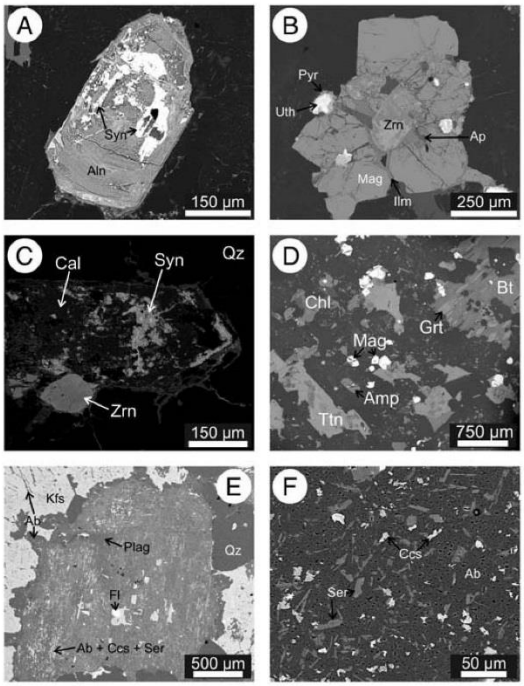

Fig. 7. BSE images, showing: A) Euhedral allanite with abundant inclusions of synchysite-(Ce), 005-1; B) mineral aggregate containing zircon, magnetite, ilmenite, *uranothorite*, fluorapatite, and pyrite, 005-1; C) allanite pseudomorphically replaced by synchysite-(Ce) and calcite; zircon is attached to the side of the (former) crystal; 005-1; D) mafic enclave containing titanite, amphibole, magnetite, and biotite; chlorite and garnet replacing biotite, 007-4; E) plagioclase replaced by porous albite + calc-silicates + sericite; narrow albite rim between plagioclase and alkali feldspar grains; F) calc-silicate (prehnite, pumpellyite, epidote) and sericite inclusions in porous albite. Abbreviations: Ab-albite; Aln-allanite; Amp-amphibole; Ap-fluorapatite; Bt-biotite; Cal-calcite; Ccs-calc-silicate minerals; Chl-chlorite; Fl-fluorite; Grt-garnet; Ilm-ilmenite; Kfs-K-feldspar; Mag-magnetite; Plag-plagioclase; Pyr-pyrite; Qz-quartz; Ser-Sericite; Syn-synchysite; Ttn-titanite; Uth-*uranothorite*; Zrn-zircon.

content (mean 1.22 wt% but up to as much as 2.09 wt%), indicate substitution of SiO_4^{4-} by $(OH,F)_4^{4-}$. The chondrite-normalised REY patterns are relatively flat, although slightly enriched in REY with HREE being more enriched than LREE. Europium is somewhat inconsistent showing slightly negative to positive anomalies (Fig. 8A).

The composition of chlorite is dependent on the presence of garnet. Without garnet, chlorite is Fe-rich and reflects the composition of the biotite it has replaced (Fe/Mg = 1.62 in Granite A to 2.54 in Granite B; Fig. 6E). If garnet is present, chlorite is Mg-rich (Fe/Mg = 0.46) indicating that garnet and chlorite have been formed at the same time during biotite alteration, i.e., Fe and Mg have been incorporated within garnet and chlorite, respectively. Very rarely pumpellyite-Mg can be observed as narrow rims surrounding garnet (Table 3).

Allanite contains abundant inclusions of synchysite-(Ce) or has been pseudomorphically replaced by calcite and synchysite-(Ce) (Fig. 7A, C). The white grains, observed in Granite A, are a porous, crumbly assemblage of titanite, rutile, calcite, and quartz (Fig. 9D). Rutile, calcite, and quartz may have replaced titanite.

The vein in sample 007-4 contains prehnite (>90%), and minor chlorite and epidote (Fig. 9E). It is assumed that this calc-silicate bearing vein is contemporaneous with calc-silicate formation inside the feldspar and biotite.

Unusual starlet inclusions of pyrite indicate later overprinting of *uranothorite* (Fig. 9F).

4.1.2. Granite C

Granite C, as observed in drillholes MRC009, MRM751, MRM763, MRM843, MRM873 and MRM893, is markedly finer-grained than either Granite A (yellow) or Granite B (green), but shares a similar mineral paragenesis: perthitic alkali feldspar, plagioclase, quartz, biotite, and accessories. Amphibole or possible alteration products thereof could not be observed. Like the other granites, igneous alkali feldspar could not be observed, but is implied. (Pre-existing) alkali feldspar grains are reddened and inclusion rich. Plagioclase grains show some variance in colour across the sample suite, from almost white to dark brown. The plagioclase is oligoclase, slightly more Na-rich than in Granite B (An_{13}). Biotite is Fe-rich, but slightly less than in Granite B ($Annite_{60}$), and has much less Ti (Table 3, Fig. 6B).

Accessory minerals include *uranothorite*, zircon, magnetite, ilmenite, fluorapatite, monazite, fluorite and synchysite-(Ce). *Uranothorite* (~200 µm) is the primary magmatic U-mineral. Contrary to Granites A and B, *uranothorite* in Granite C contains a significant concentration of P, as indicated by EDAX analysis, which may indicate later recrystallisation at lower temperatures. Zircon is eu- to subhedral and has a zoned or patchy appearance. The size of zircon grains varies slightly between 50 and 250 µm. Fluorapatite is very rare and could only be observed in a few samples, where it occurs as inclusions in chlorite. Monazite is presumably magmatic, but generally uncommon. Fluorite is always anhedral and occurs as grains in the granite (~100 µm) or as inclusions in feldspar (<50 µm). It is unclear whether the abundant synchysite-(Ce) represents an igneous LREE-dominant mineral, or is alternatively of hydrothermal origin.

As in Granites A and B, the accessories form aggregates not exceeding 1 mm (Fig. 10A). The mineral composition of these aggregates is similar to Granites A and B, with (former) magnetite grains as main component. These aggregates in Granite C do, however, always contain fluorite, as inclusions in hematite or along grain boundaries, and fluorapatite is conspicuously missing. *Uranothorite* is mostly found within these aggregates, rarely occurs it as inclusions in chlorite. Sample 873-1 contains small amounts of allanite as inclusions in chlorite (Fig. 10B).

4.1.3. Hydrothermal alteration overprint

Granite C shows similar textures and mineral replacements as seen in the other granites albeit with slight differences. Furthermore, the styles of alteration seem to be more diverse. Alkali feldspar shows comparable textures and overprints with Granites A and B.

The cores of plagioclase grains are replaced by highly porous albite with sericite inclusions, yet calc-silicates are missing, except in sample 873-4 (Fig. 10C). Fluorite and calcite are more abundant, but as mentioned above, may be of magmatic origin. Biotite and Fe-(Ti)-oxides are almost completely replaced. Biotite is replaced by chlorite and rutile. Magnetite is replaced by hematite, whereas ilmenite is replaced by an intergrowth of hematite and rutile (Fig. 10A); rarely it is replaced by pseudorutile ($Fe_2Ti_3O_9$).

The aggregates of accessories also contain small grains of K-feldspar (Fig. 10A). These grains are unusual, as they are barely porous, and do not have albite inclusions. It can thus be assumed that this is a newly-formed K-feldspar.

More diverse assemblages, indicating local scale mobility of REY, include REE-minerals such as monazite associated with fluorite along veins. In few samples, abundant chlorite with tiny inclusions of sericite replaces quartz (sample 843-2; Fig. 10D).

Extensive albitisation (+ sericitisation) of plagioclase, resulting in 'white feldspar grains' in hand specimen, is also observed (e.g., sample 873-5; Fig. 10F). In this case, however, sericite becomes more abundant, forming symplectitic intergrowths with albite (relative proportions of 40 and 60 modal%, respectively). Alteration of feldspars in Granite C

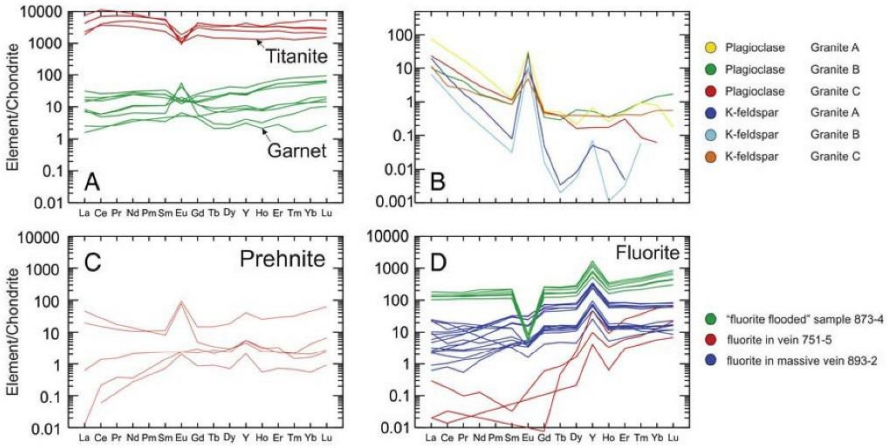

Fig. 8. Chondrite-normalised REY fractionation patterns for selected minerals. A) REY in titanite and garnet; titanite shows a flat pattern and slightly negative Eu-anomaly; garnet shows flat to slightly HREE enriched patterns with erratic positive to negative Eu-anomalies. B) average REY-content for plagioclase and K-feldspar in the three main granites; missing values are below minimum detection limits; plagioclase shows always the same pattern with a strongly positive Eu-anomaly; K-feldspar in Granite C shows a regular pattern as known from other HIS granites (Kontonikas-Charos et al., 2017); in Granites A and B the values are much lower and often below detection limit, indicating REY loss during replacement. C) REY pattern in prehnite; prehnite grains show irregular patterns, either reflecting the REY pattern of plagioclase which they have replaced, or often showing a lower REY-content without any Eu-anomaly. D) REY-patterns in fluorite; the three different fluorites show 3 distinct patterns; flat patterns with a strongly negative Eu-anomaly in the "fluorite flooded" sample; overall lower REY-content and little to no Eu-anomaly in the massive fluorite + quartz + hematite vein; even lower REY-content with a strong enrichment in HREE in the fluorite + chlorite + quartz vein.

also comprises abundant clay minerals (e.g., sample 845-2) or dusty hematite inclusions leading to red-staining (e.g., sample 762-1). In such cases complete replacement of accessory magnetite leading to cavities (Fig. 11A) is also observed.

A greater volume of fluorite than the average of Granite C is characteristic of some areas (e.g., sample 873-4; Fig. 12F). Core logging showed areas where fluorite constitutes 15% of the core, even though in the studied sample fluorite is less abundant (<5%). In this case fluorite occurs interstitial to feldspar-quartz assemblages and displays either straight or scalloped contacts with the other minerals (Fig. 10E). Such relationships and the strong negative Eu-anomaly (Fig. 8D) are indicative of magmatic or early hydrothermal origin, prior to vein fluorite. These fluorite rich areas contain calc-silicate inclusions in albite replacing plagioclase.

Table 4
Average titanite element content ($n = 5$), acquired by LA-ICP-MS; oxides in wt%, elements in ppm; internal calibration using Si = 14.20 wt%.

SiO_2	30.87	La	955.04
TiO_2	32.31	Ce	4053.60
Al_2O_3	2.14	Pr	631.78
CaO	28.99	Nd	2896.00
K_2O	<mdl	Sm	701.10
Na_2O	0.05	Eu	74.05
MgO	0.12	Gd	708.74
FeO	2.50	Tb	111.81
Total	96.97	Dy	745.78
Rb	0.32	Y	4638.80
Sr	7.86	Ho	154.65
Ba	1.87	Er	499.64
Mn	954.92	Tm	72.03
P	127.20	Yb	513.94
Zr	744.44	Lu	74.43
Hf	64.44	Bi	0.78
Nb	2253.48	Th	285.76
Ta	157.29	U	285.94
Sn	420.06	Cu	0.96
W	11.21	Zn	1.36

4.1.4. Vein assemblages

Granite C is weakly-fractured and veins are abundant, showing highly varying compositions and internal textures from one sample to the next. The main minerals in the veins are hematite, chlorite, sericite, quartz, fluorite, clay minerals (illite, montmorillonite), as well as minor biotite, K-feldspar, coffinite, monazite, xenotime, *uranothorite*, and synchysite-(Ce).

The most widespread vein type are narrow veinlets, typically not exceeding 1 mm in width, and containing chlorite (± sericite ± quartz) (Figs. 4D and 5D). These veinlets, ubiquitous across the sample suite, show no preferred orientation. The quartz in these veinlets grows syntaxially on quartz within the surrounding rock. Other vein types contain (purple) fluorite + quartz + hematite (Fig. 5E), hematite + coffinite, quartz + hematite (Figs. 5F and 12A), and calcite + synchysite-(Ce); they are (sub)vertical. Veins dominated by clay minerals vary strongly in colour from white over orange and red to dark brown. The veins bearing purple fluorite (+ quartz + hematite ± K-feldspar) are by far the largest reaching up to 7 cm in width. All vein types contain chlorite and sericite.

Temporal relationships between different veins are ambiguous, e.g., the quartz + hematite veins might be part of the same generation as the quartz ± hematite in the fluorite veins. The spatial separation of veins, e.g., hematite + coffinite veins in the deeper parts of the drillhole and clay mineral veins in the shallower parts, further impedes an accurate assessment of their relationships and relative timing.

Some veins contain mostly hematite (>95 vol%) and minor biotite and chlorite (e.g., sample 009-3). Boundaries between the hematite and quartz in the surrounding granite are straight, between the hematite and surrounding feldspar, however, they are irregular and in the latter case, the hematite can contain feldspar inclusions, indicative of replacement and hematitisation of feldspar (Fig. 11B).

Quartz-rich (80 vol%) veins in the metasomatite comprise minor hematite and K-feldspar. The lack of porosity in the latter is evidence this is of hydrothermal origin (e.g., sample 751-2). Wide veins (up to 600 μm) are filled with specular hematite (50 vol%), quartz (30 vol%), and a fine-grained intergrowth of illite, hematite, and minor chlorite (20 vol%)

Table 5
Average electron microprobe microanalytical data (wt%) for the calc-silicates; garnet, epidote, pumpellyite, prehnite.

Garnet			Epidote			Pumpellyite	Fe-rich	Mg-rich	Prehnite		
Granite	B ($n = 18$)	A ($n = 14$)	Granite	B ($n = 6$)	A ($n = 4$)	Granite	A + B ($n = 3$)	A ($n = 4$)	Granite	B ($n = 13$)	A ($n = 7$)
CaO	31.93	33.79	CaO	23.00	22.56	CaO	22.84	22.62	CaO	25.72	24.49
MgO	0.04	0.07	MgO	0.01	0.01	MgO	0.18	3.99	MgO	0.01	1.02
TiO_2	1.12	0.43	TiO_2	0.04	0.02	TiO_2	0.10	0.39	TiO_2	<mdl	0.01
SiO_2	32.73	34.48	SiO_2	36.90	37.69	SiO_2	36.24	36.49	SiO_2	42.18	42.78
Al_2O_3	7.76	7.12	Al_2O_3	26.53	23.42	Al_2O_3	26.38	25.62	Al_2O_3	23.97	22.24
Fe_2O_3	18.70	20.95	Fe_2O_3	9.15	12.47	FeO	7.46	1.95	FeO	0.82	2.39
MnO	0.16	0.16	MnO	0.21	0.23	MnO	0.13	0.08	MnO	0.02	0.09
Cl	0.01	0.02	Cl	0.01	<mdl	Cl	0.01	<mdl	Cl	<mdl	0.01
F	1.15	1.31	F	0.03	<mdl	F	0.03	0.41	F	<mdl	0.01
K_2O	0.01	0.02	K_2O	0.03	0.01	K_2O	0.02	0.06	K_2O	<mdl	0.01
P_2O_5	0.02	0.02	P_2O_5	0.02	0.03	P_2O_5	0.01	0.02	P_2O_5	0.08	0.01
Na_2O	0.03	<mdl	Na_2O	0.01	0.07	Na_2O	0.02	0.03	Na_2O	0.01	0.06
SrO	<mdl	<mdl	SrO	0.10	0.04	SrO	0.02	<mdl	SrO	0.18	<mdl
Total	93.66	98.38	Total	96.02	96.55	Total	93.43	91.66	Total	92.99	93.11

Calculated formula (12 O atoms)			Calculated formula (12.5 O atoms)			Calculated formula (12 O atoms)			Calculated formula (11 O atoms)		
Formula $A_3B2C_3O_{12}$			Formula $A_2BC_2D_3O_{11}(O,OH)_2$			Formula $A_2BC_2D_3O_{11}(OH)_2 \cdot H_2O$			Formula $A_2B_2C_3O_{10}(OH)_2$		
Ca	3.01	3.05	Ca	1.99	1.96	Ca	1.95	1.93	Ca	1.95	1.86
Mg	0.01	0.01	Mg	0.001	0.001	K	0.001	0.01	Mg	0.001	0.11
K	0.001	0.001	K	0.001	0.001	Na	0.001	0.001	K	—	0.001
Na	0.01	—	Na	0.001	0.01	Sr	0.001	—	Na	0.001	0.01
Mn	0.01	0.01	Mn	0.01	0.02	Total	1.96	1.94	Mn	0.001	0.01
Total	3.03	3.08	Sr	0.001	0.001				Sr	0.01	—
			Total	2.01	1.99	Mg	0.02	0.47	Total	1.96	1.99
Al	0.80	0.71				Mn	0.01	0.01			
Fe^{3+}	1.24	1.33	Al	2.52	2.24	Fe^{2+}	0.50	0.13	Al	2.00	1.86
Total	2.04	2.04	Fe^{3+}	0.50	0.69	Al	0.48	0.40	Fe^{2+}	0.05	0.14
			Total	3.02	2.93	Total	1.01	1.01	Total	2.05	2.00
Si	2.88	2.91									
Ti	0.07	0.03	Si	2.97	3.06	Al	2.00	2.00	Si	2.99	3.04
P	0.001	0.001	Ti	0.001	0.001	Total	2.00	2.00	Ti	0.001	0.001
Total	2.96	2.94	P	0.001	0.001				P	0.01	0.001
	8.03	8.05	Total	2.98	3.06	Si	2.89	2.90	Total	2.99	3.04
						Ti	0.01	0.02			
% Andradite	61	65				P	0.001	0.001			
% Grossular	39	35				Total	2.90	2.93			

(sample 751-4; Fig. 11C). Other, comparably wide veins (400 μm) are filled instead with euhedral quartz (30 vol%), fluorite (20 vol%), and an intergrowth of chlorite and sericite (50 vol%); the latter replaces fluorite (Fig. 11D). The vein also contains trace amounts of xenotime and hematite.

Other veins are U-bearing and contain abundant coffinite (60 vol%) associated with hematite (40 vol%) (e.g., sample 762-4; Fig. 11E). Such veins are highly porous and the skeletal appearance of coffinite may indicate multiple episodes of vein opening leading to superimposed mineral replacements. REY- and Cu-rich veins (REY up to 1450 ppm and Cu up to 700 ppm) are filled with quartz (40 vol%), K-feldspar (10 vol%), clay minerals (illite and montmorillonite, 50 vol%), xenotime, minor hematite, and trace amounts of synchysite-(Ce) (sample 762-5). Quartz grains in the vein always have a rim of K-feldspar, and K-feldspar only rarely occurs as grains, which may be an indicator for replacement of quartz by the clay minerals with K-feldspar as intermediate product. Xenotime is locally concentrated, where it comprises up to 20 vol% of the vein fill. The colour of the vein fill is variable changing from yellow to brown with increasing hematite content.

In samples with abundant chlorite alteration, *uranothorite* occurs along small quartz veins, also comprising minor chlorite and rutile (e.g., sample 843-3). In other cases, chlorite is the dominant component along the veins (e.g., sample 845-4) and these veins are also unusually rich in pyrite, the latter also occurs in the surrounding rock. Such pyrite has been partially replaced by uraninite and coffinite (Fig. 11F). The abundant small, black veinlets found in the red Granite C, e.g., samples 843-3 and 893-3, contain chlorite (>95%). Fluorite veins contain euhedral purple fluorite (50 vol%), pure quartz, hematite-inclusion rich quartz, and minor K-feldspar and chlorite (e.g., sample 893-2). In this case the fluorite shows lower REY content compared to the disseminated/patchy fluorite (see above; fluorite-rich sample 873-4), and the Eu-anomaly is much less pronounced (Fig. 8D). It is unclear whether zones of distinct mineral assemblages represent several generations of vein fill that are related to independent events, or rhythmic filling of a vein by a single event. The chlorite in all veins is highly variable in its composition. Chamosite- and clinochlore-dominant chlorites co-exist.

4.1.5. Aplite and metasomatite

Dykes and sills of two minor fine-grained granitoids are observed in the red granite (C): an aplitic phase; and a phase with micrographic and granophyric intergrowth, informally called metasomatite, which is lacking igneous textures. Both aplite and metasomatite have an orange to red appearance comparable to Granite C. Both consist of K-feldspar, albite, quartz, as well as minor biotite and accessories.

The aplitic samples are strongly altered, and their primary igneous assemblage can only be inferred based on whole-rock geochemistry. The main minerals form a symplectitic mesh (Fig. 13A). Whereas albite and quartz can be identified as grains (~0.4 mm in size), K-feldspar forms a groundmass for the other two components. Albite and K-feldspar are highly porous; in the K-feldspar pores are very small and homogenous in size (around 1 μm), in the albite pores vary in size between 2 and 30 μm. In contrast to the aforementioned granites, K-feldspar does not contain albite inclusions. Albite grains contain minor sericite and hematite inclusions. The only mafic mineral is

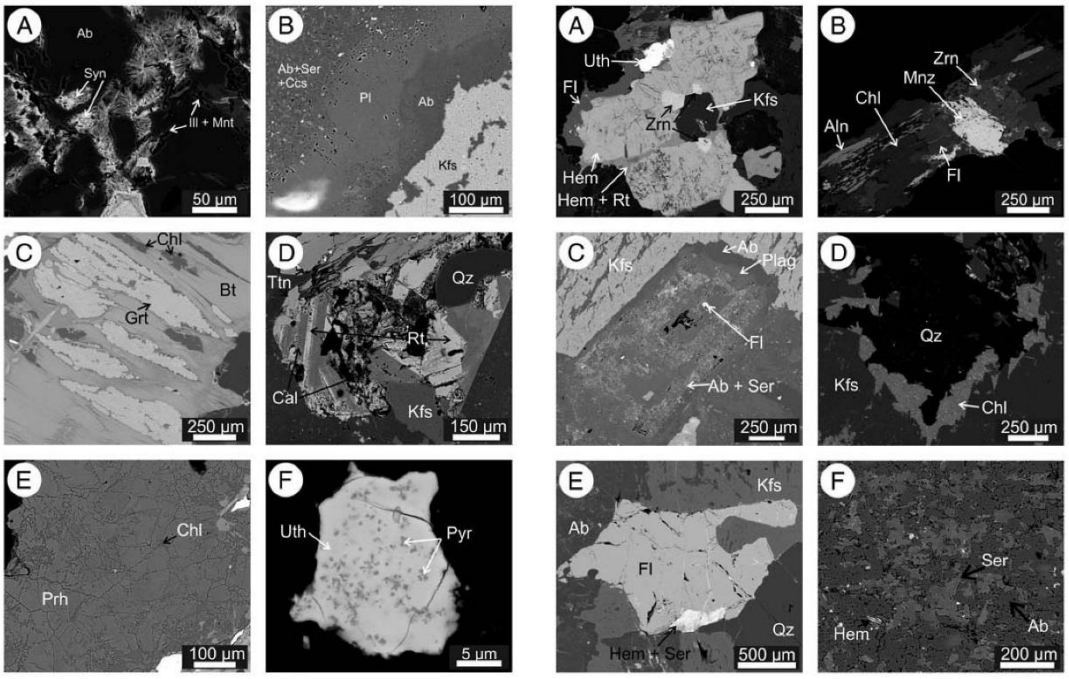

Fig. 9. BSE images, showing: A) synchysite-(Ce) and montmorillonite replacing albite; B) a small rim of plagioclase often remains; a small albite rim between (former) plagioclase and (former) alkali feldspar grains; C) garnet and chlorite replacing biotite; the chlorite is Mg-rich, 007-3; D) calcite and rutile replacing titanite, 007-1; E) vein bearing prehnite, and minor chlorite and epidote; F) Granite B; small *uranothorite* grain with pyrite starlets as inclusions; 005-2. Abbreviations: Ab-albite; Bt-biotite; Cal-calcite; Ccs-calc-silicate minerals; Chl-chlorite; Grt-garnet; Ill-illite; Kfs-K-feldspar; Mnt-montmorillonite; Prh-prehnite; Pyr-pyrite; Qz-quartz; Rt-rutile; Ser-sericite; Syn-synchysite; Ttn-titanite; Uth-*uranothorite*.

Fig. 10. BSE images, showing A) Granite C; mineral aggregate of hematite, zircon, rutile, fluorite, and *uranothorite*; the large K-feldspar in the centre is of hydrothermal origin and presumably pseudomorphically replacing another mineral; 751-1. B) Granite C; grains of allanite, monazite, and zircon in chlorite; 873-1. C) Usual replacement of plagioclase in Granite C; porous albite and sericite replace plagioclase; calc-silicates are missing; small rim of albite between plagioclase and alkali-feldspar. D) Replacement of quartz by chlorite, K-feldspar is unaffected. E) Granite C; fluorite grain in surrounded by quartz and feldspar; 873-4. F) Extensive sericitisation "white alteration", 873-5. Abbreviations: Ab-albite; Aln-allanite; Chl-chlorite; Fl-fluorite; Hem-hematite; Kfs-K-feldspar; Mnz-monazite; Plag-plagioclase; Rt-rutile; Ser-sericite; Uth-*uranothorite*; Zrn-zircon.

minor biotite, which often contains dense inclusions of hematite. The main accessories are hematite, zircon, and euxenite-(Y). All accessory grains are usually <50 µm. Zircon is subhedral with a patchy and vuggy appearance (Fig. 13B). Euxenite and hematite are both anhedral and often in contact with each other. Euxenite has a crumbly, partially decomposed appearance (Fig. 13C). Trace amounts, sometimes only single grains, of synchysite-(Ce), xenotime, and uraninite are also observed. Uraninite is anhedral and occurs as grains, not larger than 8 µm, along grain boundaries or rarely in zircon. All samples of the metasomatite are strongly altered and recrystallised, and the pre-existing igneous assemblage can only be assumed. Potassium feldspar, albite, and quartz are main components, and form a fine-grained, micrographic or granophyric intergrowth (Fig. 13D). Both feldspars are highly porous. The main accessories are hematite, rutile, euxenite-(Y) and pyrite. Several unusual textures could be observed. Biotite seems to replace hematite and rutile (Fig. 13E). In contrast to the aplite where euxenite occurs as grains of (presumably) igneous origin, euxenite in the metasomatite appears to replace rutile, occurs as infill within narrow (<10 µm) veins, or replaces pyrite, together with K-feldspar (Fig. 13F).

The general appearance of feldspars across the whole sample suite (inclusion-rich, reddened alkali feldspar, and yellow green or reddened plagioclase) indicates that no single sample is completely free of alteration. Nevertheless, the colour differences between granite types, as well as samples of the same phase, indicate different styles and degrees of alteration. Furthermore, it is unclear, if the abundant clay, in veins as well as replacing feldspar, is of hydrothermal origin, or alternatively, the product of weathering. Increasing clay content from bottom to top of the drillholes, and the presence of cerianite (CeO_2), is indicative of strongly oxidising conditions, concordant with some degree of weathering in all samples.

In the following sections, samples are referred to as 'least-altered', if they are representative for the majority of the rock in the drillcores and show undisturbed trace element patterns, e.g. no Ce-anomalies.

4.2. Whole rock geochemistry

Whole-rock analyses of least altered samples of all phases show values for the main oxides characteristic for granites (Table 6). These analyses are used to discriminate among different types of granitoids and their geochemical affiliation. Two diagrams, QAP (Streckeisen, 1974) and Ab-An-Or (Barker, 1979) based on CIPW normative minerals, are used to differentiate between different rocks types in this sample suite. For the QAP diagram albite is divided between alkali feldspar (Or + ⅓Ab) and plagioclase (An + ⅔Ab), as shown for other HIS-granites (Kontonikas-Charos et al., 2017). The resulting composition of the granites fits the estimates of main mineral composition in the hand specimens (Table 2). All samples cluster in the granite field, with some

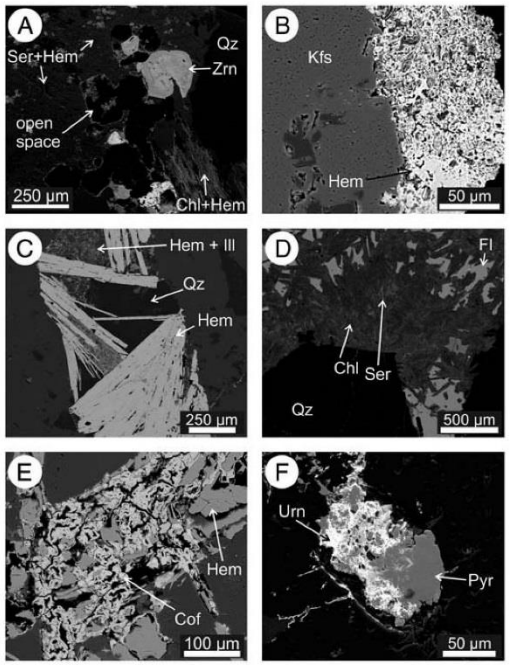

Fig. 11. BSE images, showing A) dissolved magnetite grains leaving hollow space behind; 762-1. B) Granite C; hematitisation of K-feldspar; the hematite in the vein has an irregular boundary with K-feldspar and replaces it; 009-3. C) Granite C; vein fill of hematite; quartz; and illite; the hematite shows two different appearances, as specular crystals of 500 µm and as fine-grained intergrowth with illite; 751-4. D) Granite C; vein fill of quartz, fluorite, chlorite, and sericite; mm size euhedral quartz grows syntaxially on quartz of the surrounding rock; fluorite is replaced by an intergrowth of chlorite and sericite; 751-5. E) Granite C; coffinite + hematite vein; the coffinite has a skeletal appearance; 762-4. F) Granite C; uraninite replacing pyrite; 845-4. Abbreviations: Chl-chlorite; Cof-coffinite; Fl-fluorite; Hem-hematite; Ill-illite; Kfs-K-feldspar; Pyr-pyrite; Qz-quartz; Ser-sericite; Urn-uraninite; Zrn-zircon.

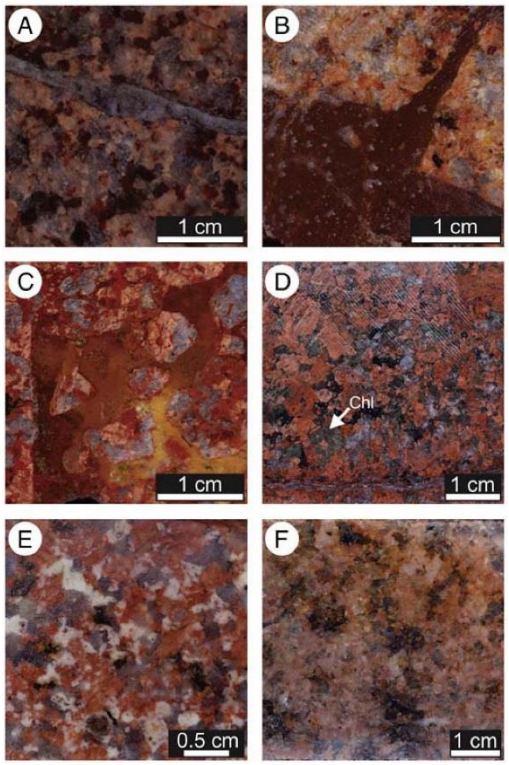

Fig. 12. A) Granite C; quartz vein and dark brown colouration of the surrounding rock, which is the result of complete replacement of feldspar grains by sericite and hematite; 762-1. B) Granite C; brown clay mineral vein, C-762-6. C) Granite C; yellow to red Cu- and REE-rich clay mineral vein; the vein contains illite/montmorillonite, quartz, K-feldspar, and minor xenotime; 762-5. D) Granite C; "chlorite alteration"; chlorite has replaced quartz and albite, and itself has been replaced by sericite; 843-2. E) Granite C; "white alteration", which is actually albitisation of plagioclase, followed by extensive sericitisation; 873-5. F) Granite C; "fluorite flooding"; the fluorite occurs as individual grains, indicating that it is igneous; 873-4. (For interpretation of the references to colour in this figure legend, the reader is referred to the web version of this article.)

strongly altered samples stretching close to the 'alkali feldspar granite' field (Fig. 14A). Two Na-rich metasomatite samples stretch slightly in direction of the plagioclase apex. In the Ab-An-Or diagram all samples cluster in the granite field, with strongly altered samples shifted to the Or-apex (Fig. 14B). In the B-A diagram (Debon and Le Fort, 1983) Granites A (yellow) and B (green) are metaluminous, whereas Granite C, as well as the aplite and metasomatite, are meta- to peraluminous, but still within the compositional range expected for A2 granites (after Cuney, 2014). The small values for the indices A ($\pm$20) and B (<70) indicate strongly fractionated granites, with Granite A being the least fractionated. In the Co-Th plot (Hastie et al., 2007) all samples plot in the high-K calc-alkaline granite field (Fig. 14D). The 10,000 * Ga/Al ratio is usually larger than 2.6, which is indicative of A-type granitoids (Whalen et al., 1987; Fig. 14E). Further classification into A1 or A2 subtypes proves difficult, as the samples scatter across the fields (Eby, 1992; Fig. 14F). The least-fractionated granite (A) is clearly an A2 granite, all other granites are presumably A2, but lost their A2 properties during fractionation, e.g. crystallisation of HREE-bearing minerals.

4.2.1. Trace element geochemistry

The trace elements (Electronic Appendix D) plotted against the assumed content of the continental crust (Rudnick and Gao, 2003; Electronic Appendix E) show rather similar patterns for all granitic phases, which match patterns known from other HIS granites, e.g., Roxby Downs Granite (Table 6). Barium and Sr are strongly depleted, whereas K and Rb are enriched, indicating crystallisation of plagioclase, and high alkali feldspar content, respectively. The light rare earth elements (LREE) are enriched in Granites A, B, and C, and strongly depleted in both the aplite and metasomatite relative to continental crust values. All granites show a slight relative enrichment in heavy rare earth elements and yttrium (HREE + Y). Niobium and Ta are slightly enriched in Granites A and B, more strongly in Granite C and the aplite, and markedly enriched in the metasomatic rock. Zirconium is barely to strongly enriched in Granites A, B, and C, but strongly depleted in the aplite and the metasomatically altered rock.

Granite B shows an average of 23 ppm U, Granite A 10 ppm, the aplitic phase 21 ppm, and the metasomatite 43 ppm. The U content of Granite C is erratic between 6 and 81 ppm (Fig. 15A); this is probably the result of U mobility in this granite type. The Th/U ratio is crucial for the expected U mineral species within a granite (Cuney, 2014). The average Th/U of granitic rocks in the world is 4, which just reflects the Th/U of bulk earth (Cuney, 2014), and indicates that Th and U behave similarly during

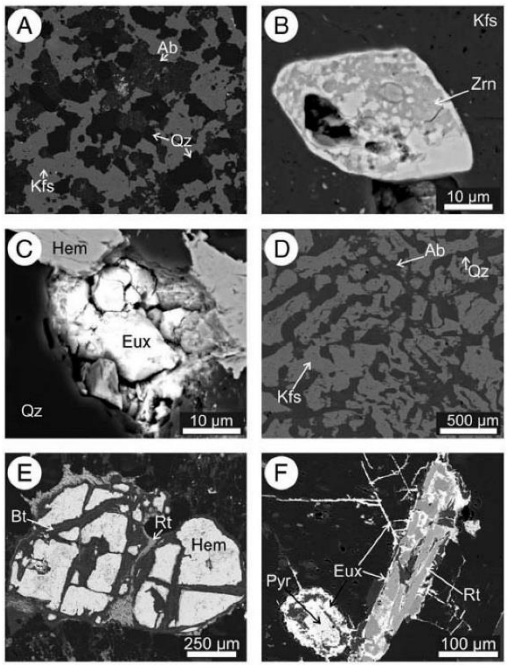

Fig. 13. BSE images, showing A) Aplite; fine-grained intergrowth of K-feldspar, quartz, and albite; the albite is porous and partly sericitised; grain boundaries inside the K-feldspar cannot be identified, leaving the impression of quartz and albite in a K-feldspar matrix; 009-1. B) Aplite; partly dissolved zircon showing internal compositional differences; 009-1. C) Aplite; crumbling euxenite-(Y) with hematite and quartz; 009-1. D) Metasomatite; micrographic intergrowth of K-feldspar, quartz, and albite, giving the rock its name; 762-2A. E) Metasomatite; biotite partially replacing hematite; the rutile is unaffected; 762-2B. F) Metasomatite; euxenite-(Y) as rim around pyrite, replacing rutile, and as small veinlets; 762-2B. Abbreviations: Ab-albite; Bt-biotite; Eux-euxenite, Hem-hematite; Kfs-K-feldspar; Pyr-pyrite; Qz-quartz; Rt-rutile; Zrn-zircon.

fractionation. The average Th/U for the least fractionated granite (A) is 4.2, for Granite B 3.2, for the aplite 0.9, for the metasomatite 0.7. Granite C is again very erratic with values between 11.9 and 0.8 (Fig. 15A).

4.2.2. Rare earth element distributions

The three main granite types show similar REY fractionation patterns, but these patterns are still sufficiently different to allow a distinction of varieties based on their REY properties. Granite A has the highest REY content (Fig. 15B). The LREE show a steep trend, the light HREE are slightly more enriched than the heavier HREE (Fig. 15C). The Eu-anomaly is moderately negative with an average Eu/Eu* of 0.54. Granite B shows a steeper trend for the LREE, the HREE contents are significantly lower than in Granites A and C (Fig. 15C). The Eu-anomaly is moderately negative around 0.49 (Fig. 15B). Granite C, shows a similar LREE pattern, the heavier HREE are more strongly enriched than the lighter HREE (Fig. 15C). The Eu-anomaly is pronounced negative with 0.25 (Fig. 15B). Two of 24 samples show a negative Ce-anomaly. In sample 762-5 all REE and Y are strongly enriched; ΣREY is 1450 ppm, around 4 times that of the average of Granite C.

Aplite and metasomatite appear LREE-depleted compared to the other three granitoid phases (Fig. 15C). ΣREY is <100 ppm and ~130 ppm in the aplitic phase and metasomatic, respectively (Fig. 15B). The Eu-anomalies are pronounced negative. The REY patterns of these two granites can be explained by fractionation of a LREE-bearing mineral, e.g. monazite, from the melt, which is in accordance with their highly fractionated nature. However, the variance in their concentrations, and presence of LREE in the metasomatite and HREE in the aplite, point to REY mobility and at least some degree of hydrothermal enrichment or depletion.

5. Discussion

5.1. Granitoid petrogenesis

The mineral paragenesis of Granites A and B fits the general pattern expected from metaluminous granites with ~1% Ca (Cuney and Friedrich, 1987). The main LREE-bearing mineral is allanite, Ti is partially incorporated in titanite, and Ca-amphiboles can be observed. The HREE in Granite A are mainly hosted in titanite; as indicated by trace element data (Table 4). This mineral is rather rare in Granite B, but HREE contents are also low. This may indicate early fractionation of titanite, depleting HREE within the melt. This hypothesis is supported by low concentrations of Ti and Zr in Granite B compared to Granite A (Table 6). Zirconium is readily incorporated into titanite (concentrations of up to several thousand ppm are measured).

The distinct, negative Eu-anomaly seen in Granite C indicates that it is more strongly fractionated than Granites A and B (Fig. 15B). This is also supported by the lower concentrations of Ca, Ba, and Sr, which fractionate with plagioclase, as well as the higher contents of Nb, Ta, and Rb. The low Ca content of this granite, mean 0.4 wt%, allows the crystallisation of monazite in a few samples. The higher content of Zr, Ti, and HREE in Granite C may indicate that there was no fractionation of titanite.

The aplite and its associated metasomatite are both strongly fractionated, as indicated by very strong depletion of Zr and Ti, and strong enrichment in Nb, Ta, and U. The micrographic to granophyric textures in the metasomatite are clearly a result of later recrystallisation.

A Th/U ratio of around 4 in a granitic melt leads to the incorporation of U into thorite (*uranothorite*); dedicated U minerals do not form (Cuney, 2014). Granites A and B fit this pattern with respect to their U/Th ratio and mineralogy. The Th/U ratios in Granite C are highly disturbed, the presence of *uranothorite* indicates a Th/U ratio of 2 to 6 (Cuney, 2014). Th/U ratios exceeding 6, as found in a few samples, indicate leaching of U, whereas Th/U ratios <2 are an indicator of later hydrothermal enrichment in U.

The aplite contains euxenite-(Y) as the main U-bearing mineral, which can be expected considering the high Nb/U, and low Th/U ratios (Cuney, 2014). Minor uraninite can be found along grain boundaries, characteristic for very low Th/U ratios (<1) and high U solubility. The U-bearing mineral in the metasomatite is also euxenite-(Y), which is clearly of hydrothermal origin. In the case of the metasomatite, high Nb/U and low Th/U may be the result of an influx of fluids rich in Nb, U, Y and HREE, leading to formation of euxenite.

5.2. Hydrothermal alteration

The defining character of plagioclase replacement in these granites is the creation of porosity, indicating a change in volume and a loss of elements. There is however, also evidence for input of new elements resulting from other fluid-mineral reactions in adjacent areas leading to pore filling (e.g., sericite, calcite, and hematite, Figs. 7 and 9–12). The porosity is considered the result of differences in solubility between albite (less soluble) and plagioclase (more soluble) which means that more plagioclase is dissolved than albite precipitated (Hövelmann et al., 2010). This re-equilibration takes place along a sharp interface between parent and product (Engvik et al., 2008) and leads to pseudomorphic mineral replacement as the case for feldspar alteration in the studied granites. During this type of replacement reaction, the dissolution and reprecipitation are interface-coupled (coupled dissolution

Table 6
Whole-rock geochemistry; major oxides in wt%; U in ppm.

Sample name	Lithology	SiO_2	TiO_2	Al_2O_3	FeO	MnO	MgO	CaO	K_2O	Na_2O	P_2O_5	Total	LOI-1000	Total + LOI	U	Th/U
007-1	A	71.88	0.50	13.00	3.16	0.05	0.63	1.44	5.89	2.68	0.06	99.25	0.94	100.19	10	4.36
007-2	A	70.66	0.55	12.81	3.36	0.05	0.63	1.20	5.57	2.74	0.06	97.57	1.19	98.76	11	2.29
007-4	A	70.30	0.48	12.41	3.42	0.08	0.61	1.40	5.55	2.63	0.06	96.88	1.55	98.43	12	5.55
005-1	B	76.27	0.12	11.77	1.54	0.01	0.13	0.81	5.88	2.57	<0.02	99.11	0.75	99.86	24	3.22
005-2	B	75.45	0.10	11.75	1.65	0.01	0.12	0.80	5.95	2.60	<0.02	98.43	0.92	99.35	23	3.15
009-1	Aplite	74.90	0.03	12.81	1.09	<0.01	0.05	0.17	6.69	2.72	<0.02	98.46	0.96	99.42	17	1.25
873-3	Aplite	73.49	0.07	12.77	1.24	<0.01	0.07	0.57	6.83	2.82	<0.02	97.85	0.69	98.54	22	0.55
751-2	Metasomatite	75.24	0.08	12.77	1.83	<0.01	0.10	0.41	4.96	3.88	<0.02	99.27	0.78	100.05	30	0.91
762-2A	Metasomatite	74.64	0.06	12.64	1.36	<0.01	0.08	0.98	4.52	4.00	<0.02	98.28	0.79	99.07	65	0.53
762-2B	Metasomatite	75.18	0.04	12.91	1.03	<0.01	0.05	0.71	6.36	3.28	<0.02	99.55	0.67	100.22	33	0.62
009-2	C	74.81	0.20	12.75	2.17	<0.01	0.22	0.38	5.85	3.02	<0.02	99.40	0.95	100.35	7	11.87
751-1	C	74.13	0.16	12.43	1.87	<0.01	0.18	0.46	6.38	2.74	<0.02	98.35	1.05	99.40	13	6.30
762-1	C	75.45	0.15	11.17	3.32	<0.01	0.30	0.25	7.48	0.80	<0.02	98.91	1.19	100.10	11	7.10
762-4	C	74.15	0.16	12.13	2.25	0.01	0.23	0.34	6.73	2.22	<0.02	98.23	1.40	99.63	38	2.09
762-5	C	75.52	0.10	10.32	2.87	<0.01	0.50	0.13	6.18	0.89	<0.02	96.50	2.72	99.22	40	1.59
843-1	C	73.94	0.15	12.13	2.16	0.01	0.22	0.52	5.66	2.91	<0.02	97.69	0.89	98.58	20	3.81
845-1	C	74.34	0.15	12.81	1.69	0.01	0.22	0.63	6.05	3.06	<0.02	98.95	0.83	99.78	62	1.26
845-2	C	74.60	0.16	12.45	1.74	0.01	0.61	0.13	6.54	1.68	<0.02	97.92	2.13	100.05	24	3.48
845-4	C	74.62	0.12	12.55	1.79	0.01	0.35	0.42	6.31	2.82	<0.02	98.99	1.27	100.26	81	0.79
873-1	C	74.32	0.16	12.51	1.81	0.01	0.25	0.77	5.67	3.06	<0.02	98.56	0.87	99.43	56	1.52
873-2	C	75.30	0.14	12.56	1.38	<0.01	0.17	0.15	5.96	3.11	0.02	98.80	0.93	99.73	6	10.29
873-4	C	74.51	0.16	12.62	1.65	0.04	0.27	0.62	5.81	3.07	0.04	98.77	0.80	99.57	50	1.63
873-5	C	74.62	0.14	12.89	1.88	<0.01	0.15	0.10	6.37	2.40	<0.02	98.54	1.33	99.87	17	4.13
893-3	C	75.39	0.14	12.24	1.69	0.01	0.18	0.46	5.91	2.80	<0.02	98.83	0.80	99.63	16	4.81
843-2	C	61.76	0.22	16.67	5.91	0.13	1.36	0.14	10.77	0.38	0.02	97.34	2.12	99.46	74	2.15

reprecipitation reaction; CDRR) and the process of plagioclase replacement can be described as albitisation. Engvik et al. (2008) assume that an external source of Na is needed, but albitisation can also be achieved by plagioclase losing its anorthite component without gaining new elements.

$$Na_{0.8}Ca_{0.2}Al_{1.2}Si_{2.8}O_8 \rightarrow 0.8\ NaAlSi_3O_8 + 0.2\ Ca^{2+} + 0.4\ Al^{3+} + 0.4\ SiO_4{}^{4-} \quad (1)$$

Input of Na is not needed, and may even be lost to a small degree. This reaction requires a medium to take place, which is presumably an initial deuteric fluid. This alteration stage, occurring immediately after magmatic crystallisation, is however followed by release of hydrothermal fluids as indicated by formation of highly complex replacement assemblages, including newly-formed K-feldspar, calc-silicates, REE-mineral, fluorite, hematite, etc. The released Ca, Al, and Si behave slightly differently in Granites A and B compared to Granite C. In Granite C, Ca appears to have been lost, and secondary Ca-bearing minerals could not be found except for synchysite and minor calcite. Nonetheless, in all studied granites the Al and Si are incorporated into sericite, its texture, small inclusions in albite, indicates that alteration at this stage is pervasive and driven via CDRR (Kontonikas-Charos et al., 2014, 2017, 2018). In Granites A and B, Ca is incorporated into calc-silicates; prehnite, pumpellyite, and epidote. The ratio Ca/Al/Si is 1:2:2 in anorthite and 2:2:3 to 2:3:3 in the calc-silicates, which is compensated by Al and Si being incorporated into sericite (Plümper and Putnis, 2009). External Ca is not needed, the Ca is 'self-sourced' from replaced anorthite. Sericite formation requires a source of K, which is most probably alkali feldspar, as biotite is only partially altered in Granites A and B, and plagioclase itself does not release enough K during alteration (Plümper and Putnis, 2009). The complete replacement reaction can be expressed as:

$$[\text{Granites A} + \text{B}]\text{: oligoclase} + K^+(aq.) + OH^-(aq.) \rightarrow \text{albite} + \text{calc-silicates} + \text{sericite} \quad (2)$$

$$[\text{Granite C}]\text{: oligoclase} + K^+(aq.) + OH^-(aq.) \rightarrow \text{albite} + \text{sericite} + Ca^+(aq.) \quad (3)$$

The presence of prehnite indicates temperatures below 400 °C. The Ca needed for replacement of biotite by garnet is most probably sourced from plagioclase. The element contents of biotite and calcic garnet, e.g., Al/Si ratios, are similar, indicating a simple exchange of K and Mg with Ca. The small rim of chlorite around garnet may be an intermediate product or a reverse reaction.

The fluid responsible for these replacements contains CO_2, as indicated by small inclusions of calcite within albite. The same fluid may have played a role in the replacement of allanite by calcite and synchysite, and the reaction of titanite with CO_2 to form calcite and rutile. The reaction of titanite with CO_2 is almost pressure independent and relies only on temperature and fCO_2. The calcite-synchysite-bearing vein is a further indicator for a fluid containing Ca, CO_2, and F. The REY in synchysite could have been leached from feldspar and from REE-bearing minerals such as allanite and titanite. This evidence further strengthens the hypothesis of contemporaneous alteration of feldspar, allanite, titanite, and, partially, also biotite, via a CO_2-rich fluid. Although not propylitic alteration in the strictest sense due to the absence of epidote, other hydrous Ca-minerals, including prehnite and pumpellyite, are present.

Whole rock geochemical data for Granites A, B and C do not support strong mobility of REY, although this is impossible to prove unequivocally without mass-balance calculations, which are in turn unreliable due to all rocks being altered to one degree or another. The synchysite-(Ce), associated with clay minerals, is presumably later than the feldspar replacement, but may source its REY from pre-existing allanite and feldspars. Fluorapatite and monazite are rare in Granite C; Phosphorus was removed from the melt during fractionation.

The fluorite-rich assemblages contain calc-silicates, indicating that enrichment in fluorite was contemporaneous with feldspar alteration and can presumably also be linked to early (deuteric) fluids. This argument is further supported by the characteristic chondrite-normalised REY fractionation trends for this fluorite (Fig. 8D), showing high ΣREE and a pronounced negative Eu-anomaly. The flat REY trends in garnet can be expected for iron-rich calcic garnet, where the substitution $Ca^{2+}Si^{4+} \leftrightarrow REE^{3+}Fe^{3+}$ appears to prefer LREE over HREE, while $Ca^{2+}Si^{4+} \leftrightarrow REE^{3+}Al^{3+}$ prefers HREE over LREE, producing the characteristic HREE + Y enriched REY-trends for grossular (Gaspar et al., 2008). In the granites of this study this effect might be enhanced by the garnets incorporating mostly REY released during feldspar alteration, which are strongly LREE-enriched.

The abundant veins in Granite C are clearly later than the pervasive alteration by deuteric fluids, which shows a change from a porosity-

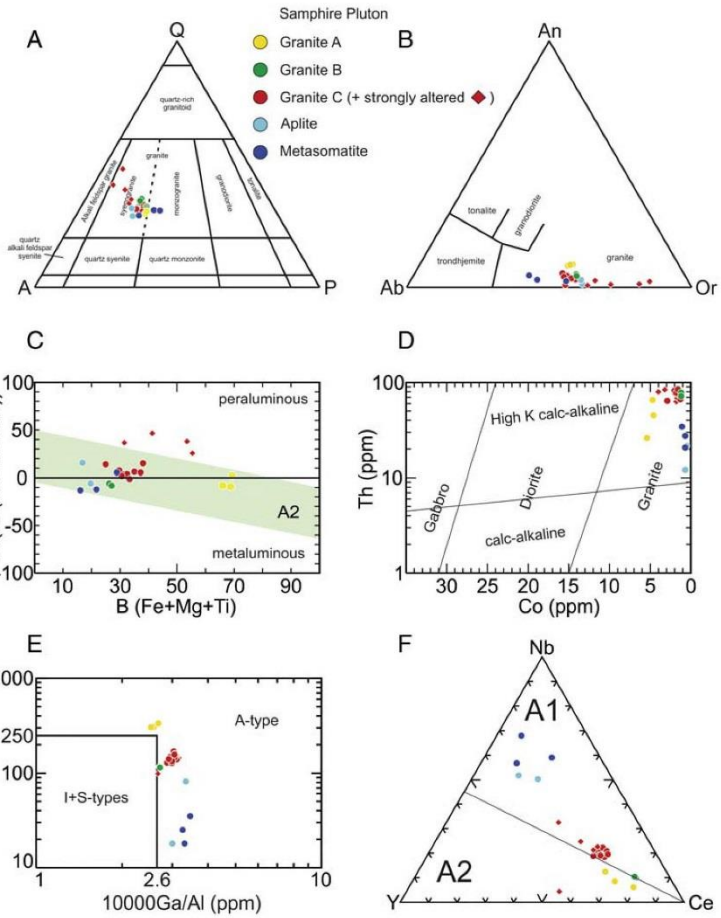

Fig. 14. A) Quartz - Alkali feldspar - Plagioclase (QAP) diagram (Streckeisen, 1974); all samples are clustered in the granite field. B) Albite – Anorthite – K-feldspar diagram (Barker, 1979); all samples are classified as granite. C) B-A diagram (Debon and Le Fort, 1983); samples are met- to peraluminous, and within a sector typical for A2-granites (after Cuney, 2014). D) Th-Co diagram (Hastie et al., 2007); all points plot in the High-K calc-alkaline granite field. E) 10,000 × Ga/Al vs. Zr; classification diagram (Whalen et al., 1987); all samples classify as A-type granites. F) Ce-Y-Nb ternary plot (Eby, 1992); Granite A classifies as A2, the other granites are presumably A2, but lost HREE during fractionation.

based alteration regime to a vein-dominated one. The relative timing of veins is, however, difficult to constrain as they are rarely in contact with one another. In general, a trend can be observed from pervasive alteration without significant H^+-metasomatism to vein formation with strong influx of hydrolytic alteration. The high pyrite content in sample 845-4, which is subsequently replaced by uraninite and coffinite, shows a change from early hydrothermal conditions, during which pyrite is deposited, to a late oxidising environment, depositing U-minerals. The hematite + coffinite and fluorite + quartz + hematite veins form under these oxidising conditions. Such a pattern is commonly observed in ore systems (e.g., in the felsic phases of the Bushveld Complex; Bailie and Robb, 2004), and in particular, from vein-hosted U deposits worldwide, e.g., Jachymov, Czech Republic, and in several Canadian U deposits (Ruzicka, 1993). The veins are later overprinted by chlorite + sericite, as well as the clay mineral veins, further supporting the idea that later veins contain more hydrated minerals with less K, Ca, and Na. Chlorite and sericite are not indicators of certain conditions and are presumably part of every alteration and vein assemblages. Additional constraints may be obtained from a forthcoming detailed geochronological study.

5.3. Implications for uranium mineralisation

The observed Th/U ratios in Granite C are highly disturbed and a strong indicator for mobility of uranium and probable dissolution of primary uranium minerals, which is further supported by the presence of coffinite in veins and clearly hydrothermal coffinite and uraninite in the granite surrounding the veins. The spatial association between abundance of U minerals and veining indicates that U was mobile during the vein-dominated regime, and that veins were an important conduit for U transport. The original U content can only be assumed; considering an initial Th/U ratio of ~3.5, similar to Granite B, a U content of 25 ppm can be assumed. This would correspond with similar Th/U ratios and U contents in other HIS granites, e.g., the Roxby Downs Granite.

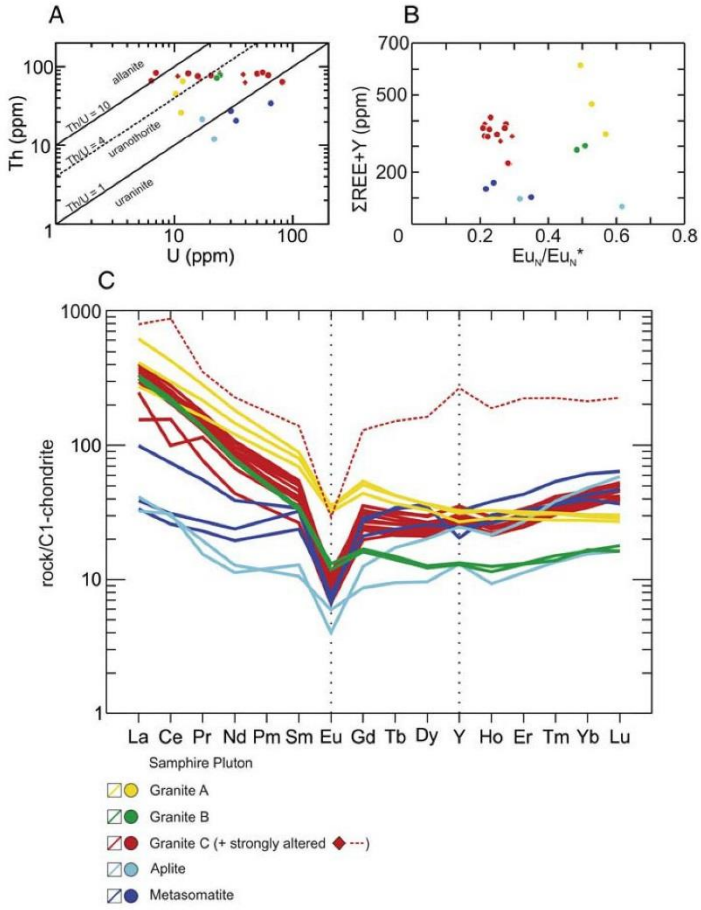

Fig. 15. A) U (ppm) vs. Th (ppm); Th/U = 4 is the assumed ratio of bulk earth; the expected U minerals and their boundaries are from Cuney, 2014. B) Eu-anomaly vs. Σ(REE + Y); EuN chondrite-normalised Eu value; EuN* = (SmN + GdN) / 2. C) C1-chondrite-normalised REE + Y values.

A late oxidising assemblage of hematite + fluorite + uraninite can be found in several ore deposits, especially vein-hosted U ones (e.g., Ruzicka, 1993; Bailie and Robb, 2004). We cannot be sure that the hematite in these assemblages is not secondary. In the granites studied here, fluorite and U-minerals are spatially separated, yet nevertheless both associated with hematite.

The abundant pores are not interconnected, as indicated by their shape. They are open during the feldspar replacement, but readily lose their interconnections during later coarsening (Engvik et al., 2008). Uranium may, however, have undergone some degree of transport while the pores were open. As mentioned feldspar alteration is strongly associated with calcite and CO_2-rich fluids. Such fluids are able to transport U, as seen in several vein-type uranium deposits, e.g., in Canada or China (Hu et al., 2017; Liang et al., 2017).

Uranium minerals in veins are only observed in the deeper parts of the core, which is a consequence of later overprinting and remobilisation by the clay mineral veins. The abundant xenotime in the clay veins may be a remnant of remobilised phases representing intermediate solid solutions in the system thorite–xenotime–zircon–coffinite, found in the coffinite-bearing veins. It is possible that the U in the overlying sediment-hosted deposit was largely leached from uraninite- and coffinite-bearing veins, which served as protore.

HIS granites are generally rich in U, and the South Australian Heat Flow Anomaly (SAHFA) indicates widespread radioactive isotopes (U, Th, K) in the basement of the eastern Gawler Craton (Neumann et al., 2000). The HIS granites are the result of widespread crustal melting, which might have concentrated the U from the basement.

6. Concluding remarks

This study has documented and characterised three geochemically distinct types of granite. All display complex alteration signatures and multiphase crosscutting veining, which increase in intensity closer to the deposit. Alteration of feldspars resembles that seen in Hiltaba-aged granites on a regional scale with a marked spatial association to U-bearing iron-oxide copper gold style mineralisation. Calc-silicates are a minor yet significant component of the Samphire granites. The marked enrichment in U, as hydrothermal U minerals, in upper parts

of the granites and the crosscutting veins are interpreted as evidence for U mobility and likely represent a source of uranium which was subsequently mobilised into the cover rocks.

The data and interpretations presented here represent a valuable first step towards a comprehensive genetic model for the Samphire uranium system. Further work will target the geochronology of uranium mineralisation and hydrothermal events in the basement and in overlying sediments, and the mineralogy and depositional environment of sediment-hosted uranium mineralisation.

Supplementary data to this article can be found online at https://doi.org/10.1016/j.lithos.2017.11.031.

Acknowledgements

U.D. acknowledges receipt of a Ph.D. scholarship from the Carthew Family Trust. The assistance of staff at Adelaide Microscopy with microanalytical work is gratefully acknowledged. N.J.C. acknowledges support from the ARC Research Hub for Australian Copper-Uranium. This publication benefitted from earlier work within an honours thesis by Goldsmith (2014). We appreciate comments from Lithos reviewers Michel Cuney and Reimar Seltmann, and Editor-in-Chief Nelson Eby, which helped us improve our manuscript.

References

Allen, S.R., McPhie, J., Ferris, G., Simpson, C., 2008. Evolution and architecture of a large felsic Igneous Province in western Laurentia: the 1.6 Ga Gawler Range Volcanics, South Australia. Journal of Volcanology and Geothermal Research 172, 132–147.

Allen, S.R., Simpson, C.J., McPhie, J., Daly, S.J., 2003. Stratigraphy, distribution and geochemistry of widespread felsic volcanic units in the Mesoproterozoic Gawler Range Volcanics, South Australia. Australian Journal of Earth Sciences 50, 97–112.

Bailie, R.H., Robb, L.J., 2004. Polymetallic mineralization in the granites of the Bushveld Complex - examples from the central southeastern lobe. South African Journal of Geology 107, 633–652.

Barker, F., 1979. Trondhjemite: definition, environment and hypotheses of origin. Trondhjemites, Dacites and Related Rocks. Elsevier, Amsterdam pp. 1-12.

Budd, A.R., Wyborn, L.A.I., Bastrakova, I.V., 2002. The metallogenic potential of Australian proterozoic granites. Geoscience Australia Record 2001/12.

Creaser, R.A., Fanning, C.M., 1993. A U-Pb zircon study of the Mesoproterozoic Charleston Granite, Gawler Craton, South Australia. Australian Journal of Earth Sciences 40, 519–526.

Cuney, M., 2014. Felsic magmatism and uranium deposits. Bulletin de la Societe Geologique de France 185 (2), 75–92.

Cuney, M., Friedrich, M., 1987. Physicochemical and crystal-chemical controls on accessory mineral paragenesis in granitoids: implications for uranium metallogenesis. Bulletin de Mineralogie 110, 235–247.

Debon, F., Le Fort, P., 1983. A chemical–mineralogical classification of common plutonic rocks and associations. Earth and Environmental Science, Transactions of The Royal Society of Edinburgh 73, 135–149.

Daly, S.J., Fanning, C.M., Fairclough, M.C., 1998. Tectonic evolution and exploration potential of the Gawler Craton, South Australia. AGSO Journal of Australian Geology and Geophysics 17, 145–168.

Eby, G.N., 1992. Chemical subdivision of the A-type granitoids: petrogenetic and tectonic implications. Geology 20, 641–644.

Ehrig, K., McPhie, J., Kamenetsky, V., 2012. Geology and mineralogical zonation of the Olympic Dam iron oxide Cu-U-Au-Ag deposit, South Australia. Economic Geology, Special Publication 16, 237–267.

Engvik, A.K., Putnis, A., Fitz Gerald, J.D., Austrheim, H., 2008. Albitization of granitic rocks: the mechanism of replacement of oligoclase by albite. The Canadian Mineralogist 46, 1401–1415.

Ferris, G., Schwarz, M., Heithersay, P., 2002. The geological framework, distribution and controls of Fe-oxide Cu-Au mineralisation in the Gawler Craton, South Australia: part 1: geological and tectonic framework. In: Porter, T.M. (Ed.), Hydrothermal Iron Oxide Copper-Gold Related Deposits: A Global Perspective. 2. Adelaide, PGC Publishing, pp. 9–31.

Fraser, G.L., McAvaney, S., Neumann, N., Szpunar, M., Reid, A., 2010. Discovery of early Mesoarchean crust in the eastern Gawler Craton, South Australia. Precambrian Research 179, 1–21.

Fraser, G.L., Neumann, N.L., 2010. New SHRIMP U-Pb zircon ages from the Gawler Craton and Curnamona Province, South Australia, 2008–2010. Geoscience Australia, Record, 2010/16.

Gaspar, M., Knaack, C., Meinert, L.D., Moretti, R., 2008. REE in skarn systems: a LA-ICP-MS study of garnets from the Crown Jewel gold deposit. Geochimica et Cosmochimica Acta 72, 185–205.

Goldsmith, S.D., 2014. The Samphire Project: A Distal IOCG and Evidence for Mesoarchean Crust in the Gawler Craton. unpublished Honours thesis. University of Adelaide.

Goodwin, S., 2010. Geochemical and Isotopic Investigation Into the Tectonic Setting of Mesoarchean and Paleoproterozoic Granitoid Suites Within the Eastern Gawler Craton, South Australia. unpublished Honours thesis. University of Adelaide.

Hastie, A.R., Kerr, A.C., Pearce, J.A., Mitchell, S.F., 2007. Classification of altered volcanic island arc rocks using immobile trace elements: development of the Th–Co discrimination diagram. Journal of Petrology 48, 2341–2357.

Hitzman, M.W., Valenta, R.K., 2005. Uranium in iron oxide-copper-gold (IOCG) systems. Economic Geology 100, 1657–1660.

Hövelmann, J., Putnis, A., Geisler, T., Schmidt, B.C., Golla-Schindler, U., 2010. The replacement of plagioclase feldspars by albite: observations from hydrothermal experiments. Contributions to Mineralogy and Petrology 159, 43–59.

Hou, B., Fabris, A.J., Keeling, J.L., Fairclough, M.C., 2007. Cainozoic palaeochannel-hosted uranium and current exploration methods, South Australia. MESA Journal 46, 34–39.

Hou, B., Fabris, A.J., Michaelsen, B.H., Katona, L.F., Keeling, J.L., Stoian, L., Wilson, T.C., Fairclough, M.C., Cowley, W.M., 2012. Paleodrainage and Cenozoic costal barriers of South Australia: a new map and GIS dataset. MESA Journal 66, 26–32.

Hou, B., Keeling, J., Li, Z., 2017. Paleovalley-related uranium deposits in Australia and China: a review of geological and exploration models and methods. Ore Geology Reviews 88, 201–234.

Howard, K.E., Reid, A., Hand, M., Barovich, K., Belousova, E., 2006. Does the Kalinjala Shear Zone represent a palaeosuture zone? MESA Journal 43, 16–20.

Hu, R., Bi, X., Zhou, M., Peng, J., Su, W., Liu, S., Qi, H., 2017. Uranium metallogenesis in South China and its relationship to crustal extension during the Cretaceous to Tertiary. Economic Geology 103, 583–598.

Kontonikas-Charos, A., Ciobanu, C.L., Cook, N.J., 2014. Albitization and redistribution of REE and Y in IOCG systems: insights from Moonta-Wallaroo, Yorke Peninsula, South Australia. Lithos 208-209, 178–201.

Kontonikas-Charos, A., Ciobanu, C.L., Cook, N.J., Ehrig, K., Krneta, S., Kamenetsky, V.S., 2017. Feldspar evolution in the Roxby Downs Granite, host to Fe-oxide Cu-Au-(U) mineralisation at Olympic Dam, South Australia. Ore Geology Reviews 80, 838–859.

Kontonikas-Charos, A., Ciobanu, C.L., Cook, N.J., Ehrig, K., Krneta, S., Kamenetsky, V.S., 2018. Rare earth element geochemistry of feldspars: examples from Fe-oxide Cu-Au systems in the Olympic Cu-Au Province, South Australia. Mineralogy and Petrology in press. https://doi.org/10.1007/s00710-017-0533-z.

Liang, R., Chi, G., Ashton, K., Blamey, N., Fayek, M., 2017. Fluid compositions and P-T conditions of vein-type uranium mineralization in the Beaverlodge uranium district, northern Saskatchewan, Canada. Ore Geology Reviews 80, 460–483.

McAvaney, S., Thiel, S., Wade, C.E., 2016. The Kalinjala Shear Zone - intracontinental shear zone or palaeosuture? Paper Presented at the Australian Earth Science Convention, Adelaide

Neumann, N., Sandiford, M., Foden, J., 2000. Regional geochemistry and continental heat flow: implications for the origin of the South Australian heat flow anomaly. Earth and Planetary Science Letters 183, 107–120.

Parker, A.J., 1980. The Kalinjala Mylonite Zone, Eastern Eyre Peninsula. Quarterly Geological Notes - Geological Survey of South Australia 76, 6–11.

Parker, A.J., 1993. Kimban orogeny. In: Drexel, J.F., Preiss, W.V., Parker, A.J. (Eds.), The Geology of South Australia: The Precambrian (Vol. 1). Geological Survey of South Australia, Adelaide.

Parker, A.J., Fanning, C.M., 1998. Whyalla, South Australia: explanatory notes, 1:250000 geological series: sheet SI53-8. In: Drexel, J.F. (Ed.), Geology - South Australia. PIRSA publications and display branch, Adelaide.

Plümper, O., Putnis, A., 2009. The complex hydrothermal history of granitic rocks: multiple feldspar replacement reactions under subsolidus conditions. Journal of Petrology 50, 967–987.

Reid, A., Hand, M., 2012. Mesoarchean to Mesoproterozoic evolution of the southern Gawler Craton, South Australia. Episodes 35, 216–225.

Reid, A., Jagodzinski, E., Gerhard, F., 2017. Project PGC03-01: Geochronology from the Samphire Uranium Project. In: Jagodzinski, E.A., Reid, A.J. (Eds.), PACE Geochronology: Results of collaborative geochronology projects 2013–2015, Report Book 2015/00003. Department of the Premier and Cabinet, South Australia, Adelaide, pp. 10–28.

Rudnick, R.L., Gao, S., 2003. 3.01 - composition of the continental crust. In: Holland, H.D., Turekian, K.K. (Eds.), Treatise on Geochemistry (Vol. 3: The Crust) Oxford. pp. 1-64.

Ruzicka, V., 1993. Vein uranium deposits. Ore Geology Reviews 8, 247–276.

Skirrow, R.G., Bastrakov, E.N., Davidson, G., Raymond, O.L., Heithersay, P., 2002. The geological framework, distribution and controls of Fe-oxide Cu-Au mineralisation in the Gawler Craton, South Australia: part II - alteration and mineralisation. In: Porter, T.M. (Ed.), Hydrothermal Iron Oxide Copper-Gold & Related Deposits: A Global Perspective. 2. Adelaide, PGC Publishing, pp. 33–47.

Skirrow, R.G., Bastrakov, E.N., Barovich, K., Fraser, G.L., Creaser, R.A., 2007. Timing of iron oxide Cu-Au-(U) hydrothermal activity and Nd isotope constraints on metal sources in the Gawler Craton, South Australia. Economic Geology 102, 1441–1470.

Streckeisen, A., 1974. Classification and nomenclature of plutonic rocks. Geologische Rundschau 63, 773–786.

Szpunar, M., Hand, M., Barovich, K., Jagodzinski, E., Belousova, E., 2011. Isotopic and geochemical constraints on the Paleoproterozoic Hutchison Group, southern Australia: implications for Paleoproterozoic continental reconstructions. Precambrian Research 187, 99–126.

UraniumSA, 2007. Uranium discovery. ASX RELEASE 12 December 2007. 1–4 pp, http://www.asx.com.au/asx/statistics/displayAnnouncement.do?display=pdf&idsId=00794394.

UraniumSA, 2013. SAMPHIRE PROJECT UPDATE. ASX RELEASE 27 September 2013. 1–27 pp. http://www.asx.com.au/asx/statistics/displayAnnouncement.do?display=pdf&idsId=01448164.

UraniumSA, 2014. Significant upside targeting high grade unconformity uranium mineralisation Blackbush deposit, Samphire Project. ASX RELEASE 25 July 2014. 1–8 pp. http://www.asx.com.au/asx/statistics/displayAnnouncement.do?display=pdf&idsId=01536222.

Whalen, J.B., Currie, K.L., Chappell, B.W., 1987. A-type granites: geochemical characteristics, discrimination and petrogenesis. Contributions to Mineralogy and Petrology 95, 407–419.

Wingate, M.T.D., Campbell, I.H., Compston, W., Gibson, G.M., 1998. Ion microprobe U–Pb ages for Neoproterozoic basaltic magmatism in south-central Australia and implications for the breakup of Rodinia. Precambrian Research 87, 135–159.

Yeates, G., 1990. Middleback Range iron ore deposits. In: Hughes, F.E. (Ed.), Geology of the Mineral Deposits of Australia & Papua New Guinea. 2. The AusIMM, Melbourne, pp. 1045–1048.

CHAPTER 3

MICRON- TO NANOSCALE CHARACTERISATION AND U-PB GEOCHRONOLOGY OF ZIRCON FROM GRANITES OF THE SAMPHIRE PLUTON, SOUTH AUSTRALIA

Urs Domnick[1], Nigel J. Cook[1], Cristiana L. Ciobanu[1], Liam Courtney-Davies[1], Marija Dmitrijeva[1], Max R. Verdugo-Ihl[1], Jing Xu[1,2], William Keyser[1], Ashley Slattery[3], Allen K. Kennedy[4], Russel Bluck[5]

[1] *School of Chemical Engineering and Advanced Materials, The University of Adelaide, Adelaide, SA 5005, Australia*

[2] *Key Laboratory of Mineral Resources, Institute of Geology and Geophysics, Chinese Academy of Sciences, Beijing, 100029, China*

[3] *Adelaide Microscopy, The University of Adelaide, Adelaide, SA 5005, Australia*

[4] *John de Laeter Centre, Curtin University, Bentley, WA 6102, Australia*

[5] *Samphire Uranium Pty Ltd., 28 Greenhill Road, Wayville, SA 5034, Australia*

Article Submitted to Precambrian Research, 11th November, 2019

Statement of Authorship

Title of Paper	Micron- to Nanoscale Characterisation and U-Pb Geochronology of Zircon From Granites of The Samphire Pluton, South Australia
Publication Status	☐ Published ☐ Accepted for Publication ☐ Unpublished and Unsubmitted work written in manuscript style ☑ Submitted for Publication
Publication Details	Article Submitted to Precambrian Research, 11th November, 2019

Principal Author

Name of Principal Author (Candidate)	Urs Domnick		
Contribution to the Paper	Analytical work, data processing, interpretation, wrote manuscript		
Overall percentage (%)	50		
Certification:	This paper reports on original research I conducted during the period of my Higher Degree by Research candidature and is not subject to any obligations or contractual agreements with a third party that would constrain its inclusion in this thesis. I am the primary author of this paper.		
Signature		Date	14/11/2019

Co-Author Contributions

By signing the Statement of Authorship, each author certifies that:

i. the candidate's stated contribution to the publication is accurate (as detailed above);

ii. permission is granted for the candidate in include the publication in the thesis; and

iii. the sum of all co-author contributions is equal to 100% less the candidate's stated contribution.

Name of Co-Author	Nigel J. Cook		
Contribution to the Paper	assisted with data processing, interpretation, wrote manuscript		
Overall percentage (%)	15		
Signature		Date	14/11/2019

Name of Co-Author	Cristiana L. Ciobanu		
Contribution to the Paper	assisted with analytical work, data processing and interpretation, evaluation of manuscript		
Overall percentage (%)	10		
Signature		Date	14/11/2019

Name of Co-Author	Liam Courtney-Davies		
Contribution to the Paper	assisted with analytical work, data processing, evaluation of manuscript		
Overall percentage (%)	5		
Signature		Date	14/11/2019

Name of Co-Author	Marija Dmitrijeva		
Contribution to the Paper	assisted with analytical work, data processing, evaluation of manuscript		
Overall percentage (%)	5		
Signature		Date	14/11/2019

Name of Co-Author	Max R. Verdugo-Ihl
Contribution to the Paper	assisted with analytical work, data processing, evaluation of manuscript

Overall percentage (%)	5		
Signature		Date	14/11/2019

Name of Co-Author	Jing Xu		
Contribution to the Paper	assisted with analytical work		
Overall percentage (%)	2.5		
Signature		Date	14/11/2019

Name of Co-Author	William Keyser		
Contribution to the Paper	assisted with analytical work		
Overall percentage (%)	2.5		
Signature		Date	14/11/2019

Name of Co-Author	Ashley Slattery		
Contribution to the Paper	operated TEM		
Overall percentage (%)	2		
Signature		Date	14/11/2019

Name of Co-Author	Allen K. Kennedy		
Contribution to the Paper	assisted with analytical work, evaluation of manuscript		
Overall percentage (%)	2		
Signature		Date	14/11/2019

Name of Co-Author	Russel Bluck		
Contribution to the Paper	evaluation of manuscript		
Overall percentage (%)	1		
Signature	(in absence, signed by Nigel Cook)	Date	14/11/2019

Abstract

Zircon from three distinct granites within the Samphire Pluton, South Australia, are characterised at the micron- to nanoscale. Sensitive high-resolution ion microprobe (SHRIMP) U-Pb zircon dating generated $^{207}Pb/^{206}Pb$ weighted average ages of 1586 ± 9.3 Ma, 1583.2 ± 8.5 Ma and 1578 ± 9.5 Ma for Granites A, B and C, respectively. Although zircons from all three granites display evidence of hydrothermal overprinting, this is most strongly expressed in the distinct, yellowish granite (Granite C). Alteration is expressed as variation in the concentrations of HREE + Y, Th and Pb, whereby grain margins are relatively enriched in these elements and both Zr and Si are depleted. Altered zircon cores have high U contents relative to grain margins, which are appreciably poorer in this element, whereas Th is strongly enriched within crosscutting microfractures. Coupled with the relative enrichment in non-formula elements and marked disturbance of U-Th-Pb isotope ratios, the nanoscale observations of nanoparticles implying mobility of Pb and other elements, nanofractures and structural defects demonstrate that zircon in Granite C has undergone multi-stage alteration impacting upon accurate dating. Importantly, and with implications for analogous systems elsewhere, our results confirm open system U-Pb behaviour in Hiltaba Suite zircon. The three granites comprising the Samphire pluton probably represent temporally distinct phases of a larger magmatic system. SHRIMP U-Pb zircon geochronology cannot, however, confidently resolve any statistical differences in their age. Zircons within the most altered Granite (C), directly underlying the Blackbush uranium deposit contain convincing micron- to nanoscale evidence for an alteration event that triggered uranium remobilisation.

1. Introduction

The Eastern Gawler Craton, South Australia, is of global economic importance as the host to the World-class Olympic Dam Cu-U-Au-Ag deposit and a diverse range of other copper and/or gold deposits (Reid, 2017, and references therein). Iron-oxide copper gold (IOCG) mineralisation is associated with emplacement of ~1.6 Ga granitoids forming the Hiltaba Suite (HS) and is well

recognised throughout the eastern Gawler Craton, defining the Cu-Au Olympic Province (Skirrow et al., 2007). Granitoids of similar age are also known within bedrock on the Eyre Peninsula, e.g., the Samphire Pluton (SP) and the Charleston Granite (Creaser and Fanning, 1993; Fig. 1). Any extension of the IOCG province further westwards is still under debate. Petrological-geochemical study of granites from the Samphire Pluton (Domnick et al., 2018) has shown three distinct granitoids within the Samphire Pluton, which correspond to domains interpreted from geophysical data (Bluck and Brown, 2017; Fig. 1C).

Prior U-Pb zircon dating of two of the three granites, using sensitive high-resolution ion microprobe (SHRIMP), yielded $^{207}Pb/^{206}Pb$ weighted average ages of 1583 ± 4 Ma and 1585 ± 7 Ma (Reid et al., 2017). Such a statistical overlap for granites of distinct appearance indicates either short-lived magmatic activity, colouring due to alteration, and/or differences in fractionation due to differences in crustal assimilation. A range of U/Pb dates have been reported for HS granites in the Moonta-Wallaroo District on the Yorke Peninsula. These include the Tickera Pluton, likely connected to, or part of the same batholith body as the Samphire Pluton, where four separate granitic samples from Point Riley, ranging from 'fresh' to highly altered and deformed, yielded U/Pb dates of 1577 ± 7 Ma, up to 1597 ± 7 Ma (SHRIMP; Fanning et al., 2007). Zircon from each of these samples exhibit Pb loss, with the 'youngest' sample experiencing the most.

Granite 'fertility' with respect to the release of hydrothermal fluids capable of precipitating IOCG-style mineralisation was addressed at the micron- to nanoscale by Courtney-Davies et al. (2019). This study investigated representative zircons from ~1850 Ma Donington Suite and ~1590 Ma Hiltaba Suite granitoids from across the Olympic Province and Eyre Peninsula. Each sampled granite was also characterised in terms of U-Pb age. The study demonstrated that early Fe- and Cl-metasomatism, pre-dating metamictization, is pronounced in locations that host IOCG mineralisation and that a mottling of zircon by chloro–hydroxy–zircon nanoprecipitates is strongly indicative of proximity to known deposits. Zircon from the Charleston Granite, which features alkali-calcic alteration typical of IOCG mineralisation (Keyser et al., 2019), was shown to lack such nanoprecipitates (Courtney Davies

et al., 2019) despite the fact that the zircon displays Fe metasomatism, alongside enrichment in a wider range of non-formula elements (e.g., Ca or Ti).

The objective of the present study was to obtain U-Pb zircon ages for each of the three granites as defined by Domnick et al. (2018), in an attempt to understand the observed differences in appearance. Secondly, following the approach of Courtney-Davies et al. (2019), we aimed to characterise the dated zircon from each granite in terms of geochemistry and textures at the micron- and nanoscale. We thus aim to evaluate the U-Pb isotopic data by nanoscale study of dated zircon grains displaying a range of U-Pb systematics. The results have significance in terms of defining the 'fertility' of the Samphire Pluton as another HS granite with potential for generation of IOCG-style mineralisation.

2. Background

The Samphire Pluton is located on the northeastern Eyre Peninsula, a region characterised by Donington Suite granites, the ~2.0 Ga Warrow Quartzite and a diverse range of 1.79–1.63 Ga igneous rocks and associated sediments (Szpunar et al., 2011; Reid and Hand, 2012, and references therein; Fig. 1B, C). The spatial extent of the Samphire Pluton under the Spencer Gulf is poorly defined, but geophysical data indicates HS-affiliated intrusions under the Spencer Gulf and a possible connection between the Samphire Pluton and HS granites on the Yorke Peninsula, e.g., the Tickera Granite, which may form a single batholith.

Eocene sandstones of the Kanaka Beds fill a paleochannel overlying granites of the Samphire Pluton and host uranium mineralisation. The Blackbush and adjacent Plumbush prospects (SP; Fig. 1A) have a combined estimated inferred resource of 64.5 million tonnes of mineralisation at a bulk grade of 230 ppm, containing 14,850 tonnes U_3O_8 at a cut-off of 100 ppm U_3O_8 (Samphire Uranium, 2019).

In a petrographic study aimed at characterising granites in the Samphire area and their relationships with U mineralisation in the suprajacent cover sequence, Domnick et al. (2018) recognised three distinct granitoids forming the Samphire Pluton (Fig. 1C, D). The southern part of the pluton was

referred to as the green granite (Granite B). The northern part, immediately underlying the Blackbush deposit, is comprised by the red granite (Granite C), characterised by reddened feldspars, high U content and disturbed Th/U ratios. Granites B and C are separated by an arcuate domain of the so-called yellow granite (Granite A). The latter appears significantly less evolved than the other two, as indicated by higher CaO and lower U contents.

The geochemistry of the three granites does not clearly define a single evolutionary path of fractionation and differentiation and thus may not be related to one another within a single petrogenetic model (Domnick et al., 2018). All granite types are anomalously rich in U relative to crustal averages. The highly variable Th/U, as well as the presence of hydrothermal U minerals (mostly coffinite) within granites and veins, are clear evidence of U mobility. Domnick et al. (2018) proposed that U may have been pre-concentrated in veins in the upper parts of the pluton during a hydrothermal event that post-dated granite emplacement. After deposition of the sedimentary cover above a major unconformity, the U was leached and migrated upwards.

Coffinite from sandstone and saprolite were dated via chemical (microprobe) U-Pb methods yielding a weighted average age of 17.01 ± 0.16 Ma, strongly indicating a single coffinite-forming event at that time (Domnick et al., in review).

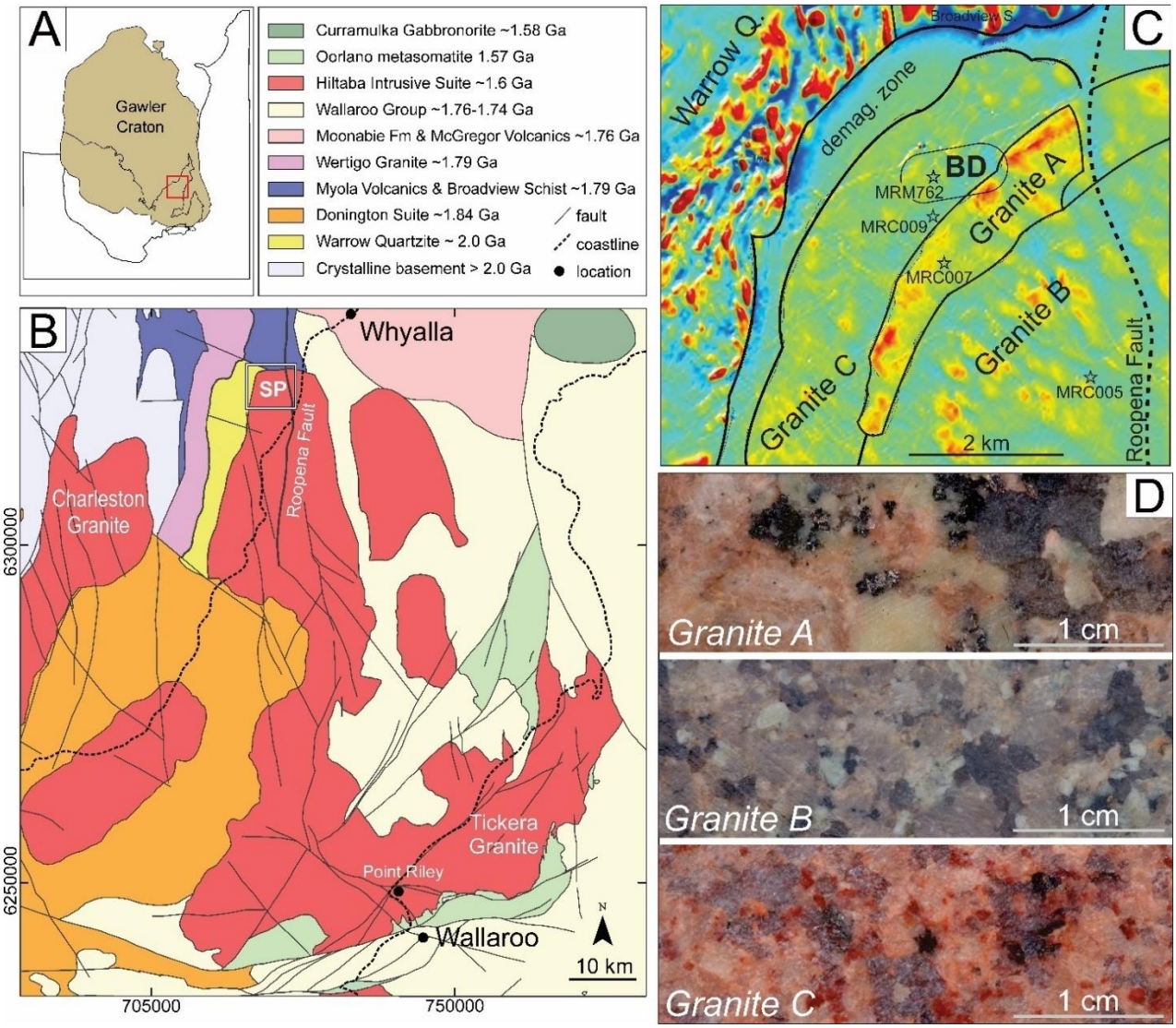

Figure 1. (A) Sketch map of the Gawler Craton showing location of study area (red square). (B) Simplified map of the bedrock geology of eastern Eyre Peninsula and Western Yorke Peninsula; SP − Samphire Pluton. (C) Geophysical map of the northwestern edge of the Samphire Pluton; BD − Blackbush deposit, mineralised Eocene sediment. (D) Representative photographs of the dated granites.

3. Sampling and analytical methodology

3.1. Sample suite and preparation

Three representative samples were selected for this study, one from each drill core intersecting intervals typical of each granite, taking care to avoid any veins and cracks. The sample size was 1 kg from each from drill holes MRC 005 (Granite B) and MRC 007a (Granite A), and 2 kg from MRM 762 (Granite C). The larger volume of the latter was to counter the expected low quality of zircons

based on earlier findings of highly metamict and/or altered zircons in polished blocks of granites from this drillcore. The two U-Pb zircon ages published by Reid et al. (2017) are from: (i) Granite B from a different section of the same drillhole (MRC 005) sampled here; and (ii) Granite C from drillhole MRC 009, which lies north of the drillhole sampled in the present study (Fig. 1C).

A brief description of the three granites given in Domnick et al. (2018) is summarised here. Granite A and B are coarse-grained and consist primarily of reddened alkali feldspar and greenish-white plagioclase, surrounded by quartz and mafic minerals (Fig. 1D). In both cases, alkali feldspar has been replaced by patch perthite, while plagioclase grains have largely been replaced by an assemblage of albite + sericite ± Ca-silicates. Granite A contains roughly double the amount of mafic minerals as in Granite B, mainly biotite and hornblende, which are partly replaced by chlorite ± titanite ± garnet. Granite A is the least fractionated of the three granites (~71 wt.% SiO_2), containing on average 310 ppm Zr, 11 ppm U and 84 ppm HREE + Y. Although displaying comparable mineralogy, Granite B is more fractionated (~76 wt.% SiO_2), and as a result, also contains more U (24 ppm), and less Zr (120 ppm) and HREE + Y (35 ppm).

Granite C (MRM 762; Fig. 1D) is a red, medium-grained granite, containing alkali feldspar and plagioclase, which are both strongly reddened, and quartz. Alkali feldspar has been replaced by patch perthite; plagioclase has been replaced by albite ± sericite. Biotite, the main mafic mineral, has been replaced by chlorite ± rutile. Granite C is weakly fractured and hosts veins with varying mineralogy. It is the most fractionated of the three granites with ~75 wt.% SiO_2, 150 ppm Zr, 75 ppm HREE+Y, and highly variable U (7 to 81 ppm).

Zircon grain separates were generated by Geotrack (Melbourne). Samples were crushed using a jaw crusher and disc pulveriser, and zircon separated using a Wilfley Table, Franz isodynamic separators and heavy liquid mineral separation. Handpicked grains were mounted on 2.5 cm-diameter epoxy resin blocks.

Selected zircon grains in each granite were dated via SHRIMP. From each granite, one representative, oscillatory-zoned grain was analysed in detail by electron probe microanalysis

(EPMA), focusing on the subtle differences in chemistry between dark and bright bands. Grains dated by SHRIMP were analysed by laser-ablation inductively coupled plasma-mass spectrometry (LA-ICP-MS) for trace element concentrations. Selected grains in each sample were also mapped by LA-ICP-MS for trace element and U-Pb isotope distributions.

3.2. Micron- and nanoscale analytical techniques

All sample characterisation was undertaken at Adelaide Microscopy, The University of Adelaide. The mounted grains were examined in transmitted light using a Nikon petrographic microscope, and in secondary electron (SEM) and backscattered electron mode (BSE) using a FEI Quanta 450 SEM with energy-dispersive X-ray (EDX) spectrometric capability. Cathodoluminescence (CL) imaging, with emphasis on zonation patterns and core-rim textures, was undertaken using a FEI Quanta 600 MLA SEM. All CL imaging was done using the same settings (15 kV, 6.5 nm spot size).

Quantitative compositional data for zircon was obtained using a Cameca SX-Five electron probe microanalyser for major and minor elements. Determination of trace element concentrations was performed via LA-ICP-MS spot analysis using a RESOlution-LR excimer laser microprobe coupled with an Agilent 7900x Quadrupole ICP-MS). In addition, LA-ICP-MS was used for mapping of selected elements and U-Th-Pb isotopes. Analytical settings, parameters, primary and secondary standards are as given by Courtney-Davies et al. (2019).

Thinned foils for investigation by high-angle annular dark-field scanning transmission electron microscopy (HAADF STEM) were prepared from dated zircon grains (marked on concordia diagrams shown below). Similar approaches were followed as outlined by Courtney-Davies et al. (2019), with analogous objectives to identify features that might impact on the accuracy of geochronological data. Preparation of thinned (<100 nm) foils for transmission electron microscopy (TEM) study was performed from the mineral separate grains mounted in a polished block using a FEI-Helios nanoLab dual focused ion beam scanning electron microscope (FIB-SEM), following procedures outlined by Ciobanu et al. (2011). Each TEM foil was attached to a copper grid. Thinned TEM foils were analysed

using HAADF STEM imaging and STEM EDX mapping using an ultra-high resolution, probe-corrected, FEI Titan Themis S/TEM operated at 200 kV in the same laboratory.

3.3. Sensitive high-resolution ion microprobe

Zircon grains were dated using a SHRIMP-II at the John de Laeter Centre (Curtin University of Technology, Western Australia). Geochronological data was acquired in a continuous session over three days in October 2017. The analytical methodology broadly follows those described by Compston et al. (1984) and Williams (1998). Measurements were made during six cycles through nine magnetic-field values. The resultant data set for all peaks over all cycles is used to calculate count rates and isotopic ratios, at the mid-point in time for the entire analysis. Decay constants used are those recommended by IUGS and ^{235}U was calculated using the decay constant of Steiger and Jäger (1977). The primary reference material analysed was the zircon FC-1 (1099.0 ± 0.6 Ma; Coyner et al., 2004).

Spot analyses were 20–30 μm in diameter for both standards and unknowns, with a mass-filtered O_2^- primary beam of 2–3 nA. Data for each spot are collected in sets of 6 or 7 scans through the mass range of $^{196}Zr_2O^+$, $^{204}Pb^+$, background, $^{206}Pb^+$, $^{207}Pb^+$, $^{208}Pb^+$, $^{238}U^+$, $^{248}ThO^+$, and $^{254}UO^+$. Concentrations of U, Th and Pb are calculated using a similar approach with the unknown referenced to the standard with known U, Th and Pb abundances (Compston et al., 1984; Claoué-Long et al., 1995; Williams, 1998). Uncertainties attributed to individual analyses include errors from counting statistics, the common-Pb correction and the U-Pb calibration error based on the reproducibility of U-Pb measurements of the standard, which are presented at the 1-sigma level. Uncertainty boxes shown in $^{207}Pb/^{206}Pb$ weighted average diagrams are also 1 sigma. Common Pb was corrected for using the ^{204}Pb method rather than ^{208}Pb method due to the relatively high concentrations of Th (Williams, 1998) and low measured ^{204}Pb. Isotopic measurements were reduced by off-line programs using standard procedures (SQUID; Ludwig, 2009), and data plots were constructed using ISOPLOT 4.1 (Ludwig, 2012).

4. Results

4.1. Zircon petrography

Studied zircon grains from the three granites display a variety of sizes, textures and morphologies on CL images (Fig. 2A-C), as well as varying degrees of alteration.

Grains from Granite A are sub- to euhedral and slightly rounded, between <100 and 250 µm in size, and have width to length ratios ranging from 1:1 to 1:3. They rarely contain inclusions. CL imaging shows that most display oscillatory zoning, although some grains appear to be either weakly zoned or contain irregular, patchy compositional zoning. Zoned grains show either darker cores and brighter rims, or brighter cores and darker rims on the CL images; a minority are uniformly dark or bright.

Zircons from Granite B show a greater variation in both size and shape. They are <100 µm to 300 µm in size with aspect ratios of 1:1 to 1:3, although rare acicular zircon up to 1:10 was observed (but not analysed). Most are euhedral and slightly rounded, and rarely contain inclusions of feldspar and apatite. CL imaging showed that most analysed grains display oscillatory zoning, and more rarely, sectorial zoning or an irregular patchiness. As in Granite A, grains are uniformly dark or bright, or have darker cores with brighter rims, or *vice versa* (Fig. 3A).

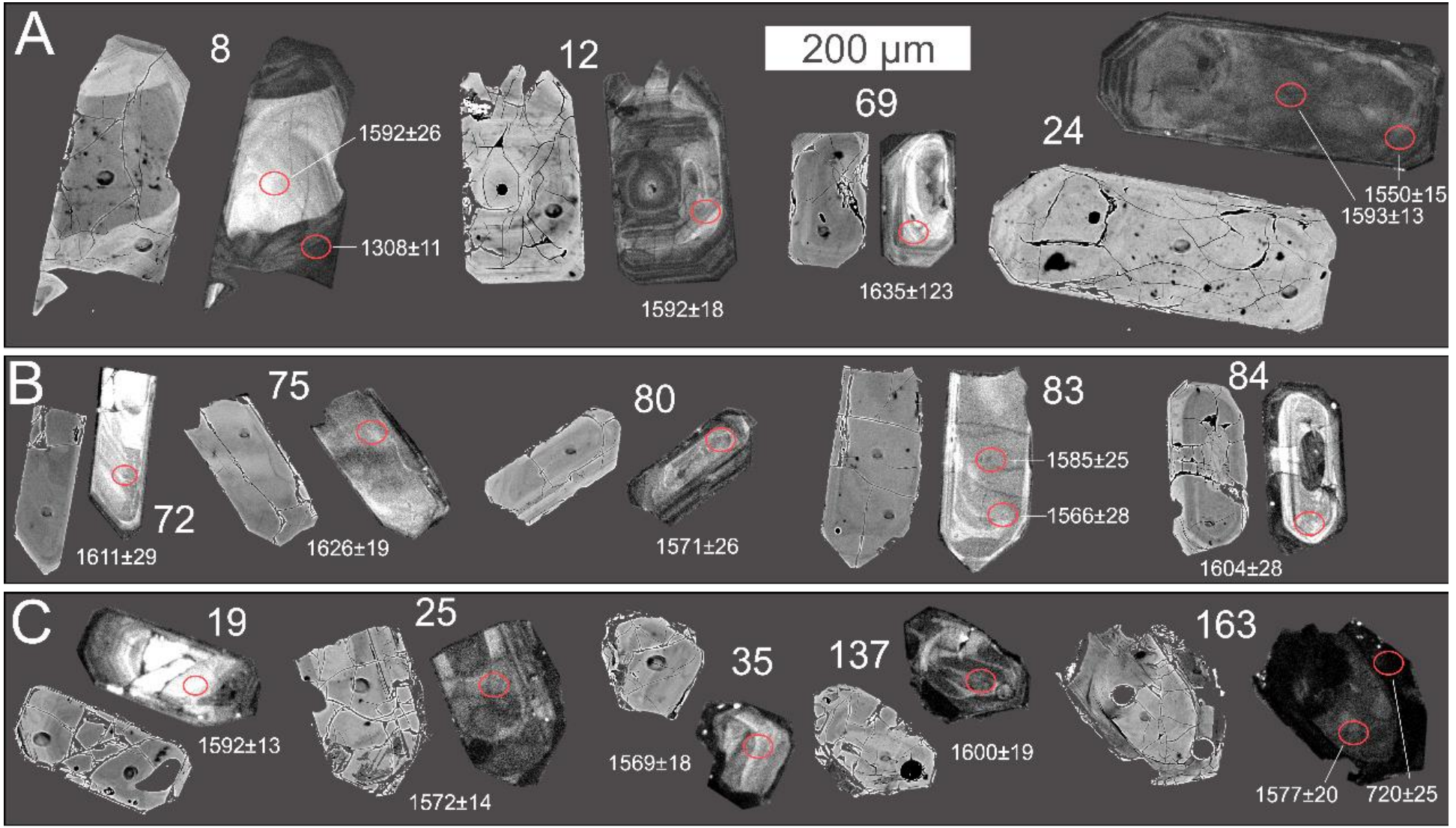

Figure 2. (A-C) Paired BSE (left) and CL (right) images of selected zircon grains from Granites A, B and C, respectively, with ages obtained.

Zircons from Granite C are significantly smaller and appear less pristine than those in either Granite A or B. They also show greater irregularity in grain shape and morphology compared to the other two granites (Fig. 3A). Analysed grains are <100 to 200 µm in size with aspect ratios of 1:1 to 1:3 and are mostly subhedral. While zircons in Granites A and B mainly have smooth margins, zircon grains in Granite C often appear jagged. Microfractures and domains with enhanced porosity are common (Fig. 3C), whereas inclusions are rare. CL imaging shows that most grains display oscillatory zoning although rare grains that are homogenous or patchy were also observed. Uniformly dark and bright grains are observed, as well as darker cores and brighter rims, and brighter cores and darker rims. Some grains show an almost black rim on CL images, which is extremely metamict and porous.

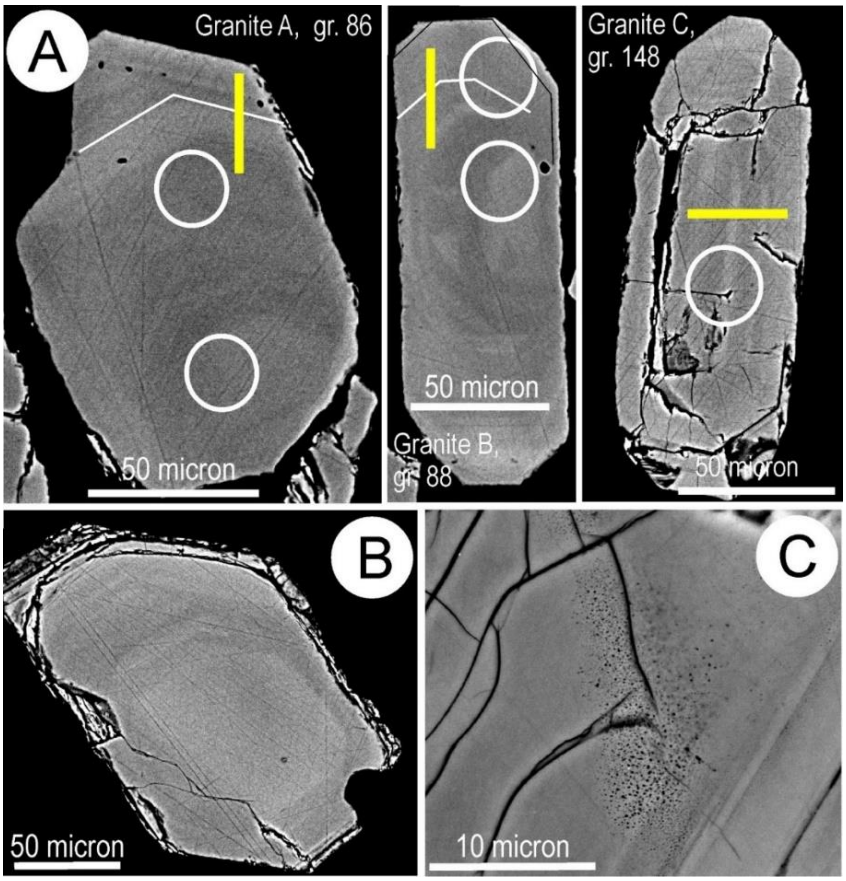

Figure 3. (A) BSE images showing dated zircon grains in Granites A, B and C. White circles represent SHRIMP analysis spots; yellow bars show location of extracted FIB cuts. (B) Representative zircon grain from Granite C displaying oscillatory zoning and corroded margins. (C) Detail of a similar zircon grain from Granite C showing irregular domains with high degree of sub-µm-scale porosity.

4.2. Zircon geochemistry

EPMA data was obtained only from those dated zircon grains that have been prepared for nanoscale analysis for comparative purposes, including an additional grain, displaying alteration as in Figure 3C. EPMA datasets (Appendix Table A1) for zircon show analytical totals between 99.0 and 101.7 wt.%. HfO_2 (1.2–1.6 wt.%), P_2O_5 (700–3,000 ppm) and Y_2O_3 (400–3,000 ppm) are the only minor elements above minimum detection limits (mdl) in all analyses, whereas UO_2 and ThO_2 (up to 710 and 240 ppm, respectively) are rarely below mdl. Sporadically, PbO appears at measurable concentrations. Most other elements are either below mdl or are only present in a very limited number of analyses; this includes F, Cl, Na_2O, K_2O, Sc_2O_3, TiO_2, Al_2O_3, MnO, Nb_2O_5, Fe_2O_3 and all $(REE)_2O_3$, except for Er_2O_3 and Yb_2O_3.

Importantly, the EPMA dataset does not reveal any significant geochemical difference between selected zircon in the three different granites. The brighter areas in BSE images show, on average, slightly higher concentrations of REE + Y, U and Th. For example, in a typical zircon from Granite A, bright domains have 1,600 ppm Y_2O_3, 165 ppm ThO_2 and 280 ppm UO_2, whereas dark areas have 640 ppm Y_2O_3, and both ThO_2 and UO_2 are below their respective mdl values. Additionally, in Granite C, the bright bands have slightly higher HfO_2 and CaO than the dark bands (~1.6 wt.% and ~1,300 ppm, and ~1.4 wt.% and ~160 ppm, respectively).

A single spot analysis of a metamict rim on a zircon grain from Granite C shows a significant increase of every measured analyte with a corresponding decrease of SiO_2 and ZrO_2. Several elements reach wt.% concentrations: 1.0 wt.% CaO; 1.0 wt.% Fe_2O_3; 2.0 wt.% Y_2O_3; and 2.8 wt.% HfO_2. Thousands of ppm of other elements are also present, including F (~6,400 ppm), Al_2O_3 (~4,700 ppm), ThO_2 (~6,400 ppm) and UO_2 (~2,100 ppm). The low analytical total (96%) is taken to indicate either the presence of H_2O, or potentially, other elements not included in the analytical set-up.

LA-ICP-MS spot analysis was carried out on multiple grains from all three granites. Laser spot size cannot, however, discriminate between dark and bright bands/areas, thus averaging out the obtained data. The LA-ICP-MS dataset (Appendix Table A2) largely confirms the EPMA dataset.

Elements not detectable with EPMA only appear at low concentrations: Sn, Nb, Mn (<10 ppm), Ti, Al (<20 ppm) and Fe (<30 ppm). REE patterns are typical of zircon, displaying very low LREE, strong positive Ce-anomalies, and high HREE + Y.

To better understand associations among the elements within LA-ICP-MS dataset, Principal Component Analysis (PCA) was carried out (Fig. 4A, B). The PC1-PC2 loadings show three distinct groups of elements. Group 1 comprised of Fe, Mn, Al and LREE (excluding Ce) all has positive loadings on PC1. Group 2 with an association of HREE, Y and P has negative loadings on PC1 and positive on PC2. Lastly, Group 3 represented by U, Th, Pb, Ce, Ta, and Hf, has negative loadings on both PC1 and PC2. Hafnium is distributed equally across all the zircons thus not discriminating different zircon type, however it plots together with Group 3, which are elements normally found in the zircon lattice.

Group 1 includes all elements whose concentration is primarily determined by non-magmatic processes, notably Fe, Al and Mn, which are associated with alteration. Concentrations of Group 1 elements have the highest ranges across the three granites (Fig. 3C) and are dependent on how pristine the zircon is. Contrary to Group 1 elements, which increase during fractionation in zircons of Granites B and C, Nb only increases in Granite C, hence this is not included in the group, although it has a positive PC1 value.

Rare earth elements display a continuous trend from very negative to slightly negative PC1 (Group 2, Lu to Gd) to slightly positive to strongly positive (Group 1, Eu to La). Such a trend can be explained by HREE incorporation into the crystal lattice and LREE association with alteration. Cerium, the most abundant among the LREE, plots in a displaced position from the other REE (Fig. 4B), and is positioned next to the Group 1 elements.

Several elements do not readily fit into the three-group division. The Ca position in the PC1-PC2 projection is erratic, however Ca loadings on both PCs are very minor, thus suggesting that Ca concentration is influenced by a process unrelated to the Fe-Mn-Al-LREE increase in the zircon LA-ICP-MS data. Nevertheless, Ca, as well as Sn and Ti, are only present at trace levels and are often

below the detection limit. They also have low loadings on PC1-PC2 and thus are not important for the interpretation of PC1-PC2 projection. Chondrite-normalised fractionation patterns (Fig. 5) display no major differences among the granites, although Granite B is the lowest in ΣREY and also features a marked positive Ce anomaly.

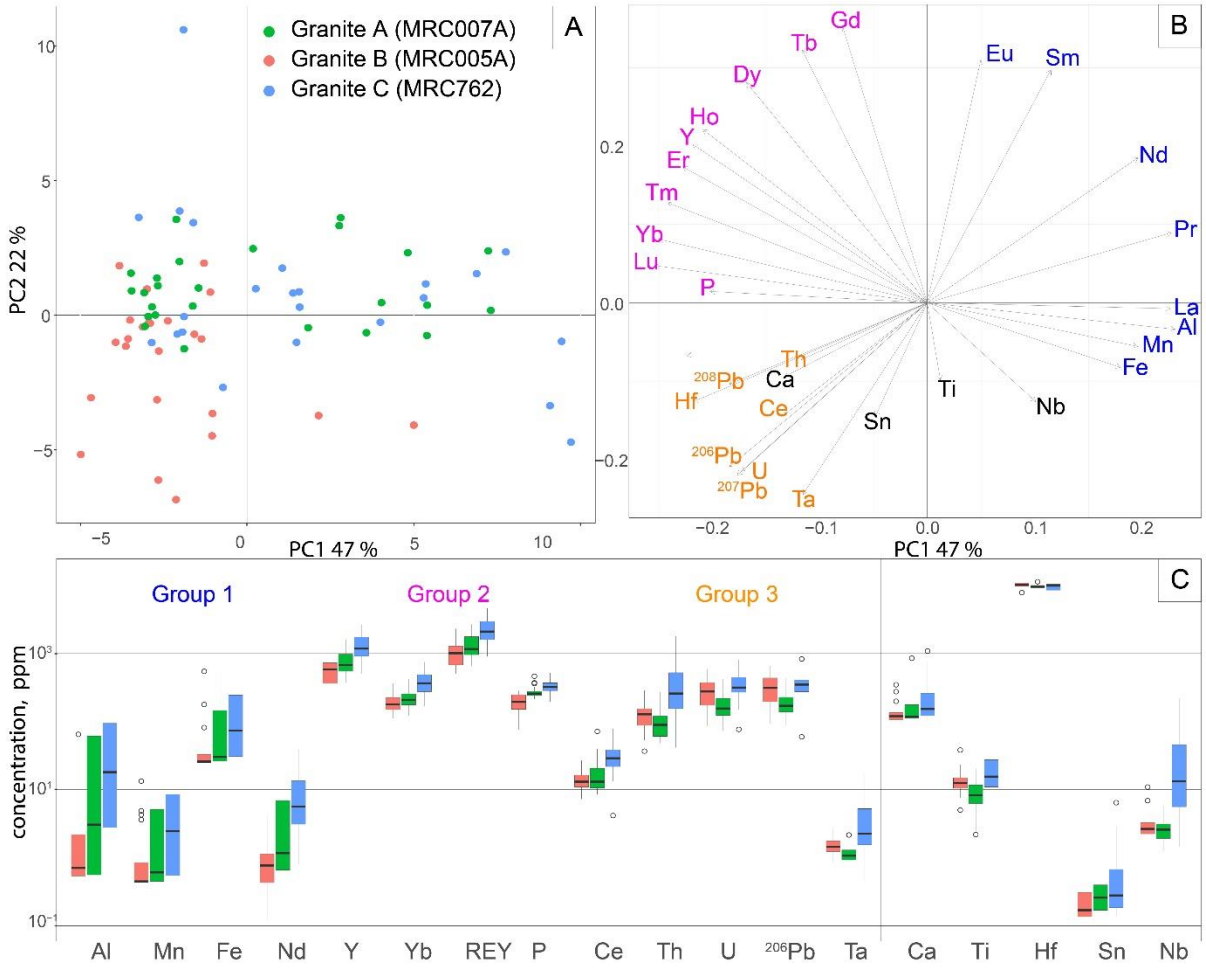

Figure 4. (A) PCA scores showing the distinction among zircons from Granites A, B and C; (B) PCA loadings displaying the associations among trace elements as groups 1, 2 and 3; (C) box-and-whisker diagrams of groups of trace elements in zircons.

LA-ICP-MS element mapping of selected zircon grains from all three granites was undertaken to understand the distribution of relevant elements (Fig. 6). This includes elements usually present in magmatic zircon, e.g., U, Th, HREE and Y (where they substitute for Zr), elements usually associated with hydrothermal overprinting, e.g., Fe and LREE, as well as the three most abundant Pb isotopes, the product of radioactive decay. All mapped grains display compositional differences between core and rim with respect to U, Th, Y and the heaviest REE, as well as radiogenic Pb, which mirrors U

and Th. Furthermore, all mapped grains display microfractures, which are always relatively enriched in REE + Y and Fe compared to the grain itself. Uranium and Th also display an increase in such microfractures within some grains. Thorium is strongly enriched in microfractures crosscutting zircons from Granite C (Fig. 6). The margins of all grains show significantly different element concentrations than the cores. Both Zr and Si are markedly depleted indicating partial to complete replacement by other phases. All grains display evidence of hydrothermal overprinting and marked increase in Fe. Overprinting is only weakly expressed in zircon from Granites A and B, with slight increases in REE, Th, U and Pb noted, but is far stronger in zircon from Granite C, especially with respect to HREE + Y, Th and Pb. The altered core in zircon from sample 009-2 (Granite C) has high U, but the grain margins are appreciably lower in this element. This is tentatively interpreted in terms of a U + Th overprint as for Granites A and B, and later leaching of U.

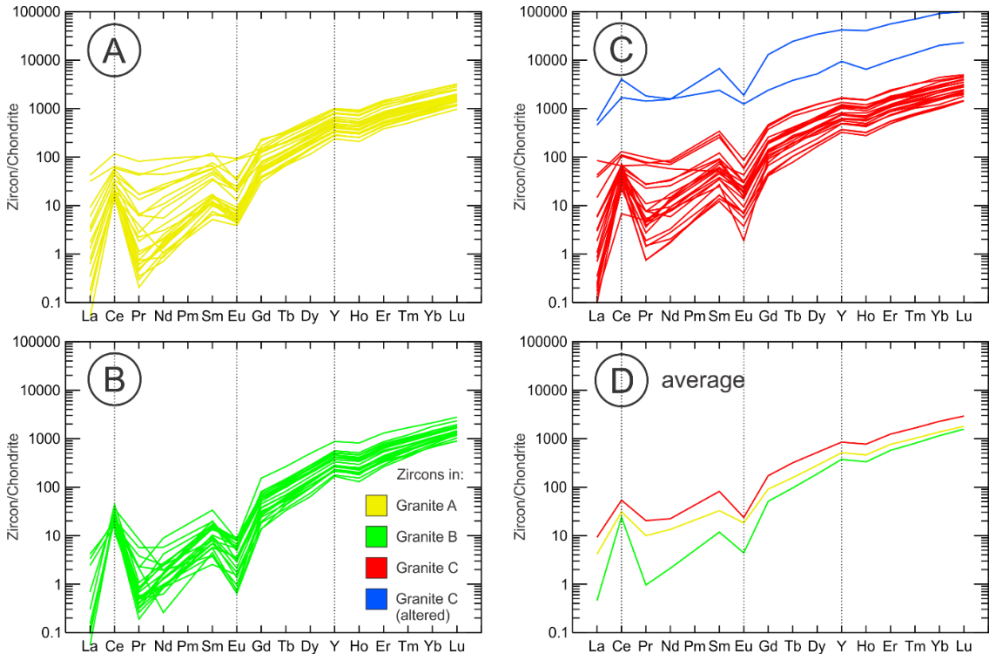

Figure 5. Chondrite-normalised REE fractionation trends for zircon in the different granites.

Mapping of U/Th in zircon (Fig. 6) shows a value of around 2 in unaltered grains. Zircon margins in Granites A and B show higher U/Th due to a stronger enrichment of U compared to Th. In Granite C, this trend is reversed, with strongly decreased U/Th on grain margins. The most altered zircon grains in Granite C sometimes show increased U/Th in the core (Fig. 6).

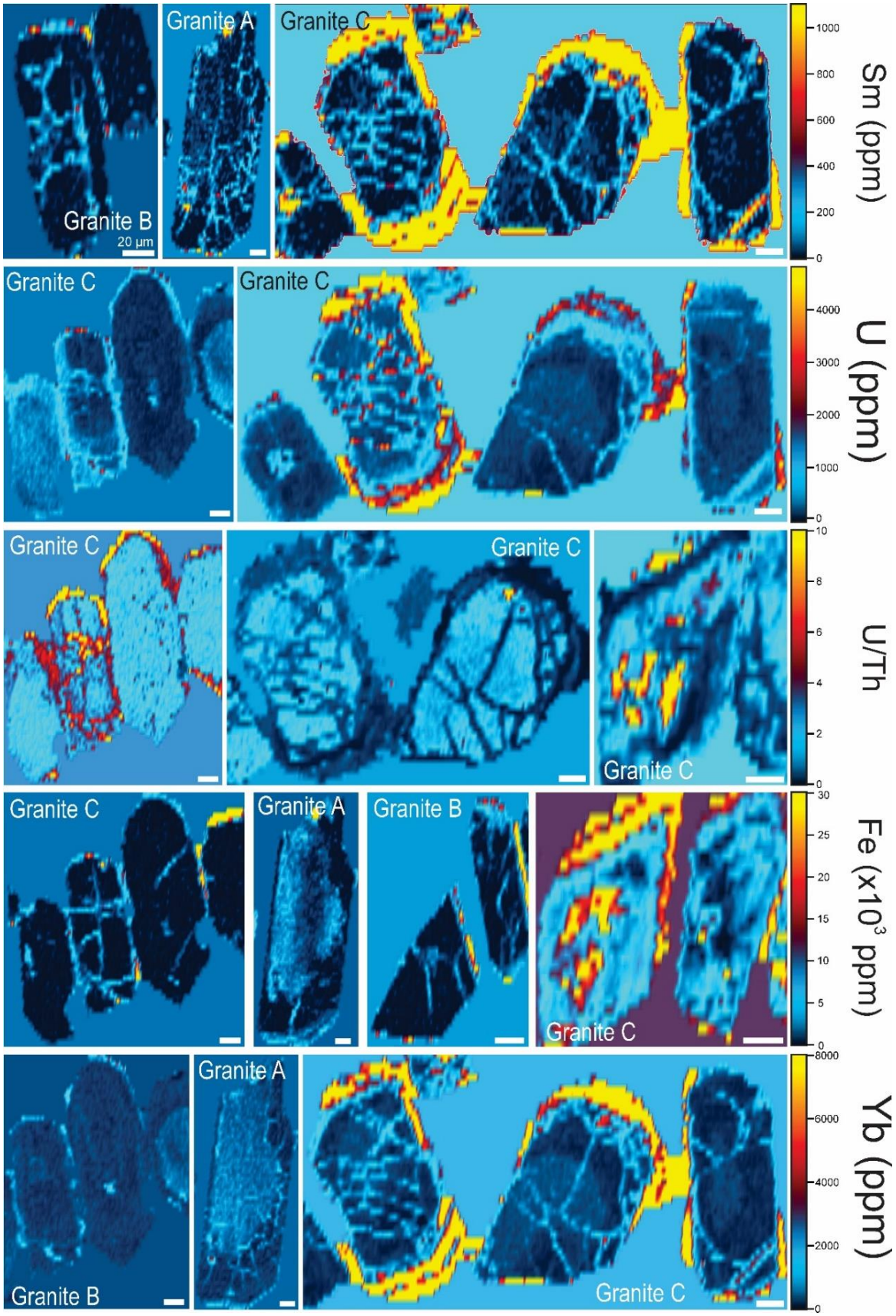

Figure 6. Selected LA-ICP-MS maps of zircon grains from the three granites. Note, in particular, the REE- and Fe-rich rims on zircon from Granite C. Scales are a uniform 20 microns. Sm and Yb are chosen as representative of middle and heavy rare earth elements, respectively.

4.3. SHRIMP U-Pb zircon dating

Uranium-Pb zircon ages were obtained from the three geochemically distinct granite samples via SHRIMP (Fig. 7). Geochronological and U-Th-Pb geochemical data is presented in Table 1.

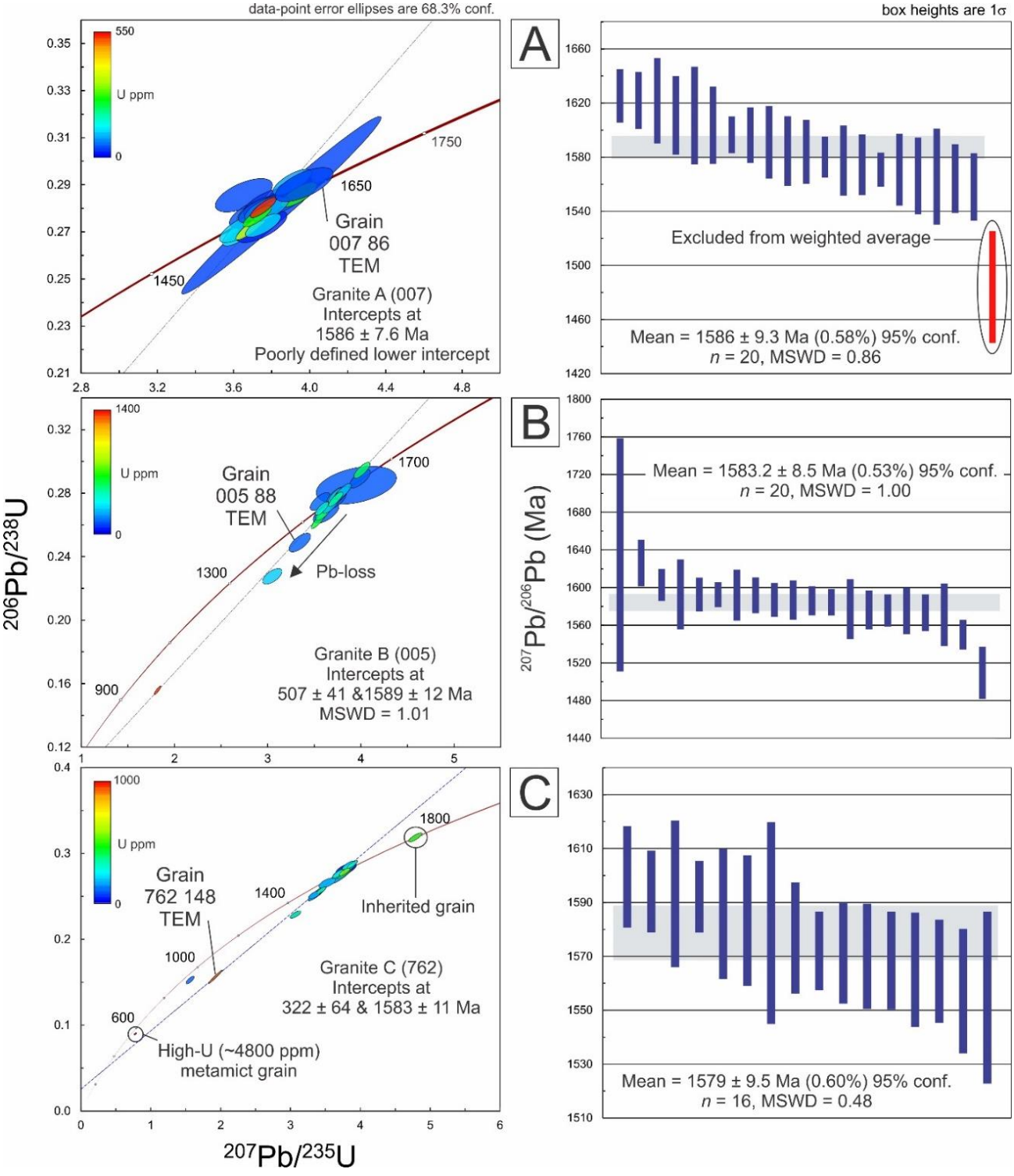

Figure 7. (Left) Concordia diagrams for zircons from Granites A, B and C, and; (right) $^{207}Pb/^{206}Pb$ weighted averages for each granite. Grains selected for nanoscale study are marked.

4.3.1. Granite A (MRC007A)

Data consists of 21 analyses from 20 grains, with all points selected within or close to grain cores (Appendix Table A3). Concentrations of U ranged from 113 to 537 ppm (193 ppm average), with average Th/U of 0.762. The data clusters around concordia (18/21 points within uncertainty of concordia; Fig. 7A), although two points plot reversely discordant (up to -10% discordancy) and one discordantly (5%). An upper intercept age of 1586 ± 7.6 Ma and a poorly constrained lower intercept of -894 ± 1500 Ma (MSWD = 1.12; n = 21) is obtained from the data without rejections. Individual $^{207}Pb/^{206}Pb$ dates range from 1626 to 1485 Ma, with uncertainties ranging between 41 and 12 Ma. A mean $^{207}Pb/^{206}Pb$ weighted average of 1586 ± 9.3 Ma (MSWD = 0.06; n = 20) is produced when rejecting one reversely discordant point (spot 007.40, -10% discordancy), which agrees with the upper intercept age.

4.3.2. Granite B (MRC005A)

A larger spread in geochronological and geochemical data is seen in this sample, containing 21 spots collected from 19 grains. Nineteen spots have been selected within or close to grain cores, two spots targeted rims, but were grouped together (Fig. 7B). Uranium concentrations range from 106 to 1359 ppm (333 ppm average) with a slightly lower Th/U of 0.503. Analyses are predominantly within uncertainty of concordia; three points are, however, strongly discordant (10 to 31%) and define a discordia line of 1589 ± 12 and 507 ± 41 Ma (MSWD = 0.95; n = 21). Individual $^{207}Pb/^{206}Pb$ dates range from 1627 to 1308 Ma, with uncertainties ranging between 37 and 13 Ma. The obtained $^{207}Pb/^{206}Pb$ weighted average of 1583.2 ± 8.5 Ma (MSWD = 1.00; n = 20) required rejection of the most discordant point (dup 005.5) due to extreme Pb-loss.

4.3.3. Granite C (MRC762)

Granite C shows the largest spread in data, as expected, due to the higher degree of alteration of zircon grains in this sample. Twenty spots were collected from 19 grains within or close to grain cores, except for a single spot on an overgrowth, which was treated separately (Fig. 7C). One

concordant analysis (spot 762.47, $^{207}Pb/^{206}Pb$ = 1783 Ma) is inherited from a nearby igneous rock, and therefore not included in age calculations. Concentrations of U range from 59 to 930 ppm (average 310 ppm). The highest Th/U was measured in this sample (0.816). Four points plot discordantly (36 to 14 %), while the remaining points cluster near concordia. All points lie along a discordia line defining an upper and lower intercept age of 1583 ± 11 and 322 ± 64 Ma (MSWD = 0.53; *n*=17), respectively, apart from point 762.45, which is not included in the calculation. Individual $^{207}Pb/^{206}Pb$ dates range from 1600 to 1057 Ma, with uncertainties ranging between 37 and 13 Ma. The $^{207}Pb/^{206}Pb$ weighted average age of 1578 ± 9.5 Ma (MSWD = 0.48; *n* = 16) required rejection of the most discordant points (763.45 and its duplicate 762.49) to extract an acceptable MSWD for the most concordant population.

The spot selected for analysis on the overgrowth contains 4808 ppm U and has a very low Th/U of 0.117. The point is highly discordant (24%) and does not lie along the discordia line defined by the other spots of this sample. Its $^{207}Pb/^{206}Pb$ age is 720 ± 25 Ma.

4.4. Grain-scale isotope distributions

LA-ICP-MS isotope mapping shows that $^{206}Pb/^{238}U$ isotope ratios are typically disturbed on grain margins and along microfractures (Fig. 8). The ratios generally decrease, indicating either Pb loss, or late addition of U. In Granites A and B, this alteration is less pronounced, with several grains displaying only partially disturbed margins. In Granite C, however, all analysed grains are heavily affected, with wide disturbed zones along margins and adjacent to microfractures; several grains are comprehensively altered with disturbed Pb/U ratios also exhibited in grain cores. In all grains, zones with disturbed ratios correlate with higher contents of Pb and U, which is presumably the result of metamictisation facilitating fluid access, alteration and grain-scale remobilisation, but also, potentially deposition of Pb and U from an external fluid.

The $^{208}Pb/^{232}Th$ ratio is slightly disturbed in Granite A and B along margins and microfractures. Usually, the ratio is increased, but some grains exhibit a decreased ratio along microfractures. A comparison of ratio maps with ^{208}Pb content reveals a correlation of increased Pb and $^{208}Pb/^{232}Th$,

indicating accumulation of ^{208}Pb in altered areas. ^{232}Th contents do not correlate with ratios, but the (magmatic) differences of high-Th and low-Th areas might overcome small changes by alteration.

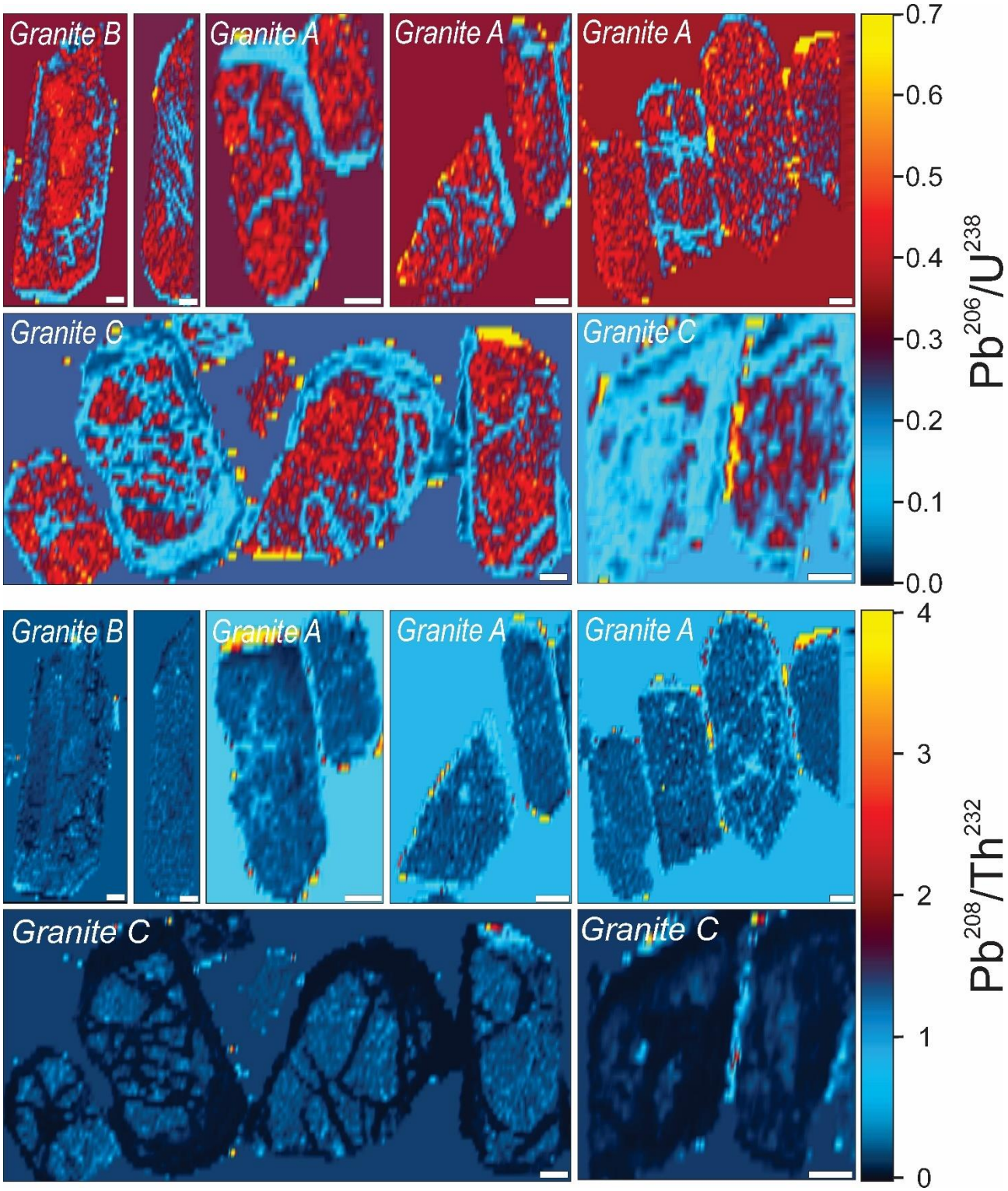

Figure 8. LA-ICP-MS isotope maps for $^{206}Pb/^{238}U$ and $^{208}Pb/^{232}Th$ in selected zircons from Granites A, B and C.

In Granite C, the $^{208}Pb/^{232}Th$ ratio is heavily disturbed in the same areas that show disturbed Pb/U ratios. The ratio is severely decreased, contrary to Granites A and B. Yet, ^{208}Pb is enriched in altered areas, but at orders of magnitude less than the enrichment of Th.

4.5. Nanoscale zircon characterisation

HAADF STEM imaging of the zircons from the three samples shows that fine-scale zoning is present in parts of the foils (Fig. 9A-C and Appendix Figure A1). STEM EDX maps of such zoned areas do not, however, show any measurable variation in major/minor element content, implying that the image contrast represents a cumulative effect of the different trace elements present, but that are individually below the sensitivity of the detectors.

The investigated zircon grain from Granite B shows a microfracture crosscutting the primary zoning (Fig. 9B). Voids (dark on HAADF STEM image), tens of nm in width, occur along this fracture. Zircon from Granite C is crosscut by a micro-veinlet filled with secondary minerals (see below) running through the middle part of a funnel-shaped area of bright contrast, roughly 2 µm in length and opening to a width of ~1 µm; this veinlet extends below the funnel-shaped area (Fig. 9D, E). Darkening at the direct contact to the veinlet indicates marginal reaction and the late character of the vein relative to the bright contrast area. Nanometre-wide fractures occurring parallel to the veinlet show bright inclusions at the end (Fig. 9F). Alteration expressed as 'darkening' along short defects results in a basket-weave texture throughout the bright domain (Fig. 9G). Such effects increase in intensity close to the veinlet (Fig. 9H). The bright inclusions at the tip of the trail (Fig. 9F) are Pb-bearing nanoparticles (NP), most likely galena (Fig. 9I-K). The dark tail of one such Pb-bearing NP could be a pore (Fig. 9I).

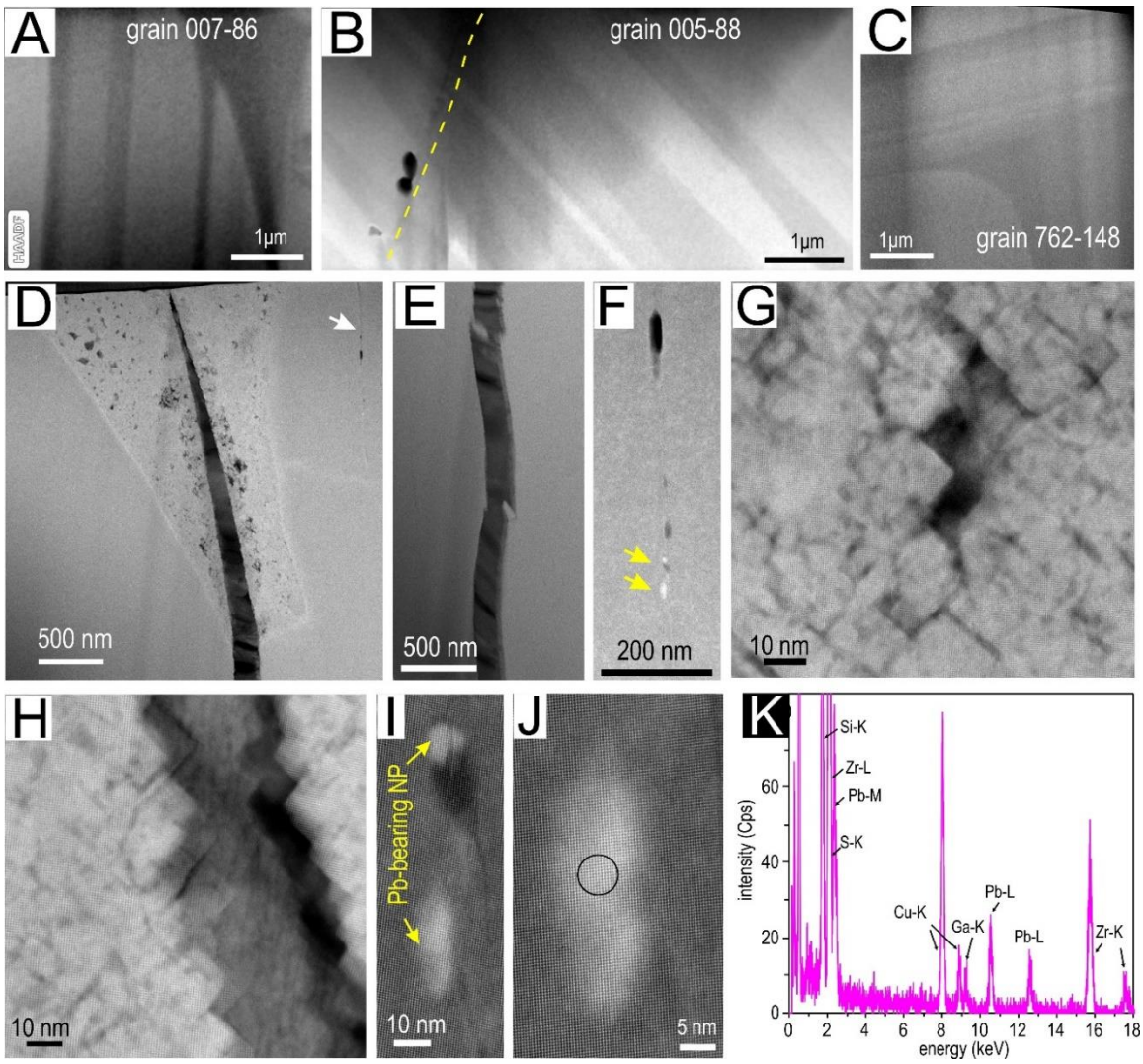

Figure 9. HAADF STEM images showing nanoscale aspects of zircon. (A-C) Primary zonation patterns in zircon from Granites A, B and C, respectively, crosscut by a microfracture (dashed line) in (B). (D, E) Funnel-shaped, brighter area crosscut by a fracture continuing outside this structure. (F) Micro-crack, a few nm-wide, with Pb-bearing NPs (arrowed). (G, H) Basket-weave alteration throughout the funnel-shaped area in (D). In (H), note the increase in intensity next to the veinlet. (I, J) Detail of the Pb-bearing NPs along the trail shown in (F). (K) Spectrum from the area on (J) marked by circle. The Cu signal is from the grid.

Mapping of the bright area shows relative enrichment in Ca and Y (Fig. 10A). EDX profiles obtained across this area show the presence of elements indicative of a chlorite + mica assemblage within the crosscutting veinlet (Fig. 10B, profiles #1, 2). The variation in distribution of Fe, Al, Mg, K and F from one location to another indicates a fine-grained intergrowth between the two phyllosilicates, with a predominance of Fe-rich chlorite. Strong Y-enrichment at the vein boundary and irregular distributions of both Ca and Y distributions are noted along profile #2.

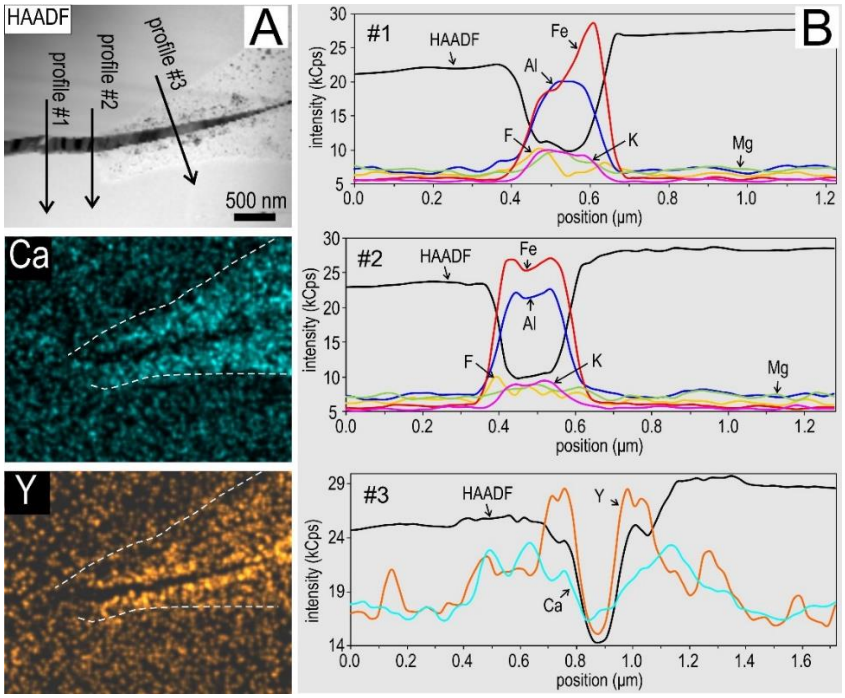

Figure 10. (A) HAADF image and STEM EDX element maps for the funnel-shaped area in zircon from Granite C (grain 762-148) showing enrichment in Ca and Y. Profiles as marked in (A) showing elements present and their variation across the veinlet in the middle (#1 and 2) and outside the funnel-shaped area (#3).

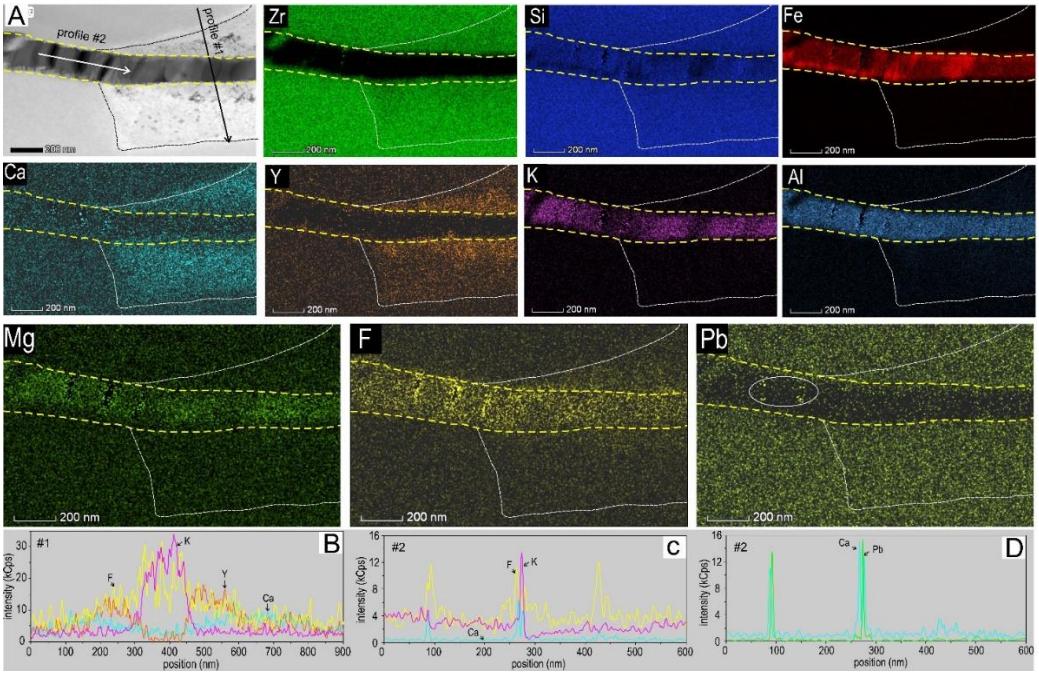

Figure 11. (A) HAADF image and STEM EDX element maps at the same or higher magnification within and surrounding the same veinlet shown in Figure 10. (B) Profiles as marked in (A) showing element variation across (profile #1 shown in (B)) and along the veinlet (profile #2 shown in (C) and (D)). Based on mapped elements the vein filling likely comprises Fe-rich chlorite and micas. The positive correlation between K and F along the profiles is characteristic of micas. The irregular spikes of F, Ca- and Pb indicate formation of mineral NPs such as fluorite and Pb-carbonates.

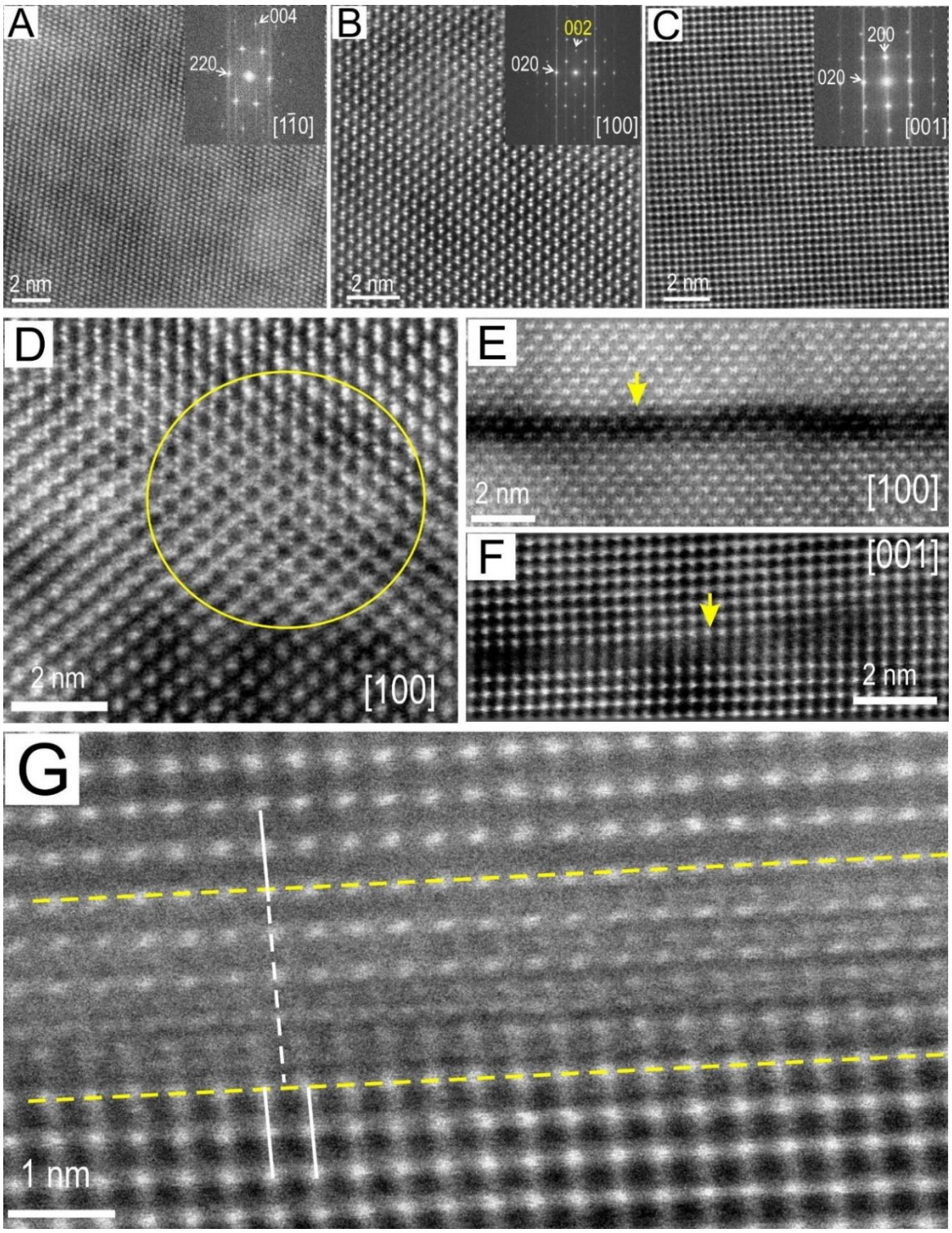

Figure 12. High-resolution HAADF STEM images showing undisturbed zircon (A-C) and defects (D-G). (A-C) Zircon in Granite A, B and C, respectively, oriented on zones axes as marked, and corresponding FFT patterns from the images. (D) Stretching defect in zircon from grain 88 (Granite C). (E, F) Darkening effects along nm-wide fractures (arrowed) observed on different zone axes in zircon from Granites B and C, respectively. (G) Detail of screw dislocation defects (white lines) across the fracture (yellow dashed line) in (F). Atomic arrangements on the three zone axes are comparable with the crystal models and STEM simulations given in Courtney-Davies et al. (2019).

Mapping this area at higher resolution (Fig. 11A) shows a 'nuggety' accumulation of F and also Pb. A profile taken across the Y-Ca-bearing domain (Fig. 11B) shows a strong correlation between K and F. These elements are likely concentrated within mica (sericite?) filling the veinlet. EDX profiles taken along the veinlet shows peaks for F that are not associated with K and peaks of Pb associated with Ca, interpretable in terms of fluorite and Pb-carbonate NPs (Fig. 11C, D).

High-resolution HAADF STEM imaging of zircon (Fig. 12) shows a largely undisturbed crystal lattice, except in areas surrounding fractures and the funnel-shaped Y-Ca-bearing zone in grain 762-148 from Granite C. Zircon orientations differ in the three samples, as shown by the zone axes taken with tilt closest to zero (Fig. 12A-C). Defects showing lattice stretching are present in the areas surrounding fractures from Granite B (grain 005-88; Fig. 12D). Thin defects, a few nm in width and some tens of nm in length, show darkening on HAADF STEM images (Fig. 12E). The same darkening effect is observed, associated with screw dislocations along the trail of NPs in zircon from Granite C (Fig. 12F, G).

5. Discussion

5.1. Significance of the zircon ages

The ages acquired for all three granites are within uncertainty of one another and also lie within statistical uncertainty of ages reported by Reid et al. (2017). The three granites are contemporaneous with the Charleston Granite to the southwest (1585 ± 5 Ma; Creaser and Fanning, 1993), and firmly within the timeframe of HS granitoids on the Yorke Peninsula. Similar small Hiltaba-age intrusions forming a larger multiphasic pluton are known from Yorke Peninsula on the eastern side of the Spencer Gulf, where the Tickera Granite pluton displays granites of varying age and mineralogy (1591 ± 19 Ma to 1577 ± 7 Ma; Fanning et al., 2007); see summary in Figure 13. Our results do not permit a definitive answer as to whether they represent discrete phases within a larger magmatic complex, as suggested by Domnick et al. (2018) based upon their petrography, geochemistry and degrees of alteration.

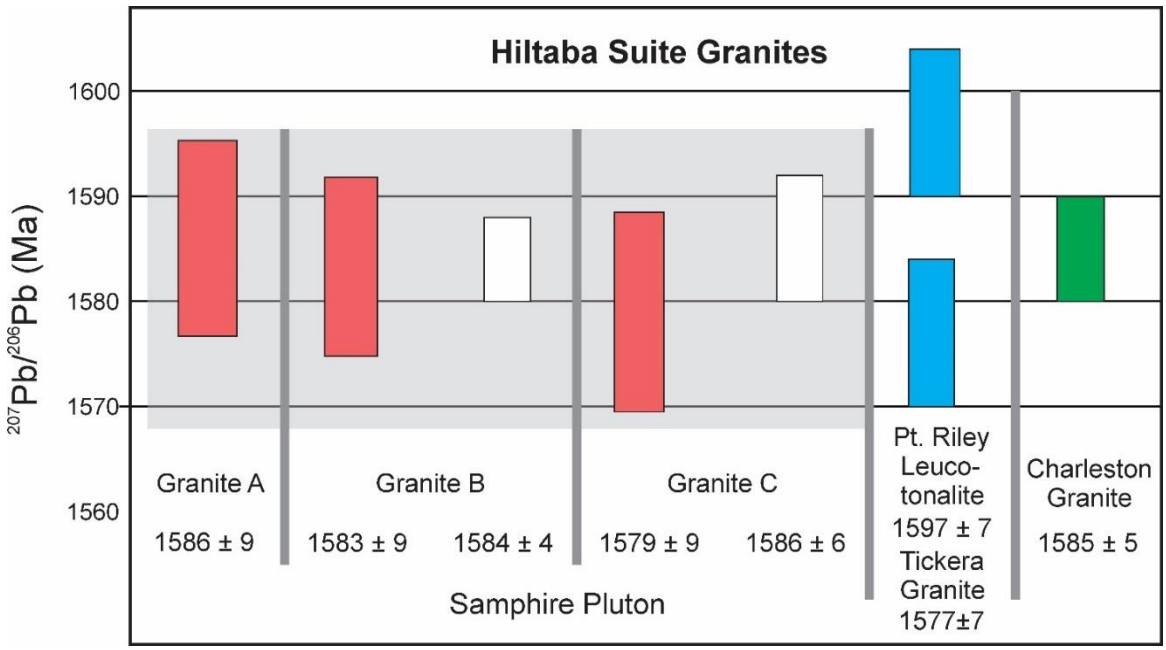

Figure 13. $^{207}Pb/^{206}Pb$ weighted average ages for the Samphire Pluton granite dated here (in red) and from Reid et al., 2017 (in white) and other nearby Hiltaba Suite granites (Creaser and Fanning; 1993; Fanning et al., 2007).

The provenance of the inherited grain in Granite C with a $^{207}Pb/^{206}Pb$ date of ~1783 Ma is possibly derived from the Myola Volcanics or contemporaneous sedimentary units represented by the Broadview Schist (Parker and Fanning, 1988; McAvaney and Wade, 2015), which are in contact with the northern edge of Granite C. An analogous inherited grain of similar age is reported in Reid et al. (2017). The Myola Volcanics are mafic to felsic, which in turn leads to mafic-rich to quartz-rich units in the Broadview Schist. Assimilation of those mafic-rich units may also explain the relatively high concentrations of Ti, Mg, Fe and Co in Granite C. Inherited zircon grains aged ~1763 Ma are mentioned by Fanning et al. (2007) from the Tickera Granite. Corroboration of relatively 'young' HS zircon ages reported here, supports protracted intrusion of HS granites across the eastern Gawler Craton.

5.2. Comparison between zircons of the Samphire Pluton and assessment of U-Pb open system behaviour

Several differences between the three granites can be drawn based on zircon geochemistry. Despite the overlap between all three granites on the PC1-PC2 plot, Granite B shows a different distribution

relative to the other two (Fig. 4A). Further evidence is given by the relative concentrations of actinides *versus* others element groups among the three granites (Fig. 4C), as well as by the pronounced positive Ce anomaly shown by Granite B relative to the other two granites (Figs. 4b; 5). Granite C stands out by marked relative enrichment in Nb, Ti, Th and Ta. Later addition of Nb can be attributed to input from the spatially associated, high-Nb aplitic and micropegmatitic sills and dykes that crosscut the granite (Domnick et al., 2018), with an episode of hydrothermal alteration driven by the emplacement of these late melts.

The porous, metamict rims shown by several zircon grains from Granite C express a clear hydrothermal signature, e.g., high (L)REE + Y, Ca, Fe, U, Th (Fig. 4C), and markedly disturbed U-Th-Pb isotope ratios. Although this alteration is only observable on the micron-scale as chemically distinct grain rims, it can be recognised down to the nanoscale. Domains of crystal lattice weakness penetrated by nanofractures have facilitated fluid percolation, and thus grain-scale remobilisation of elements, i.e., Ca + Y enrichment and vein filling by phyllosilicates (Figs. 10 and 11).

Such geochemical differences among zircons from the three granites are significant in that this study was focussed on granites with freshest appearance and on zircon grains selected from mineral concentrates. Granite B is most likely produced from melt batches with higher crustal contamination, whereas Granite C is clearly most affected by post-magmatic alteration. Although this alteration is associated with fluid circulation along open fractures, sharing some similarities with features observed in the Charleston Granite (Courtney-Davies et al., 2019), it demonstrably does not include evidence for early Fe-Cl-metasomatism as shown for zircons from Hiltaba Suite granitoids in the Olympic Dam district in the same publication. For example, zircon grains from the latter display oscillatory zoning with respect to Fe and the presence of chloro–hydroxy–zircon nanoprecipitates.

Nanoscale characterisation of grains in domains adjacent to SHRIMP spot analysis shows an excellent correlation with the U-Pb isotope data (Fig. 7). Zircon grain 007-86 (from Granite A) is free of any lattice scale defects, fractures or inclusions, and yields concordant U/Pb analyses. In contrast, U/Pb measured in grains 005-86 and 762-148 from Granites B and C, respectively, plot discordantly

and both zircons display lattice scale defects and fractures. Furthermore, the presence of Pb-bearing NPs along fine fractures and veinlets filled with secondary phyllosilicates (Figs. 9F, J and 11A, C), supporting the occurrence of alteration assisted Pb-loss from the 762-418 zircon (Fig. 7). The effects of alteration and Ca-Y-bearing domains superimposed by phyllosilicate-filled fractures support multi-stage fluid percolation of zircon in Granite C.

6. Implications and Conclusions

These results, particularly observation of Pb-bearing inclusions (implying Pb mobility), microfractures, the relative enrichment in non-formula elements, and marked disturbance of U-Th-Pb isotope ratios, demonstrate that zircon in Granite C has undergone multi-stage alteration, a feature that carries significance for accurate dating. Importantly, and with implications for analogous systems elsewhere, our results provide insights into the nature of open system U-Pb behaviour at the nano-scale in altered or metamict zircon, whereby relatively pristine grains contain non-formulae element enrichment in micro-fractures. Caution should be taken when interpreting large ranges in age (e.g., ~15 Ma) of single HS plutons (e.g., Tickera), as open system behaviour likely exerts the primary control on measured age accuracy, rather than protracted granite crystallisation.

However, the geochemical differences among trace elements such as actinides (magmatic origin) in the analysed zircon grains support the idea of temporally distinct phases of a larger magmatic system forming the Samphire Pluton. However, SHRIMP U-Pb zircon geochronology, both here and in the previous study of Reid et al. (2017), could not resolve any statistical differences in age. Improved resolution of age relationships is possible if alternative chemical abrasion-isotope dilution thermal ionisation mass spectrometry techniques are used. For example, this method has been successfully applied to analogous research questions elsewhere for Mesoproterozoic granites of South Australia (Cherry et al., 2018; Courtney-Davies, in review). The zircon studied from Hiltaba-affiliated granites from the Eyre Peninsula (Charleston and Samphire), despite being ‘promising’, does not match the ‘fertility’ characteristics indicative of IOCG mineralisation as in those from the

Olympic Cu-Au Province in the eastern Gawler Craton. Although more dedicated studies of zircon on a greater number of samples would be required to clarify this issue, differences in erosion rates, level of exposure or tectonic regimes could also explain the results obtained so far.

Zircons within the most altered Granite C underlying the Blackbush deposit nonetheless contain convincing micron- to nanoscale evidence for an alteration event that triggered remobilisation of U. This is consistent with current genetic models for the Blackbush uranium deposit, which is largely hosted within the overlying cover sequence. In this model (Domnick et al., in review), U is mobilised and pre-concentrated within veins near the roof of the granite, making it more accessible to later fluids that transported U into the cover sequence. The Samphire area is close to the Roopena Fault, the northern extension of the Kalinjala Mylonite Zone, a major lithospheric boundary. Subordinate branches of the Roopena Fault cross the Samphire granites as part of a broader fault splay system also characterised by abundant veining (of unknown, potentially multiple age). This prompted Domnick et al. (in review) to speculate about the critical role of repeated fault reactivation in controlling fluid-driven alteration at all scales, and the driving force in the distribution of U mineralisation as observed today.

Supplementary Materials

Appendix Table A1. Complete EPMA dataset and calculated formulae.
Appendix Table A2. Complete LA-ICP-MS data for zircon (ppm).
Appendix Table A3. Data for U-Pb dating of zircon.
Appendix Figure A1. HAADF STEM images showing the three zircon foils studied.

Acknowledgements

U.D. acknowledges receipt of a Ph.D. scholarship from the Carthew Family Trust. The assistance of staff at Adelaide Microscopy with microanalytical work is gratefully acknowledged. N.J.C. acknowledges support from the ARC Research Hub for Australian Copper Uranium (Grant IH130200033). C.L.C., L.C-D., M.R.V-I., W.K. and M.D. acknowledge funding from the 'FOX' project (Trace elements in iron oxides: deportment, distribution and application in ore genesis, geochronology, exploration and mineral processing), supported by BHP Olympic Dam and the South Australian Government Mining and Petroleum Services Centre of Excellence.

7. References

Bluck, R., Brown, C., 2017. Characterisation of the Samphire Granite, Hiltaba Suite, northeastern Eyre Peninsula. MESA Journal 85, 31-40.

Cherry, A., Ehrig, K., Kamenetsky, V., McPhie, J., Crowley, J., Kamenetsky, M., 2018. Precise geochronological constraints on the origin, setting and incorporation of ca. 1.59 Ga surficial facies into the Olympic Dam Breccia Complex, South Australia. Precambrian Research 315, 162-178.

Ciobanu, C.L., Cook, N.J., Utsunomiya, S., Pring, A., Green, L., 2011. Focussed ion beam - transmission electron microscopy applications in ore mineralogy: bridging micron- and nanoscale observations. Ore Geology Reviews 42, 6-31.

Claoué-Long, J.C., Compston, W., Roberts, J., Fanning, C.M., 1995. Two Carboniferous ages: a comparison of SHRIMP zircon dating with conventional zircon ages and $^{40}Ar/^{39}Ar$ analysis. Geochronology time scales and global stratigraphic correlation. SEPM Special Publication 54, 3-21.

Compston, W., Williams, I.S., Meyer, C.E., 1984. U-Pb geochronology of zircons from lunar breccia 73217 using a sensitive high-mass resolution ion microprobe, Proceedings of the fourteenth Lunar and Planetary Science Conference, Part 2: Journal of Geophysical Research 89, Supplement, B525 B534.

Courtney-Davies, L., Ciobanu, C.L., Verdugo-Ihl, M.R., Slattery, A., Cook, N.J., Dmitrijeva, M., Keyser, W., Wade, B.P., Domnick, U.I., Ehrig, K., Xu, J., Kontonikas-Charos, A., 2019. Zircon at the nanoscale records metasomatic processes leading to large magmatic-hydrothermal ore systems. Minerals 2019, 9, 364.

Courtney-Davies, L., Ciobanu, C.L., Tapster, S.R., Cook, N.J., Ehrig, K., Crowley, J.L., Verdugo-Ihl, M.R., Wade, B.P., Condon, D.J., in review. Opening the Magmatic-Hydrothermal Window: High-Precision U-Pb Geochronology of the Mesoproterozoic Olympic Dam Cu-U-Au-Ag Deposit, South Australia. Economic Geology.

Coyner, S.J., Kamenov, G.D., Mueller, P.A., Rao, V., Foster, D.A., 2004. FC-1: a Zircon Reference Standard for the Determination of Hf Isotopic Compositions via Laser Ablation ICP-MS. American Geophysical Union, Fall Meeting 2004, abstract V51C-0584

Creaser, R.A., Fanning, C.M., 1993. A U-Pb zircon study of the Mesoproterozoic Charleston Granite, Gawler Craton, South Australia. Australian Journal of Earth Sciences 40, 519-526.

Domnick, U, Cook, N.J., Bluck, R., Brown, C., Ciobanu, C.L., 2018. Petrography of granitoids from the Samphire Pluton, South Australia: implications for uranium mineralisation in overlying sediments. Lithos 300–301, 1–19.

Domnick, U., Cook, N.J., Ciobanu, C.L., Wade, B.P., Bluck, R., in review. A mineralization age for the Blackbush unconformity-related uranium deposit, Eyre Peninsula, South Australia. Minerals.

Fanning, C.M., Reid, A.J., Teale, G.S., 2007. A geochronological framework for the Gawler Craton, South Australia, Geological Survey of South Australia. Bulletin, 55, 258 pp.

Keyser, W., Ciobanu, C.L., Cook, N.J., Courtney-Davies, L., Kennedy, A., Wade, B.P., Ehrig, K., Dmitrijeva, M., Kontonikas-Charos, A., Feltus, H., Johnson, G., 2019. Petrographic and geochronological constraints on the granitic basement to the Middleback Ranges, South Australia. Precambrian Research 324, 170-193.

Ludwig, K.R.A., 2009. SQUID 2.50: A User's manual: Berkeley Geochronology Center, Special Publication No. 5, 110, Berkeley, California.

Ludwig, K.R.A., 2012. Isoplot/Ex rev. 4.1: A Geochronological Toolkit for Microsoft Excel; Berkeley Geochronology Centre Special Publication No.5, 75; Berkeley Geochronology Centre: Berkeley, California.

McAvaney, S.O., Wade, C.E., 2015. Stratigraphy of the lower Gawler Range Volcanics in the Roopena area, northeastern Eyre Peninsula, Geological Survey of South Australia. Report Book, 2015/00021, 420 pp.

Parker, A.J., Fanning, C.M., 1998. Whyalla, South Australia. Explanatory Notes 1:250 000 Geological Series Sheet SI53-8, Geological Survey of South Australia, 52 pp.

Reid, A.J., 2017. Geology and metallogeny of the Gawler Craton. In: Australian Ore Deposits (G.N. Phillips (Ed.), The Australasian Institute of Mining and Metallurgy, Melbourne, p. 589-594.

Reid. A., Hand, M., 2012. Mesoarchaean to Mesoproterozoic evolution of the southern Gawler Craton, South Australia. Episodes 35, 216–225.

Reid, A., Jagodzinski, E., Gerhard, F., 2017. Project PGC03-01: Geochronology from the Samphire Uranium Project. In: Jagodzinski, E.A., Reid, A.J. (Eds.), PACE Geochronology: Results of collaborative geochronology projects 2013–2015, Report Book 2015/00003. Department of the Premier and Cabinet, South Australia, Adelaide, pp. 10–28.

Samphire Uranium, 2019. http://www.samphireuranium.com.au/

Skirrow, R.G., Bastrakov, E.N., Barovich, K., Fraser, G.L., Creaser, R.A., Fanning, C M., Raymond, O.L., Davison G.J., 2007. Timing of iron oxide Cu-Au-(U) hydrothermal activity and Nd isotope constraints on metal sources in the Gawler craton, South Australia. Economic Geology 102, 1441–1470.

Szpunar, M., Hand, M., Barovich, K., Jagodzinski, E., Belousova, E., 2011. Isotopic and geochemical constraints on the Paleoproterozoic Hutchison Group, southern Australia: implications for Paleoproterozoic continental reconstructions. Precambrian Research 187, 99–126.

Steiger, R.H., Jäger, E., 1977. Subcommission on geochronology: Convention on the use of decay constants in geo- and cosmochronology. Earth and Planetary Science Letters 36, 359-362.

Williams, I.S., 1998. U-Th-Pb geochronology by ion microprobe. Applications of microanalytical techniques to understanding mineralizing processes. Reviews in Economic Geology 7, 1-35.

CHAPTER 4

A MINERALISATION AGE FOR THE SEDIMENT-HOSTED BLACKBUSH URANIUM PROSPECT, NORTH-EASTERN EYRE PENINSULA, SOUTH AUSTRALIA

Urs Domnick [1], Nigel J. Cook [1], Cristiana L. Ciobanu [1], Benjamin P. Wade [2],

Russel Bluck [3]

[1] *School of Chemical Engineering and Advanced Materials, The University of Adelaide, Adelaide, SA 5005, Australia*

[2] *Adelaide Microscopy, The University of Adelaide, Adelaide, SA 5005, Australia*

[3] *Samphire Uranium Pty Ltd., 28 Greenhill Road, Wayville, SA 5034, Australia*

Article Submitted to Minerals, 10th November, 2019

Statement of Authorship

Title of Paper	A Mineralisation Age for the Sediment-Hosted Blackbush uranium Prospect, North-Eastern Eyre Peninsula, South Australia.
Publication Status	☑ Published ☐ Accepted for Publication ☐ Unpublished and Unsubmitted w ork w ritten in manuscript style ☐ Submitted for Publication
Publication Details	Domnick, U., Cook, N.J., Ciobanu, C.L., Wade, B.P., Bluck, R., 2020. A Mineralisation Age for the Sediment-Hosted Blackbush uranium Prospect, North-Eastern Eyre Peninsula, South Australia. Minerals, 10, 191.

Principal Author

Name of Principal Author (Candidate)	Urs Domnick		
Contribution to the Paper	analytical work, data processing, interpretation, manuscript		
Overall percentage (%)	60		
Certification:	This paper reports on original research I conducted during the period of my Higher Degree by Research candidature and is not subject to any obligations or contractual agreements with a third party that would constrain its inclusion in this thesis. I am the primary author of this paper.		
Signature		Date	14/11/2019

Co-Author Contributions

By signing the Statement of Authorship, each author certifies that:

i. the candidate's stated contribution to the publication is accurate (as detailed above);

ii. permission is granted for the candidate in include the publication in the thesis; and

iii. the sum of all co-author contributions is equal to 100% less the candidate's stated contribution.

Name of Co-Author	Nigel J. Cook
Contribution to the Paper	interpretation, manuscipt
Overall percentage (%)	25

1		Date	14/11/2019

Name of Co-Author	Cristiana L. Ciobanu		
Contribution to the Paper	evaluation of manuscript		
Overall percentage (%)	5		
Signature		Date	14/11/2019

Name of Co-Author	Benjamin P. Wade		
Contribution to the Paper	assisted with analytical work, data processing, evaluation of manuscript		
Overall percentage (%)	5		
Signature		Date	14/11/2019

Name of Co-Author	Russel Bluck		
Contribution to the Paper	provided samples, evaluation of manuscript		
Overall percentage (%)	5		
Signature	(in absence, signed by Nigel Cook)	Date	14/11/2019

minerals

MDPI

Article

A Mineralisation Age for the Sediment-Hosted Blackbush Uranium Prospect, North-Eastern Eyre Peninsula, South Australia

Urs Domnick [1], Nigel J. Cook [1,*], Cristiana L. Ciobanu [1], Benjamin P. Wade [2], Liam Courtney-Davies [1] and Russel Bluck [3]

1 School of Chemical Engineering and Advanced Materials, The University of Adelaide, Adelaide, SA 5005, Australia; urs.domnick@adelaide.edu.au (U.D.); cristiana.ciobanu@adelaide.edu.au (C.L.C.); liam.courtney-davies@adelaide.edu.au (L.C.-D.)

2 Adelaide Microscopy, The University of Adelaide, Adelaide, SA 5005, Australia; benjamin.wade@adelaide.edu.au

3 Samphire Uranium Pty Ltd., 28 Greenhill Road, Wayville, SA 5034, Australia; rbluck@uraniumsa.com.au

* Correspondence: nigel.cook@adelaide.edu.au; Tel.: +61-405-826-057

Received: 9 November 2019; Accepted: 17 February 2020; Published: 20 February 2020

check for updates

Abstract: The Blackbush uranium prospect (~12,580 tonnes U at 85 ppm cut-off) is located on the Eyre Peninsula of South Australia. Blackbush was discovered in 2007 and is currently the single example of sediment-hosted uranium mineralisation investigated in any detail in the Gawler Craton. Uranium is hosted within Eocene sandstones of the Kanaka Beds and, subordinately, within a massive saprolite derived from the subjacent Hiltaba-aged (~1585 Ma) granites, affiliated with the Samphire Pluton. Uranium is mainly present as coffinite in different lithologies, mineralisation styles and mineral associations. In the sandstone and saprolite, coffinite occurs intergrown with framboidal Fe-sulphides and lignite, as well as coatings around, and filling fractures within, grains of quartz. Microprobe U–Pb dating of coffinite hosted in sedimentary units yielded a narrow age range, with a weighted average of 16.98 ± 0.16 Ma (343 individual analyses), strongly indicating a single coffinite-forming event at that time. Coffinite in subjacent saprolite generated a broader age range from 28 Ma to 20 Ma. Vein-hosted coffinite yielded similar ages (from 12 to 25 Ma), albeit with a greater range. Uraninite in the vein is distinctly older (42 to 38 Ma). The 17 ± 0.16 Ma age for sandstone-hosted mineralisation roughly coincides with tectonic movement as indicated by the presence of horst and graben structures in the Eocene sedimentary rocks hosting uranium mineralisation but not in stratigraphically younger sedimentary rocks. The new ages for hydrothermal minerals support a conceptual genetic model in which uranium was initially sourced from granite bedrock, then pre-concentrated into veins within that granite, and is subsequently dissolved and reprecipitated as coffinite in younger sediments as a result of low-temperature hydrothermal activity associated with tectonic events during the Tertiary. The ages obtained here for uranium minerals within the different lithologies in the Blackbush prospect support a conceptual genetic model in which tectonic movement along the reactivated Roopena Fault, which triggered the flow of U-rich fluids into the cover sequence. The timing of mineralisation provides information that can help optimise exploration programs for analogous uranium resources within shallow buried sediments across the region. The model presented here can be predicted to apply to sediment-hosted U-mineralisation in cratons elsewhere.

Keywords: uranium mineralisation; Eyre Peninsula; Blackbush uranium prospect; U–Pb microprobe geochronology; Kanaka Beds; coffinite

1. Introduction

South Australia has long been recognised as being exceptionally well endowed with uranium resources. All currently economically relevant deposits are associated with high-U Mesoproterozoic felsic rocks [1]. In the Gawler Craton, iron-oxide copper-gold (IOCG) deposits are genetically related to the emplacement of Hiltaba Suite granites at ~1.6 Ga [2,3]. The supergiant Olympic Dam IOCG(U) deposit contains the largest known U resource of any uranium deposit on Earth but is primarily a copper producer with by-product U [4]. In the Curnamona Province, in the east of South Australia, sediment-hosted U deposits, like the current operating mines Beverley and Four Mile, are widespread and source their U from granites and metavolcanics of the Mesoproterozoic Ninnerie Supersuite [1].

Considering the extent of Mesoproterozoic Hiltaba-affiliated bedrock granites [5] and organic-rich sediments across the Gawler Craton (e.g., [6]), similar to those hosting U in the Curnamona Province, large sediment-hosted deposits would be expected. The Blackbush uranium prospect, located on the north-eastern Eyre Peninsula, South Australia (shown on the bedrock map included here as Figure 1) is, however, currently the only example of sediment-hosted U mineralisation in the Gawler Craton that has been investigated in any detail. Blackbush was discovered in 2007 by UraniumSA, a junior exploration company, who recognised the Kanaka Beds as highly prospective for U. The first drill hole intersected a roll front, which culminated in the discovery of Blackbush in 2007 [7], and shortly afterward, the discovery of the geologically similar Plumbush resource.

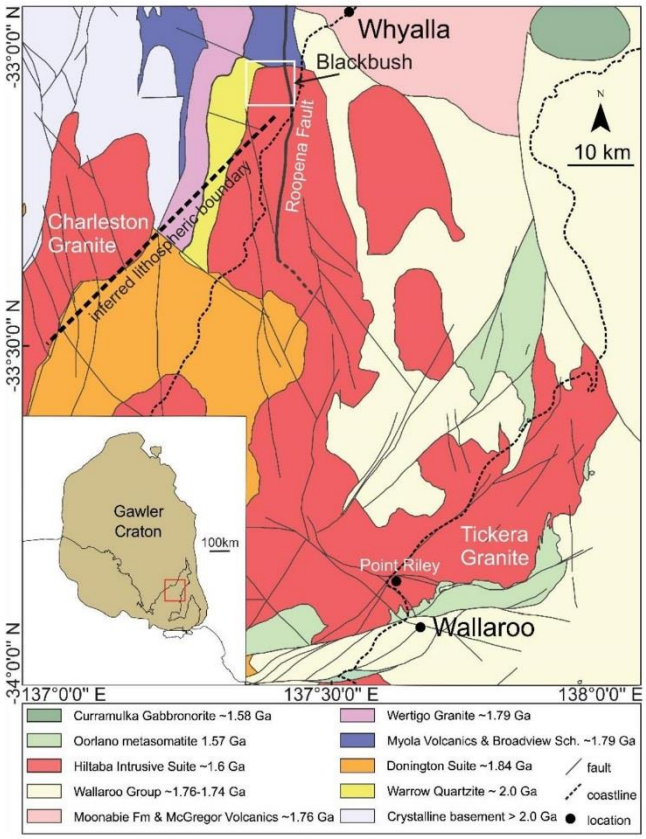

Figure 1. Simplified geological map of bedrock in the north-eastern Eyre Peninsula, Spencer Gulf and adjacent areas, with the location of Blackbush marked. Inset map locates the area within the Gawler Craton. Map based on unpublished material of Samphire Uranium Ltd.

In the Blackbush prospect, uranium is mainly hosted within Eocene siliciclastic sediments of the Kanaka Beds that fill a palaeochannel at the unconformity with subjacent granites of the Samphire pluton, affiliated with the Hiltaba Intrusive Suite. Domnick et al. [8] described the geological setting of the Samphire uranium resource, with emphasis on the geochemistry, mineralogy and alteration of granite bedrock. Three geochemically distinct granite types were identified in the Samphire Pluton [8] and correspond to domains interpreted from geophysical data [9]. All granites show complex chemical and textural alteration overprints which increase in intensity closer to Blackbush, as well as crosscutting veins [8]. Furthermore, all three granite types are anomalously rich in U relative to crustal averages [8]. The highly variable Th/U ratios (from 0.8 to 11.9), as well as the presence of hydrothermal U minerals (mostly coffinite) within all the Samphire granites and crosscutting veins were arguments favouring U mobility [8], leading to the hypothesis that cover-bound uranium was sourced from these granites. In the conceptual model for the mineralisation presented by [8], the uranium was proposed to be pre-concentrated in veins in the upper parts of the pluton during a temporally unconstrained event post-dating Proterozoic granite emplacement. Uranium was then leached and migrated upwards after deposition of the Paleogene and Neogene sedimentary cover above an unconformity that represents a gap of more than 1.5 Ga. Despite the spatial link between mineralisation and a major unconformity, Blackbush cannot be classified as an unconformity-related U deposit. This is due to a lack of conspicuous features associated with such deposits (high grade, highly saline brines, graphitic lithologies in the basement, the dominance of uraninite over coffinite, etc., e.g., [10]).

The objective of the present work is to obtain an accurate age for coffinite-dominant uranium mineralisation in the Blackbush resource, using the chemical (microprobe) age method of Bowles [11,12]. Geochronology is focussed on coffinite within the Kanaka Beds and forming the major part of the mineralisation but also in saprolite at the unconformity, as well as uraninite within granite-hosted veins immediately below. The aim was to expand the geochronological framework for the mineralisation and further validate the genetic model. An accurate age for mineralisation relative to host rock is also considered an important contribution to an exploration model applicable to the search for analogous uranium mineralisation in the region.

2. Geological Setting

2.1. Granite Bedrock

The bedrock to the Blackbush prospect is the Samphire pluton. In a petrographic study of the pluton and its relationship with uranium mineralisation in the suprajacent cover sequence, Domnick et al. [8] recognised three distinct granitoids forming the Samphire Pluton. The southern part of the pluton was informally called the green granite (Granite B) [8]. The same terminology is applied here for the sake of consistency. The northern part, immediately underlying the Blackbush mineralisation, comprises a red granite (Granite C), using the nomenclature of [8]. This is characterised by reddened feldspars, high U content, and highly heterogeneous Th/U ratios (~1 to ~10) [8]. The intensity of alteration and density of fractures and veins are increasingly abundant closer to the mineralisation. Granites B and C are separated by an arcuate domain of the so-called yellow granite (Granite A). The latter features higher CaO, and lower U content, prompting [8] to consider it may be significantly less evolved than the other two. In a subsequent publication, Domnick et al. [13] provide new SHRIMP U–Pb zircon ages for each of the three granites, unequivocally linking them to the ~1.6 Ga Hiltaba Intrusive Suite. Granite B yielded an age (weighted averages) of 1585 ± 9 Ma, Granite C 1579 ± 9 Ma, and Granite A 1588 ± 9 Ma; these data showing no statistical difference in age and overlap with U–Pb zircon ages obtained previously [14]. Petrographic observation and geochemical analysis [8,13] support a hypothesis involving late magmatic enrichment of U in the upper part of the pluton, and subsequent leaching of this U in the Paleogene.

2.2. Saprolite

The uppermost part of the granite is weathered to a massive saprolite 10–30 m in thickness [15]. Sodium and potassium are strongly decreased (<0.5 wt.%) relative to fresher granites. Feldspars have been replaced by kaolinite and minor illite, and biotite by kaolinite and rutile (possibly 'leucoxene'). The REE content of the saprolite is variable, several samples display chondrite-normalised REE fractionation patterns that are readily recognisable as compatible with an igneous origin, while other samples have strongly decreased REE with positive Ce-anomalies, as is typical for saprolite and lateritic profiles from a range of settings [16]. In the underlying granite, the magmatic light rare earth element (LREE) mineral is allanite, which is often replaced by either REE-fluorocarbonates or monazite. Monazite and xenotime are unaffected by weathering, whereas samples originally containing REE-fluorocarbonates or allanite have lost significant portions of their REE budget, except for insoluble Ce^{4+} [17].

The saprolite can be separated into three subunits [13], the lowest part of the saprolite is, like the strongly oxidised granite immediately underneath, coloured red by dispersed hematite, the middle unit is yellow and limonitic, whereas the upper unit is white-grey 'reduced' saprolite with minor pyrite. The boundaries between the units are sharp. In drillhole logs made available by UraniumSA Ltd., saprolite is defined as argillaceous brittle granitoid, which is applied to samples with as low as 10% clay. In a typical drill core, the log notes ~30 m of saprolite, the upper half is clay-dominant and the lower half feldspar-dominant. In the clay-dominant part, the uppermost ~10 m are reduced saprolites, followed downwards by ~2.5 m of limonitic saprolite and ~2.5 m of haematitic saprolite [15]. The feldspar dominant part is always hematite-bearing. Relationships between granite, saprolite and overlying lithologies are illustrated in Figure 2.

2.3. Cainozoic Sedimentary Rocks

The saprolite is overlain by the Kanaka Beds, which are widespread siliciclastic sediments of Eocene age in the Pirie Basin and have been considered as lagoonal-estuarine to lacustrine in origin [13], in accordance with regional-scale studies, notably [6]. Blackbush lies on the western edge of the basin (Figure 3). Here, the Kanaka Beds are fluviatile to marine delta sediments and confined to a palaeochannel incised into the granite [15]. The sediments are well-sorted and show upwards-fining or upwards-coarsening cycles. The grain size varies from clay to pebbles. All units in the Kanaka Beds contain organic material and finer grain size correlates with increased organic material, several upward-fining cycles are topped by lignite. The unconformity between the Eocene sediment and the saprolite is marked by a basal conglomerate, the lowest stratum of the Kanaka Beds.

The Kanaka Beds are followed up-sequence by coarse-grained, fossiliferous sand of Melton Limestone affiliation, overlain by carbonate dominated units of the Melton Limestone. Locally, clay is interbedded in sand and carbonates. The Pliocene clays of the Gibbon Beds separate the Melton Limestone from Quaternary soil. The relative timing of sedimentation is constrained from palynological data [18]. Two samples collected from carbonaceous clay and considered to represent the waning stages of sedimentation of the Kanaka Beds in the palaeochannel contained spores and pollen belonging to the *Middle Nothofagidites asperus* zone. This denotes an age of middle to late Eocene and gives an approximate upper age limit for the Kanaka Beds. A sample of lignite collected ~15 km south of Blackbush from the lowest unit of the Kanaka Beds contained the spore-pollen-zone of *Lower Nothofagidites asperus*, giving a rough lower age limit of Middle Eocene [18].

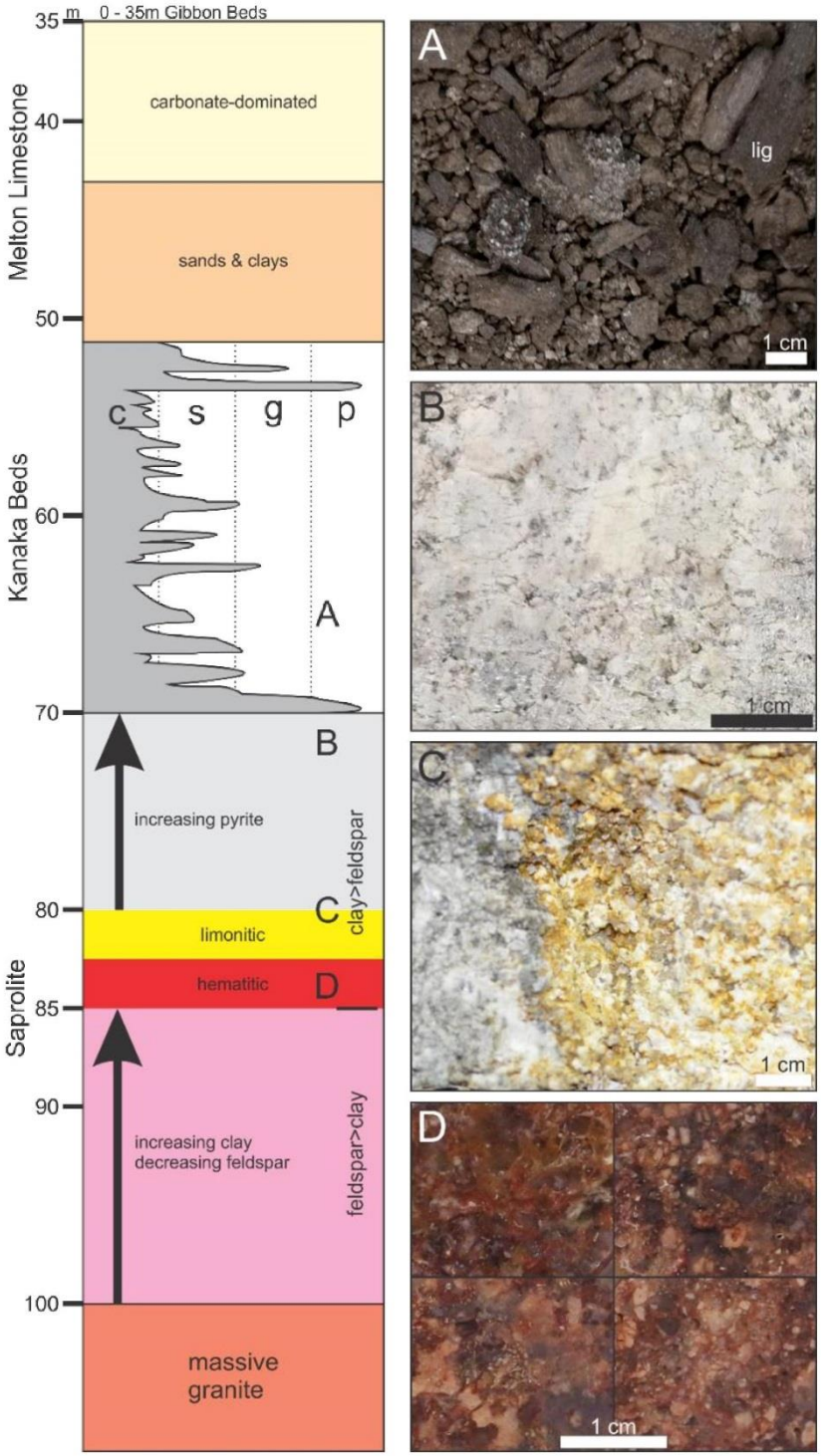

Figure 2. Simplified stratigraphic sequence through the Blackbush resource, with key lithologies indicated. (**A**) Kanaka beds (sands, lignite fragments, clay-dominant clasts); (**B**) reduced saprolite; (**C**) boundary between reduced and limonitic saprolite; (**D**) red saprolite.

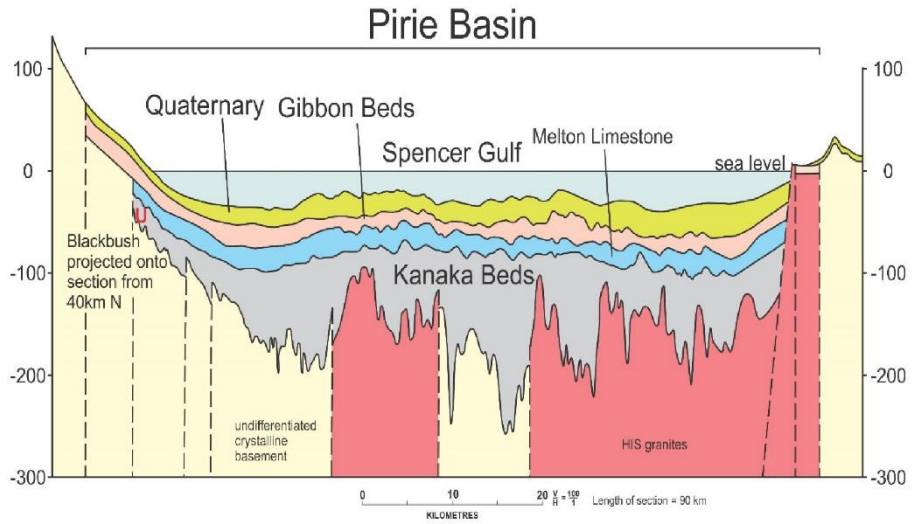

Figure 3. W-E profile of the Eyre Peninsula across the Spencer Gulf (through Point Riley, shown in Figure 1) showing the distribution of Kanaka Beds above a compartmented basement. The vertical scale (in metres) is exaggerated. Adapted from [6].

All rock units in the Blackbush area are affected by tectonic movement, as two fault systems intersect. The Roopena Fault, 6 km east of Blackbush, is a major N-S-striking lithospheric boundary, interpreted as an ancient palaeosuture. Previously considered to be ~1730 Ma in age, newer research points to an age of at least >1850 Ma, most likely >2500 Ma, with reactivation during every major orogeny. Subordinate branches of the Roopena Fault crosscut the bedrock in the Blackbush area (e.g., [19]). In addition, the Pirie Basin is undergoing subsidence since the late Miocene (~10 Ma) with the basement separating into fault blocks creating horst and graben structures. The placement of the palaeochannel hosting the Blackbush mineralisation is controlled by faults.

2.4. Uranium Mineralisation

The style of uranium mineralisation at Blackbush is diverse. Approximately 23% of the U is hosted in the saprolite, mostly stratabound along the unconformity, and to a lesser degree, discordant along faults but always restricted to the reduced saprolite. Approximately 75% is hosted within the Kanaka Beds, along the unconformity, in tabular to lenticular bodies (Figure 4) hosted within the sand, clay, or lignite, and to a small degree, as a roll front like structure. The Kanaka Beds are always organic-rich and reduced. A very small part of the U (~2%) extends into the overlying Melton Limestone sand [15].

The main U mineral is coffinite, $USiO_4$ nH_2O, where $0 < n < 2$ [20], which occurs associated with framboidal pyrite or is present as intergrowths with pyrite or clay minerals. Coffinite and traces of uraninite can also be found in hematite-coffinite-bearing veins that crosscut the underlying granite.

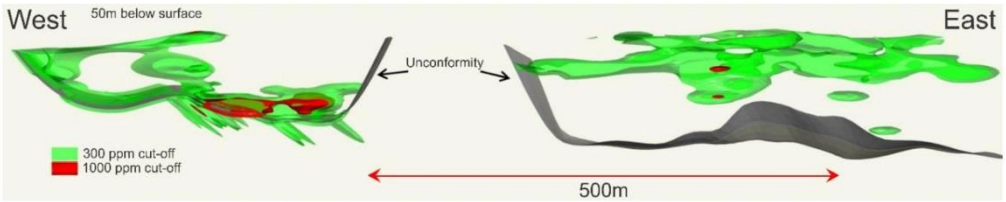

Figure 4. Schematic, simplified NW-SE three-dimensional model of eastern and central parts of the Blackbush prospect, modified after [15] and reproduced with permission.

3. Sampling and Methodology

3.1. Samples

The main objective of this study was to acquire ages for coffinite and other minor U–(Th)-minerals in different lithologies, including the mineralised sandstone, hydrothermal veins in the underlying fresh granite, and material from the saprolitic granite separating both units. The vein and saprolite samples are part of a larger sample suite and were chosen based on the presence of coffinite and subordinate uraninite. The samples representative of uranium mineralisation within the Kanaka Beds consist of nodules hosting intimately intergrown assemblages of pyrite and coffinite, as well as lignite pieces containing coffinite in pores, they were chosen based on their high U content measured via handheld XRF and ease of preparation, taking care to avoid any loss of easily soluble U minerals. All material was mounted in epoxy within one-inch blocks that were polished and consequently examined on an FEI Quanta 450 FEG scanning electron microscope in backscatter electron (BSE) mode located at Adelaide Microscopy (The University of Adelaide, Adelaide, Australia), prior to quantitative microanalysis.

3.2. EPMA Methodology

Chemical ages were acquired using a Cameca SX-Five electron probe microanalyser located in the same laboratory. Chemical compositions of coffinite and other minerals were obtained using a Cameca SX-Five Electron Probe Microanalyser (EPMA) running 'Probe for EPMA' software. All elements were analysed at 15 kV with a defocussed spot of 5 μm. Calcium, Ce, Fe, Si, P, and Th were all initially acquired using a beam current of 40 nA, and once complete, the beam current was automatically turned up to 100 nA for measurement of Pb. EPMA chemical dating studies routinely use beam currents of at least 100 nA to measure Pb.

X-ray lines and standards used were as follows: Ca Kα (plagioclase), U Mβ (synthetic UO_2), Ce Lα ($CePO_4$), Fe Kα (almandine), Si Kα (albite), P Kα (YPO_4), Th Mα (huttonite), Pb Mβ ($PbSiO_3$), and Y Lα (YPO_4). Peak counting times used were 15 s for U and Ce, 25 s for Ca, Fe, Si, and P, 30 s for Th and Y, and 50 s for Pb.

Due to the need to attain the best possible precision on Pb measurements, Pb Mβ was acquired on large PET crystals on three separate spectrometers. The Probe for EPMA software (distributed by Probe Software Inc., Eugene, OR, USA) used allows for aggregation of identical X-ray lines in which the peak-background signal intensities are summed from multiple spectrometers, then fed through the typical φ(ρz) corrections. The lead concentrations obtained when spectrometers were summed/aggregated were compared to resultant individual concentrations when each spectrometer was treated individually, and in all cases, the resultant concentration of summed spectrometers fall well within the error of individual spectrometer concentrations.

All background interpolations utilised linear 2-point backgrounds, with counting times set at 20 s for Ca, U, Ce, Fe, Si and P, 30 s for Th and Y, and 50 s for Pb. Oxygen was calculated by stoichiometry, assuming that all Fe occurs as Fe^{2+}. Matrix corrections of Armstrong-Love/Scott φ(ρz) [21] and Henke MACs were used for data reduction. The Mean Atomic Number correction was utilised for background subtraction (e.g., [22,23]). The average minimum detection limits, in wt.%, were: Ca (0.015), U (0.055), Ce (0.029), Fe (0.023), Si (0.013), P (0.011), Th (0.034), Pb (0.018), and Y (0.021). These detection limits are similar or better than those obtained in other chemical dating studies (e.g., [24]).

3.3. Data Processing

3.3.1. Contamination and Analytical Totals

The very fine-grained nature of the intergrowths of coffinite and pyrite/lignite in the sediment, and coffinite/uraninite and hematite in the vein impedes the acquisition of compositional data that is guaranteed free of any contamination. Calcium is commonly used as an indicator of alteration and associated Pb loss for the chemical dating of monazite or uraninite.

For our sample set, we chose measured iron concentrations as a proxy to identify mixed measurements that include sulphides. Contamination from Fe sulphides shifts ages to the older side, due to their minor Pb content. Any other contamination from other admixed phases does not appear to directly distort ages, but the effect of diluting U and Pb increases the scatter and errors of ages. To avoid this, each analysis of coffinite and thorite with >4 wt.% FeO or >30 wt.% SiO_2 was excluded from further consideration. For uraninite, this limit was increased to 6 wt.% FeO.

Analytical totals for coffinite (sum of all elements in wt.% oxide; Supplementary Materials) are relatively low, as is typical for this microanalytically challenging mineral (e.g., [25]). We explain this as follows. Firstly, this is the result of the presence of molecular water, with the formula of coffinite often given as $USiO_4 \cdot nH_2O$ [20] with an n value equal to 2, rather than $U(SiO_4)_{1-x}(OH)_{4x}$. A composition of $USiO_4 \cdot 2H_2O$ would correspond to a measured total of 90 wt.%, including 74 wt.% UO_2 and 16 wt.% SiO_2, with the 'missing' 10% assigned to H_2O. Secondly, poor totals correspond to elements not analysed, e.g., REE or S, although we do not believe this is ever more than 2–3 wt.%. Thirdly, and in our opinion, the overwhelming reason for poor totals is the nature of the coffinite, with abundant pore spaces and voids, an issue further compromised by small grain size.

Analyses of the dense coffinite used in this study yield totals in the range from 75 up to 93 wt.%, on average 85 wt.%. Totals below 75 wt.% were discarded. For highly porous coffinite analysed in this study, analytical totals were never higher than 79 wt.%. Analyses with totals between 50 wt.% and 79 wt.% have element ratios (and thus ages) identical to those of coffinite with high totals and are interpreted as containing voids and/or anomalously high H_2O content. All analyses with totals below 50 wt.% were discarded. These are mostly non-stoichiometric and compromised by contamination from minerals that contain non-analysed elements, such as Ti in rutile. Analytical totals for uraninite are between 72 and 81 wt.%.

Mineral formulae have not been calculated from the EPMA data and no attempt has been made to charge balance due to the number of unknowns and uncertainties, including but not restricted to the presence of molecular H_2O, the presence of pores and voids, non-analysed elements, and multiple oxidation states of U, Fe, and other elements. Each of these variables will impact the data in similar ways and their effects cannot be readily distinguished. Formulae calculations for U-minerals can be plagued by assumptions (e.g., [26]) that may be difficult or impossible to confirm without access to ultra-sensitive techniques (e.g., [27]). Despite these concerns, or the lack of the complete set of REE or Al, we are confident that precise geochemistry is not needed for chemical dating.

In total, 607 spots were analysed of which 421 (~70%) remained after quality control and processing. Of these, 343 are analyses of coffinite in the nodules of intergrown pyrite-coffinite described above. The balance is made up of 4 analyses of *uranothorite* in the saprolite, 7 spots of coffinite in the saprolite, 8 uraninite in the vein, and 59 coffinite in the vein.

3.3.2. Ages and Uncertainties

Ages were calculated iteratively using the general, widely applied age formula as defined and given by Montel et al. [28]. Although initially used to date monazite, in which U is at comparatively low levels, the formula is widely used in chemical U–Th–Pb dating studies via EPMA, and is identical to that given for minerals containing essential uranium (e.g., [11,12,24,29]) and can be used for any other U-bearing mineral that retains radiogenic Pb, irrespective of concentrations.

In the age equations used, ^{238}U refers to the atomic weight of *U* (and not the specific isotope, ^{238}U). The typical radioactive *Pb* isotopic composition can be expressed as:

$$^{208}Pb = {}^{232}Th\left(e^{\lambda_{232}t} - 1\right) \quad (1)$$

$$^{206}Pb = {}^{238}U\left(e^{\lambda_{238}t} - 1\right) \quad (2)$$

$$^{207}Pb = {}^{235}U\left(e^{\lambda_{235}t} - 1\right) \quad (3)$$

Therefore, the total *Pb* content of a mineral can be expressed as:

$$Pb = {}^{232}Th\left(e^{\lambda_{232}t} - 1\right) + {}^{238}U\left(e^{\lambda_{238}t} - 1\right) + {}^{235}U\left(e^{\lambda_{235}t} - 1\right) \quad (4)$$

Following the fact that we cannot measure isotopes of uranium via EPMA, only total *U*, we can utilise the natural uranium ratio of $^{235}U/^{238}U = 1/138.88$ in order to work out the contribution of measured *Pb* from each isotope of uranium as expressed below:

$$Pb_{conc} = \frac{Th_{conc}}{232} \times \left(e^{\lambda_{232}t} - 1\right) \times 208 + \frac{U_{conc}(0.9928)}{238.04} \times \left(e^{\lambda_{238}t} - 1\right) \times 206 + \frac{U_{conc}(0.0072)}{238.04} \times \left(e^{\lambda_{235}t} - 1\right) \times 207 \quad (5)$$

in which the denominators are the atomic weights of Th and U (i.e., 232 and 238.04, respectively), and the multiplicative values of ^{208}Pb, ^{206}Pb, and ^{207}Pb are the atomic weights of the respective Pb isotopes. Equation (5) represents the chemical dating "age equation", in which all input concentrations are in ppm, and which are then subsequently converted into atomic proportions. This equation is then solved iteratively for *t* (time) until a solution is reached.

For the propagation of uncertainty in any function $w = f(x,y,z)$, the following formula applies, assuming the variables *x*,*y*,*z* are independent:

$$\sigma_w{}^2 = \left(\frac{\delta f}{\delta x}\right)^2 \sigma_x{}^2 + \left(\frac{\delta f}{\delta y}\right)^2 \sigma_y{}^2 + \left(\frac{\delta f}{\delta z}\right)^2 \sigma_z{}^2 \quad (6)$$

Following [30], uncertainties used here have been calculated using peak and background counts, corrections for interference, ZAF etc. This can be applied to the age formula of [28], which can be generalised as $Pb = f(U,Th,t)$. Transforming the formula to acquire the unknown age error (σ_t) results in:

$$\sigma_t = \sqrt{\frac{\sigma_{Pb}{}^2 - \left(\frac{\delta f}{\delta U}\right)^2 \sigma_U{}^2 - \left(\frac{\delta f}{\delta Th}\right)^2 \sigma_{Th}{}^2}{\left(\frac{\delta f}{\delta t}\right)^2}} \quad (7)$$

Theoretically, this formula implies that 'worse' measurements of *U* and *Th* with higher uncertainties would lead to smaller age errors. In practice, all terms are very small compared to σ_{Pb}, and $\frac{\sigma Pb}{Pb} \approx \frac{\sigma t}{t}$. Although we did not include decay constant errors, all calculated ages and errors were crosschecked using precise explicit approximations of [30], which includes decay constant errors. Incorporation of systematic decay constant errors into the uncertainty propagation is not typically done for chemical dating via EPMA, predominantly due to the (relatively) imprecise nature of the chemical EPMA dating technique. Ages and errors of both methods are identical within the given precision. All weighted averages were calculated offline in Isoplot v4.15 [31].

4. Results

4.1. Petrography of Analysed Samples

4.1.1. Granite-Hosted Vein

The granite is medium-grained and weakly fractured. Most igneous minerals are partially or totally altered to secondary assemblages. Plagioclase and orthoclase have been replaced by red albite and K-feldspar, all igneous Fe^{2+}-containing minerals are replaced, e.g., biotite by chlorite, magnetite by hematite, allanite by REE-fluorocarbonates or monazite. This granite has been extensively described previously [8]. Several sections of drill core are dominated by mm- to cm-scale veins and fractures within brecciated granite. Representative of such intervals sampled for the present study are veins with a characteristic silverish to dark grey colour and highly porous filling material (Figure 5A). This

comprises hematite (grains of 10 to 50 μm width), coffinite, quartz, and traces of uraninite (Figure 5B). Coffinite is extremely fine-grained and spherical to colloform in morphology (Figure 5C). Uraninite is only present in trace amounts and occurs as intergrowths with hematite (Figure 5D).

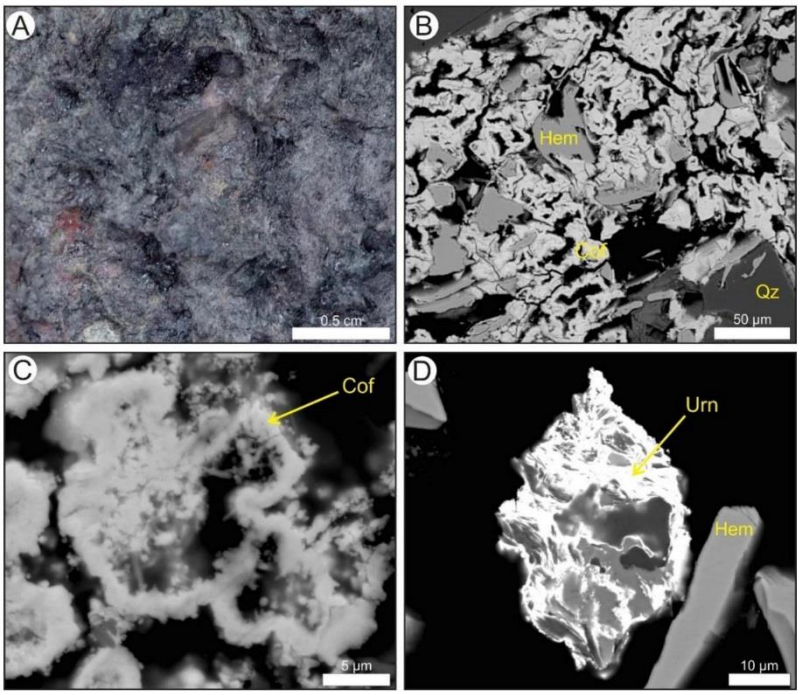

Figure 5. (**A**) Hand specimen photograph of hematite (Hem) + coffinite (Cof) + quartz (Qz) assemblage filling a vein in altered granite. (**B**–**D**) BSE images showing the intimate association between U-minerals and hematite within the vein in (A). Both coffinite and minor uraninite (Urn) are present as sub-micron, fine-grained, colloform aggregates forming rims around hematite laths, quartz grains or filling cavities.

4.1.2. Saprolite

The dated samples are from the uppermost interval comprising reduced saprolite. They contain kaolinite, quartz, pyrite (~1%), and accessory minerals like coffinite, thorite or zircon. The latter four minerals are often associated, thorite or zircon are embedded into framboidal pyrite, coffinite forms either an overgrowth on pyrite or impregnates pyrite and thorite/zircon. The dated minerals in the saprolite, *uranothorite* and coffinite are from these associations.

4.1.3. Sediment-Derived Samples

The lignite pieces are highly variable in size between 0.5 and 2 cm, always black and of irregular shape. The coffinite sits in small cavities in the lignite. The pyrite nodules are 0.2 to 1 cm in size. Although a minority of the nodules are pyrite dominant, shown in the example in Figure 6, the main component is often quartz within which fine-grained pyrite and coffinite are concentrated within fractures (Figure 7).

4.2. Composition of Dated Minerals

In the nodules dominated by pyrite or lignite, the coffinite yielded mostly analytical totals over 80 wt.%, with an average of 85 wt.%. A minority of points have lower totals. These analyses have the same element ratios as higher total analyses, indicating either contamination by non-analysed elements,

or more likely pores and voids. The coffinite is typically poor in minor and trace elements and on average contains 64 wt.% UO_2 and 17 wt.% SiO_2. Thorium is almost always below the minimum limit of detection (~350 ppm) and rarely reaches 400 ppm. Ce_2O_3 is around 0.4 wt.%, Y_2O_3 can reach up to 1.2 wt.% but is mostly very low, rarely below minimum limit of detection. On average the samples contain 1.4 wt.% CaO, although in four analyses it exceeds 3% with a maximum of 9 wt.%. This high CaO does not correlate with increased concentrations of other elements and the analytical totals are within acceptable ranges—only UO_2 seems to be slightly lower, and the higher CaO is interpreted as increased substitution of U by Ca. FeO, wherever present, is always contamination and, on average, around 0.8 wt.%; values > 4.0 wt.% were excluded. P_2O_5 is always < 1.0 wt.%.

Analytical totals of vein coffinite are consistently low in comparison (50–72 wt.%). Whereas SiO_2 (10 to 16 wt.%) is at a similar concentration as in the sediment-hosted coffinite, vein coffinite contains only half the UO_2, ~32 wt.%. Thorium oxide reaches on average 0.3 wt.%. It has high 9 to 14 wt.% Y_2O_3, but very little ~0.08 wt.% Ce_2O_3, indicating strong relative enrichment of heavy rare earth elements (HREE) over light rare earth elements (LREE). CaO ~1.8 wt.% is like the sediment coffinite. Contamination with Fe is slightly higher at ~1.2 wt.%.

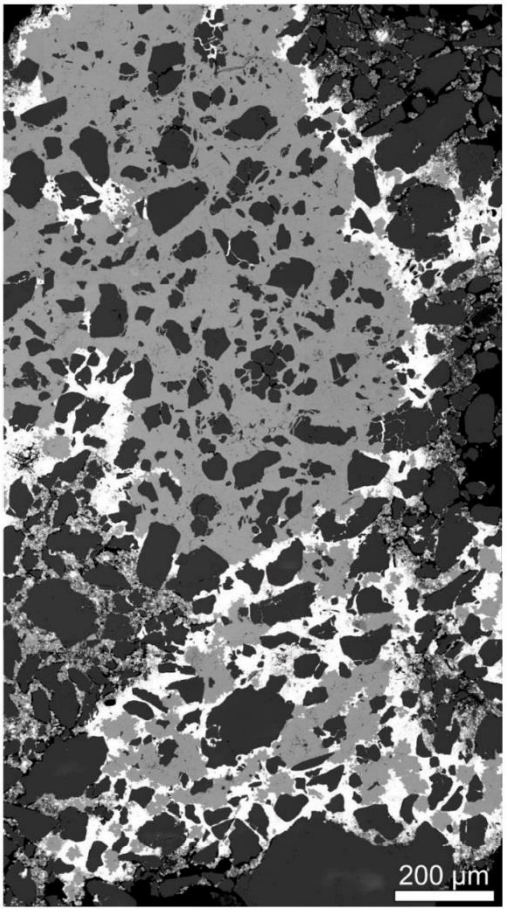

Figure 6. Backscatter electron image of a pyrite nodule. Bright—coffinite; grey—pyrite; dark—quartz.

Saprolite-hosted coffinite is distinctly ThO_2-rich, but the content is highly variable between 1.8 and 12 wt.%. Elements can be roughly separated into two groups. UO_2 and Ce_2O_3 correlate, while

ThO_2, Y_2O_3, CaO, and P_2O_5 correlate. Considering the spatial association of coffinite and thorite in the saprolite, this is interpreted as coffinite with a considerable thorite component and either the result of strong U(+Ce) enrichment of (magmatic) thorite or mobility of Th(+Ca,Y,P) over several µm, resulting in deposition of high-Th coffinite.

This is supported by analyses of high-U thorite in the saprolite, which show very similar trends. ThO_2, Y_2O_3, CaO, and P_2O_5 correlate and are significantly higher, while UO_2 and Ce_2O_3 are lower compared to high-Th coffinite.

Analysed uraninites have low analytical totals (72 to 81 wt.%). They contain 57 to 67 wt.% UO_2, 6 to 16 wt.% SiO_2, ~1.5 wt.% CaO, ~0.5 wt.% Ce_2O_3, ~1.2 wt.% Y_2O_3, and 1.5 to 5.0 wt.% FeO. At first sight, the designation uraninite seems odd, considering that SiO_2 is barely lower compared to the vein coffinite, and UO_2 reaches only the levels observed in sediment-hosted coffinite. Firstly, these analyses are geochemically distinct from endmember coffinite, e.g., by negligible P content. Secondly, all analyses are from grains visually different from coffinite. Thirdly, U, Ce, Y, and Pb correlate, indicating they are contained in the uraninite, while there is no correlation between Si, Fe, and U, indicating that Fe and Si are contamination by quartz and hematite as much as by coffinitisation of uraninite.

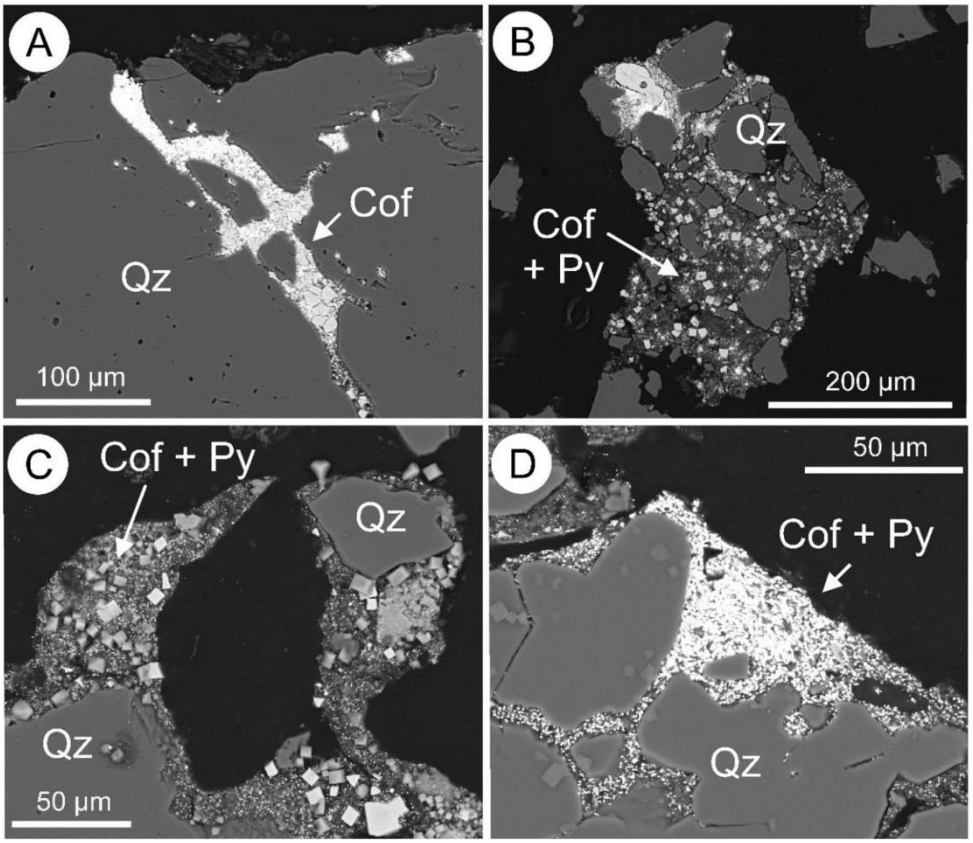

Figure 7. BSE images showing petrographic aspects of uranium mineralisation in sedimentary rocks. (**A**) Micro-crystalline coffinite (Cof) within fractures in quartz (Qz). (**B**) Micrometer-scale coffinite, pyrite (Py) and trace uraninite within fractures and voids in quartz. (**C**) Fine-grained intergrowths of coffinite and pyrite on the margins of quartz. (**D**) Fine-grained intergrowths of coffinite and pyrite within quartz.

4.3. U–Pb Microprobe Dating

The results of chemical U–Pb dating (421 spot analyses) of coffinite in all three occurrences (sandstone, saprolite and veins) are summarised in Figure 8. The resultant histogram shows a normal distribution with a weighted average age of 16.98 ± 0.16 Ma for the whole coffinite population. Uraninite from the granite-hosted vein yielded a significantly older age (40 ± 2 Ma). The full set of geochronological data are provided as Supplementary Materials.

4.3.1. Sediment-Hosted Coffinite

The ages of coffinite in the lignite and pyrite nodules are almost normally distributed between 9 and 22 Ma. The tails on both sides (kurtosis) are slightly too high. Nevertheless, it is a probability distribution and can be readily interpreted as a single event. The weighted average is 16.98 ± 0.16 Ma. The average relative error for individual single points is ~7.2% (~1.2 Ma).

There is no difference in ages or their distribution between samples or between lignite-associated and pyrite-associated coffinite. Ages do not seem affected by low totals, but age errors are usually slightly higher for those analyses due to lower concentrations.

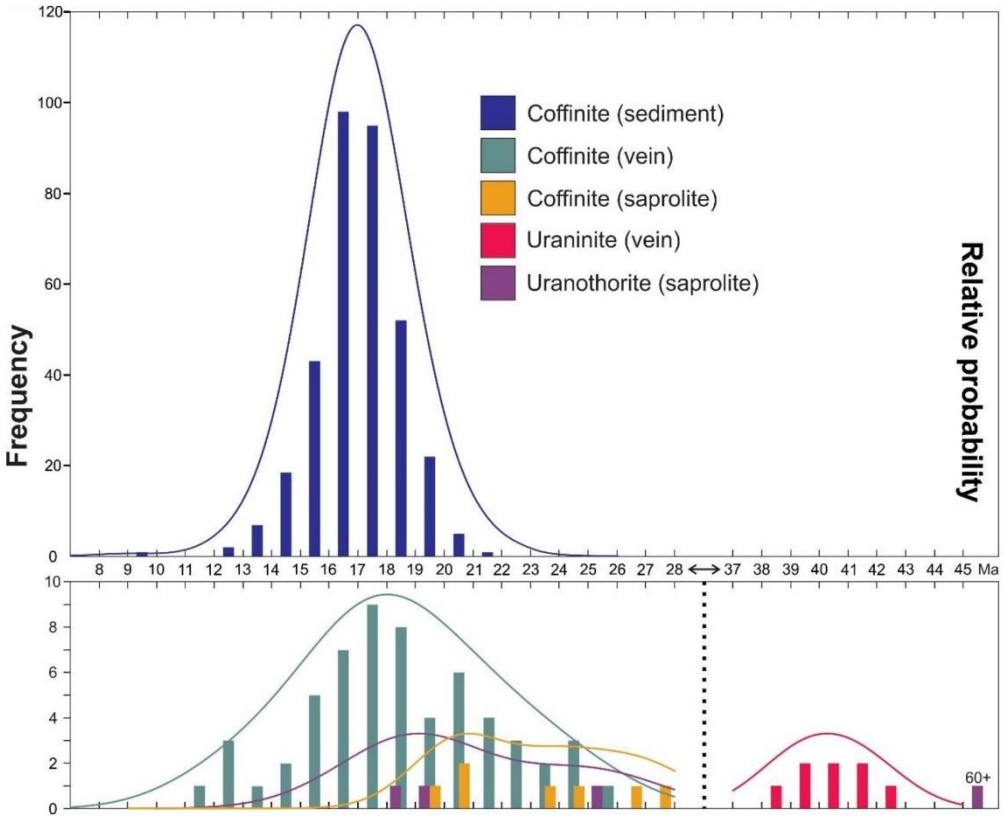

Figure 8. Histogram of obtained ages in Ma with relative probability curves superimposed. Note the normal distribution of coffinite ages.

4.3.2. Saprolite

Dating of *uranothorite* gave ages from 18 to 25 Ma. Lead loss (and thus younger ages) might have been expected but this is not the case, potentially pointing at chemical weathering prior to the

formation of U-minerals. Errors are around ~2.5 Ma for all spots (4 to 14%). These ages are likely the result of (almost) complete isotopic resetting of magmatic thorite.

The Th-rich coffinite yielded ages of 20 Ma to 28 Ma with an average relative error of 7% (~1.6 Ma). The ages are older than those of the sediment-hosted coffinite but are not unexpected considering the likely old, magmatic thorite component. The populations of both species are, however, relatively small and the ages obtained should be treated with caution.

4.3.3. Vein-Hosted Coffinite and Uraninite

Porous coffinite from the vein gave ages from 12 to 25 Ma with an average error of 13% (~2.3 Ma). This is roughly twice the relative error of coffinite analyses in the sediment. The ages show a distribution comparable to the sediment-hosted coffinite although the median is slightly shifted to ~18.5 Ma and the distribution is less symmetrical (Figure 8).

Dating of uraninite from the granite-hosted vein yielded ages of 38 to 42 Ma with an average of 40 Ma. The relative error for single points is ~3% (~1.6 Ma). There is a weak correlation between higher Fe and older age, indicating the addition of Pb by hematite. Considering the generally high Fe in these uraninite analyses, the true age of uraninite is likely lower than 40 Ma, but nevertheless still older than all dated coffinite.

5. Discussion

Precise age dating of sediment-hosted U deposits faces a variety of obstacles. The high permeability of the sediment facilitates mobility and loss of radon (Rn). The longevity of the mineralising system and the ubiquitous presence of groundwater allow for continuous migration of daughter radionuclides, e.g., Rn, Ra and Pb, from parent U. Therefore, dateable minerals like coffinite and uraninite can be considered to display relatively open system behaviour in sediment-hosted U deposits. This can lead to acquired ages rarely representing the time of U deposition. Despite this, loss and gain of elements are unlikely to ever be homogeneous across the system and the ages of minerals are very rarely completely reset. This, in turn, leads to a wide spread of ages over several Ma, or more (e.g., [32]).

The tight range of ages for dense coffinite in the sediment, describing a probability distribution with a single peak at ~17 Ma (Figure 8), can be readily interpreted as unaffected by open system behaviour and thus, would represent valuable evidence for a single coffinite-forming event during the Miocene. The coffinite in the sediment samples is fine-grained and intergrown with pyrite, but importantly, it is non-porous, which likely helped maintain a (relatively) closed system that allowed retention of Rn, Ra, and Pb. It should, however, be mentioned that these samples are possibly not fully representative, given that the main style of U mineralisation in the sediment is porous coatings on quartz grains that cannot be analysed. The ~17 Ma age obtained in this study is therefore subject to a twofold sampling bias. It could be argued that high rates of U precipitation would result in larger crystals, more easily age dated, whereas slower precipitation rates lead to fine-grained intergrowths. Secondly, the selection of very high U sediments for analysis followed by a focus on grains sufficiently large for that analysis could effectively have introduced a biased sampling of U minerals formed during a single event of major U input. In addition, rejecting analyses of highly porous U minerals because of low analytical totals could have removed much of the reset material. Lastly, a degree of open system behaviour is documented by the presence of radionuclides in groundwater at the Blackbush prospect, indicating that the assumption of closed system behaviour may not be entirely correct.

The ages obtained for the porous vein coffinite exemplify the problems mentioned above. Compared to the dense sediment-hosted coffinite, ages show a wider spread and do not follow a normal probability distribution (Figure 8). Aside from the main peak at ~18 Ma, several smaller peaks at ~12, ~20, and 24 Ma are noted. The origin of these ages cannot be resolved in greater detail, and likely do not carry any genetic information. They are the result of an unknown combination of primary coffinite deposition, open system behaviour and resetting, and, considering the presence of older uraninite in the vein, also coffinitisation of uraninite. This alteration process released radiogenic

lead due to the reduced compatibility of Pb in the coffinite structure compared to uraninite (e.g., [25]), which could be deposited on grain surfaces, further skewing the ages of highly porous coffinite.

During the Cainozoic, sedimentary basins in South Australia (Figure 9) went through very similar events and processes, which in turn led to similar suitable conditions for U deposits. In the Pirie Basin, the Eocene organic-rich Kanaka Beds were deposited, contemporaneous with the Maralinga Member in the Eucla Basin and the Eyre Formation in the Lake Eyre Basin, all of which host uranium. The age of the coffinite, ~17 Ma, coincides with the Garford Formation in the Eucla Basin, and Namba Formation in the Southern Callabonna Sub-basin. Still, it is unlikely that sedimentation occurred around 17 Ma which could have controlled coffinite formation, although the exact age of the Melton Limestone has been discussed [6,33].

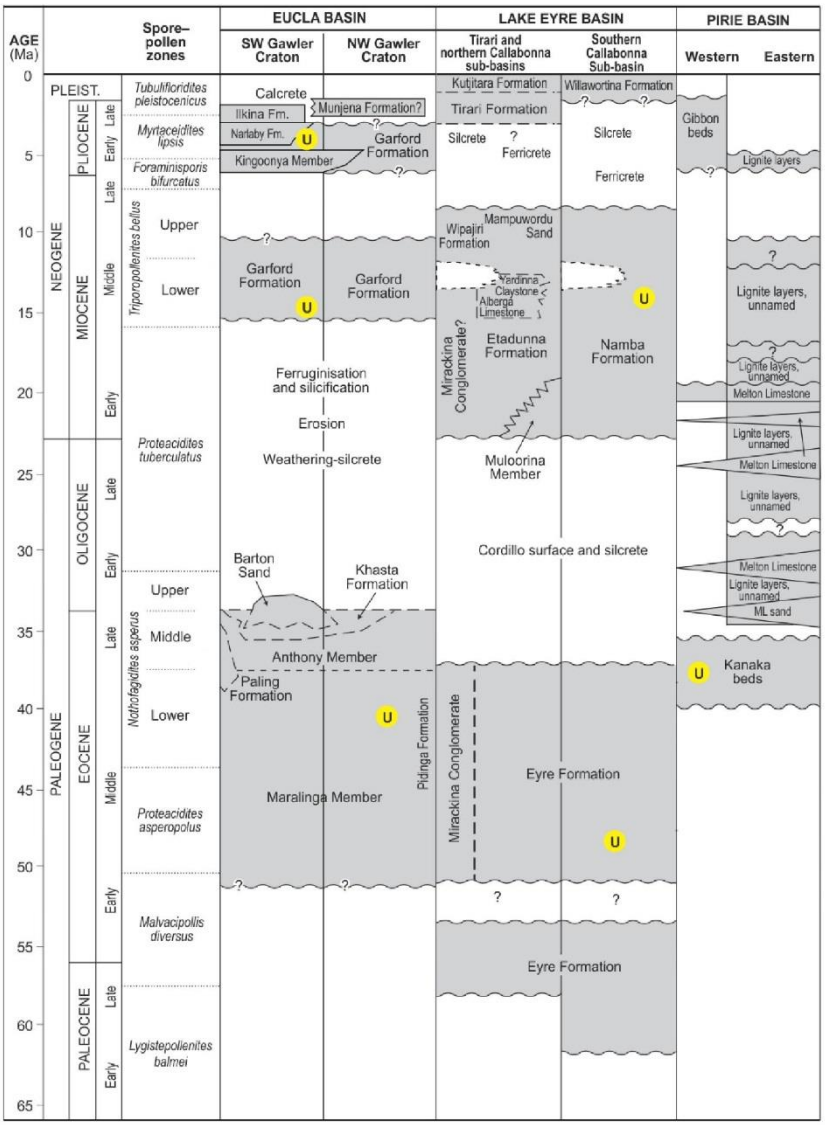

Figure 9. Comparative stratigraphy of Palaeogene-Neogene sedimentary stratigraphy in South Australian basins and adjacent areas. Figure adapted from [6].

While the Garford and Namba Formations are known to host U, the preservation of a unique 17 Ma age, inferring U immobility, is only documented in the Pirie Basin. Dating of U-minerals in other sediment-hosted U deposits in South and Western Australia typically yields young ages, e.g., 6.7 to 3.4 Ma in the Beverley deposit, Lake Frome Basin [34,35], or is unsuccessful or ambiguous due to open behaviour and repeated resetting [32].

An age of ~17 Ma does, however, coincide with the Miocene Climate Optimum [36]. The Eocene and Miocene are characterised by hot and wet climates in Southern Australia, leading to abundant vegetation and, in turn, to organic-rich channel fills. On one hand, hot and wet climates are beneficial for U deposition, e.g., by increased groundwater flow. On the other hand, slow but continuous changes in climate should lead to similarly evolving changes in U deposition, which would result in a more undulating distribution of ages instead of a single peak at 17 Ma.

A variety of vein-hosted U systems of limited size can be found on the eastern edge of the Eyre Peninsula [1]. They are associated with the Kalinjala Mylonite zone (KMZ), a major lithospheric boundary and palaeosuture between two terranes. The Roopena Fault is the northern extension of the KMZ. As mentioned above, subordinate branches of the Roopena Fault cross the prospect. In addition, even though the Roopena and the KMZ are not in direct contact (rather, they are separated by a broader fault splay system) and the Roopena Fault appears to turn south-east into the Spencer Gulf, an inferred connection between them places the lithospheric boundary very close to the Blackbush prospect. The increased level of fracturing and veining of the granite closer to the U mineralisation further supports the strong influence of fractures and fluid movement along them. The most likely explanation for the ~17 Ma age is the triggering of U-rich fluids by tectonic movement along this lithospheric boundary.

Other vein-hosted uranium mineralisation in South Australia does not have a clear source, whereas observed relationships suggest that the Blackbush prospect likely sources its U from the underlying high-U granite. The vast difference in size between them, e.g., the Hospital Prospect, Port Lincoln (5 tonnes U [37]) compared to Blackbush (12,500 tonnes U), could indicate that simple leaching of U from the basement by groundwater is a significant mechanism.

The saprolite investigated here yielded far fewer U minerals than had been expected from logs provided by UraniumSA. It remains unclear whether much U was lost during processing, or alternatively if U is instead adsorbed onto clay minerals. The distinct Th-rich character of the coffinite indicates that this is not likely representative for the mineralisation of the saprolite, and rather it is a highly U enriched magmatic thorite.

The significantly older age for the granite-hosted vein uraninite indicates this predates sedimentation of the Eocene Kanaka Beds. Quartz dissolution is greatly facilitated by organic acids, which in turn supports the precipitation of coffinite, hence it is the only U mineral in the organic-rich sediment. The presence of uraninite could indicate transport and redeposition of uranium by meteoric fluids within the exposed granite. If the uraninite predates sedimentation of the Kanaka Beds, it would indicate that (true) groundwater is unnecessary for U transport.

6. Implications and Conclusions

Coffinite ages define an almost perfect normal distribution suggestive of a single coffinite-forming event at ~17 Ma, likely triggered by tectonic movement along a major lithospheric boundary. Uncertainties remain, however, about the proportion of U brought in the system during the event, compared to simple leaching of U from the basement by groundwater. Age constraints from coffinite in the saprolite (28–20 Ma) are based on fewer analyses and, in all probability, represent incomplete resetting of older *uranothorite*. Uraninite in granite-hosted veins gives an age of 42–38 Ma. Uranium mobility would appear to predate sedimentation of the preserved cover sequence. The ages obtained here on hydrothermal minerals support a conceptual genetic model in which tectonic movement along the reactivated Roopena Fault triggered the flow of U-rich fluids into the cover sequence

The new data will assist with the optimisation of exploration strategies seeking to identify additional uranium resources in the region [38], even if some of the interpretations reached here may

suggest that Blackbush may have formed where it is due to a combination of favourable factors that may not be widely repeated. The petrographic work detailed here on the nature of the uranium minerals represents valuable background information that may assist in the eventual exploitation of the Blackbush resource, e.g., by in situ leaching.

Supplementary Materials: The following are available online at http://www.mdpi.com/2075-163X/10/2/191/s1, EPMA dataset for the analysed U minerals.

Author Contributions: U.D. and N.J.C. wrote this paper. U.D. and B.P.W. performed the analytical work, including the microprobe U–Pb dating. Data processing was carried out by U.D. and B.P.W., assisted by L.C.-D.). The project was devised by N.J.C. and R.B. and supervised by N.J.C and C.L.C. All authors have read and agreed to the published version of the manuscript.

Funding: U.D. acknowledges receipt of a Ph.D. scholarship from the Carthew Family Trust from which this project was funded. N.J.C. acknowledges additional support from the ARC Research Hub for Australian Copper-Uranium (Grant IH130200033).

Acknowledgments: We appreciate the constructive comments of Nicole Hurtig and two anonymous reviewers, which helped us improve clarity and presentation.

Conflicts of Interest: The authors declare no conflicts of interest.

References

1. Wilson, T. *Uranium and Uranium Mineral Systems in South Australia*, 3rd ed.; Report Book 2015/00011; Geological Survey of South Australia, Mineral and Energy Resources Group: Adelaide, Australia, 2015; p. 191.
2. Hitzman, M.W.; Valenta, R.K. Uranium in iron oxide-copper-gold (IOCG) systems. *Econ. Geol.* **2005**, *100*, 1657–1661. [CrossRef]
3. Skirrow, R.; Bastrakov, E.N.; Barovich, K.; Fraser, G.L.; Creaser, R.A.; Fanning, C.M.; Raymond, O.L.; Davidson, G.J. Timing of Iron Oxide Copper-Gold Hydrothermal Activity and Nd Isotope Constraints on Metal Sources in the Gawler Craton, South Australia. *Econ. Geol.* **2007**, *102*, 1441–1470. [CrossRef]
4. Ehrig, K.; McPhie, J.; Kamenetsky, V. Geology and mineralogical zonation of the Olympic Dam iron oxide Cu–U–Au–Ag deposit, South Australia. In *Geology and Genesis of Major Copper Deposits and Districts of the World, a Tribute to Richard Sillitoe*; Hedenquist, J.W., Harris, M., Camus, F., Eds.; SEG Special Publcation: Lyttelton, CO, USA, 2012; Volume 16, pp. 237–268.
5. Stewart, K.P.; Foden, J. *Mesoproterozoic Granites of South Australia*; Report Book, 2003/15; Department of Primary Industries and Resources, Government of South Australia: Adelaide, Australia, 2003.
6. Hou, B.; Fabris, A.J.; Michaelsen, B.H.; Katona, L.F.; Keeling, J.L.; Stoian, L.; Wilson, T.C.; Fairclough, M.C.; Cowley, W.M. Paleodrainage and Cenozoic coastal barriers of South Australia: A new map and GIS dataset. *MESA J.* **2012**, *66*, 26–32.
7. UraniumSA. Uranium Discovery; ASX Release 12 December 2007. Available online: https://www.asx.com.au/asxpdf/20071212/pdf/316fq84dlcgmsd.pdf (accessed on 19 February 2020).
8. Domnick, U.; Cook, N.J.; Bluck, R.; Brown, C.; Ciobanu, C.L. Petrography and geochemistry of granitoids from the Samphire Pluton, South Australia: Implications for uranium mineralisation in overlying sediments. *Lithos* **2018**, *300–301*, 1–19. [CrossRef]
9. Bluck, R.; Brown, C. Characterisation of the Samphire granite, Hiltaba Suite, northeastern Eyre Peninsula. *MESA J.* **2017**, *85*, 31–40.
10. Cuney, M. The extreme diversity of uranium deposits. *Mineral. Depos.* **2009**, *44*, 3–9. [CrossRef]
11. Bowles, J.F.W. Age dating of individual grains of uraninite in rocks from electron microprobe analyses. *Chem. Geol.* **1990**, *83*, 47–53. [CrossRef]
12. Bowles, J.F.W. Age Dating from Electron Microprobe Analyses of U, Th, and Pb: Geological Advantages and Analytical Difficulties. *Microsc. Microanal.* **2015**, *21* (Suppl. 5), 1114–1122. [CrossRef]
13. Domnick, U.; Cook, N.J.; Ciobanu, C.L.; Courtney-Davies, L.; Dmitrijeva, M.; Verdugo-Ihl, M.R.; Xu, J.; Kennedy, A.K.; Bluck, R. New geochronological constraints on the evolution of the Samphire pluton, South Australia. *Precambr. Res.* **2020**, in review.

14. Reid, A.; Jagodzinski, E.; Gerhard, F. Project PGC03–01: Geochronology from the Samphire Uranium Project. In *PACE Geochronology: Results of Collaborative Geochronology Projects 2013–2015*; Report Book 2015/00003; Jagodzinski, E.A., Reid, A.J., Eds.; Department of the Premier and Cabinet: Adelaide, Australia, 2017; pp. 10–28.
15. UraniumSA. Samphire Project Update; ASX Release 27 September 2013. Available online: https://www.asx.com.au/asxpdf/20130927/pdf/42jnqgsn2cqcgg.pdf (accessed on 19 February 2020).
16. Braun, J.-J.; Pagel, M.; Muller, J.-P.; Bilong, P.; Michard, A.; Guillet, B. Cerium anomalies in lateritic profiles. *Geochim. Cosmochim. Acta* **1990**, *54*, 781–795. [CrossRef]
17. Baes, C.F.; Mesmer, R.E. *The Hydrolysis of Cations*; Wiley: Hoboken, NJ, USA, 1976; p. 489.
18. Stoian, L.M. Palynological Analysis of Samples 53448, 2490100, and 2490112. South Australian Resources Information Gateway. 2009. Available online: http://minerals.sarig.sa.gov.au (accessed on 5 November 2019).
19. Curtis, S.; Wade, C. *Stratigraphy of the Lower Gawler Range Volcanics in the Roopena Area, North-Eastern Eyre Peninsula*; Report number: RB 2015/00021; Geological Survey of South Australia: Adelaide, Australia, 2016.
20. Deditius, A.P.; Utsunomiya, S.; Ewing, R.C. The chemical stability of coffinite, $USiO_4{\cdot}nH_2O$; 0 <n <2, associated with organic matter: A case study from Grants uranium region, New Mexico, USA. *Chem. Geol.* **2008**, *251*, 33–49.
21. Armstrong, J.T. Quantitative analysis of silicate and oxide minerals: Comparison of Monte Carlo, ZAF, and φ(ρz) procedures. In *Microbeam Analysis*; Newbury, D.E., Ed.; San Francisco Press: San Francisco, CA, USA, 1988; pp. 239–246.
22. Donovan, J.J.; Tingle, T.N. An Improved Mean Atomic Number Background Correction for Quantitative Microanalysis. *Microsc. Microanal.* **1996**, *1*, 1–7. [CrossRef]
23. Donovan, J.J.; Singer, J.W.; Armstrong, J.T. A new EPMA method for fast trace element analysis in simple matrices. *Am. Mineral.* **2016**, *101*, 1839–1853. [CrossRef]
24. Cross, A.; Jaireth, S.; Rapp, R.; Armstrong, R. Reconnaissance-style EPMA chemical U–Th–Pb dating of uraninite. *Aust. J. Earth Sci.* **2011**, *58*, 675–683. [CrossRef]
25. Macmillan, E.; Cook, N.J.; Ehrig, K.; Pring, A. Chemical and textural interpretation of late-stage coffinite and brannerite from the Olympic Dam IOCG-Ag-U deposit. *Mineral. Mag.* **2017**, *81*, 1323–1366. [CrossRef]
26. Macmillan, E.; Cook, N.J.; Ehrig, K.; Ciobanu, C.L.; Pring, A. Uraninite from the Olympic Dam IOCG-U-Ag deposit: Linking textural and compositional variation to temporal evolution. *Am. Mineral.* **2016**, *101*, 1295–1320. [CrossRef]
27. Syverson, D.D.; Etschmann, B.; Liu, W.; Ram, R.; Mei, Y.; Lanzirotti, T.; Mercadier, J.; Brugger, J. Oxidation state and coordination environment of Pb in U-bearing minerals. *Geochim. Cosmochim. Acta* **2019**, *265*, 109–131. [CrossRef]
28. Montel, J.M.; Foret, S.; Veschambre, M.; Nicollet, C.; Provost, A. Electron microprobe dating of monazite. *Chem. Geol.* **1996**, *131*, 37–53. [CrossRef]
29. Ning, W.; Wang, J.; Xiao, D.; Li, F.; Huang, B.; Fu, D. Electron Probe Microanalysis of Monazite and Its Applications to U–Th–Pb Dating of Geological Samples. *J. Earth Sci.* **2019**, *30*, 952–963. [CrossRef]
30. Sabau, G. Chemical U–Th–Pb geochronology: A precise explicit approximation of the age equation and associated errors. *Geochronometria* **2012**, *39*, 167–179. [CrossRef]
31. Ludwig, K.R. User's Manual for Isoplot 3.75. *Berkeley Geochronol. Cent. Spec. Publ.* **2012**, *5*, 75.
32. Douglas, G.B.; Butt, C.R.M.; Gray, D.J. Geology, geochemistry and mineralogy of the lignite-hosted Ambassador palaeochannel uranium and multi-element deposit, Gunbarrel Basin, Western Australia. *Mineral. Depos.* **2011**, *46*, 761–787. [CrossRef]
33. McAvaney, S.O.; Wade, C.E.; Krapf, C.B.E. *Geology of the CULTANA 1:100 000 Map Sheet (6432)*; Report Book 2014/00006; Department for Manufacturing, Innovation, Trade, Resources and Energy: Adelaide, Australia, 2014.
34. Wülser, P.-A. Uranium Metallogeny in the North Flinders Ranges Region of South Australia. Unpublished. Ph.D. Thesis, University of Adelaide, Adelaide, Australia, 2009.
35. Wülser, P.-A.; Brugger, J.; Foden, J.; Pfeifer, H.-R. The sandstone-hosted Beverley uranium deposit, Lake Frome Basin, South Australia: Mineralogy, geochemistry, and a time-constrained model for its genesis. *Econ. Geol.* **2011**, *106*, 835–867. [CrossRef]
36. Herold, N.; Huber, M.; Greenwood, D.R.; Müller, R.D.; Seton, M. Early to Middle Miocene monsoon climate in Australia. *Geology* **2011**, *39*, 3–6. [CrossRef]

37. King, D.; Woodmansee, W.C. Port Lincoln Uranium Exploration—Diamond drilling at the Hospital Prospect. In *Mining Review*; South Australia Department of Mines: Adelaide, Australia, 1956; Volume 101, pp. 32–41.
38. Hou, B.; Keeling, J.; Li, Z. Paleovalley-related uranium deposits in Australia and China: A review of geological and exploration models and methods. *Ore Geol. Rev.* **2017**, *88*, 201–234. [CrossRef]

CHAPTER 5

SUMMARY AND RECOMMENDATIONS

1 SUMMARY

The Blackbush deposit has been characterized with respect to the petrography, mineralogy and geochronology of bedrock granites and of the uranium mineralization at the unconformity and in the identified resource in overlying cover sequences. These data allow development of a holistic genetic model for the deposit, with broader application to comparable sequences elsewhere in the region and beyond. The mineralogical and compositional diversity recognized in both the granites and mineralization emphasize the need for a careful, systematic approach, and in the case of zircon geochronology, for micron-scale observations to be supplemented by characterization down to the atomic scale. The approach, involving systematic analysis of representative sample suites and backing up geochemical data with petrographic observation at an appropriate scale, as presented within this thesis, is necessary to unravel the mineralization history of the Blackbush deposit.

1.1 GRANITE CHARACTERIZATION

Research within this thesis (Domnick et al. 2018; in review) has provided additional constraints on bedrock geology, petrology, mineralogy and geochronology, and on uranium mineralization. The Samphire Pluton is multiphase and composed of three distinct intrusions, named A to C in order of fractionation. All granites show anomalously high U contents (10 – 81 ppm) relative to averages for Mesoproterozoic granites and similar patterns of alteration and metasomatism. Alkali feldspar has been replaced by patch perthite, plagioclase by albite + sericite ± Ca-silicates.

Granite C, the granite underlying the Blackbush deposit, is more strongly altered than the other two, and completely 'oxidised'. All Fe^{2+}-bearing minerals have been replaced, e.g., biotite by chlorite, or allanite by monazite or REE-fluorocarbonates. This increased alteration correlates with the increased abundance of fractures and crosscutting veins closer to the Blackbush deposit, hinting at a connection between the processes in the granite and the overlying U mineralization. The veins are highly variable in their mineralogy: quartz + hematite; hematite + coffinite; fluorite + quartz; clay-rich; or chlorite-dominated. The presence of coffinite in the veins and rarely within the granite, as well as the disturbed Th/U ratios in zircon from granite C, are interpreted as clear evidence for U mobility.

Age-dating of zircons from all three granites (U-Th, SHRIMP) yielded ages of around 1585 Ma within error of each other, showing the HIS affiliation of the three intrusions. A characterization of these zircons, down to the nanoscale, revealed hydrothermal overprinting

by U+Th+HREY-rich fluids, increasing in intensity closer to the deposit. The Th/U of zircon rims in granites A and B, and cores of zircons in granite C are similar, while the Th/U ratios of rims in granite C is greatly increased. Together with other micron- to nanoscale observations, this is convincing evidence for a later remobilization of U in the bedrock of the Blackbush deposit.

1.2 URANIUM MINERALIZATION IN COVER SEQUENCE

Investigation of uranium mineralization within saprolite and the cover sequence sedimentary rocks representing the Blackbush deposit (Domnick et al. 2020) showed that while the mineralization is diverse with respect to morphology and mineral association, it almost entirely consists of coffinite. The coffinite is hosted at the unconformity between the organic-rich Eocene Kanaka Beds and the underlying saprolite, in tabular to lenticular bodies in sand or lignite, as convex bodies of roll-front style downstream, concordant and discordant within the saprolite, and seems to extend slightly into the overlying organic-free Oligocene (?) sand. The coffinite is present as rims around framboidal pyrite, as coffinite-pyrite intergrowths, coffinite-clay intergrowths, as coatings on quartz grains, and along fractures and voids within quartz grains.

Chemical U-Pb dating of coffinite in the sediment, saprolite, and a vein in the granite yielded a weighted average age of 17.01 ± 0.16 Ma for the sediment-hosted coffinite. This tight age range is interpreted as evidence for a single coffinite forming event. The saprolite and vein coffinite revealed ages of 28 to 20 Ma, and 25 to 12 Ma, respectively. Likely deposited by the same event, their ages have a wider range and are shifted towards older ages due to smaller grain size of the coffinite and thus the increasing impact of contamination by other minerals, mainly Fe-sulphides, Pb-bearing phases within the sulphides, as well as oxides. Dating of uraninite the same granitic vein resulted in ages of 42 to 38 Ma, likely predating the Eocene Kanaka Beds.

The placement of the Blackbush deposit within 5 kilometres, likely less, of the (inferred) position of a major lithospheric boundary and palaeosuture, allows the connection of this deposit with small vein-hosted deposits associated with the Kalinjala Mylonite Zone, the southern extension of this lithospheric boundary. It is likely that the ~17 Ma age of the sediment coffinite is triggered by tectonic movement along this reactivated palaeosuture.

1.3 GENETIC MODEL

Although a distinct style of uranium mineralization in the context of South Australia, Blackbush can be considered as a hybrid deposit type formed by a combination of two different processes. The 17 Ma U event, likely associated with faults, could be called 'metamorphic', and U hosted at an unconformity resembles fault-controlled metamorphic U deposits (e.g., George 1985).

The stratabound bodies within sedimentary cover and the extensive leaching of U from the underlying granite is typical for 'normal' sediment-hosted U deposits, where U is leached and deposited by groundwater. Essential for the genesis of the Blackbush deposit and its size is likely the interplay and overlap of the two processes, even though the contribution of each remains unconstrained.

2 RECOMMENDATIONS

The research presented in this thesis could not satisfactorily answer all outstanding questions, whether as a result of inadequate sample material, the lack of dateable minerals, or data which is unequivocal, ambiguous, or potentially unintentionally biased.

2.1 FURTHER WORK ON BLACKBUSH AND REFINEMENT OF THE GENETIC MODEL

2.1.1 U mineralization

To date, research largely focused on 'visible' uranium, that is the minerals containing essential U and minerals with a significant substitution of major elements by U. It remains unclear how much U is actually adsorbed on organic matter or clay; especially in the saprolitic samples, which yielded less U minerals in the investigated sections which had been expected. As adsorption fixes U in its hexavalent state, likely as UO_2^{2+}, further research into this topic could have significant influence on the economic feasibility of in-situ leaching (ISL) of the deposit, which relies on the oxidation and thereby mobilization of U. A mismatch of geophysical data, e.g. gamma ray logs, and U minerals, as seen in the saprolite, could also be explained by the presence of radioactive elements other than U. Radium, physically separated from its parent U mineral, could be selectively enriched.

In general, U minerals in the Blackbush deposit almost certainly exhibit open system behavior, but its actual effect, mechanism, loss and gain of elements, and the location of lost elements are currently completely unknown.

The properties of the mineralizing fluid are unknown and an important aspect of further research. Investigation of different isotopic systems, e.g. O, H, or S, could reveal the source of the fluid. Analysis of S isotopes on (contemporaneous?) pyrite intergrown with coffinite would also greatly enhance the understanding of the fluid.

Considering the geological stability of the Blackbush deposit, and South Australia in general, a thorough investigation of the present-day conditions in the deposit would be highly insightful. It is likely that the groundwater properties remained relatively constant over the last ~20 Ma, so a complete picture of the groundwater could be used to assess the scale of remobilization of U in the sediment. Such a study could possibly reveal other fluids, circulating through the granite and/or along faults, which might not be identical with groundwater, noting the abundance of halite of unknown derivation in some polished samples. This would be an important step for the understanding of the Blackbush deposit.

2.1.2 Fluorite geochemistry/dating

Fluorite is an abundant mineral in the veins within granite and in fluorite flooded zones. An earlier study (Goldsmith 2014) showed the presence of two compositionally distinct types of fluorite characterized by different concentrations of trace elements in the veins.

Quantitative analysis of LA-ICP-MS has long been regarded as problematic owing to the tendency of fluorite to splinter irregularly under the laser. A new attempt to identify the optimal parameters for trace element analysis in fluorite (fluence, repetition rate, spot size) has allowed greater confidence in the resulting data (Zalensky 2019). The study has, however, also showed that crystallographic orientation relative to the laser beam is a critical, and largely uncontrollable, factor, in that, even at optimized LA-ICP-MS parameters, some analysis spots in a given sample ablate perfectly (generating high-quality data), whereas others do not.

Dating of fluorite in the veins and the fluorite flooded zones would greatly increase the understanding of the processes leading to the formation of the Blackbush deposit. Fluorite veins within Hiltaba granites, e.g., at Olympic Dam, have been ascribed to the Delemerian orogeny, which coincides with an additional input of U into the deposit.

2.1.3 Molybdenite dating

Molybdenite is a trace component of a single vein only found in drill hole MRM845. Additional geochronological constraints on the system may come from future Re-Os isotope dating of this mineral. We might assume this could provide an age for the vein - whether of Hiltaba age, or alternatively, related to a later event.

2.1.4 Ar-Ar isotopic mineral dating

UraniumSA interprets undisturbed magmatic REE patterns in the saprolite as indication for a partly non-weathering genesis of the clay-altered granite (Bluck and Brown 2017). Even though this could be explained by REE locked in refractory minerals, a thorough examination of the saprolite could yield interesting results. One important step would be the dating of clay minerals in the saprolite via Ar-Ar isotope methods. Even if the saprolite was formed solely by weathering, an approximate age for the clay minerals could potentially reveal phases of stronger and weaker weathering, result in an undulating age distribution, which would be an interesting window into the climate (and its change) during the genesis of the saprolite (as demonstrated in Mathian et al. 2019).

The mineralogy of veins in the granite is highly variable but almost always at least one K-bearing mineral is present, either (hydrothermal) K-feldspar, muscovite/illite, or biotite. Ar-Ar dating of these minerals would greatly enhance the understanding the absolute and relative timing of the different veins and their connection to the petrogenesis of the Samphire Pluton and overlying mineralization.

2.2 REGIONAL GEOLOGY

2.2.1 Crystalline basement and faults

The geology of north eastern Eyre Peninsula outside of the Blackbush deposit is poorly constrained. There is significant disagreement between the interpretations of UraniumSA and the data published by the Geological Survey of South Australia (GSSA), regarding the crystalline basement around the Samphire Pluton. Based on geophysical data the GSSA interprets the rock attached to the western side of the Samphire Pluton as Donington Suite Granite (~1.85 Ga). UraniumSA classifies this area as Warrow Quartzite (~2.0 Ga) (Bluck and Brown 2017; compare Chapter 1, Fig.1, based on data of the GSSA, with Chapter 3, Fig.1, based on UraniumSA's interpretation). Assimilation of crustal material is an important process in the petrogenesis of granites and a thorough understanding of the basement could help explain the differences between the three intrusions of the Samphire Pluton. In addition, UraniumSA identifies a possible metasedimentary carapace overlying some areas of the Samphire Pluton, likely older than the intruding HIS granite (Bluck and Brown 2017). If this could be confirmed, the presence of older overlying material would strongly indicate little to no erosion of the pluton. Considering a possible (pre-)concentration of U in the top of the pluton by late

magmatic fluids, as proposed in Domnick et al. (2018), a lack of erosion and thus preservation of this preconcentrated U could be essential for the genesis of the Blackbush deposit.

The exact location of the lithospheric boundary in the Blackbush area is unknown. The Kalinjala Mylonite Zone and the Roopena Fault are separated by a ~30 km-wide zone of splayed faults often associated with mylonite. A straight line between the northern end of Kalinjala Mylonite Zone and the Roopena Fault strikes roughly parallel to the arcuate domain of granite A of the Samphire Pluton, indicating a possibly fault-controlled intrusion placement. Further geophysical data, especially seismic lines across this area, could reveal the extent of fault systems in the basement and further strengthen the understanding of their connection to the Blackbush deposit.

2.2.2 Regional correlation of U mineralization

The ~17 Ma age of the sediment-hosted coffinite was interpreted as triggered by tectonic movement, which allows a correlation with smaller deposits on southern Eyre Peninsula (Domnick et al. 2020). These deposits are either vein hosted or disseminated in metamorphosed Donington Suite Granite, always close to the Kalinjala Mylonite Zone and often associated with sodic metasomatism (Wilson 2015). There is currently no geochronological data of any kind from these deposits. A thorough examination, including dating of U minerals and possibly other minerals, associated with the sodic metasomatism, would be an essential step to a more consolidated genetic model of the Blackbush deposit.

No sodic metasomatism was identified in the Blackbush deposit and the underlying non-clay-altered pluton. An internal report of UraniumSA mentions that the illite in the saprolite has predominantly Na and only minor K (brammallite), but it is currently unclear whether this carries any significance.

2.3 IMPLICATIONS FOR URANIUM MINERALIZATION ACROSS THE REGION

The three main factors for the genesis of the Blackbush deposit are the excellent host rock, including reductant and groundwater, a suitable source, high-U, and the fault systems. The faults greatly facilitate fluid access and thus leaching of U by fracturing the underlying HIS pluton, and they provide additional U associated with crustal scale faults. These conditions are not met anywhere else in the Gawler Craton outside of the northeastern Eyre Peninsula.

The HIS granites are not homogeneous and have significantly more U in the eastern Gawler Craton (Olympic Cu-Au province) (Stewart and Foden 2003). All HIS granites in contact with the Cainozoic sediments of the Eucla Basin are low-U. Uranium is still leached

from the granites and deposited in organic-rich sediments, but significant amounts are rarely reached. The largest (known) sediment-hosted deposit in the western Gawler Craton is the Warrior U deposit with less than 5, 000 tonnes U (Wilson 2015).

In the northern part of the Cu-Au province HIS granites are covered by hundreds of meters of younger sediments and likely unaffected by any kind of groundwater flow and metal redistribution, e.g., the Olympic Dam deposit does not extend into the overlying sediments. On the Yorke Peninsula, the eastern side of the Pirie Basin, Cainozoic sediments are less common. Locally, HIS granites are in contact with the Kanaka Beds, but they are very weakly mineralized at best. Likely because a fault system is missing that could facilitate fluid flow through the granite and focus the deposition in a certain area.

One small area remains as prospective for 'Blackbush-like' U mineralization, ~60 km south of the Blackbush deposit. The southern half of the Charleston HIS granite is overlain by Cainozoic sediments, as is a smaller, unnamed HIS-aged intrusion, ~20 km east of the Charleston granite. The Charleston granite marks the northern end of the Kalinjala Mylonite Zone and the placement of the intrusion is strongly controlled by this fault. All published geochemical data of the Charleston granite are from the northern part, where Nd isotopic data indicates strong assimilation of Archean basement of the western Gawler Craton (Creaser, 1989). The southern part of the intrusion is placed in the eastern Gawler Craton, and likely has a slightly different geochemistry, possibly with higher U, similar to the Samphire Pluton. The smaller intrusion east of the Charleston Granite might, however, be slightly too far away from the lithospheric boundary.

2.4 IMPLICATIONS FOR IOCG-STYLE MINERALIZATION

The region south of Whyalla lies at the western boundary of the Olympic Cu-Au Province and is currently considered highly prospective for IOCG-style mineralization (Wise, 2019). Such mineralization is demonstrated to have been generated by hydrothermal activity within a couple of million years following emplacement of Hiltaba Suite granitoids (as at Olympic Dam; Courtney-Davies et al., 2019a).

Only insignificant mineralization has been discovered to date at the top of, or west of the Spencer Gulf. Granite C has many of the characteristics of 'fertile' Hiltaba Suite granitoids associated with mineralization: intense albitization of feldspars; the sporadic presence of sulphides; abundant veining; and local brecciation. The strongly altered zircons documented in Chapter 3 are largely identical to those described by Courtney-Davies et al. (2019b) from the

Olympic Domain but, importantly, lack the Cl-bearing nanoprecipitates typical of fertile granites. This could be seen as persuasive evidence to support or refute the possibility of significant future discoveries of IOCG-style mineralization in this underexplored portion of the Olympic Cu-Au Province.

3 REFERENCES

Bluck, R., Brown, C., 2017. Characterisation of the Samphire granite, Hiltaba Suite, northeastern Eyre Peninsula. MESA Journal 85, 31-40.

Courtney-Davies, L., Ciobanu, C.L., Tapster, S.R., Cook, N.J., Ehrig, K.J., Crowley, J.L., Verdugo-Ihl, M.R., S.E., Wade, B.P., Condon, D.J., in review. Opening the Magmatic-Hydrothermal Window: High-Precision U-Pb Geochronology of the Mesoproterozoic Olympic Dam Cu-U-Au-Ag Deposit, South Australia. Economic Geology.

Courtney-Davies, L., Ciobanu, C.L., Verdugo-Ihl, M.R., Slattery, A., Cook, N.J., Dmitrijeva, M., Keyser, W., Wade, B.P., Domnick, U., Ehrig, K., Xu, J., Kontonikas-Charos, A., 2019. Zircon at the nanoscale records metasomatic processes leading to large magmatic-hydrothermal ore systems. Minerals 2019, 9, 364.

Creaser, R.A., 1989. The geology and petrology of Middle Proterozoic felsic magmatism of the Stuart Shelf, South Australia. PhD thesis, La Trobe University, Melbourne, unpublished.

Domnick, U, Cook, N.J., Bluck, R., Brown, C., Ciobanu, C.L., 2018. Petrography of granitoids from the Samphire Pluton, South Australia: implications for uranium mineralisation in overlying sediments. Lithos 300–301, 1–19.

Domnick, U., Cook, N.J., Ciobanu, C.L., Courtney-Davies, L., Dmitrijeva, M., Verdugo-Ihl, M.R., Xu, J., Keyser, W., Slattery, A., Kennedy, A.K., Bluck, R., in review. Micron- to nanoscale characterisation and U-Pb geochronology of zircon from granites of the samphire pluton, South Australia. Precambrian Research.

Domnick, U., Cook, N.J., Ciobanu, C.L., Wade, BP., Courtney-Davies, L., Bluck, R., 2020. A Mineralisation Age for the Sediment-Hosted Blackbush Uranium Prospect, North-Eastern Eyre Peninsula, South Australia. Minerals 10, 191; doi:10.3390/min10020191.

George, E., 1985. Les mineralisations uraniferes jurassiques liees spatialement a une discordance hercynienne. Petrographie, mineralogie, et geochimie des gisements du Rouergue (Aveyron, France). Geol. Geochim. Uranium 9, 219.

Goldsmith, S.D., 2014. The Samphire Project: A distal IOCG and evidence for Mesoarchean crust in the Gawler Craton. Honours thesis, The University of Adelaide, unpublished.

Mathian, M., Aufort, J., Braun, J., Riotte, J., Selo, M., Balan, E., Allard, T., 2019. Unraveling weathering episodes in Tertiary regoliths by kaolin-ite dating (Western Ghats, India). Gondwana Research 69, 89–105.

Stewart, K.P., Foden, J., 2003. Mesoproterozoic granites of South Australia. South Australia. Department of Primary Industries and Resources. Report Book 2003/15.

Wilson, T., 2015. Uranium and uranium mineral systems in South Australia, 3rd edition. Report Book 2015/00011, Geological Survey of South Australia, Mineral and Energy Resources Group.

Wise, T., 2019. Prospectivity modelling of the Olympic Cu–Au Province. MESA Journal 90 36-41.

Zalensky, V., 2019. Characterization of fluorite using laser ablation inductively coupled plasma mass spectrometry. Honours thesis, School of Chemical Engineering and Advanced Materials, The University of Adelaide, unpublished.

CHAPTER 6

SUPPLEMENTARY AND ADDITIONAL MATERIAL

SUPPLEMENTARY MATERIAL A

FOR CHAPTER 2 –PETROGRAPHY AND GEOCHEMISTRY OF GRANITOIDS FROM THE SAMPHIRE PLUTON, SOUTH AUSTRALIA: IMPLICATIONS FOR URANIUM MINERALISATION IN OVERLYING SEDIMENTS

ELECTRONIC APPENDIX A FOR CHAPTER 2

Methodology, analysed elements, and detection limits for whole-rock analyses by Genalysis-Intertek (Adelaide).

Element	Ag	Al	As	Ba	Be	Bi	C	Ca	Cd	Ce	Co	Cr	Cs	Cu	Dy	Er
Method	4AB/MS	FB6/OE	4AB/MS	FB6/MS	FB6/MS	4AB/MS	CSA	FB6/OE	4AB/MS	FB6/MS	4AB/MS	FB6/OE	FB6/MS	4AB/OE	FB6/MS	FB6/MS
	ppm	%	ppm	ppm	ppm	ppm	%	%	ppm	ppm	ppm	ppm	ppm	ppm	ppm	ppm
ldl	0.01	0.01	1	1	0.5	0.05	0.01	0.01	0.05	0.5	0.1	20	0.05	1	0.05	0.05
upl	500	50	2000	50000	20000	500	40	70	500	300000	2000	50000	10000	20000	50000	50000
Element	Eu	Fe	Ga	Gd	Ge	Hf	Ho	In	K	La	Li	Lu	Mg	Mn	Mo	Na
Method	FB6/MS	FB6/OE	FB6/MS	FB6/MS	4AB/MS	FB6/MS	FB6/MS	4AB/MS	FB6/OE	FB6/MS	4AB/MS	FB6/MS	FB6/OE	FB6/OE	FB6/MS	FB6/OE
Element	ppm	%	ppm	ppm	ppm	ppm	ppm	ppm	%	ppm	ppm	ppm	%	%	ppm	%
ldl	0.05	0.01	0.1	0.05	0.1	0.1	0.02	0.05	0.01	0.2	0.1	0.02	0.01	0.01	1	0.01
udl	50000	70	50000	50000	2000	50000	20000	2000	80	200000	1000	10000	60	75	10000	75
Element	Nb	Nd	Ni	P	Pb	Pr	Rb	Re	S	Sb	Sc	Se	Si	Sm	Sn	Sr
Method	FB6/MS	FB6/MS	4AB/OE	FB6/OE	4AB/OE	FB6/MS	FB6/MS	4AB/MS	CSA	FB6/MS	FB6/OE	4AB/MS	FB6/OE	FB6/MS	FB6/MS	FB6/MS
	ppm	ppm	ppm	%	ppm	ppm	ppm	ppm	%	ppm	ppm	ppm	%	ppm	ppm	ppm
ldl	0.1	0.1	1	0.01	5	0.05	0.1	0.05	0.01	0.5	2	1	0.01	0.05	1	0.5
upl	50000	200000	20000	40	10000	100000	50000	2000	50	10000	50000	2000	45	100000	50000	200000
Element	Ta	Tb	Te	Th	Ti	Tl	Tm	U3O8	V	W	Y	Yb	Zn	Zr	LOI-1000	
Method	FB6/MS	FB6/MS	4AB/MS	FB6/MS	FB6/OE	4AB/MS	FB6/MS	FB6/MS	FB6/OE	FB6/MS	FB6/MS	FB6/MS	4AB/OE	FB6/MS	LOI/GR	
	ppm	ppm	ppm	ppm	%	ppm	ppm	ppm	ppm	ppm	ppm	ppm	ppm	ppm	%	
ldl	0.1	0.02	0.1	0.05	0.005	0.02	0.05	0.5	10	1	0.5	0.05	1	1	0.01	
upl	50000	20000	2000	20000	60	500	10000	10000	50000	50000	500000	50000	20000	500000	100	

CSA	Induction Furnace Analysed by Infrared Spectrometry
4AB/MS	Multi-acid digest including Hydrofluoric, Nitric, Perchloric and Hydrochloric acids in Teflon Beakers. Analysed by Inductively Coupled Plasma Mass Spectrometry.
4AB/OE	Multi-acid digest including Hydrofluoric, Nitric, Perchloric and Hydrochloric acids in Teflon Beakers. Analysed by Inductively Coupled Plasma Optical (Atomic) Emission
FB6/MS	Lithium metaborate/tetraborate fusion Analysed by Inductively Coupled Plasma Mass Spectrometry.
FB6/OE	Lithium metaborate/tetraborate fusion Analysed by Inductively Coupled Plasma Optical (Atomic) Emission
LOI/GR	Loss on Ignition. Gravimetric Determination.
ldl / upl	Lower detection limit / Upper detection limit

ELECTRONIC APPENDIX B FOR CHAPTER 2

Electron Probe Microanalysis - standards, X-ray lines, count times and average minimum detection limits (mdl)

Element	Standard	X-ray line	Count time unknown/background	Average mdl (ppm)
Ca	Plagioclase	Ca Kα	15s / 10s	75
Mg	Almandine	Mg Kα	15s / 10s	100
Ti	Rutile	Ti Kα	15s / 10s	90
Si	Almandine	Si Kα	15s / 10s	180
Al	Almandine	Al Kα	15s / 10s	80
Fe	Almandine	Fe Kα	15s / 10s	200
Mn	Rhodonite	Mn Kα	15s / 10s	200
Cr	Cr_2O_3	Cr Kα	15s / 10s	180
Cl	Tugtupite	Cl Kα	15s / 10s	85
F	Apatite	F Kα	15s / 10s	500
K	Sanidine	K Kα	15s / 10s	70
P	Apatite	P Kα	15s / 10s	85
Na	Albite	Na Kα	15s / 10s	160
Sr	Celestite	Sr Lα	15s / 10s	230
Ba	Barite	Ba Lα	15s / 10s	250

ELECTRONIC APPENDIX C FOR CHAPTER 2

All multi-element LA-ICP-MS data was collected on a Resonetics M-50-LR 193-nm Excimer laser microprobe coupled to an Agilent 7900 Quadrupole ICP-MS (Adelaide Microscopy). Trace element spot analysis was carried out using variable spot size diameters of between 29 and 51 µm for all minerals. The laser system was operated at pulse rates of 10 Hz and power levels of 50% corresponding to laser energy output around 6-9 J/cm-2, giving an ablation rate of approximately 1.5µm/s-1. The following set of isotopes were monitored: ^{23}Na, ^{24}Mg, ^{27}Al, ^{29}Si, ^{31}P, ^{39}K, ^{43}Ca, ^{47}Ti, ^{55}Mn, ^{57}Fe, ^{65}Cu, ^{66}Zn, ^{85}Rb, ^{88}Sr ^{89}Y, ^{90}Zr, ^{93}Nb, ^{95}Mo, ^{118}Sn, ^{137}Ba, ^{139}La, ^{140}Ce, ^{141}Pr, ^{146}Nd, ^{147}Sm, ^{153}Eu, ^{157}Gd, ^{159}Tb, ^{163}Dy, ^{165}Ho, ^{166}Er, ^{169}Tm, ^{172}Yb, ^{175}Lu, ^{178}Hf, ^{181}Ta, ^{182}W, ^{206}Pb, ^{207}Pb, ^{208}Pb, ^{209}Bi, ^{232}Th, and ^{238}U. Dwell times of 0.01 seconds were used for all elements, except K, Si, P and Al, which used dwell times of 0.005 seconds, and Pb, which used a dwell time of 0.02 seconds. Average minimum detection limits are given in the table below. Analysis time for each spot analysis was a uniform 70 seconds, comprising a 30-second measurement of background (laser-off), and 40-second analysis of the unknown (laser-on). Standard reference materials for all mineral matrices were NIST-610 using coefficients given by Pearce et al. (1997). Standards were run after each 10-12 unknowns; detection limits were calculated for each element in each spot analysis. Internal calibration was achieved using ideal concentration values for Al for feldspars, Si for titanite, and prehnite, as well as Ca for garnet, and fluorite. Data reduction was performed using Iolite software (Paton et al., 2011).

Minimum detection limits (ppm)					
Na	12	La	0.002	Hf	0.007
Mg	1	Ce	0.003	Ta	0.002
Si	327	Pr	0.002	W	0.01
P	23	Nd	0.01	^{206}Pb	0.04
K	5.4	Sm	0.01	^{207}Pb	0.03
Ca	307	Eu	0.007	^{208}Pb	0.03
Ti	1	Gd	0.02	Bi	0.03
Mn	0.68	Tb	0.003	Th	0.003
Fe	14	Dy	0.01	U	0.003
Cu	0.56	Y	0.01	Zr	0.013
Zn	0.86	Ho	0.002	Nb	0.004
Rb	0.31	Er	0.007	Sn	0.47
Sr	0.02	Tm	0.002	Ba	0.04
		Yb	0.008		
		Lu	0.002		

References:

Paton, C., Hellstrom, J., Paul, B., Woodhead, J., Hergt, J., 2011. Iolite: Freeware for the visualisation and processing of mass spectrometric data. Journal of Analytical Atomic Spectrometry 26, 2508-2518.

Pearce, N.J., Perkins, W.T., Westgate, J.A., Gorton, M.P., Jackson, S.E., Neal, C.R., Chenery, S.P., 1997. A compilation of new and published major and trace element data for NIST SRM 610 and NIST SRM 612 glass reference materials. Geostandards and Geoanalytical Research 21,115-144

ELECTRONIC APPENDIX D FOR CHAPTER 2

Whole-rock geochemical analysis of all granites; oxides, totals, LOI, C and S in wt.%; trace elements in ppm. Bi, Cd, Ag, Te, Re, In, and Sb are always below detection limit

Sample	SiO_2	TiO_2	Al_2O_3	FeO	MnO	MgO	CaO	K_2O	Na_2O	P_2O_5	Total	LOI-1000	Total + LOI
Granite B (Average)	75.86	0.11	11.76	1.60	0.01	0.12	0.80	5.91	2.59	0.00	98.77	0.84	99.61
MRC005-1	76.27	0.12	11.77	1.54	0.01	0.13	0.81	5.88	2.57	0.00	99.11	0.75	99.86
MRC005-2	75.45	0.10	11.75	1.65	0.01	0.12	0.80	5.95	2.60	0.00	98.43	0.92	99.35
Granite A (Average)	70.95	0.51	12.74	3.31	0.06	0.62	1.35	5.67	2.68	0.00	97.90	1.23	99.13
MRC007-1	71.88	0.50	13.00	3.16	0.05	0.63	1.44	5.89	2.68	0.00	99.25	0.94	100.19
MRC007-2	70.66	0.55	12.81	3.36	0.05	0.63	1.20	5.57	2.74	0.00	97.57	1.19	98.76
MRC007-4	70.30	0.48	12.41	3.42	0.08	0.61	1.40	5.55	2.63	0.00	96.88	1.55	98.43
Aplite (Average)	74.19	0.05	12.79	1.16	0.00	0.06	0.37	6.76	2.77	0.00	98.16	0.83	98.98
MRC009-1	74.90	0.03	12.81	1.09	0.00	0.05	0.17	6.69	2.72	0.00	98.46	0.96	99.42
873-3	73.49	0.07	12.77	1.24	0.00	0.07	0.57	6.83	2.82	0.00	97.85	0.69	98.54
Metasomatite (Average)	75.02	0.06	12.77	1.41	0.00	0.08	0.70	5.28	3.72	0.00	99.04	0.75	99.78
751-2	75.24	0.08	12.77	1.83	0.00	0.10	0.41	4.96	3.88	0.00	99.27	0.78	100.05
762-2A	74.64	0.06	12.64	1.36	0.00	0.08	0.98	4.52	4.00	0.00	98.28	0.79	99.07
762-2B	75.18	0.04	12.91	1.03	0.00	0.05	0.71	6.36	3.28	0.00	99.55	0.67	100.22
Granite C (Average)	74.69	0.15	12.25	2.02	0.01	0.27	0.38	6.21	2.47	0.00	98.46	1.23	99.69
MRC009-2	74.81	0.20	12.75	2.17	0.00	0.22	0.38	5.85	3.02	0.00	99.40	0.95	100.35
751-1	74.13	0.16	12.43	1.87	0.00	0.18	0.46	6.38	2.74	0.00	98.35	1.05	99.40
762-1	75.45	0.15	11.17	3.32	0.00	0.30	0.25	7.48	0.80	0.00	98.91	1.19	100.10
762-4	74.15	0.16	12.13	2.25	0.01	0.23	0.34	6.73	2.22	0.00	98.23	1.40	99.63
762-5	75.52	0.10	10.32	2.87	0.00	0.50	0.13	6.18	0.89	0.00	96.50	2.72	99.22
843-1	73.94	0.15	12.13	2.16	0.01	0.22	0.52	5.66	2.91	0.00	97.69	0.89	98.58
845-1	74.34	0.15	12.81	1.69	0.01	0.22	0.63	6.05	3.06	0.00	98.95	0.83	99.78
845-2	74.60	0.16	12.45	1.74	0.01	0.61	0.13	6.54	1.68	0.00	97.92	2.13	100.05
845-4	74.62	0.12	12.55	1.79	0.01	0.35	0.42	6.31	2.82	0.00	98.99	1.27	100.26
873-1	74.32	0.16	12.51	1.81	0.01	0.25	0.77	5.67	3.06	0.00	98.56	0.87	99.43
873-2	75.30	0.14	12.56	1.38	0.00	0.17	0.15	5.96	3.11	0.02	98.80	0.93	99.73
873-4	74.51	0.16	12.62	1.65	0.04	0.27	0.62	5.81	3.07	0.04	98.77	0.80	99.57
873-5	74.62	0.14	12.89	1.88	0.00	0.15	0.10	6.37	2.40	0.00	98.54	1.33	99.87
893-3	75.39	0.14	12.24	1.69	0.01	0.18	0.46	5.91	2.80	0.00	98.83	0.80	99.63

Lower detection limit	0.01	0.01	0.05	0.5	1	0.1	5	1	1	1	1	0.1	0.1
Sample	C (%)	S (%)	Th	U3O8	Zr	Hf	Pb	Zn	Cu	W	Sn	Nb	Ta
Granite B (Average)	0		75	28	116	4	18	7	3	2	3	17	2
MRC005-1	0	<0.01	78	29	117	4	21	6	4	2	1	18	2
MRC005-2	0	<0.01	72	27	115	4	14	7	2	2	5	17	3
Granite A (Average)	0	0	46	13	316	9	29	25	6	2	5	22	2
MRC007-1	0	0	45	12	308	9	27	30	5	2	5	22	2
MRC007-2	0	0	26	13	335	9	18	20	8	2	6	24	2
MRC007-4	0	0	65	14	305	8	41	26	6	3	3	20	2
Aplite (Average)	0		17	23	50	3	21		4	3	1	50	7
MRC009-1	0	<0.01	22	20	82	5	9	<1	4	4	1	61	11
873-3	0	<0.01	12	26	18	1	33	<1	4	2	1	39	4
Metasomatite (Aver.)	0		27	51	26	2	12		4	5	3	109	9
751-2	0	<0.01	27	35	18	1	8	<1	5	6	4	110	8
762-2A	<0.01	<0.01	34	77	35	3	12	<1	4	4	3	146	13
762-2B	<0.01	<0.01	21	39	25	2	15	<1	2	4	3	71	6
Granite C (Average)	0	0	76	37	143	5	13	4	60	5	3	48	6
MRC009-2	0	0	83	8	170	6	7	3	6	5	2	44	5
751-1	0	<0.01	82	15	160	6	9	1	5	8	3	52	6
762-1	0	<0.01	76	13	140	5	11	8	2	12	3	46	6
762-4	0	0	80	45	145	6	14	3	35	9	16	52	7
762-5	0	<0.01	63	47	99	3	14	8	711	9	2	44	4
843-1	0	<0.01	77	24	153	6	10	4	3	4	2	50	7
845-1	0	0	78	73	148	6	21	1	8	3	2	45	6
845-2	0	0	84	29	152	5	7	5	41	3	2	54	6
845-4	0	0	64	96	129	5	7	3	9	3	2	42	5
873-1	0	<0.01	85	66	147	5	29	2	5	2	2	45	7
873-2	0	<0.01	66	8	128	5	10	6	7	3	2	49	7
873-4	0	<0.01	82	59	157	6	18	2	6	3	2	52	7
873-5	0	0	69	20	134	5	7	4	4	3	2	46	6
893-3	<0.01	<0.01	76	19	141	5	15	5	2	4	2	46	6

Lower detection limit	1	0.1	0.5	0.1	20	10	1	1	0.5	0.05	0.1	0.1	0.1	1	2	1	0.02
Sample	Ba	Rb	Sr	Co	Cr	V	Ni	As	Be	Cs	Ga	Ge	Li	Mo	Sc	Se	Tl
Granite B (Average)	180	430	39	1	20		1		4	4	17	0	13	2	3		1
MRC005-1	186	417	40	1	<20	<10	<1	<1	5	3	17	0	14	1	<2	<1	1
MRC005-2	174	442	38	1	20	<10	1	<1	4	4	17	0	13	2	3	<1	1
Granite A (Average)	923	301	123	5		20	2		3	4	18	1	16	1	8	2	1
MRC007-1	970	316	136	5	<20	24	2	<1	3	4	18	1	18	1	8	2	1
MRC007-2	914	295	125	5	<20	26	<1	<1	3	4	18	1	15	2	9	1	1
MRC007-4	885	292	110	5	<20	10	1	<1	3	3	17	1	15	1	7	2	1
Aplite (Average)	51	694	15	1	20		1		5	3	22	1	5				2
MRC009-1	67	637	14	1	<20	<10	1	<1	5	3	23	1	4	<1	<2	<1	2
873-3	35	752	16	1	20	<10	<1	<1	6	4	20	0	5	<1	<2	<1	2
Metasomatite (Aver.)	34	645	9	1	28			1	8	6	23	0	3	1	2	2	2
751-2	50	579	8	1	<20	<10	<1	<1	6	3	22	0	3	1	2	2	2
762-2A	23	556	10	1	<20	<10	<1	1	10	6	23	1	3	<1	2	2	2
762-2B	28	799	10	1	28	<10	<1	<1	7	9	22	1	3	<1	<2	1	2
Granite C (Average)	141	638	19	2	21	21	2	4	7	6	20	0	8	8	3	2	2
MRC009-2	209	600	38	2	<20	<10	<1	<1	8	5	21	1	8	<1	4	1	2
751-1	144	680	18	2	<20	20	2	<1	5	4	20	1	5	<1	4	1	2
762-1	227	746	12	1	<20	<10	1	<1	5	18	18	0	10	<1	3	<1	3
762-4	129	697	13	4	<20	22	2	<1	8	8	20	1	7	10	3	<1	3
762-5	150	472	17	2	<20	21	2	3	9	6	15	1	12	<1	3	6	2
843-1	115	622	22	2	<20	<10	1	6	7	5	20	0	4	<1	4	3	2
845-1	121	637	22	2	<20	<10	<1	<1	7	4	20	0	4	7	3	1	2
845-2	144	631	15	3	<20	<10	<1	<1	11	3	20	0	11	<1	3	2	2
845-4	122	622	15	3	21	<10	<1	<1	7	2	19	0	7	14	3	2	2
873-1	109	614	26	2	<20	<10	<1	<1	7	4	20	1	11	1	3	2	2
873-2	119	642	19	1	21	<10	<1	3	8	5	20	0	6	<1	3	1	2
873-4	137	645	27	2	<20	<10	<1	<1	7	5	20	1	9	<1	3	1	2
873-5	128	700	14	2	<20	<10	<1	<1	7	4	20	0	6	<1	3	<1	2
893-3	121	620	15	2	<20	<10	1	<1	8	5	19	0	4	<1	2	1	2

Lower detection limit	0.2	0.5	0.05	0.1	0.05	0.05	0.05	0.02	0.05	0.5	0.02	0.05	0.05	0.05	0.02
Sample	La	Ce	Pr	Nd	Sm	Eu	Gd	Tb	Dy	Y	Ho	Er	Tm	Yb	Lu
Granite B (Average)	76	131	13	36	5	1	3	1	3	20	1	2	0	3	0
MRC005-1	78	135	13	36	5	1	3	1	3	21	1	2	0	3	0
MRC005-2	73	127	13	35	5	1	3	1	3	20	1	2	0	3	0
Granite A (Average)	102	189	21	69	12	2	10	1	9	47	2	5	1	5	1
MRC007-1	97	180	20	67	12	2	10	2	9	51	2	5	1	5	1
MRC007-2	64	128	15	56	10	2	9	1	8	42	2	5	1	5	1
MRC007-4	146	259	27	84	13	2	11	2	9	48	2	5	1	5	1
Aplite (Average)	9	18	2	6	2	0	2	0	4	29	1	3	1	5	1
MRC009-1	8	19	1	5	2	0	3	1	5	38	1	4	1	8	1
873-3	10	18	2	6	2	0	2	0	2	20	1	2	0	3	0
Metasomatite (Aver.)	13	26	3	13	5	0	5	1	8	40	2	6	1	8	1
751-2	23	45	5	18	5	0	6	1	9	32	2	5	1	7	1
762-2A	9	19	3	11	5	0	6	1	9	50	2	7	1	10	2
762-2B	8	16	2	9	4	0	4	1	6	38	1	5	1	7	1
Granite C (Average)	85	162	15	43	8	1	7	1	9	72	2	7	1	9	1
MRC009-2	95	148	16	48	8	1	6	1	7	45	1	5	1	6	1
751-1	93	169	17	50	8	1	7	1	7	45	1	5	1	8	1
762-1	69	124	12	35	6	0	5	1	6	47	1	5	1	7	1
762-4	79	135	13	37	6	1	5	1	5	44	1	4	1	6	1
762-5	189	538	33	106	21	2	27	6	41	417	11	37	6	36	6
843-1	74	135	14	42	8	1	6	1	7	40	1	4	1	6	1
845-1	82	145	14	41	7	0	6	1	6	48	1	5	1	7	1
845-2	87	146	15	45	8	1	7	1	7	54	2	6	1	8	1
845-4	78	134	13	37	6	0	5	1	6	45	1	4	1	6	1
873-1	79	142	14	42	8	0	6	1	8	55	2	5	1	8	1
873-2	58	60	11	31	5	0	5	1	6	43	1	5	1	7	1
873-4	90	155	14	39	6	0	5	1	5	42	1	4	1	7	1
873-5	36	94	7	20	4	0	4	1	5	44	1	5	1	7	1
893-3	78	137	13	37	6	0	5	1	6	46	2	5	1	7	1

ELECTRONIC APPENDIX E FOR CHAPTER 2

Selected elements normalised vs. the average values of the upper continental crust (Rudnick and Gao, 2004), Roxby Downs Granite data provided by Kontonikas-Charos (unpublished)

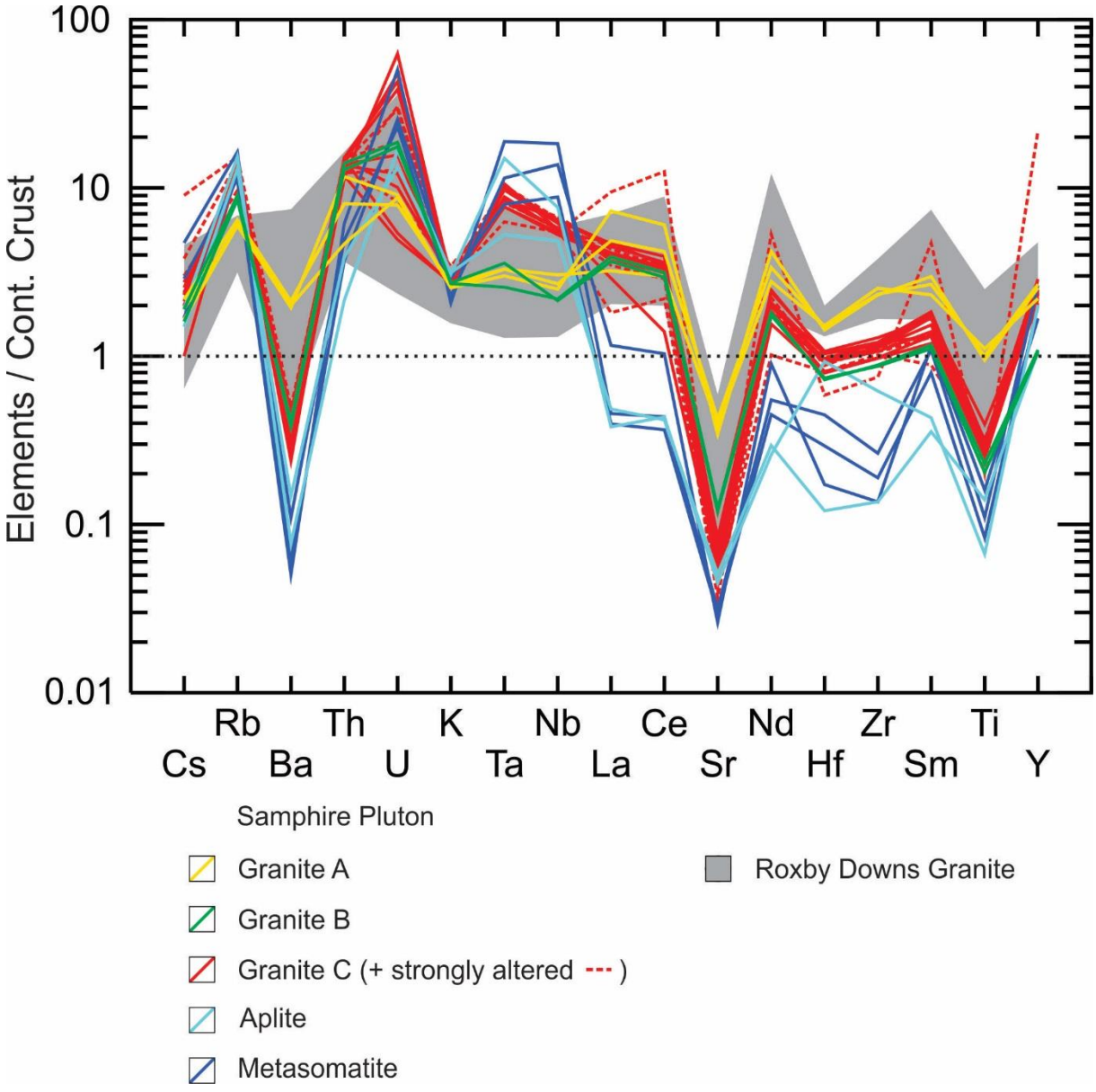

SUPPLEMENTARY MATERIAL B

FOR CHAPTER 3 –MICRON- TO NANOSCALE CHARACTERISATION AND U-PB GEOCHRONOLOGY OF ZIRCON FROM GRANITES OF THE SAMPHIRE PLUTON, SOUTH AUSTRALIA

ELECTRONIC APPENDIX A FOR CHAPTER 3

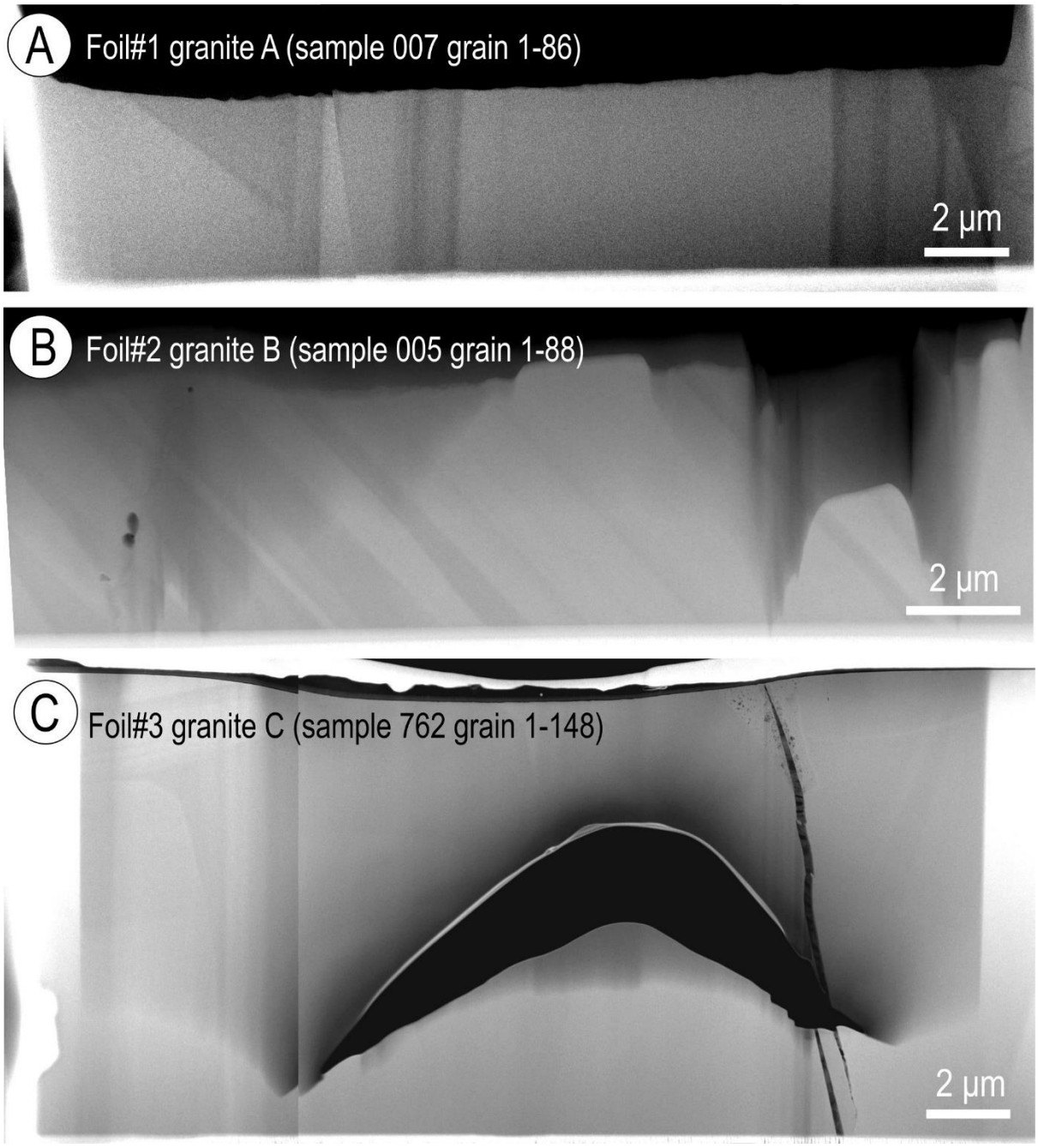

HAADF STEM images showing the three zircon foils studied. Note the sub-micron-scale oscillatory zoning on (B). Only parts of the foils show zoning in (A) and (C).

ELECTRONIC APPENDIX B FOR CHAPTER 3 – TABLE A1 EPMA

Appendix Table A1. Complete EPMA dataset and calculated formulae

	Sample/analysis	Na_2O	MgO	Al_2O_3	SiO_2	P_2O_5	K_2O	CaO	Sc_2O_3	TiO_2	MnO	Fe_2O_3	Y_2O_3	ZrO_2	Nb_2O_5	Ce_2O_3	Pr_2O_3	Nd_2O_3	Sm_2O_3	Eu_2O_3	Gd_2O_3	Tb_2O_3	Dy_2O_3	Ho_2O_3	Er_2O_3	Tm_2O_3	Yb_2O_3	Lu_2O_3	HfO_2	PbO	ThO_2	UO_2	F	Cl	Sum	H_2O (calc.)	-F=O	-Cl=O	Sum^A	Na
Type	Average mdl	0.023	0.007	0.006	0.022	0.01	0.005	0.009	0.012	0.004	0.011	0.024	0.008	0.049	0.017	0.009	0.044	0.041	0.043	0.023	0.046	0.024	0.025	0.05	0.027	0.027	0.028	0.029	0.096	0.014	0.01	0.011	0.055	0.007							**Formulae calculation**
Bright	762_148_bright1	<mdl	0.01	<mdl	32.95	0.33	<mdl	<mdl	<mdl	0.01	<mdl	0.04	0.28	65.16	<mdl	<mdl	<mdl	0.05	<mdl	<mdl	<mdl	0.03	0.05	*0.02*	0.08	*0.01*	0.09	*0.02*	1.34	0.03	0.02	0.05	<mdl	<mdl	100.56	0.00	0.00	0.00	100.56	0.000
Bright	762_148_bright2	<mdl	0.02	0.17	32.21	0.23	0.02	0.21	<mdl	0.04	0.02	1.28	0.29	61.97	<mdl	0.02	<mdl	<mdl	<mdl	<mdl	0.05	*0.01*	0.06	*0.02*	0.08	*0.01*	0.08	*0.01*	1.33	0.03	<mdl	0.07	0.06	0.02	98.30	0.01	0.03	0.00	98.28	0.000
Bright	762 148 bright 4	<mdl	<mdl	<mdl	31.90	0.20	<mdl	0.06	<mdl	0.01	<mdl	0.03	0.11	64.46	<mdl	<mdl	<mdl	0.05	0.05	<mdl	<mdl	<mdl	0.03	*0.01*	0.06	*0.01*	0.08	*0.01*	1.44	<mdl	<mdl	0.02	<mdl	<mdl	98.53	0.03	0.00	0.00	98.56	0.000
	mean (n=3)	<mdl	0.02	<mdl	32.35	0.26	<mdl	0.14	<mdl	0.02	<mdl	0.45	0.23	63.86	<mdl	<mdl	<mdl	0.05	<mdl	<mdl	<mdl	0.02	0.05	0.02	0.07	0.01	0.08	0.01	1.37	0.03	<mdl	0.04	<mdl	<mdl	99.13	0.01	0.01	0.00	99.13	0.000
Dark	762_148_dark1	<mdl	0.01	<mdl	33.19	0.16	<mdl	0.02	<mdl	<mdl	<mdl	0.03	0.15	65.08	<mdl	<mdl	<mdl	<mdl	0.05	<mdl	0.07	0.04	0.04	0.05	0.06	*0.01*	0.05	*0.01*	1.24	0.02	<mdl	0.02	<mdl	<mdl	100.29	0.01	0.00	0.00	100.30	0.000
Dark	762_148_dark2	0.03	0.01	<mdl	31.72	0.29	<mdl	0.08	<mdl	0.01	<mdl	0.14	0.66	63.16	<mdl	<mdl	<mdl	<mdl	<mdl	<mdl	0.09	*0.01*	0.08	*0.03*	0.14	0.05	0.15	0.03	1.20	0.04	0.06	0.14	<mdl	0.01	98.12	0.05	0.00	0.00	98.17	0.002
Dark	762_148_dark3	<mdl	<mdl	<mdl	32.36	0.25	<mdl	0.01	<mdl	0.01	<mdl	0.04	0.24	64.52	<mdl	<mdl	<mdl	<mdl	<mdl	<mdl	<mdl	0.06	*0.01*	0.04	*0.02*	0.08	*0.01*	0.07	*0.01*	1.23	0.02	<mdl	0.03	<mdl	<mdl	98.99	0.00	0.00	0.00	99.00	0.000
	mean (n=3)	<mdl	0.01	<mdl	32.42	0.23	<mdl	0.04	<mdl	0.01	<mdl	0.07	0.35	64.25	<mdl	<mdl	<mdl	<mdl	<mdl	<mdl	0.07	0.02	0.06	0.03	0.09	0.02	0.09	0.02	1.22	0.02	<mdl	0.07	<mdl	<mdl	99.13	0.02	0.00	0.00	99.15	0.001
Bright	762_171_bright1	<mdl	0.01	<mdl	32.95	0.11	<mdl	<mdl	<mdl	0.01	<mdl	<mdl	0.08	64.95	<mdl	<mdl	<mdl	<mdl	<mdl	<mdl	<mdl	<mdl	<mdl	<mdl	0.06	*0.01*	0.06	*0.01*	1.39	0.02	0.02	0.03	<mdl	<mdl	99.70	0.00	0.00	0.00	99.70	0.000
Bright	762_171_bright2	<mdl	0.01	<mdl	32.77	0.11	<mdl	<mdl	<mdl	0.01	<mdl	<mdl	0.07	64.99	<mdl	<mdl	<mdl	<mdl	<mdl	<mdl	<mdl	<mdl	<mdl	<mdl	0.05	<mdl	<mdl	<mdl	1.34	0.02	0.03	0.02	<mdl	<mdl	99.41	0.00	0.00	0.00	99.41	0.000
	mean (n=2)	<mdl	0.01	<mdl	32.86	0.11	<mdl	<mdl	<mdl	0.01	<mdl	<mdl	0.08	64.97	<mdl	<mdl	<mdl	<mdl	<mdl	<mdl	<mdl	<mdl	<mdl	<mdl	0.05	<mdl	<mdl	<mdl	1.36	0.02	0.02	0.03	<mdl	<mdl	99.56	0.00	0.00	0.00	99.56	0.000
Dark	762_171_dark1	<mdl	0.01	<mdl	32.70	0.09	<mdl	<mdl	<mdl	0.01	0.02	<mdl	0.05	65.11	<mdl	<mdl	<mdl	0.04	<mdl	0.03	0.05	*0.01*	0.03	0.07	0.06	*0.01*	0.04	*0.01*	1.15	0.01	0.01	0.02	<mdl	<mdl	99.51	0.01	0.00	0.00	99.53	0.000
Dark	762_171_dark2	<mdl	0.01	<mdl	33.35	0.10	<mdl	<mdl	<mdl	0.01	<mdl	<mdl	0.05	64.71	<mdl	<mdl	<mdl	<mdl	<mdl	<mdl	<mdl	<mdl	0.04	*0.01*	0.03	<mdl	<mdl	<mdl	1.19	<mdl	<mdl	0.01	<mdl	<mdl	99.52	0.00	0.00	0.00	99.52	0.000
Dark	762_171_darkest1	<mdl	0.13	0.47	28.70	0.28	0.01	1.08	0.11	0.06	0.05	1.02	1.92	56.77	0.35	0.04	<mdl	<mdl	0.07	<mdl	0.20	0.08	0.32	*0.09*	0.33	0.05	0.56	0.10	2.76	0.03	0.64	0.21	0.64	0.02	97.04	1.93	0.27	0.00	98.69	0.000
	mean (n=3)	<mdl	0.05	<mdl	31.58	0.15	<mdl	<mdl	<mdl	0.03	0.03	<mdl	0.67	62.20	<mdl	<mdl	<mdl	<mdl	<mdl	<mdl	0.12	0.04	0.13	0.06	0.14	0.03	0.30	0.05	1.70	0.02	0.32	0.08	<mdl	<mdl	98.69	0.65	0.09	0.00	99.25	0.000
Bright	005 088 bright 1	<mdl	0.01	<mdl	32.44	0.12	<mdl	0.03	<mdl	0.01	<mdl	<mdl	0.20	64.97	<mdl	<mdl	<mdl	<mdl	<mdl	<mdl	0.06	*0.01*	0.06	*0.02*	0.08	*0.01*	0.05	*0.01*	1.22	0.02	0.02	0.03	<mdl	<mdl	99.34	0.02	0.00	0.00	99.36	0.000
Bright	005 088 bright 2	<mdl	0.01	<mdl	32.57	0.13	0.01	0.02	<mdl	0.01	<mdl	0.03	0.19	64.61	<mdl	<mdl	<mdl	<mdl	<mdl	<mdl	<mdl	<mdl	0.04	*0.01*	0.05	*0.01*	0.03	*0.00*	1.14	0.03	0.02	0.02	<mdl	<mdl	98.92	0.01	0.00	0.00	98.93	0.000
Bright	005 088 bright 3	<mdl	0.01	<mdl	32.68	0.10	<mdl	0.02	<mdl	0.01	<mdl	0.07	64.62	<mdl	<mdl	<mdl	<mdl	<mdl	<mdl	<mdl	0.06	0.03	0.04	*0.01*	0.06	*0.01*	0.04	*0.00*	1.29	0.03	<mdl	0.03	<mdl	<mdl	99.09	0.01	0.00	0.00	99.09	0.000
Bright	005 088 bright 4	<mdl	<mdl	<mdl	33.45	0.13	<mdl	0.04	<mdl	0.01	<mdl	0.03	0.18	65.50	<mdl	<mdl	0.05	<mdl	<mdl	<mdl	0.08	0.04	0.05	*0.02*	0.07	0.04	0.08	<mdl	1.18	0.04	0.02	0.01	<mdl	<mdl	101.00	0.02	0.00	0.00	101.02	0.000
Bright	005 088 bright 5	0.03	0.02	<mdl	32.60	0.10	<mdl	0.02	<mdl	0.01	<mdl	<mdl	0.07	65.61	<mdl	<mdl	<mdl	<mdl	<mdl	<mdl	0.05	*0.01*	0.03	*0.01*	0.04	*0.01*	0.03	*0.00*	1.29	0.02	0.02	0.03	<mdl	<mdl	99.98	0.00	0.00	0.00	99.98	0.002
	mean (n=5)	<mdl	0.01	<mdl	32.75	0.12	<mdl	0.02	<mdl	0.01	<mdl	<mdl	0.14	65.06	<mdl	<mdl	<mdl	<mdl	<mdl	<mdl	0.06	0.02	0.04	0.01	0.06	0.01	0.05	0.00	1.22	0.03	0.02	0.02	<mdl	<mdl	99.66	0.01	0.00	0.00	99.68	0.000
Dark	005 088 dark 1	<mdl	0.01	0.01	32.48	0.11	<mdl	0.02	<mdl	0.01	<mdl	<mdl	0.05	64.91	<mdl	<mdl	<mdl	<mdl	<mdl	<mdl	<mdl	0.04	0.04	*0.01*	0.06	0.03	0.05	<mdl	1.20	0.02	<mdl	<mdl	<mdl	<mdl	99.04	0.00	0.00	0.00	99.05	0.000
Dark	005 088 dark 2	<mdl	0.01	<mdl	32.54	0.09	<mdl	0.02	<mdl	0.01	<mdl	0.03	0.04	65.02	<mdl	<mdl	<mdl	0.05	<mdl	<mdl	0.06	*0.01*	0.03	0.05	0.07	0.03	0.04	0.03	1.27	0.02	<mdl	<mdl	<mdl	<mdl	99.41	0.01	0.00	0.00	99.42	0.000
Dark	005 088 dark 3	0.04	0.02	0.01	33.76	0.10	0.01	0.04	<mdl	0.01	<mdl	0.03	0.08	63.11	<mdl	<mdl	<mdl	<mdl	<mdl	<mdl	<mdl	<mdl	<mdl	<mdl	0.05	*0.01*	0.03	*0.00*	1.16	0.02	<mdl	<mdl	<mdl	<mdl	98.46	0.00	0.00	0.00	98.46	0.002
Dark	005 088 dark 4	<mdl	0.01	<mdl	32.30	0.08	0.01	0.02	<mdl	0.01	<mdl	<mdl	0.03	64.96	<mdl	<mdl	<mdl	<mdl	<mdl	<mdl	<mdl	<mdl	0.03	*0.01*	0.04	<mdl	<mdl	<mdl	1.29	<mdl	<mdl	<mdl	<mdl	<mdl	98.78	0.00	0.00	0.00	98.78	0.000
Dark	005 088 dark 5	<mdl	0.01	<mdl	33.21	0.09	0.01	0.02	<mdl	0.01	<mdl	<mdl	0.06	65.07	<mdl	<mdl	<mdl	<mdl	<mdl	<mdl	<mdl	<mdl	0.03	*0.01*	0.06	<mdl	<mdl	<mdl	1.23	0.02	<mdl	0.02	0.06	<mdl	99.90	0.00	0.03	0.00	99.87	0.000
	mean (n=5)	<mdl	0.01	<mdl	32.86	0.09	0.01	0.02	<mdl	0.01	<mdl	<mdl	0.05	64.61	<mdl	<mdl	<mdl	<mdl	<mdl	<mdl	<mdl	<mdl	0.03	0.02	0.06	0.02	0.04	<mdl	1.23	0.02	<mdl	<mdl	<mdl	<mdl	99.12	0.00	0.01	0.00	99.11	0.000
Bright	007 086 bright 1	<mdl	<mdl	<mdl	33.10	0.09	<mdl	0.02	<mdl	0.01	<mdl	<mdl	0.04	65.88	0.02	<mdl	<mdl	<mdl	<mdl	<mdl	0.06	<mdl	<mdl	<mdl	0.04	<mdl	<mdl	<mdl	1.24	0.03	<mdl	0.02	<mdl	<mdl	100.57	0.00	0.00	0.00	100.57	0.000
Bright	007 086 bright 2	<mdl	<mdl	<mdl	33.46	0.12	<mdl	0.03	<mdl	0.01	<mdl	<mdl	0.09	65.45	<mdl	0.01	<mdl	<mdl	0.05	<mdl	<mdl	<mdl	<mdl	<mdl	0.05	<mdl	<mdl	<mdl	1.31	0.02	0.02	0.04	<mdl	<mdl	100.66	0.00	0.00	0.00	100.66	0.000
Bright	007 086 bright 3	<mdl	0.02	<mdl	33.34	0.11	<mdl	0.02	<mdl	0.01	<mdl	<mdl	0.13	65.83	<mdl	<mdl	0.04	<mdl	0.05	<mdl	<mdl	<mdl	0.03	*0.01*	0.06	*0.01*	0.05	*0.01*	1.23	0.03	0.02	0.02	<mdl	<mdl	101.01	0.01	0.00	0.00	101.02	0.000
Bright	007 086 bright 4	<mdl	0.01	<mdl	32.89	0.10	<mdl	0.01	<mdl	0.01	<mdl	0.03	0.05	65.65	<mdl	<mdl	<mdl	<mdl	<mdl	<mdl	0.07	0.03	<mdl	<mdl	0.03	<mdl	<mdl	<mdl	1.23	<mdl	<mdl	0.02	<mdl	<mdl	100.10	0.00	0.00	0.00	100.10	0.000
Bright	007 086 bright 5	<mdl	0.01	<mdl	32.70	0.11	<mdl	0.02	<mdl	0.01	<mdl	0.03	0.07	65.68	<mdl	<mdl	<mdl	<mdl	<mdl	<mdl	<mdl	<mdl	0.04	*0.01*	0.06	*0.01*	0.03	*0.00*	1.09	0.02	<mdl	0.01	<mdl	<mdl	99.91	0.00	0.00	0.00	99.91	0.000
	mean (n=5)	<mdl	0.01	<mdl	33.10	0.11	<mdl	0.02	<mdl	0.01	<mdl	<mdl	0.08	65.70	<mdl	<mdl	<mdl	<mdl	<mdl	<mdl	<mdl	<mdl	<mdl	<mdl	0.05	<mdl	<mdl	<mdl	1.22	0.02	<mdl	0.02	<mdl	<mdl	100.45	0.00	0.00	0.00	100.45	0.000
Dark	007 086 dark 1	<mdl	0.01	0.01	33.14	0.11	<mdl	0.02	<mdl	0.01	<mdl	<mdl	0.07	65.12	<mdl	<mdl	<mdl	<mdl	<mdl	<mdl	<mdl	0.03	0.03	*0.01*	0.06	*0.01*	0.05	0.03	1.20	0.02	<mdl	0.02	<mdl	<mdl	99.96	0.01	0.00	0.00	99.96	0.000
Dark	007 086 dark 2	<mdl	0.01	<mdl	32.61	0.09	<mdl	0.02	<mdl	0.01	<mdl	<mdl	0.05	65.07	<mdl	<mdl	<mdl	<mdl	<mdl	<mdl	<mdl	<mdl	<mdl	<mdl	0.04	*0.01*	0.04	*0.01*	1.27	<mdl	<mdl	<mdl	<mdl	<mdl	99.20	0.00	0.00	0.00	99.20	0.000
Dark	007 086 dark 3	0.03	0.01	0.01	33.19	0.12	<mdl	0.01	<mdl	0.01	0.01	0.03	0.09	65.32	<mdl	<mdl	<mdl	<mdl	<mdl	<mdl	0.06	*0.01*	0.03	*0.01*	0.06	0.04	0.07	<mdl	1.17	0.02	<mdl	0.02	<mdl	<mdl	100.31	0.00	0.00	0.00	100.31	0.002
Dark	007 086 dark 4	0.03	0.01	<mdl	32.33	0.11	<mdl	0.02	<mdl	0.01	<mdl	0.03	0.07	66.15	<mdl	<mdl	<mdl	<mdl	<mdl	<mdl	<mdl	<mdl	<mdl	<mdl	0.05	*0.01*	0.03	*0.00*	1.25	0.02	<mdl	0.02	<mdl	<mdl	100.14	0.20	0.00	0.00	100.34	0.002
Dark	007 086 dark 5	<mdl	<mdl	<mdl	32.52	0.12	<mdl	0.02	<mdl	0.01	<mdl	<mdl	0.09	65.13	0.02	<mdl	<mdl	<mdl	<mdl	<mdl	<mdl	<mdl	0.04	*0.01*	0.05	<mdl	<mdl	<mdl	1.23	<mdl	0.02	0.03	<mdl	<mdl	99.29	0.00	0.00	0.00	99.29	0.000
	mean (n=5)	<mdl	0.01	<mdl	32.76	0.11	<mdl	0.02	<mdl	0.01	<mdl	<mdl	0.07	65.36	<mdl	<mdl	<mdl	<mdl	<mdl	<mdl	<mdl	<mdl	0.03	0.01	0.05	0.01	0.05	0.01	1.22	0.02	<mdl	0.02	<mdl	<mdl	99.78	0.04	0.00	0.00	99.82	0.001

TABLE A1 EPMA CONTINUED

K	∑I-site	Mg	Al	Ca	Sc	Mn	Fe	Y	Zr	Nb	Ce	Pr	Nd	Sm	Eu	Gd	Tb	Dy	Ho	Er	Tm	Yb	Lu	REE*	Hf	Pb	Th	U	∑A-site	Al	Si	P	Ti	Si*	∑B-site	F	Cl	OH	O	age (Ga)	MW	U (ppm)	$^{238}U^{C}$ (ppm)	$^{235}U^{D}$ (ppm)	Th (ppm)	α-decays/mg
0.000	0.000	0.001	0.000	0.000	0.000	0.000	0.001	0.005	0.967	0.000	0.000	0.000	0.001	0.000	0.000	0.000	0.000	0.001	0.000	0.001	0.000	0.002	0.000	0.009	0.012	0.000	0.000	0.000	0.989	0.000	1.002	0.009	0.000	0.000	1.011	0.000	0.000	0.000	3.999	1.59	184	438	437	0.8	152	3.52E+15
0.001	0.001	0.001	0.006	0.007	0.000	0.001	0.030	0.005	0.933	0.000	0.000	0.000	0.000	0.000	0.000	0.001	0.000	0.001	0.000	0.001	0.000	0.002	0.000	0.009	0.012	0.000	0.000	0.001	0.999	0.000	0.994	0.006	0.001	0.000	1.001	0.006	0.001	0.002	3.967	1.59	182.5	587	586	1.1	0	4.43E+15
0.000	0.000	0.000	0.002	0.000	0.000	0.001	0.002	0.979	0.000	0.000	0.000	0.001	0.001	0.000	0.000	0.000	0.000	0.000	0.000	0.001	0.000	0.002	0.000	0.006	0.013	0.000	0.000	0.000	1.000	0.000	0.993	0.005	0.000	0.001	1.000	0.000	0.000	0.006	3.992	1.59	184.5	143	143	0.3	0	1.07E+15
0.000	0.000	0.000	0.002	0.003	0.000	0.000	0.010	0.004	0.959	0.000	0.000	0.000	0.000	0.000	0.000	0.000	0.000	0.000	0.000	0.001	0.000	0.002	0.000	0.008	0.012	0.000	0.000	0.000	0.996	0.000	0.997	0.007	0.000	0.000	1.004	0.002	0.000	0.003	3.986	1.59	183.7	389	389	0.7	51	3.00E+15
0.000	0.000	0.001	0.000	0.001	0.000	0.000	0.001	0.002	0.966	0.000	0.000	0.000	0.000	0.001	0.000	0.001	0.000	0.000	0.001	0.001	0.000	0.001	0.000	0.007	0.011	0.000	0.000	0.000	0.986	0.000	1.010	0.004	0.000	0.000	1.015	0.000	0.000	0.002	3.996	1.59	183.6	190	190	0.4	0	1.43E+15
0.000	0.002	0.000	0.000	0.003	0.000	0.000	0.003	0.011	0.963	0.000	0.000	0.000	0.000	0.000	0.000	0.001	0.000	0.001	0.000	0.001	0.001	0.003	0.000	0.018	0.011	0.000	0.000	0.001	1.000	0.000	0.992	0.008	0.000	0.000	1.000	0.000	0.000	0.010	3.985	1.59	184.7	1263	1261	2.4	537	1.03E+16
0.000	0.000	0.000	0.000	0.000	0.000	0.000	0.001	0.004	0.973	0.000	0.000	0.000	0.000	0.000	0.000	0.000	0.001	0.000	0.000	0.000	0.001	0.000	0.001	0.008	0.011	0.000	0.000	0.000	0.993	0.000	1.001	0.007	0.000	0.000	1.007	0.000	0.000	0.001	3.998	1.59	184.1	292	292	0.6	0	2.18E+15
0.000	0.001	0.000	0.000	0.001	0.000	0.000	0.002	0.006	0.967	0.000	0.000	0.000	0.000	0.000	0.000	0.000	0.001	0.000	0.001	0.000	0.001	0.000	0.002	0.000	0.011	0.011	0.000	0.000	0.993	0.000	1.001	0.006	0.000	0.000	1.007	0.000	0.000	0.004	3.993	1.59	184.1	582	581	1.1	179	4.62E+15
0.000	0.000	0.000	0.000	0.000	0.000	0.000	0.000	0.001	0.971	0.000	0.000	0.000	0.000	0.000	0.000	0.000	0.000	0.000	0.000	0.001	0.000	0.001	0.000	0.003	0.012	0.000	0.000	0.000	0.987	0.000	1.010	0.003	0.000	0.000	1.013	0.000	0.000	0.000	3.999	1.59	183.7	298	297	0.6	166	2.50E+15
0.000	0.000	0.001	0.000	0.000	0.000	0.000	0.000	0.001	0.975	0.000	0.000	0.000	0.000	0.000	0.000	0.000	0.000	0.000	0.000	0.001	0.000	0.000	0.000	0.002	0.012	0.000	0.000	0.000	0.989	0.000	1.008	0.003	0.000	0.000	1.011	0.000	0.000	0.000	4.000	1.59	183.7	188	188	0.4	232	1.78E+15
0.000	0.000	0.001	0.000	0.000	0.000	0.000	0.000	0.001	0.973	0.000	0.000	0.000	0.000	0.000	0.000	0.000	0.000	0.000	0.000	0.001	0.000	0.001	0.000	0.003	0.012	0.000	0.000	0.000	0.988	0.000	1.009	0.003	0.000	0.000	1.012	0.000	0.000	0.000	3.999	1.59	183.7	243	243	0.5	199	2.14E+15
0.000	0.000	0.000	0.000	0.000	0.000	0.000	0.000	0.001	0.976	0.000	0.000	0.000	0.001	0.000	0.000	0.001	0.000	0.000	0.001	0.001	0.000	0.001	0.000	0.005	0.010	0.000	0.000	0.000	0.992	0.000	1.006	0.002	0.000	0.000	1.008	0.000	0.000	0.002	3.997	1.59	184	188	187	0.4	104	1.57E+15
0.000	0.001	0.000	0.000	0.000	0.000	0.000	0.001	0.965	0.000	0.000	0.000	0.000	0.000	0.000	0.000	0.000	0.000	0.000	0.000	0.000	0.000	0.000	0.000	0.002	0.010	0.000	0.000	0.000	0.977	0.000	1.020	0.003	0.000	0.000	1.023	0.000	0.000	0.000	4.000	1.59	182.8	116	116	0.2	0	8.76E+14
0.000	0.000	0.006	0.000	0.035	0.003	0.001	0.023	0.031	0.843	0.005	0.000	0.000	0.000	0.001	0.000	0.002	0.001	0.003	0.001	0.003	0.001	0.011	0.001	0.057	0.024	0.000	0.004	0.001	1.000	0.017	0.874	0.007	0.001	0.101	1.000	0.061	0.001	0.391	3.487	1.59	181.6	1875	1872	3.6	5639	2.34E+16
0.000	0.000	0.002	0.000	0.012	0.001	0.001	0.008	0.011	0.928	0.002	0.000	0.000	0.000	0.000	0.000	0.001	0.000	0.001	0.001	0.001	0.000	0.004	0.000	0.021	0.015	0.000	0.002	0.001	0.990	0.006	0.966	0.004	0.001	0.034	1.010	0.020	0.000	0.131	3.828	1.59	182.8	726	725	1.4	1914	8.60E+15
0.000	0.000	0.000	0.000	0.001	0.000	0.000	0.000	0.003	0.977	0.000	0.000	0.000	0.000	0.000	0.000	0.000	0.001	0.000	0.001	0.000	0.001	0.000	0.001	0.006	0.011	0.000	0.000	0.000	0.996	0.000	1.001	0.003	0.000	0.000	1.004	0.000	0.000	0.003	3.995	1.59	184.2	254	254	0.5	199	2.22E+15
0.000	0.000	0.000	0.000	0.001	0.000	0.000	0.000	0.001	0.973	0.000	0.000	0.000	0.000	0.000	0.000	0.000	0.000	0.000	0.000	0.001	0.000	0.001	0.000	0.005	0.010	0.000	0.000	0.000	0.990	0.000	1.006	0.003	0.000	0.000	1.010	0.000	0.000	0.001	3.997	1.59	183.7	137	137	0.3	202	1.35E+15
0.000	0.000	0.001	0.000	0.001	0.000	0.000	0.000	0.001	0.972	0.000	0.000	0.000	0.000	0.000	0.000	0.000	0.001	0.000	0.000	0.001	0.000	0.001	0.000	0.004	0.011	0.000	0.000	0.000	0.989	0.000	1.008	0.003	0.000	0.000	1.011	0.000	0.000	0.001	3.998	1.59	183.8	249	248	0.5	0	1.86E+15
0.000	0.000	0.000	0.000	0.001	0.000	0.000	0.001	0.003	0.965	0.000	0.000	0.001	0.000	0.000	0.000	0.000	0.001	0.000	0.001	0.000	0.001	0.000	0.002	0.000	0.008	0.010	0.000	0.000	0.986	0.000	1.011	0.003	0.000	0.000	1.015	0.000	0.000	0.005	3.994	1.59	183.6	114	114	0.2	203	1.18E+15
0.000	0.002	0.001	0.000	0.001	0.000	0.000	0.000	0.001	0.981	0.000	0.000	0.000	0.000	0.000	0.000	0.000	0.001	0.000	0.000	0.000	0.000	0.001	0.000	0.003	0.011	0.000	0.000	0.000	0.997	0.000	1.000	0.003	0.000	0.000	1.003	0.000	0.000	0.000	3.999	1.59	184.3	299	298	0.6	144	2.46E+15
0.000	0.000	0.000	0.000	0.001	0.000	0.000	0.000	0.002	0.974	0.000	0.000	0.000	0.000	0.000	0.000	0.000	0.001	0.000	0.000	0.000	0.001	0.000	0.001	0.000	0.005	0.011	0.000	0.000	0.992	0.000	1.005	0.003	0.000	0.000	1.008	0.000	0.000	0.002	3.997	1.59	183.9	211	210	0.4	150	1.81E+15
0.000	0.000	0.001	0.000	0.001	0.000	0.000	0.000	0.001	0.978	0.000	0.000	0.000	0.000	0.000	0.000	0.000	0.000	0.000	0.000	0.001	0.000	0.001	0.000	0.004	0.011	0.000	0.000	0.000	0.994	0.000	1.004	0.003	0.000	0.000	1.006	0.000	0.000	0.001	3.998	1.59	183.9	0	0	0	0	0.00E+00
0.000	0.000	0.000	0.000	0.001	0.000	0.000	0.001	0.001	0.977	0.000	0.000	0.000	0.001	0.000	0.000	0.001	0.000	0.000	0.001	0.001	0.000	0.001	0.000	0.005	0.011	0.000	0.000	0.000	0.995	0.000	1.003	0.002	0.000	0.000	1.005	0.000	0.000	0.002	3.996	1.59	184.2	0	0	0	0	0.00E+00
0.000	0.002	0.001	0.001	0.001	0.000	0.000	0.001	0.001	0.945	0.000	0.000	0.000	0.000	0.000	0.000	0.000	0.000	0.000	0.000	0.001	0.000	0.001	0.000	0.002	0.010	0.000	0.000	0.000	0.961	0.000	1.037	0.003	0.000	0.000	1.039	0.000	0.000	0.000	3.999	1.59	181.7	0	0	0	0	0.00E+00
0.000	0.000	0.001	0.000	0.001	0.000	0.000	0.000	0.001	0.982	0.000	0.000	0.000	0.000	0.000	0.000	0.000	0.000	0.000	0.000	0.000	0.000	0.000	0.000	0.001	0.011	0.000	0.000	0.000	0.996	0.000	1.002	0.002	0.000	0.000	1.004	0.000	0.000	0.000	3.999	1.59	184.1	0	0	0	0	0.00E+00
0.000	0.000	0.000	0.000	0.001	0.000	0.000	0.000	0.001	0.969	0.000	0.000	0.000	0.000	0.000	0.000	0.000	0.000	0.000	0.000	0.001	0.000	0.001	0.000	0.002	0.011	0.000	0.000	0.000	0.983	0.000	1.014	0.002	0.000	0.000	1.017	0.006	0.000	0.000	3.996	1.59	183.3	132	132	0.3	0	9.89E+14
0.000	0.001	0.001	0.000	0.001	0.000	0.000	0.000	0.001	0.970	0.000	0.000	0.000	0.000	0.000	0.000	0.000	0.000	0.000	0.000	0.001	0.000	0.000	0.000	0.003	0.011	0.000	0.000	0.000	0.986	0.000	1.012	0.002	0.000	0.000	1.014	0.001	0.000	0.001	3.998	1.59	183.4	26	26	0.1	0	1.98E+14
0.000	0.000	0.000	0.000	0.001	0.000	0.000	0.000	0.001	0.977	0.000	0.000	0.000	0.000	0.000	0.000	0.001	0.000	0.000	0.000	0.000	0.000	0.000	0.000	0.002	0.011	0.000	0.000	0.000	0.991	0.000	1.007	0.002	0.000	0.000	1.009	0.000	0.000	0.000	4.000	1.59	183.8	212	211	0.4	0	1.58E+15
0.000	0.000	0.000	0.000	0.001	0.000	0.000	0.000	0.002	0.967	0.000	0.000	0.000	0.000	0.001	0.000	0.000	0.000	0.000	0.000	0.001	0.000	0.000	0.000	0.003	0.011	0.000	0.000	0.000	0.983	0.000	1.014	0.003	0.000	0.000	1.017	0.000	0.000	0.000	3.999	1.59	183.3	316	316	0.6	148	2.61E+15
0.000	0.001	0.000	0.001	0.000	0.000	0.000	0.002	0.971	0.000	0.000	0.001	0.000	0.001	0.000	0.000	0.000	0.000	0.000	0.000	0.001	0.000	0.001	0.000	0.005	0.011	0.000	0.000	0.000	0.989	0.000	1.008	0.003	0.000	0.000	1.011	0.000	0.000	0.003	3.996	1.59	183.7	145	144	0.3	133	1.30E+15
0.000	0.000	0.001	0.000	0.000	0.000	0.000	0.001	0.001	0.978	0.000	0.000	0.000	0.000	0.000	0.000	0.001	0.000	0.000	0.000	0.000	0.000	0.000	0.000	0.002	0.011	0.000	0.000	0.000	0.993	0.000	1.005	0.003	0.000	0.000	1.008	0.000	0.000	0.000	3.999	1.59	183.8	128	128	0.2	0	9.60E+14
0.000	0.000	0.001	0.000	0.001	0.000	0.000	0.001	0.001	0.981	0.000	0.000	0.000	0.000	0.000	0.000	0.000	0.000	0.000	0.000	0.001	0.000	0.001	0.000	0.003	0.010	0.000	0.000	0.000	0.996	0.000	1.002	0.003	0.000	0.000	1.005	0.000	0.000	0.000	3.998	1.59	183.9	109	109	0.2	0	8.15E+14
0.000	0.000	0.000	0.000	0.001	0.000	0.000	0.000	0.001	0.975	0.000	0.000	0.000	0.000	0.000	0.000	0.000	0.000	0.000	0.000	0.000	0.000	0.000	0.000	0.003	0.011	0.000	0.000	0.000	0.990	0.000	1.007	0.003	0.000	0.000	1.010	0.000	0.000	0.001	3.998	1.59	183.7	182	182	0.3	56	1.45E+15
0.000	0.000	0.001	0.000	0.001	0.000	0.000	0.000	0.001	0.969	0.000	0.000	0.000	0.000	0.000	0.000	0.000	0.000	0.000	0.000	0.001	0.000	0.001	0.000	0.004	0.011	0.000	0.000	0.000	0.986	0.000	1.012	0.003	0.000	0.000	1.015	0.000	0.000	0.001	3.997	1.59	183.4	181	180	0.3	0	1.35E+15
0.000	0.000	0.000	0.001	0.000	0.000	0.000	0.001	0.978	0.000	0.000	0.000	0.000	0.000	0.000	0.000	0.000	0.000	0.000	0.000	0.001	0.000	0.001	0.000	0.002	0.011	0.000	0.000	0.000	0.992	0.000	1.005	0.002	0.000	0.000	1.008	0.000	0.000	0.000	3.999	1.59	183.8	0	0	0	0	0.00E+00
0.000	0.002	0.001	0.001	0.000	0.000	0.000	0.001	0.002	0.969	0.000	0.000	0.000	0.000	0.000	0.000	0.000	0.001	0.000	0.000	0.000	0.001	0.000	0.001	0.000	0.005	0.010	0.000	0.000	0.987	0.000	1.010	0.003	0.000	0.000	1.013	0.000	0.000	0.000	3.998	1.59	183.5	184	183	0.4	0	1.37E+15
0.000	0.002	0.001	0.000	0.001	0.000	0.000	0.001	0.001	0.985	0.000	0.000	0.000	0.000	0.000	0.000	0.000	0.000	0.000	0.000	0.000	0.000	0.001	0.000	0.002	0.011	0.000	0.000	0.000	1.000	0.000	0.987	0.003	0.000	0.010	1.000	0.000	0.000	0.041	3.959	1.59	184.1	147	146	0.3	0	1.10E+15
0.000	0.000	0.000	0.001	0.000	0.000	0.000	0.002	0.979	0.000	0.000	0.000	0.000	0.000	0.000	0.000	0.000	0.000	0.000	0.000	0.001	0.000	0.000	0.000	0.003	0.011	0.000	0.000	0.000	0.994	0.000	1.003	0.003	0.000	0.000	1.006	0.000	0.000	0.000	4.000	1.59	184	289	289	0.6	177	2.45E+15
0.000	0.001	0.000	0.000	0.001	0.000	0.000	0.000	0.001	0.976	0.000	0.000	0.000	0.000	0.000	0.000	0.000	0.000	0.000	0.000	0.001	0.000	0.001	0.000	0.003	0.011	0.000	0.000	0.000	0.992	0.000	1.003	0.003	0.000	0.002	1.008	0.000	0.000	0.008	3.991	1.59	183.8	160	160	0.3	35	1.25E+15

Numbers in italics correspond to interpolated values based on adjacent HREE, where both were >mdl; if Lu was below detection, It was extrapoalted from the slope from Tm and Yb

La_2O_3 was measssured, but consistently below minimumm detection limits (0.008 wt%)

[A] Sum including calculated H_2O and corrected for F and Cl

[B] Calculated Si substituted by $4H^+$ considering the hydrogarnet substitution type substitution

[C] Calculated ^{238}U concentration considering formation at indicated age and initial $^{238}U/^{235}U = 137.8$

[D] Calculated ^{235}U concentration considering formation at indicated age and initial $^{238}U/^{235}U = 137.8$

REE*: denotes the sum of Sc, Y and all lanthanides

MW: mean weight for zircon obtained from calcualted zircon mineral formula

Mean values calculated only for those groups wherein less than 50% of the data is missing

ELECTRONIC APPENDIX B FOR CHAPTER 3 – TABLE A2 LA-ICP-MS

Appendix Table A2. Complete LA-ICP-MS data for zircon (ppm)

Granite	Sample	Grain No.	Area	Analysis	Al	P	Ca	Ti	Mn	Fe	Y	Nb	Sn	La	Ce	Pr	Nd	Sm	Eu	Gd	Tb	Dy	Ho	Er	Tm	Yb	Lu	Hf	Ta	^{206}Pb	^{207}Pb	^{208}Pb	∑Pb	Th	U
B	005	G30	C	Samphire-005-G30-core-1	0.59	276	120	11.5	<0.45	<25.7	642	3.18	<0.17	<0.015	16	0.031	0.63	1.22	0.314	11.8	3.69	51.3	20.7	103	23.5	217	43.8	11000	2.29	75	7.28	10.4	92.7	124	286
		G31	C	Samphire-005-G31-core-1	<0.49	76.2	<103	5.47	<0.43	<23.8	358	2.02	0.13	<0.016	8.75	0.05	0.59	1.05	0.101	3.96	1.86	24.8	10.8	60.7	14.4	142	29.7	10800	1.39	76.2	7.58	7.31	91.1	88.3	276
		G32	C	Samphire-005-G32-core-1	1.66	153	<119	10.2	<0.43	<24.6	521	1.99	<0.15	<0.012	10.7	0.039	0.61	1.49	0.168	9.29	3.05	41.8	16.6	88.2	18.6	178	35.5	9750	0.994	47	5.07	5.94	58	74.8	174
		G40	C	Samphire-005-G40-core-1	<0.53	180	347	8.19	<0.45	32.8	647	2.65	0.35	0.036	12.3	0.025	0.39	1.57	0.35	10.5	4	49.4	21.3	105	22.1	204	41.9	10600	1.3	68.7	6.68	10.5	85.9	131	268
		G42	C	Samphire-005-G42-core-1	<0.54	171	<115	2.58	<0.43	<24	347	2.72	0.17	<0.012	10.5	<0.01	0.121	0.68	0.037	2.77	1.6	24.1	10.2	62.5	15	150	32	10800	1.92	101	9.68	9.74	121	120	384
		G45	C	Samphire-005-G45-core-1	<0.54	150	<108	2.49	<0.43	<24.2	427	2.64	<0.136	<0.008	10.9	0.018	0.4	0.85	0.043	6.31	2.18	31.2	13.2	73.7	16.6	170	35.1	11300	1.63	90.6	8.64	9.73	109	116	328
		G52	C	Samphire-005-G52-core-1	7.19	255	136	12.6	<0.44	<24.5	878	5.16	<0.15	<0.012	21	0.038	0.81	3.08	0.284	16.7	5.5	71.6	28.9	143	30.3	304	59	10900	2.66	157	14.8	23.2	195	287	591
		G59	C	Samphire-005-G59-core-1	1.63	93.5	<122	9.8	<0.45	<26.1	280	1.96	<0.13	0.013	15.7	0.048	0.46	0.58	0.038	3.78	1.36	18.9	8.71	47.2	12.3	130	31.3	12300	1.82	95.3	10.5	12.1	118	154	373
		G71	C	Samphire-005-G71-core-1	2.6	237	<103	8.74	0.85	47.6	727	3.12	0.21	<0.018	22	<0.015	0.9	2.23	0.521	13.2	4.43	60.7	22.3	116	23.8	245	49.2	10300	1.65	66.9	6.79	14.1	87.8	168	258
			R1	Samphire-005-G71-Rim1-1	2.18	152	107	11.9	3.62	81.6	413	3.05	<0.107	0.022	17.9	0.039	0.43	1.04	0.19	5.79	2.36	32.5	12.7	64.8	14.8	156	33.6	10800	1.61	70.1	6.81	10.6	87.5	128	268
			R2	Samphire-005-G71-Rim2-1	<0.65	139	<128	6.6	0.8	<29.3	262	2.24	0.36	<0.017	14.6	0.054	0.4	0.39	0.089	2.82	1.23	16.1	7.33	43.6	10.7	121	26.1	10100	1.48	112	11.4	14.3	138	142	342
		G76	Grey	Samphire-005-G76-grey-1	<0.55	251	<101	5.23	<0.42	<24.9	750	2.47	0.24	<0.012	12.3	0.028	1.05	2.38	0.386	13.5	4.96	64.2	23.9	120	25.4	220	44.6	9720	1.24	41.8	4.3	7.59	53.7	96	159
			White	Samphire-005-G76-white-1	0.71	195	275	8.15	4.28	<25.3	952	4.28	<0.117	<0.008	20.3	0.074	1.32	2.2	0.287	17.1	5.87	79.3	30.4	154	33.6	302	61.8	11100	1.81	115	10.9	17.7	143	210	430
		G80	C1	Samphire-005-G80-core-1	0.76	92.8	<97.1	3.28	<0.41	<23.5	363	2.26	<0.12	0.98	11.2	0.218	0.9	0.59	0.056	4.94	1.66	24.7	11.4	59.2	14	154	31.8	10400	1.41	105	10	9.94	125	119	367
			C2	Samphire-005-G80-core-2	11.9	109	<156	7.26	<0.59	<33.7	444	6.9	0.44	0.783	13.1	0.536	2.67	2.97	0.169	7.6	2.56	33.9	13.6	73.7	17	174	37.1	9460	1.66	125	11.6	13.1	150	136	391
		G81	C-grey	Samphire-005-G81-coregrey-1	5.67	238	198	21.2	0.82	<25.8	586	2.25	0.33	<0.009	16.3	0.082	1.13	2.59	0.497	12.7	4.14	49.7	19.4	93.8	18.9	180	35.4	9860	1.11	28.5	2.84	5.8	37.1	68.3	106
		G82	C	Samphire-005-G82-core-1	2.85	283	<127	8.07	1.4	32.9	782	3.93	0.17	0.163	19	0.072	1.95	2.41	0.383	15	4.74	63.7	26	122	25.8	246	49.5	9410	1.82	113	10.9	18.2	142	191	387
		G84	C	Samphire-005-G84-core-1	<0.51	196	<106	9.8	1.21	<25.4	812	1.86	0.3	0.028	12.9	0.072	1.21	2.4	0.294	16.5	5.14	69.8	26.3	131	27.1	245	48.8	10100	1.29	65.7	6.37	10.8	82.9	137	242
		G88	C	Samphire-005-G88-core-1	<0.61	280	151	15.2	<0.45	<25.4	583	1.99	<0.126	<0.012	11.2	0.037	0.74	2.61	0.32	10.4	3.79	48.8	19.1	94.5	19.2	179	36.1	9720	0.981	39.5	4.02	6.95	50.5	78.7	138
			R	Samphire-005-G88-rim-1	<0.5	248	<109	13.8	<0.44	<25.8	662	3.37	0.31	<0.015	15.5	0.065	0.77	2.1	0.456	11.5	4.22	53.9	22	106	23.1	211	42.7	10400	1.77	75	7.02	10.9	92.9	131	278
		G89	C	Samphire-005-G89-core-1	1.02	187	<125	12.4	<0.46	38.1	331	1.38	<0.15	<0.019	7.27	0.047	0.29	1.39	0.124	6.56	1.97	27.8	10.8	54.5	11.3	116	22.6	10000	0.952	22.5	2.31	2.72	27.5	36.8	85.5
			R	Samphire-005-G89-rim-1	1.36	153	<111	8.03	<0.45	<25.1	430	2.24	0.33	<0.017	11	0.03	0.42	0.87	0.209	7.82	2.58	35.5	14.2	69.6	15.3	146	30.3	10400	1.05	43.2	4.25	5.4	52.8	69.2	164
		G92	C	Samphire-005-G92-core-1	64.9	240	<136	18.1	4.89	546	350	10.9	<0.15	0.574	9.96	0.36	1.14	1.23	0.079	5.33	2.14	27.7	11	58.6	11.9	113	22.8	8630	0.862	36.2	3.92	5.2	45.4	53	143
			R	Samphire-005-G92-rim-1	<0.67	220	184	5.75	13.4	178	1370	2.96	<0.21	0.025	16.2	0.206	4.17	5.14	0.478	31.4	9.9	125	46.1	215	42.9	361	70.2	7810	1.39	128	12.3	27.8	168	287	403
		G94	C	Samphire-005-G94-core-1	<0.52	270	<104	14.8	0.44	<26.3	721	3.28	0.45	0.071	27	0.102	1.26	2.03	0.498	14.4	4.93	60	23.4	114	24.3	225	45.4	9930	1.45	58.1	6.4	14.2	78.7	177	224

TABLE A2 LA-ICP-MS CONTINUED

		G03	C	Samphire-007-G03-core-1	145	235	275	10.7	3.12	297	731	2.69	0.5	0.41	12.6	0.6	2.55	5.06	1.2	15.7	5.26	62.5	24.2	115	24.6	218	40.9	10000	0.81	48.2	4.54	7.64	60.4	87.5	178
			R	Samphire-007-G03-rim-1	143	276	136	20.7	11.1	229	1070	5.79	0.26	1.39	33.3	1.6	12.7	8.88	5.17	25.1	7.82	94.5	34.1	169	35.4	316	64	10600	2.16	96	10.1	16.1	122	205	376
		G04	C	Samphire-007-G04-core-1	54.4	371	298	24.6	5.11	146	1470	4.58	0.61	2.15	35.9	4.02	28.5	18.3	1.89	47.6	11.8	139	47.8	221	42.5	381	71.2	9640	1.51	80	7.73	17.7	105	200	334
			R	Samphire-007-G04-rim-1	78.6	463	176	15.7	6.63	600	844	5.42	0.33	0.85	26.9	1.63	11.1	8.65	1.1	21.1	6.45	72.8	29	136	26.4	240	48	9790	2.16	88.1	9.65	12.2	110	151	333
		G08	R	Samphire-007-G08-rim-1	0.95	219	<105	9.99	<0.44	<26.3	435	1.66	0.21	<0.017	9.25	<0.01	0.48	0.99	0.363	7.63	2.48	36.4	14.4	70.6	15.8	141	29.7	9760	0.984	28.7	3.1	4.24	36.1	50.1	103
			C	Samphire-007-G08-core-1	<0.56	242	<113	8.1	<0.43	<25.1	547	2.74	0.46	<0.015	13	0.043	0.86	1.9	0.242	10.2	3.49	45.2	17.6	85.6	18.5	178	35.3	10000	1.35	38.8	3.6	6.34	48.7	80.6	145
		G13	C	Samphire-007-G13-core-1	<0.56	219	<109	19.1	<0.46	35	619	2.49	<0.121	<0.015	13.1	0.047	0.72	2.17	0.469	11.6	4.21	55.1	20.3	101	21.1	191	37	9480	1.1	32.7	3.12	7.03	42.9	89.4	124
			R1	Samphire-007-G13-rim-1	5.27	261	204	12.8	<0.42	<25.4	549	1.74	0.53	0.042	10.6	0.07	0.4	1.5	0.372	9.98	3.45	45.8	18	88.8	18.7	176	35	9700	1.01	25.2	2.59	4.99	32.8	60.8	94.4
			R2	Samphire-007-G13-rim2-1	121	214	851	7.96	37.7	469	907	3.46	<0.11	7.46	39.4	4.32	20.5	10.2	1.16	28	7.35	80.3	27.2	133	27.7	243	49.2	9220	1.07	69.5	6.94	9.92	86.3	100	371
		G16	C	Samphire-007-G16-core-1	<0.53	257	<114	11.4	<0.45	<25.6	451	1.89	<0.16	<0.015	9.6	0.028	0.51	1	0.311	8.19	2.64	38.8	14.3	72.8	15.2	154	28.8	10000	0.828	26.8	2.68	4.14	33.6	53.2	103
			R	Samphire-007-G16-rim-1	<0.56	241	284	8.5	0.61	<26.2	444	1.93	<0.14	0.012	9.69	0.033	0.33	1.16	0.259	7.55	2.92	36.4	14.3	74.7	15.7	148	30.2	10500	1.03	33.4	3.44	4.56	41.4	57.4	128
		G17	R	Samphire-007-G17-rim-1	<0.52	226	<103	14.8	<0.44	<25.6	632	2.76	0.15	<0.015	11.1	0.093	0.98	2.44	0.281	12.9	3.95	55.4	20.8	98.3	21.9	208	40.5	9900	1.44	40.8	3.69	6.6	51.1	85.3	155
A	007		C	Samphire-007-G17-core-1	<0.57	277	<97.2	14.7	<0.45	<27	721	2.59	0.52	<0.012	13.7	0.107	0.92	1.72	0.314	14.2	4.94	64.5	23.8	115	23.8	218	44.3	9770	1.3	44.7	4.67	8.03	57.4	104	169
		G18	C	Samphire-007-G18-core-1	20.2	243	223	14.1	4.38	133	545	1.49	0.52	0.081	8.65	0.213	1.43	1.62	0.274	10.6	3.78	49.1	17.8	85	17.2	166	31.1	8520	0.719	35	4.02	7.18	46.2	58.5	104
			R	Samphire-007-G18-rim-1	185	241	<96.7	13.4	9.38	483	633	2.58	0.4	0.146	12.7	0.174	1.86	2.61	0.348	12.3	4.33	52.3	20.1	104	21.9	195	39.5	9600	1.27	33.3	3.64	5.82	42.7	69.8	133
		G21	R	Samphire-007-G21-rim-1	87.3	234	<114	19.2	7.24	138	1280	1.92	0.24	0.305	17.3	0.578	6.88	7.48	1.42	30.2	10.9	123	42.1	202	37.6	321	60.9	8810	1.03	34.4	5.39	13.2	53	115	128
			C	Samphire-007-G21-core-1	1.34	248	<114	12.2	0.7	<27.1	516	1.26	0.3	<0.009	8.46	0.044	0.8	1.83	0.384	12.1	3.79	45.3	16.9	81.6	16.9	155	30.8	8910	0.673	21.3	2.18	4.54	28	48.2	73
		G28	C	Samphire-007-G28-core-1	<0.53	255	<111	13.2	<0.45	<26.1	1230	2.51	<0.17	0.185	17.5	0.264	4.1	5.55	0.75	26.5	9.21	110	40.3	192	39.4	352	63.4	9960	1.3	54.2	6.24	13.2	73.6	174	211
			R	Samphire-007-G28-rim-1	<0.64	322	<121	11	<0.53	<30.2	373	1.65	0.33	0.083	9.39	0.02	0.43	0.79	0.224	6.27	2.5	29	11.8	63.4	12.7	121	24.6	8660	0.885	29.4	2.98	4.92	37.3	52.5	95.8
		G29	C	Samphire-007-G29-core-1	3.06	269	114	20.5	<0.47	<26.8	621	1.97	0.308	0.029	12	0.071	1.17	2.43	0.539	10.8	4.13	54.1	20.6	100	20.6	190	37.6	8980	0.933	35.2	3.57	7.36	46.2	85	129
			R	Samphire-007-G29-rim-1	38.8	321	<117	31.6	5.07	145	1580	3.01	0.228	0.671	20.5	1.25	10.4	11.7	2.12	44.2	12.7	153	52.4	242	47.2	417	77.6	8300	1.23	67.8	8.7	24	101	196	368
		G87	R	Samphire-007-G87-rim-1	61.1	286	126	11.4	9.94	147	974	3.16	0.18	9.99	71.7	7.73	43	16.5	5.38	31.3	7.37	87.6	30.3	142	29.5	256	50.7	9630	0.897	43.8	4.77	9.37	57.9	120	218
			C	Samphire-007-G87-core-1	19.7	361	<117	5.16	1.75	57.2	1480	3.34	<0.15	0.8	28.7	0.63	5.02	6.74	1.21	34.9	11.8	130	50	234	48.4	419	81.5	11300	1.63	105	10.6	21.3	137	272	418
		G86	C	Samphire-007-G86-core-1	<0.52	271	<118	14.4	0.47	<26.4	767	3.12	0.28	<0.013	13.7	0.058	0.63	2.32	0.428	16.7	5.12	69.9	25.1	125	25.4	226	46.1	9740	1.11	46.2	4.35	8.36	58.9	103	167
			R	Samphire-007-G86-rim-1	<0.6	260	<109	12.3	<0.45	<26.4	676	2.88	<0.17	<0.012	13.4	0.047	0.66	1.71	0.346	12.2	4.37	55.9	21.5	107	22.4	203	42	9600	0.996	44.8	4.64	8.07	57.5	95.9	165

TABLE A2 LA-ICP-MS CONTINUED

C	762	G171	C1	Samphire-762-G171-core-1	0.93	272	316	17	<0.44	<25.3	760	5.33	0.31	<0.012	27.6	0.136	1.3	2.46	0.416	13.8	4.92	60.1	24	123	27.2	255	51.6	10300	2.02	83.6	8.09	17.3	109	213	315
			C2	Samphire-762-G171-core-2	83.6	290	241	28.2	3.93	73.8	1290	145	0.68	1.43	36.6	2.65	15.2	18.5	1.78	42.5	15	146	45.8	200	42.5	397	72.5	10900	4.76	70.9	6.97	12.6	90.5	1790	273
			R	Samphire-762-G171-rim-1	3.42	227	269	15.9	0.69	<23.9	509	7.19	0.3	0.048	22.6	0.142	0.95	1.87	0.217	8.44	2.92	41.9	15.6	80.6	18.5	168	36.2	10500	1.51	60.8	6.22	10.6	77.7	150	231
		G163	C	Samphire-762-G163-core-1	106	520	375	11	9.44	637	1590	43	0.67	1.36	41.6	2.56	15.9	14	1.78	40.4	12.8	145	50.7	244	51.3	462	89.5	8060	2.5	71.7	6.4	17.9	96.1	291	296
		G162	C	Samphire-762-G162-core-1	38.3	295	<111	19.8	2.85	73.3	979	48.2	1.01	0.7	28.9	1.03	6.84	12.2	0.84	27.2	9.3	99.3	33.4	142	31.9	282	54	10000	2.7	82.7	8.94	16.6	108	256	328
			R	Samphire-762-G162-rim-1	6.46	294	<134	11.3	0.69	150	777	13.3	0.27	0.165	16	0.72	2.74	5.36	0.54	20.6	7.43	74.9	25.9	119	26	207	45.5	8730	1.28	83.4	8.42	16.8	109	160	264
		G161	C	Samphire-762-G161-core-1	3.33	279	<123	3.91	<0.54	<31.6	953	17.8	0.28	0.053	13.4	0.179	1.54	4.14	0.11	18.8	6.34	87.7	32	157	30.5	271	49.3	9950	6.5	128	14.8	12.5	155	110	349
		G149	C	Samphire-762-G149-core-1	22.4	261	226	12.9	2.59	40.2	1160	14.3	0.18	0.439	32.8	0.723	4.37	6.96	1.16	25.3	8.17	105	36.2	176	37.1	365	71.4	10200	2.26	76.4	7.24	18.3	102	232	300
			R	Samphire-762-G149-rim-1	18.1	264	<113	16.4	2.46	194	1210	16.6	<0.17	0.201	27.3	0.514	3.53	5.28	0.79	28.2	9.19	111	38.9	191	38.9	363	71.3	9890	1.72	83.7	8.95	22.9	116	277	315
		G148	R	Samphire-762-G148-rim-1	150	500	<126	861	27.1	1790	1170	38.5	1.51	20	40.4	6.49	26.7	7.66	0.9	22.7	7.01	99.4	40	202	45	403	79.9	13600	6.19	96.5	10.2	12.9	120	64.5	593
			C	Samphire-762-G148-core-1	<0.63	326	<119	5.2	<0.52	<29.5	1640	1.45	<0.175	0.034	4.16	0.466	5.96	10.9	2.5	52.9	15.3	169	58.5	256	46.7	405	78.1	7380	0.44	14.3	1.01	2.35	17.6	41.6	76.7
		G147	C	Samphire-762-G147-core-1	2.31	196	<121	12	<0.5	<30.9	574	2.66	<0.19	<0.017	17.3	0.071	0.8	2.54	0.321	8.75	3.85	47.9	18.3	89.5	18.8	176	36.3	7830	0.819	46.8	5.22	11.8	63.8	121	149
		G142	C	Samphire-762-G142-core-1	20.3	344	429	29.9	1.7	<30.5	877	12.8	0.25	0.71	28.2	0.427	3.93	3.79	0.39	15.7	7.33	82.2	27.9	144	28.3	280	58.7	10600	2.51	57.9	6.19	15.1	79.2	258	291
			R	Samphire-762-G142-rim-1	198	425	254	48.2	27	310	2610	150	0.82	9.03	67.7	7.44	32.8	39	3.49	88	30.6	308	85.4	400	79.9	749	127	9680	15.6	77	8.4	28.7	114	972	668
		G137	C	Samphire-762-G137-core-1	224	381	1080	92.3	18.3	1320	2540	219	0.4	3.46	63.5	7.1	39.8	52	5	95.4	31.8	314	84.6	377	82.2	656	119	8950	5.77	83.8	8.57	21	113	978	323
		G135	C-white	Samphire-762-G135-rimwhite-1	528	344	<202	1530	66.7	1730	963	120	2.93	1.37	31.7	2.15	12	13.5	1.02	25.8	10.4	103	31.5	155	32.2	316	62.3	11400	16.8	99	11	21.8	132	536	393
		G126	C	Samphire-762-G126-core-1	<0.66	362	153	18.5	<0.49	<29.4	1180	1.87	0.16	0.081	21	0.259	4.37	5.79	1.14	29.3	9.56	105	38.9	180	35.8	317	62.3	8330	0.93	55.4	5.07	17.2	77.7	186	184
			R	Samphire-762-G126-rim-1	<0.69	307	<134	17.4	<0.55	<32.7	579	3.57	0.3	0.023	18.6	0.071	0.84	2.12	0.418	9.56	3.87	48.9	18	90.6	20.1	182	37.3	8410	1.16	56.1	6.12	12.2	74.4	125	175
		G94	C	Samphire-762-G94-core-1	3.89	319	226	15.2	<0.45	76.9	1800	8.5	0.16	0.04	23.6	0.439	5.64	8.61	1.12	40.7	12.7	158	56.9	268	51.9	473	88.3	10500	1.72	86.6	8.02	24.4	119	342	323
		G64	C	Samphire-762-G64-core-1	<0.6	328	<117	10.7	0.63	<29.4	1900	3.38	<0.136	0.058	33.4	0.342	6.57	9.22	1.71	43.8	13.7	173	59.9	299	57.8	525	102	8410	1.59	164	16.7	49.3	230	508	530
			R-inner	Samphire-762-G64-innerrim-1	20.6	376	<127	11.9	2.63	148	1780	6.73	0.23	0.755	36.4	0.721	8.24	9.44	1.28	40.4	12.9	155	59.2	275	54.8	499	99.9	8610	1.86	149	15	42.3	207	471	507
			R-outer	Samphire-762-G64-outerrim-1	11.3	322	<99	11.1	7.71	193	1700	5.88	0.26	0.251	44	0.373	3.65	7.75	1.39	38.9	12.2	148	56.2	269	54.4	508	99.8	10100	2.41	159	15.8	44.6	220	548	608

ELECTRONIC APPENDIX B FOR CHAPTER 3 – TABLES A3 SHRIMP

GRANITE A

Spot Name	Date/Time	4-corr %com 206	4-corr %com 208	4-corr 208Pb* /206Pb*	% err	ppm U	ppm Th	4-corr ppm 206*	4-corr ppm 208*	232Th /238U	% err	Total 206Pb /238U	% err	Total 208Pb /232Th	% err
MRC007.31	2017-10-19, 23:48	0.06	0.48	0.294	1.4	113	114	26	7.9	1.04	1.07	0.272	1.6	0.077	2.4
MRC007.32	2017-10-20, 00:06	0.00	0.00	0.200	3.9	126	82	30	6.1	0.68	1.48	0.281	8.8	0.083	9.8
MRC007.33	2017-10-20, 00:25	-0.07	-0.67	0.248	1.0	314	263	77	19.3	0.86	0.77	0.286	1.2	0.081	1.7
MRC007.34	2017-10-20, 01:07	0.04	0.55	0.181	1.5	186	117	43	7.9	0.65	0.41	0.272	1.4	0.076	2.0
MRC007.35	2017-10-20, 01:26	0.19	2.13	0.192	2.0	132	84	32	6.1	0.66	0.48	0.279	1.6	0.083	2.3
MRC007.36	2017-10-20, 01:44	0.09	0.92	0.226	1.6	173	129	41	9.5	0.77	0.95	0.280	1.4	0.083	2.2
MRC007.37	2017-10-20, 02:26	0.08	0.64	0.272	1.2	208	187	49	13.4	0.93	1.07	0.274	2.2	0.081	2.7
MRC007.38	2017-10-20, 02:45	0.00	0.00	0.204	1.5	139	95	34	7.0	0.71	0.46	0.284	1.5	0.082	2.2
MRC007.39	2017-10-20, 03:03	-0.20	-2.71	0.171	2.2	128	73	32	5.5	0.59	0.52	0.290	1.6	0.081	2.5
MRC007.40	2017-10-20, 03:45	0.33	2.85	0.249	1.9	129	111	32	7.9	0.89	0.79	0.287	1.6	0.082	2.3
MRC007A.1	2017-10-23, 00:25	0.06	0.64	0.200	4.7	537	362	129	26.2	0.70	4.13	0.281	1.0	0.081	6.3
MRC007A.2	2017-10-23, 00:44	0.08	0.87	0.194	3.1	401	267	94	18.4	0.69	1.86	0.273	1.4	0.077	3.8
MRC007A.3	2017-10-23, 01:02	0.04	0.49	0.162	1.4	123	68	30	4.9	0.57	0.38	0.282	1.3	0.081	1.9
MRC007A.4	2017-10-23, 01:43	0.11	1.07	0.223	1.3	132	100	32	7.1	0.79	0.35	0.280	1.3	0.080	1.8
MRC007A.5	2017-10-23, 02:02	-0.09	-1.14	0.175	1.6	113	67	28	4.9	0.61	0.41	0.287	1.4	0.082	2.0
MRC007A.6	2017-10-23, 02:20	0.08	1.03	0.173	1.3	192	110	45	7.8	0.60	0.31	0.273	1.2	0.080	1.7
MRC007A.7	2017-10-23, 03:02	0.11	1.15	0.217	1.9	162	121	41	8.9	0.77	0.94	0.292	1.2	0.083	2.4
MRC007A.8	2017-10-23, 03:20	0.07	0.60	0.272	1.2	121	112	29	8.1	0.96	0.87	0.283	1.3	0.081	1.9
MRC007A.9	2017-10-23, 03:39	-0.03	-0.34	0.185	1.1	172	106	41	7.7	0.64	0.60	0.280	1.2	0.081	1.7
MRC007A.10	2017-10-23, 04:20	0.04	0.35	0.275	0.7	311	291	74	20.5	0.97	0.37	0.277	1.1	0.079	1.3
MRC007A.11	2017-10-23, 04:39	0.20	2.21	0.196	1.4	150	100	36	7.2	0.68	0.74	0.281	1.3	0.082	1.9

																---------- 204 corrected ----------					
204corr 206Pb /238U Age	1σ err	204corr 207Pb /206Pb Age	1σ err	204corr 208Pb /232Th Age	1σ err	% Dis-cor-dant	4corr 208* /232	% err	Total 238 /206	% err	Total 207 /206	% err	4corr 238 /206*	% err	4corr 207* /206*	% err	4corr 207* /235	% err	4corr 206* /238	% err	err corr
1552	23	1622	31	1499	35	+5	0.077	2.4	3.67	1.6	0.100	1.57	3.67	1.6	0.100	1.7	3.7	2.3	0.272	1.6	0.7
1598	125	1611	29	1618	152	+1	0.083	9.8	3.55	8.8	0.099	1.54	3.55	8.8	0.099	1.5	3.9	9.0	0.281	8.8	1.0
1621	17	1626	19	1594	27	+0	0.082	1.7	3.50	1.2	0.099	0.98	3.50	1.2	0.100	1.0	3.9	1.6	0.286	1.2	0.8
1548	20	1571	26	1473	30	+2	0.076	2.1	3.68	1.4	0.098	1.33	3.68	1.4	0.097	1.4	3.6	2.0	0.271	1.4	0.7
1582	22	1566	35	1570	40	-1	0.081	2.6	3.59	1.6	0.099	1.58	3.59	1.6	0.097	1.9	3.7	2.4	0.278	1.6	0.6
1590	20	1566	28	1596	36	-2	0.082	2.3	3.57	1.4	0.098	1.35	3.58	1.4	0.097	1.5	3.7	2.1	0.280	1.4	0.7
1558	31	1585	25	1555	41	+2	0.080	2.7	3.66	2.2	0.099	1.26	3.66	2.2	0.098	1.4	3.7	2.6	0.273	2.2	0.9
1611	22	1604	28	1589	34	-0	0.082	2.2	3.52	1.5	0.099	1.51	3.52	1.5	0.099	1.5	3.9	2.2	0.284	1.5	0.7
1642	24	1611	36	1622	45	-2	0.084	2.9	3.45	1.6	0.098	1.65	3.45	1.7	0.099	1.9	4.0	2.5	0.290	1.7	0.7
1620	24	1485	41	1547	40	-10	0.080	2.7	3.49	1.6	0.096	1.61	3.50	1.6	0.093	2.2	3.7	2.7	0.286	1.6	0.6
1593	14	1571	12	1566	95	-2	0.081	6.3	3.56	1.0	0.098	0.62	3.57	1.0	0.097	0.6	3.8	1.2	0.280	1.0	0.8
1554	20	1597	13	1495	55	+3	0.077	3.8	3.67	1.4	0.099	0.65	3.67	1.4	0.099	0.7	3.7	1.6	0.273	1.4	0.9
1601	19	1584	23	1558	29	-1	0.080	2.0	3.55	1.3	0.098	1.19	3.55	1.3	0.098	1.2	3.8	1.8	0.282	1.3	0.7
1589	18	1565	25	1542	28	-2	0.079	1.9	3.57	1.3	0.098	1.19	3.58	1.3	0.097	1.3	3.7	1.9	0.280	1.3	0.7
1630	20	1591	26	1602	33	-3	0.083	2.2	3.48	1.4	0.097	1.32	3.48	1.4	0.098	1.4	3.9	2.0	0.288	1.4	0.7
1555	17	1622	21	1538	26	+5	0.079	1.8	3.66	1.2	0.101	1.03	3.67	1.2	0.100	1.1	3.8	1.6	0.273	1.2	0.7
1648	18	1575	22	1593	38	-5	0.082	2.5	3.43	1.2	0.098	1.06	3.43	1.2	0.097	1.2	3.9	1.7	0.291	1.2	0.7
1603	19	1558	25	1556	30	-3	0.080	2.0	3.54	1.3	0.097	1.21	3.54	1.3	0.097	1.3	3.8	1.9	0.282	1.3	0.7
1590	17	1597	20	1581	27	+0	0.081	1.8	3.58	1.2	0.098	1.06	3.58	1.2	0.099	1.1	3.8	1.6	0.280	1.2	0.8
1575	15	1580	15	1529	20	+0	0.079	1.3	3.61	1.1	0.098	0.75	3.61	1.1	0.098	0.8	3.7	1.3	0.277	1.1	0.8
1591	18	1578	25	1557	31	-1	0.080	2.1	3.56	1.3	0.099	1.13	3.57	1.3	0.098	1.4	3.8	1.9	0.280	1.3	0.7

GRANITE B

Spot Name	Date/Time	4-corr %com 206	4-corr %com 208	4-corr 208Pb* /206Pb*	% err	ppm U	ppm Th	4-corr ppm 206*	4-corr ppm 208*	232Th /238U	% err	Total 206Pb /238U	% err	Total 208Pb /232Th	% err
MRC005.1	2017-10-19, 14:39	-0.26	-4.94	0.122	3.0	108	44	25	3.1	0.42	0.62	0.267	1.6	0.075	2.7
MRC005.2	2017-10-19, 14:58	0.00	0.00	0.207	1.6	116	81	25	5.2	0.72	0.47	0.249	1.6	0.071	2.3
MRC005.3	2017-10-19, 15:16	-0.02	-0.41	0.106	1.2	385	136	90	9.6	0.37	0.31	0.271	1.8	0.078	2.1
MRC005.4	2017-10-19, 16:42	-0.18	-2.53	0.160	2.1	251	137	49	7.9	0.56	0.81	0.227	1.4	0.063	2.4
MRC005.5	2017-10-19, 17:48	0.05	0.80	0.132	1.3	512	226	118	15.7	0.46	0.32	0.268	1.2	0.078	1.7
MRC005.6	2017-10-19, 18:07	1.83	4.69	0.837	4.4	23	59	5	4.1	2.67	1.33	0.250	4.6	0.081	6.0
MRC005.7	2017-10-19, 19:23	-0.04	-1.00	0.084	1.4	532	148	135	11.5	0.29	0.57	0.294	1.1	0.086	1.8
MRC005.8	2017-10-19, 19:42	0.03	0.33	0.184	1.1	273	168	65	12.2	0.64	0.80	0.279	1.2	0.081	1.8
MRC005.9	2017-10-19, 20:01	0.04	0.65	0.131	2.7	213	91	51	6.7	0.44	1.54	0.279	1.3	0.083	3.3
MRC005.10	2017-10-19, 21:17	-0.02	-0.26	0.135	1.0	484	218	115	15.7	0.46	0.27	0.276	1.1	0.080	1.5
MRC005.11	2017-10-19, 21:36	0.71	6.67	0.223	6.6	106	73	26	5.9	0.71	0.51	0.287	2.8	0.096	6.5
MRC005.12	2017-10-19, 21:54	-0.03	-0.36	0.175	1.2	247	142	59	10.4	0.59	0.34	0.278	1.3	0.081	1.7
MRC005.1…dup1	2017-10-23, 04:57	0.04	0.54	0.164	1.5	123	69	30	5.0	0.58	0.39	0.289	1.3	0.082	2.0
MRC005.2…dup1	2017-10-23, 05:39	0.04	0.51	0.180	1.0	247	144	58	10.5	0.60	0.28	0.272	1.1	0.082	1.5
MRC005.3…dup1	2017-10-23, 05:57	-0.02	-0.31	0.157	1.1	225	120	54	8.6	0.55	0.29	0.281	1.2	0.080	1.6
MRC005.4…dup1	2017-10-23, 06:16	0.09	1.03	0.184	1.5	111	68	26	4.9	0.63	0.78	0.276	1.4	0.081	2.1
MRC005.5…dup1	2017-10-23, 06:57	0.13	5.40	0.049	1.5	1359	214	182	9.0	0.16	0.18	0.156	1.2	0.050	1.5
MRC005.6…dup1	2017-10-23, 07:16	0.22	4.94	0.093	1.9	582	178	132	12.4	0.32	2.44	0.264	1.4	0.082	3.2
MRC005.7…dup1	2017-10-23, 07:35	0.07	1.20	0.121	1.3	231	93	56	6.8	0.42	0.88	0.280	1.2	0.082	1.8
MRC005.8…dup1	2017-10-23, 08:16	0.15	2.24	0.147	1.8	123	62	29	4.3	0.52	0.40	0.275	1.3	0.079	2.0
MRC005.9…dup1	2017-10-23, 08:34	0.00	0.00	0.162	0.8	392	212	94	15.3	0.56	0.73	0.278	1.9	0.080	2.2
MRC005.10…dup1	2017-10-23, 08:53	0.11	1.53	0.163	1.8	380	207	88	14.5	0.56	1.66	0.271	1.0	0.080	2.6

								---------- 204 corrected ----------											
204corr 206Pb /238U Age	1σ err	204corr 207Pb /206Pb Age	1σ err	204corr 208Pb /232Th Age	1σ err	% Dis-cor-dant	4corr 208* /232	% err	Total 238 /206	% err	Total 207 /206	% err	4corr 238 /206*	% err	4corr 207* /206*	% err	4corr 207* /235	% err	4corr 206* /238	% err	err corr
1530	22	1593	37	1532	53	+4	0.079	3.6	3.74	1.6	0.096	1.64	3.73	1.6	0.098	2.0	3.6	2.5	0.27	1.6	0.6
1434	20	1578	31	1395	31	+10	0.071	2.3	4.02	1.6	0.098	1.68	4.02	1.6	0.098	1.7	3.3	2.3	0.25	1.6	0.7
1546	24	1576	17	1533	32	+2	0.079	2.2	3.69	1.8	0.097	0.87	3.69	1.8	0.097	0.9	3.6	2.0	0.27	1.8	0.9
1323	17	1572	33	1263	34	+17	0.064	2.8	4.40	1.4	0.096	1.53	4.39	1.4	0.097	1.7	3.1	2.3	0.23	1.4	0.6
1528	16	1574	19	1509	26	+3	0.078	1.8	3.74	1.2	0.098	0.97	3.74	1.2	0.097	1.0	3.6	1.6	0.27	1.2	0.8
1416	60	1118	333	1500	100	-30	0.077	6.9	4.00	4.6	0.093	6.10	4.07	4.8	0.077	16.7	2.6	17.4	0.25	4.8	0.3
1664	17	1603	16	1676	31	-4	0.086	1.9	3.40	1.1	0.099	0.86	3.39	1.1	0.099	0.9	4.0	1.4	0.29	1.1	0.8
1585	17	1577	20	1569	28	-1	0.081	1.9	3.59	1.2	0.098	1.05	3.59	1.2	0.097	1.1	3.7	1.6	0.28	1.2	0.8
1585	19	1576	24	1606	52	-1	0.083	3.4	3.59	1.3	0.098	1.24	3.59	1.3	0.097	1.3	3.7	1.8	0.28	1.3	0.7
1573	15	1587	15	1566	22	+1	0.081	1.5	3.62	1.1	0.098	0.79	3.62	1.1	0.098	0.8	3.7	1.4	0.28	1.1	0.8
1617	40	1635	123	1735	114	+1	0.090	6.9	3.48	2.8	0.107	5.94	3.51	2.8	0.101	6.6	4.0	7.2	0.29	2.8	0.4
1580	18	1587	20	1586	27	+0	0.082	1.8	3.60	1.3	0.098	1.06	3.60	1.3	0.098	1.1	3.8	1.7	0.28	1.3	0.8
1638	19	1627	24	1592	31	-1	0.082	2.0	3.46	1.3	0.100	1.25	3.46	1.3	0.100	1.3	4.0	1.9	0.29	1.3	0.7
1551	16	1587	18	1585	24	+3	0.082	1.5	3.67	1.1	0.098	0.90	3.68	1.1	0.098	0.9	3.7	1.5	0.27	1.1	0.8
1598	16	1593	17	1560	24	-0	0.080	1.6	3.56	1.2	0.098	0.92	3.55	1.2	0.098	0.9	3.8	1.5	0.28	1.2	0.8
1569	19	1592	26	1560	33	+2	0.080	2.2	3.63	1.4	0.099	1.30	3.63	1.4	0.098	1.4	3.7	2.0	0.28	1.4	0.7
934	10	1308	11	931	18	+31	0.047	1.9	6.40	1.2	0.086	0.50	6.41	1.2	0.085	0.6	1.8	1.3	0.16	1.2	0.9
1507	19	1585	14	1514	49	+6	0.078	3.4	3.79	1.4	0.100	0.60	3.80	1.4	0.098	0.7	3.6	1.6	0.26	1.4	0.9
1589	16	1592	18	1572	30	+0	0.081	2.0	3.57	1.2	0.099	0.92	3.58	1.2	0.098	1.0	3.8	1.5	0.28	1.2	0.8
1566	19	1510	27	1502	33	-4	0.077	2.3	3.63	1.3	0.095	1.24	3.64	1.3	0.094	1.4	3.6	2.0	0.27	1.3	0.7
1582	27	1593	13	1565	33	+1	0.080	2.2	3.59	1.9	0.098	0.69	3.59	1.9	0.098	0.7	3.8	2.0	0.28	1.9	0.9
1543	14	1550	15	1526	39	+1	0.078	2.7	3.69	1.0	0.097	0.73	3.70	1.0	0.096	0.8	3.6	1.3	0.27	1.0	0.8

GRANITE C

Spot Name	Date/Time	4-corr %com 206	4-corr %com 208	4-corr 208Pb* /206Pb*	% err	ppm U	ppm Th	4-corr ppm 206*	4-corr ppm 208*	232Th /238U	% err	Total 206Pb /238U	% err	Total 208Pb /232Th	% err
MRM762.41	2017-10-20, 04:04	-0.05	-0.58	0.190	1.6	169	104	40	7.7	0.64	1.35	0.276	2.6	0.082	3.3
MRM762.42	2017-10-20, 04:24	0.05	0.45	0.231	1.0	385	376	92	21.6	1.01	0.83	0.280	2.1	0.064	2.4
MRM762.43	2017-10-20, 05:07	0.24	2.19	0.236	1.6	179	142	41	9.7	0.82	0.40	0.267	1.5	0.078	2.0
MRM762.44	2017-10-20, 05:26	0.10	0.79	0.283	1.1	245	231	60	17.1	0.98	0.82	0.283	1.3	0.083	1.9
MRM762.45	2017-10-20, 05:45	0.17	2.63	0.138	3.8	412	189	54	7.5	0.47	1.41	0.153	2.0	0.046	4.2
MRM762.46	2017-10-20, 06:27	0.11	1.02	0.238	1.0	359	293	85	20.4	0.84	0.27	0.276	1.2	0.079	1.5
MRM762.47	2017-10-20, 06:46	0.04	1.18	0.079	1.3	513	164	140	11.2	0.33	1.37	0.319	1.1	0.078	2.1
MRM762.48	2017-10-20, 07:05	0.04	0.62	0.159	0.9	559	309	134	21.6	0.57	0.82	0.279	1.1	0.078	1.6
MRM762.49	2017-10-20, 07:48	0.06	0.56	0.219	1.1	336	303	66	14.6	0.93	2.33	0.229	1.2	0.054	2.8
MRM762.50	2017-10-20, 08:06	0.33	12.39	0.050	3.5	4808	543	372	18.7	0.12	1.95	0.090	0.9	0.044	3.4
MRM762.42…dup1	2017-10-22, 17:27	-0.02	-0.32	0.168	1.2	309	178	76	12.9	0.59	0.22	0.287	1.0	0.081	1.6
MRM762.43…dup1	2017-10-22, 17:46	0.10	1.12	0.194	0.8	336	348	74	14.6	1.07	0.93	0.258	1.0	0.047	1.5
MRM762.41…dup1	2017-10-22, 18:05	0.15	1.08	0.302	1.6	59	58	14	4.3	1.02	1.98	0.283	1.6	0.084	3.0
MRM762.44…dup1	2017-10-22, 18:54	0.08	0.61	0.271	1.0	170	173	37	10.1	1.05	0.27	0.254	2.2	0.066	2.4
MRM762.45…dup1	2017-10-22, 20:07	0.06	0.48	0.283	1.4	216	208	52	14.9	0.99	0.40	0.282	1.5	0.081	2.1
MRM762.46…dup1	2017-10-22, 20:25	0.09	0.61	0.316	0.8	212	222	50	16.1	1.08	0.46	0.277	1.1	0.081	1.5
MRM762.47…dup1	2017-10-22, 20:44	0.12	0.86	0.310	1.0	155	217	34	10.5	1.45	1.03	0.252	1.2	0.054	1.9
MRM762.48…dup1	2017-10-22, 21:59	0.06	0.59	0.243	0.9	210	173	52	12.7	0.85	0.27	0.287	1.2	0.082	1.5
MRM762.49…dup1	2017-10-22, 22:17	0.12	1.15	0.223	2.0	930	665	125	28.2	0.74	1.01	0.157	3.4	0.048	4.1
MRM762.50…dup1	2017-10-22, 22:36	0.13	1.30	0.223	1.2	139	103	34	7.6	0.77	0.34	0.285	1.3	0.084	1.7

														---------- 204 corrected ----------						
204corr 206Pb /238U Age	1σ err	204corr 207Pb /206Pb Age	1σ err	204corr 208Pb /232Th Age	1σ err	% Dis-cor-dant	4corr 208* /232	% err	Total 238 /206	% err	Total 207 /206	% err	4corr 238 /206*	% err	4corr 207* /206*	% err	4corr 207* /235	% err	4corr 206* /238	% err	err corr
1571	36	1593	27	1598	52	+2	0.082	3.4	3.62	2.6	0.098	1.39	3.62	2.6	0.098	1.4	3.7	3.0	0.28	2.6	0.9
1589	29	1600	19	1253	29	+1	0.064	2.4	3.58	2.1	0.099	0.95	3.58	2.1	0.099	1.0	3.8	2.3	0.28	2.1	0.9
1520	20	1555	32	1493	32	+3	0.077	2.2	3.75	1.5	0.098	1.36	3.76	1.5	0.096	1.7	3.5	2.2	0.27	1.5	0.7
1606	19	1586	24	1598	29	-1	0.082	1.9	3.53	1.3	0.099	1.16	3.53	1.3	0.098	1.3	3.8	1.8	0.28	1.3	0.7
917	17	1057	32	879	38	+14	0.044	4.4	6.53	2.0	0.076	1.28	6.54	2.0	0.075	1.6	1.6	2.5	0.15	2.0	0.8
1570	17	1570	19	1516	23	+0	0.078	1.6	3.62	1.2	0.098	0.92	3.63	1.2	0.097	1.0	3.7	1.6	0.28	1.2	0.8
1785	17	1783	14	1492	32	-0	0.077	2.2	3.13	1.1	0.109	0.72	3.14	1.1	0.109	0.7	4.8	1.3	0.32	1.1	0.8
1586	15	1594	15	1516	24	+1	0.078	1.6	3.58	1.1	0.099	0.76	3.59	1.1	0.098	0.8	3.8	1.4	0.28	1.1	0.8
1330	15	1577	20	1062	29	+17	0.054	2.9	4.36	1.2	0.098	1.03	4.36	1.2	0.098	1.1	3.1	1.7	0.23	1.2	0.8
556	5	720	25	761	29	+24	0.038	3.9	11.06	0.9	0.066	1.00	11.10	0.9	0.063	1.2	0.8	1.5	0.09	0.9	0.6
1629	15	1592	13	1579	24	-3	0.081	1.6	3.48	1.0	0.098	0.69	3.48	1.0	0.098	0.7	3.9	1.3	0.29	1.0	0.8
1476	13	1572	14	922	14	+7	0.047	1.6	3.88	1.0	0.098	0.70	3.89	1.0	0.097	0.8	3.5	1.3	0.26	1.0	0.8
1602	23	1583	37	1618	48	-1	0.083	3.1	3.54	1.6	0.099	1.74	3.54	1.6	0.098	2.0	3.8	2.6	0.28	1.6	0.6
1456	28	1565	21	1282	30	+8	0.065	2.4	3.94	2.2	0.098	1.04	3.95	2.2	0.097	1.1	3.4	2.4	0.25	2.2	0.9
1598	21	1569	18	1562	31	-2	0.080	2.1	3.55	1.5	0.098	0.90	3.55	1.5	0.097	1.0	3.8	1.8	0.28	1.5	0.8
1575	16	1565	19	1569	22	-1	0.081	1.5	3.61	1.1	0.098	0.93	3.61	1.1	0.097	1.0	3.7	1.5	0.28	1.1	0.7
1450	16	1557	23	1060	20	+8	0.054	1.9	3.96	1.2	0.098	1.08	3.97	1.2	0.096	1.2	3.4	1.7	0.25	1.2	0.7
1624	17	1571	18	1593	23	-4	0.082	1.5	3.49	1.2	0.098	0.92	3.49	1.2	0.097	1.0	3.8	1.5	0.29	1.2	0.8
937	30	1417	13	934	37	+36	0.047	4.1	6.38	3.4	0.091	0.60	6.39	3.4	0.090	0.7	1.9	3.5	0.16	3.4	1.0
1613	18	1583	24	1603	28	-2	0.083	1.8	3.51	1.3	0.099	1.13	3.52	1.3	0.098	1.3	3.8	1.8	0.28	1.3	0.7

SUPPLEMENTARY MATERIAL C

FOR CHAPTER 4 – A MINERALISATION AGE FOR THE SEDIMENT-HOSTED BLACKBUSH URANIUM PROSPECT, NORTH-EASTERN EYRE PENINSULA, SOUTH AUSTRALIA

ELECTRONIC APPENDIX A FOR CHAPTER 4 – EPMA

														Error 1Sigma	
SAMPLE	CaO	UO2	Ce2O3	FeO	SiO2	P2O5	ThO2	PbO	Y2O3	TOTAL	U %ERR	Pb %ERR	Age (Ma)	Ma	rel.
Coffinite, sediment															
Un 10 18700_2	1.187	56.779	0.485	0.316	14.997	0.731	0.000	0.136	0.401	75.034	0.333	7.159	18.11	1.29	7%
Un 4 18700_2	1.358	55.831	0.415	0.078	16.427	0.688	0.000	0.131	0.211	75.139	0.337	7.896	17.62	1.39	8%
Un 10 18700_2	1.384	57.730	0.425	0.312	14.549	0.779	0.000	0.137	0.142	75.458	0.331	7.411	17.92	1.32	7%
Un 10 18700_2	1.425	57.702	0.457	0.023	14.775	0.778	0.012	0.137	0.351	75.660	0.331	7.443	17.92	1.33	7%
Un 26 19600_4	1.064	59.078	0.208	0.621	13.969	0.604	0.012	0.071	0.119	75.745	0.325	11.828	9.02	1.07	12%
Un 10 18700_2	1.364	57.899	0.488	0.273	14.877	0.695	0.000	0.110	0.198	75.904	0.330	9.211	14.32	1.32	9%
Un 9 19600_2	2.031	58.942	0.252	0.126	14.010	0.652	0.000	0.143	0.066	76.222	0.327	7.269	18.26	1.32	7%
Un 18 04693_2	1.097	59.202	0.200	0.422	14.678	0.578	0.000	0.136	0.006	76.318	0.325	7.661	17.28	1.32	8%
Un 20 18700_3	1.040	50.941	0.156	2.090	21.777	0.542	0.000	0.125	0.065	76.735	0.357	7.854	18.46	1.45	8%
Un 3 18700_1	1.448	57.529	0.472	0.258	16.146	0.694	0.000	0.122	0.240	76.909	0.331	8.516	15.99	1.36	8%
Un 4 18700_2	1.190	58.640	0.404	0.797	15.549	0.478	0.000	0.135	0.111	77.306	0.328	7.714	17.41	1.34	8%
Un 10 18700_2	1.219	59.339	0.366	0.510	15.188	0.590	0.000	0.118	0.112	77.443	0.326	8.294	15.04	1.24	8%
Un 27 18700_4	1.337	57.081	0.497	1.426	16.654	0.698	0.000	0.152	0.227	78.071	0.333	6.599	20.05	1.32	7%
Un 27 18700_4	1.299	58.468	0.543	0.389	16.415	0.712	0.000	0.136	0.314	78.275	0.329	7.325	17.50	1.28	7%
Un 27 18700_4	2.205	56.106	0.473	2.255	16.466	0.655	0.000	0.135	0.227	78.521	0.337	7.359	18.17	1.33	7%
Un 20 18700_3	1.075	58.375	0.153	1.977	16.100	0.682	0.018	0.152	0.015	78.547	0.329	6.876	19.62	1.34	7%
Un 7 04693_1	0.911	59.541	0.259	1.288	16.076	0.563	0.000	0.137	0.029	78.804	0.326	7.602	17.37	1.32	8%
Un 4 18700_2	1.436	58.856	0.483	0.666	16.470	0.732	0.000	0.120	0.213	78.975	0.328	8.600	15.32	1.31	9%
Un 27 18700_4	1.376	57.806	0.509	1.500	16.714	0.701	0.000	0.138	0.275	79.019	0.331	7.208	17.94	1.29	7%
Un 27 18700_4	1.573	59.386	0.575	0.134	16.369	0.667	0.007	0.147	0.186	79.043	0.326	6.945	18.61	1.29	7%
Un 9 19600_2	1.241	61.005	0.283	0.421	15.294	0.631	0.001	0.146	0.086	79.109	0.321	6.951	18.06	1.25	7%
Un 27 18700_4	1.427	58.996	0.487	1.091	16.096	0.760	0.000	0.122	0.246	79.225	0.327	8.392	15.61	1.31	8%
Un 18 04693_2	0.682	52.495	0.262	1.310	23.794	0.531	0.000	0.122	0.047	79.243	0.352	8.557	17.45	1.49	9%
Un 26 19600_4	1.185	61.530	0.225	0.560	15.051	0.727	0.000	0.169	0.057	79.504	0.319	6.070	20.69	1.25	6%
Un 3 18700_1	1.486	59.665	0.478	0.317	16.774	0.719	0.000	0.130	0.226	79.795	0.326	7.944	16.37	1.30	8%
Un 20 18700_3	1.111	61.242	0.266	0.776	15.562	0.658	0.010	0.126	0.067	79.819	0.321	8.093	15.56	1.26	8%
Un 27 18700_4	1.567	59.303	0.569	1.119	16.293	0.758	0.000	0.153	0.238	80.001	0.327	6.607	19.40	1.28	7%
Un 27 18700_4	1.483	60.179	0.515	0.399	16.420	0.793	0.000	0.135	0.302	80.225	0.324	7.519	16.88	1.27	8%
Un 10 18700_2	1.423	60.593	0.402	1.353	15.602	0.645	0.000	0.125	0.083	80.225	0.323	7.914	15.61	1.23	8%
Un 4 18700_2	1.401	59.179	0.532	0.708	17.314	0.779	0.000	0.130	0.338	80.382	0.327	7.850	16.61	1.30	8%
Un 27 18700_4	1.461	60.403	0.554	0.754	16.474	0.768	0.005	0.143	0.232	80.794	0.323	7.016	17.80	1.25	7%
Un 18 04693_2	0.883	58.688	0.397	0.894	19.747	0.575	0.000	0.116	0.047	81.347	0.330	9.054	14.88	1.34	9%
Un 26 19600_4	1.235	62.960	0.292	0.431	15.659	0.750	0.000	0.145	0.064	81.536	0.316	7.176	17.33	1.24	7%
Un 27 18700_4	1.405	56.944	0.479	2.980	18.766	0.681	0.000	0.142	0.188	81.585	0.335	7.074	18.80	1.33	7%
Un 27 18700_4	1.463	62.720	0.476	0.081	15.873	0.781	0.000	0.145	0.188	81.727	0.317	7.265	17.45	1.26	7%
Un 10 18700_2	1.467	62.101	0.540	0.160	16.315	0.768	0.000	0.138	0.272	81.761	0.319	7.334	16.74	1.22	7%
Un 3 18700_1	1.427	61.295	0.514	0.286	17.064	0.729	0.000	0.141	0.310	81.765	0.322	7.375	17.36	1.28	7%
Un 10 18700_2	1.416	63.098	0.365	0.298	16.112	0.588	0.000	0.142	0.108	82.127	0.316	7.253	16.92	1.22	7%
Un 8 06460_1	1.017	60.553	0.771	0.909	17.344	0.721	0.000	0.137	0.718	82.169	0.324	7.539	17.08	1.28	8%
Un 26 19600_4	3.530	62.947	0.252	0.838	13.666	0.771	0.000	0.166	0.024	82.195	0.316	6.340	19.86	1.26	6%
Un 7 04693_1	0.937	61.665	0.206	1.399	17.307	0.604	0.000	0.145	0.025	82.288	0.321	7.377	17.76	1.31	7%
Un 27 18700_4	1.443	61.760	0.566	0.693	16.913	0.744	0.000	0.137	0.274	82.530	0.320	7.512	16.74	1.25	7%
Un 7 04693_1	1.042	61.030	0.340	0.471	18.932	0.617	0.000	0.134	0.020	82.585	0.323	7.852	16.52	1.29	8%
Un 10 18700_2	1.433	62.977	0.551	0.231	16.263	0.739	0.000	0.131	0.298	82.623	0.316	7.948	15.69	1.24	8%
Un 18 04693_2	0.820	59.924	0.119	2.587	18.460	0.613	0.000	0.099	0.000	82.623	0.327	10.292	12.50	1.28	10%
Un 20 18700_3	1.216	63.624	0.207	1.315	15.291	0.811	0.008	0.151	0.043	82.666	0.314	6.995	17.94	1.25	7%
Un 3 18700_1	1.502	60.511	0.546	1.139	17.923	0.708	0.000	0.131	0.279	82.738	0.323	8.052	16.37	1.32	8%
Un 7 04693_1	1.099	63.894	0.249	0.768	16.133	0.541	0.000	0.140	0.011	82.836	0.314	7.472	16.52	1.23	7%
Un 9 19600_2	1.424	64.465	0.201	0.602	15.154	0.872	0.000	0.144	0.027	82.889	0.312	7.256	16.86	1.22	7%
Un 10 18700_2	1.315	62.824	0.527	0.231	16.806	0.767	0.000	0.140	0.438	83.048	0.317	7.334	16.83	1.23	7%
Un 11 17900_2	1.061	62.224	0.662	0.886	17.005	0.524	0.000	0.139	0.783	83.284	0.318	7.581	16.89	1.28	8%
Un 4 18700_2	1.423	61.685	0.563	1.192	17.181	0.760	0.000	0.151	0.376	83.332	0.320	6.963	18.47	1.28	7%
Un 4 18700_2	1.510	61.778	0.537	1.595	16.765	0.744	0.000	0.163	0.270	83.363	0.320	6.412	19.87	1.27	6%
Un 26 19600_4	1.293	64.570	0.182	0.682	15.692	0.839	0.000	0.113	0.046	83.418	0.312	8.316	13.22	1.10	8%
Un 27 18700_4	1.391	61.760	0.527	1.608	16.938	0.770	0.012	0.152	0.291	83.449	0.320	6.707	18.54	1.24	7%
Un 4 18700_2	1.495	64.218	0.492	0.074	15.900	0.756	0.000	0.131	0.395	83.462	0.314	8.022	15.39	1.23	8%
Un 7 04693_1	1.017	61.875	0.299	1.824	17.705	0.599	0.000	0.137	0.030	83.485	0.320	7.694	16.68	1.28	8%
Un 27 18700_4	1.542	63.108	0.530	0.206	17.059	0.752	0.000	0.139	0.219	83.555	0.317	7.596	16.56	1.25	8%
Un 18 04693_2	1.071	62.190	0.290	0.501	18.693	0.625	0.000	0.158	0.034	83.562	0.320	6.724	19.11	1.28	7%
Un 3 18700_1	1.459	62.550	0.537	0.385	17.490	0.730	0.000	0.145	0.316	83.612	0.320	7.142	17.51	1.25	7%
Un 17 06460_2	1.018	62.191	0.712	0.969	17.174	0.694	0.000	0.141	0.723	83.622	0.319	7.458	17.03	1.27	7%
Un 27 18700_4	1.570	63.307	0.550	0.322	16.749	0.833	0.000	0.155	0.241	83.726	0.316	6.738	18.51	1.24	7%
Un 9 19600_2	1.675	64.108	0.207	0.924	16.040	0.771	0.000	0.127	0.029	83.881	0.314	8.345	14.89	1.24	8%
Un 10 18700_2	1.433	63.957	0.547	0.134	16.696	0.834	0.007	0.137	0.196	83.942	0.314	7.681	16.15	1.24	8%
Un 17 06460_2	1.241	62.041	0.796	1.021	17.375	0.768	0.000	0.160	0.588	83.989	0.319	6.513	19.38	1.26	6%
Un 7 04693_1	1.145	63.684	0.347	0.384	17.603	0.661	0.000	0.126	0.083	84.033	0.315	8.360	14.97	1.25	8%
Un 4 18700_2	1.269	63.599	0.357	2.834	15.200	0.575	0.016	0.149	0.096	84.097	0.314	7.062	17.71	1.25	7%
Un 7 04693_1	1.104	64.485	0.323	0.634	16.772	0.630	0.000	0.117	0.038	84.103	0.313	9.258	13.68	1.26	9%
Un 27 18700_4	1.516	63.884	0.547	0.068	16.914	0.775	0.000	0.131	0.296	84.131	0.314	7.821	15.47	1.21	8%
Un 6 17900_1	1.001	63.026	0.613	0.282	17.480	0.537	0.000	0.152	1.202	84.292	0.317	6.895	18.13	1.25	7%
Un 9 19600_2	1.294	58.223	0.271	0.340	23.208	0.777	0.000	0.148	0.060	84.320	0.333	6.986	19.18	1.34	7%

Un 7 04693_1	0.918	63.471	0.383	0.655	18.141	0.621	0.000	0.135	0.034	84.358	0.316	7.891	16.01	1.26	8%
Un 4 18700_2	1.464	65.823	0.385	0.131	15.640	0.661	0.000	0.142	0.137	84.383	0.310	7.401	16.26	1.20	7%
Un 18 04693_2	0.858	62.157	0.296	0.873	19.522	0.610	0.000	0.126	0.021	84.462	0.320	8.353	15.33	1.28	8%
Un 10 18700_2	1.291	64.592	0.517	0.145	16.472	0.859	0.000	0.145	0.463	84.484	0.312	7.123	16.92	1.20	7%
Un 10 18700_2	1.404	64.471	0.577	0.217	16.532	0.831	0.000	0.147	0.377	84.558	0.313	6.915	17.24	1.19	7%
Un 3 18700_1	1.578	63.678	0.513	0.215	17.408	0.767	0.040	0.158	0.268	84.627	0.315	6.703	18.72	1.25	7%
Un 26 19600_4	1.156	64.610	0.219	0.502	17.302	0.728	0.000	0.148	0.025	84.689	0.312	7.204	17.22	1.24	7%
Un 4 18700_2	1.400	62.342	0.545	0.535	18.631	0.810	0.000	0.137	0.348	84.749	0.320	7.660	16.60	1.27	8%
Un 9 19600_2	2.106	65.229	0.185	0.167	16.074	0.840	0.000	0.152	0.039	84.791	0.311	6.984	17.61	1.23	7%
Un 3 18700_1	1.561	64.221	0.579	0.078	17.228	0.750	0.000	0.124	0.273	84.815	0.313	8.493	14.51	1.23	8%
Un 18 04693_2	1.087	65.248	0.375	0.340	17.207	0.602	0.000	0.146	0.060	85.066	0.311	7.221	16.88	1.22	7%
Un 9 19600_2	1.498	63.723	0.237	0.938	17.577	0.909	0.000	0.157	0.046	85.086	0.315	6.719	18.58	1.25	7%
Un 4 18700_2	1.548	65.100	0.564	0.085	16.551	0.814	0.011	0.154	0.278	85.103	0.312	6.894	17.79	1.22	7%
Un 6 17900_1	1.235	63.525	0.697	0.238	17.556	0.768	0.000	0.156	0.985	85.160	0.316	6.759	18.50	1.25	7%
Un 17 06460_2	1.091	62.030	0.891	3.150	16.511	0.883	0.000	0.162	0.482	85.202	0.320	6.384	19.73	1.26	6%
Un 27 18700_4	1.558	64.332	0.579	0.094	17.377	0.830	0.000	0.140	0.298	85.210	0.313	7.210	16.38	1.18	7%
Un 27 18700_4	1.491	62.680	0.530	2.026	17.337	0.794	0.000	0.154	0.236	85.247	0.318	6.785	18.50	1.25	7%
Un 8 06460_1	1.152	63.006	0.890	2.228	16.720	0.749	0.000	0.164	0.381	85.290	0.317	6.480	19.66	1.27	6%
Un 10 18700_2	1.351	64.755	0.620	0.195	17.002	0.816	0.000	0.147	0.424	85.310	0.312	7.108	17.16	1.22	7%
Un 11 17900_2	1.054	63.212	0.767	0.248	18.036	0.773	0.000	0.115	1.110	85.316	0.316	9.102	13.71	1.25	9%
Un 7 04693_1	1.083	64.858	0.229	0.427	18.087	0.531	0.000	0.149	0.000	85.362	0.312	7.111	17.28	1.23	7%
Un 11 17900_2	1.024	64.348	0.674	0.440	17.198	0.620	0.000	0.142	0.929	85.374	0.313	7.393	16.61	1.22	7%
Un 7 04693_1	0.955	63.871	0.263	0.946	18.621	0.570	0.000	0.151	0.026	85.403	0.315	6.972	17.87	1.24	7%
Un 6 17900_1	1.144	64.062	0.696	0.351	17.263	0.742	0.000	0.120	1.107	85.485	0.315	8.786	14.15	1.24	9%
Un 27 18700_4	1.498	64.797	0.527	0.112	17.318	0.820	0.004	0.143	0.275	85.493	0.312	7.192	16.59	1.19	7%
Un 20 18700_3	1.292	66.745	0.268	0.996	15.208	0.830	0.000	0.143	0.036	85.518	0.306	7.216	16.14	1.16	7%
Un 6 17900_1	1.173	64.980	0.663	0.333	16.627	0.617	0.000	0.148	0.979	85.518	0.312	7.148	17.13	1.22	7%
Un 11 17900_2	1.051	64.323	0.712	0.175	17.539	0.671	0.000	0.149	1.002	85.622	0.313	7.072	17.44	1.23	7%
Un 26 19600_4	1.233	66.288	0.250	0.362	16.692	0.758	0.000	0.145	0.063	85.791	0.308	7.337	16.49	1.21	7%
Un 7 04693_1	1.189	66.681	0.237	0.362	16.519	0.622	0.000	0.159	0.038	85.807	0.307	6.685	17.93	1.20	7%
Un 5 19600_1	1.236	65.334	0.194	2.445	15.609	0.801	0.000	0.155	0.037	85.811	0.310	6.858	17.92	1.23	7%
Un 7 04693_1	1.086	66.172	0.251	0.429	17.237	0.531	0.000	0.133	0.013	85.852	0.309	7.979	15.15	1.21	8%
Un 10 18700_2	1.356	65.304	0.601	0.542	16.590	0.882	0.000	0.150	0.463	85.888	0.310	6.981	17.34	1.21	7%
Un 17 06460_2	1.067	63.030	0.729	0.879	18.273	0.934	0.005	0.171	0.801	85.888	0.318	6.193	20.42	1.26	6%
Un 20 18700_3	1.979	65.097	0.210	1.734	15.989	0.705	0.000	0.150	0.026	85.890	0.311	7.017	17.41	1.22	7%
Un 27 18700_4	1.556	65.033	0.522	0.041	17.573	0.865	0.000	0.136	0.274	86.001	0.311	7.708	15.77	1.21	8%
Un 6 17900_1	1.037	63.628	0.712	0.349	18.714	0.597	0.000	0.137	0.868	86.042	0.316	7.646	16.21	1.24	8%
Un 9 19600_2	2.165	66.080	0.239	0.106	16.420	0.800	0.013	0.158	0.079	86.060	0.309	6.784	18.01	1.22	7%
Un 26 19600_4	1.078	66.842	0.184	0.661	16.399	0.750	0.000	0.163	0.013	86.089	0.306	6.591	18.36	1.21	7%
Un 10 18700_2	1.221	65.587	0.564	0.138	16.935	0.924	0.030	0.148	0.543	86.091	0.310	6.809	17.06	1.16	7%
Un 7 04693_1	1.009	65.698	0.279	1.181	17.274	0.492	0.000	0.129	0.040	86.103	0.310	8.230	14.84	1.22	8%
Un 11 17900_2	1.070	65.034	0.708	0.307	17.556	0.563	0.000	0.139	0.748	86.125	0.311	7.571	16.17	1.22	8%
Un 5 19600_1	1.854	65.942	0.230	0.837	16.338	0.720	0.000	0.154	0.058	86.133	0.309	6.846	17.66	1.21	7%
Un 9 19600_2	1.976	64.889	0.172	2.484	15.669	0.768	0.000	0.170	0.030	86.157	0.312	6.262	19.70	1.23	6%
Un 3 18700_1	1.513	65.082	0.574	0.214	17.532	0.732	0.000	0.143	0.373	86.163	0.312	7.426	16.62	1.23	7%
Un 11 17900_2	0.854	55.271	0.666	0.718	26.993	0.611	0.000	0.118	0.938	86.168	0.344	8.538	16.06	1.37	9%
Un 18 04693_2	1.032	63.183	0.312	2.222	18.638	0.657	0.000	0.131	0.018	86.194	0.317	8.041	15.69	1.26	8%
Un 7 04693_1	0.936	65.039	0.335	1.138	17.939	0.652	0.000	0.124	0.065	86.228	0.312	8.585	14.37	1.23	9%
Un 7 04693_1	0.917	62.868	0.255	1.871	19.550	0.589	0.000	0.143	0.059	86.251	0.318	7.456	17.13	1.27	7%
Un 18 04693_2	0.953	67.580	0.336	0.297	16.386	0.571	0.000	0.143	0.025	86.292	0.305	7.471	15.99	1.19	7%
Un 6 17900_1	1.091	65.543	0.683	0.395	16.754	0.727	0.000	0.163	0.942	86.298	0.311	6.515	18.79	1.22	6%
Un 10 18700_2	1.371	65.697	0.570	0.161	17.112	0.841	0.000	0.167	0.390	86.310	0.310	6.139	19.21	1.18	6%
Un 10 18700_2	1.386	66.440	0.436	0.276	16.819	0.724	0.000	0.141	0.120	86.343	0.308	7.512	16.02	1.20	7%
Un 14 19600_3a	1.394	64.618	0.286	0.567	18.369	0.865	0.000	0.157	0.096	86.353	0.312	6.588	18.33	1.20	7%
Un 11 17900_2	0.991	65.354	0.676	0.130	17.496	0.633	0.000	0.150	0.936	86.365	0.310	6.972	17.25	1.20	7%
Un 5 19600_1	1.687	65.115	0.250	2.156	16.180	0.746	0.000	0.144	0.100	86.377	0.311	7.405	16.65	1.23	7%
Un 4 18700_2	1.605	65.483	0.575	0.090	17.261	0.846	0.000	0.142	0.386	86.389	0.311	7.514	16.34	1.22	7%
Un 5 19600_1	1.721	66.873	0.288	0.094	16.382	0.861	0.000	0.143	0.042	86.404	0.307	7.407	16.16	1.19	7%
Un 10 18700_2	1.475	66.976	0.404	0.345	16.319	0.648	0.000	0.141	0.100	86.407	0.306	7.486	15.91	1.19	7%
Un 11 17900_2	1.012	65.150	0.653	0.676	17.516	0.613	0.000	0.142	0.723	86.486	0.311	7.409	16.40	1.21	7%
Un 10 18700_2	1.292	65.944	0.579	0.160	16.980	0.910	0.007	0.143	0.528	86.543	0.309	7.393	16.31	1.20	7%
Un 7 04693_1	1.048	61.937	0.239	1.183	21.439	0.577	0.000	0.129	0.009	86.561	0.322	8.220	15.75	1.29	8%
Un 20 18700_3	1.014	63.752	0.184	3.885	16.870	0.723	0.000	0.166	0.029	86.621	0.315	6.404	19.57	1.25	6%
Un 20 18700_3	1.526	66.543	0.170	1.339	16.090	0.766	0.000	0.148	0.055	86.636	0.307	7.182	16.76	1.20	7%
Un 26 19600_4	5.120	63.183	0.224	1.409	15.790	0.741	0.000	0.155	0.022	86.644	0.317	6.702	18.44	1.23	7%
Un 20 18700_3	1.338	67.123	0.201	0.605	16.293	0.887	0.000	0.163	0.049	86.658	0.306	6.480	18.25	1.18	6%
Un 7 04693_1	1.001	64.560	0.201	1.196	18.939	0.665	0.000	0.153	0.000	86.716	0.313	6.905	17.91	1.23	7%
Un 7 04693_1	1.214	65.416	0.267	0.582	18.438	0.685	0.000	0.132	0.025	86.759	0.311	8.141	15.22	1.24	8%
Un 17 06460_2	1.092	63.722	0.869	1.764	17.865	0.763	0.000	0.126	0.565	86.766	0.315	8.364	14.89	1.24	8%
Un 20 18700_3	1.780	66.006	0.237	0.164	17.651	0.736	0.000	0.155	0.070	86.799	0.309	6.647	17.67	1.17	7%
Un 27 18700_4	1.531	66.080	0.547	0.066	17.402	0.822	0.000	0.138	0.287	86.872	0.309	7.462	15.75	1.17	7%
Un 6 17900_1	1.061	65.188	0.690	0.168	17.908	0.682	0.000	0.149	1.052	86.899	0.312	7.120	17.21	1.22	7%
Un 6 17900_1	0.997	65.363	0.690	0.520	17.710	0.652	0.000	0.168	0.813	86.914	0.311	6.124	19.38	1.18	6%
Un 9 19600_2	1.631	67.444	0.277	0.050	16.541	0.791	0.016	0.152	0.043	86.945	0.306	6.996	16.95	1.18	7%
Un 20 18700_3	1.900	67.482	0.159	0.457	16.063	0.823	0.000	0.134	0.030	87.049	0.305	7.924	15.00	1.19	8%

ELECTRONIC APPENDIX FOR CHAPTER 4 – CONTINUED

Un 27 18700_4	1.544	65.439	0.567	0.052	18.254	0.803	0.006	0.151	0.263	87.080	0.311	6.784	17.42	1.18	7%
Un 27 18700_4	1.535	66.531	0.594	0.075	17.309	0.753	0.000	0.133	0.216	87.147	0.308	8.003	15.06	1.20	8%
Un 9 19600_2	1.492	66.435	0.221	0.877	17.209	0.740	0.001	0.130	0.061	87.167	0.308	8.184	14.72	1.20	8%
Un 9 19600_2	1.523	67.942	0.220	0.828	15.631	0.815	0.000	0.156	0.054	87.169	0.304	6.779	17.29	1.17	7%
Un 3 18700_1	1.482	65.172	0.572	0.285	17.987	0.892	0.010	0.147	0.623	87.171	0.313	7.184	17.04	1.22	7%
Un 5 19600_1	1.521	67.273	0.314	0.301	16.639	0.743	0.000	0.160	0.234	87.184	0.306	6.614	17.97	1.18	7%
Un 6 17900_1	1.346	65.434	0.736	0.091	17.287	0.839	0.000	0.168	1.288	87.189	0.311	6.355	19.29	1.22	6%
Un 9 19600_2	1.479	66.773	0.295	0.587	16.956	0.843	0.000	0.148	0.112	87.193	0.307	7.208	16.68	1.20	7%
Un 27 18700_4	1.583	67.510	0.425	0.150	16.546	0.782	0.000	0.128	0.103	87.227	0.305	8.066	14.30	1.15	8%
Un 9 19600_2	1.307	65.526	0.267	0.930	18.078	0.722	0.000	0.151	0.281	87.261	0.311	7.015	17.34	1.21	7%
Un 6 17900_1	1.165	65.802	0.609	0.206	17.797	0.596	0.000	0.172	1.011	87.359	0.310	6.165	19.71	1.21	6%
Un 3 18700_1	1.447	65.962	0.516	0.157	17.737	0.900	0.000	0.158	0.545	87.422	0.310	6.695	18.00	1.20	7%
Un 9 19600_2	1.763	66.811	0.223	1.659	15.982	0.784	0.000	0.147	0.103	87.472	0.307	7.264	16.54	1.20	7%
Un 20 18700_3	1.375	66.764	0.222	0.407	17.785	0.749	0.000	0.151	0.067	87.521	0.307	7.031	17.09	1.20	7%
Un 11 17900_2	1.137	66.805	0.697	0.349	17.050	0.646	0.000	0.151	0.695	87.529	0.307	7.001	17.07	1.19	7%
Un 26 19600_4	0.995	66.713	0.267	0.730	17.936	0.573	0.000	0.147	0.214	87.575	0.307	7.189	16.61	1.19	7%
Un 6 17900_1	1.140	66.786	0.722	0.592	16.919	0.623	0.000	0.139	0.670	87.591	0.308	7.667	15.68	1.20	8%
Un 27 18700_4	1.350	65.745	0.585	0.157	18.123	0.866	0.026	0.133	0.616	87.601	0.310	7.791	15.24	1.18	8%
Un 6 17900_1	1.326	66.384	0.662	0.297	17.700	0.663	0.004	0.149	0.417	87.602	0.308	7.125	16.89	1.20	7%
Un 26 19600_4	1.157	68.097	0.144	0.278	17.075	0.686	0.000	0.147	0.028	87.612	0.303	7.240	16.32	1.18	7%
Un 6 17900_1	1.162	66.140	0.730	0.441	17.541	0.618	0.000	0.142	0.841	87.615	0.309	7.475	16.18	1.21	7%
Un 26 19600_4	1.536	67.493	0.159	1.107	16.323	0.833	0.000	0.141	0.027	87.619	0.305	7.322	15.79	1.15	7%
Un 18 04693_2	1.123	67.494	0.180	0.477	17.615	0.567	0.000	0.163	0.022	87.642	0.305	6.616	18.25	1.20	7%
Un 26 19600_4	1.088	66.681	0.250	0.896	17.929	0.562	0.000	0.152	0.096	87.654	0.307	7.024	17.14	1.20	7%
Un 20 18700_3	1.876	68.103	0.287	0.121	16.292	0.771	0.000	0.141	0.082	87.675	0.303	7.324	15.65	1.14	7%
Un 26 19600_4	1.127	66.520	0.359	0.557	17.763	0.723	0.000	0.149	0.482	87.681	0.308	7.144	16.91	1.20	7%
Un 18 04693_2	1.107	66.422	0.303	0.246	18.892	0.560	0.000	0.142	0.030	87.701	0.308	7.473	16.10	1.20	7%
Un 20 18700_3	1.081	67.287	0.249	1.601	16.531	0.793	0.000	0.150	0.095	87.787	0.305	7.146	16.81	1.20	7%
Un 26 19600_4	1.207	68.308	0.226	0.433	16.731	0.730	0.000	0.132	0.064	87.832	0.302	7.773	14.58	1.13	8%
Un 26 19600_4	1.200	68.274	0.233	0.994	16.174	0.750	0.000	0.162	0.064	87.851	0.303	6.451	17.86	1.15	6%
Un 6 17900_1	1.201	67.127	0.770	0.190	16.988	0.714	0.000	0.145	0.718	87.853	0.307	7.362	16.28	1.20	7%
Un 20 18700_3	2.099	68.306	0.194	0.198	15.990	0.832	0.000	0.158	0.080	87.856	0.303	6.766	17.43	1.18	7%
Un 26 19600_4	1.094	69.236	0.156	0.411	16.152	0.665	0.000	0.160	0.013	87.888	0.300	6.696	17.44	1.16	7%
Un 20 18700_3	1.239	66.281	0.212	3.162	16.103	0.757	0.000	0.150	0.001	87.904	0.308	7.074	17.06	1.20	7%
Un 11 17900_2	1.089	65.639	0.690	0.489	18.656	0.568	0.000	0.154	0.638	87.922	0.310	6.805	17.65	1.20	7%
Un 5 19600_1	1.170	68.858	0.232	0.706	16.015	0.753	0.000	0.164	0.034	87.932	0.303	6.525	17.93	1.17	7%
Un 5 19600_1	1.577	66.621	0.225	1.853	16.739	0.742	0.009	0.156	0.029	87.950	0.308	6.843	17.63	1.20	7%
Un 6 17900_1	1.132	67.142	0.721	0.089	17.087	0.661	0.000	0.165	0.959	87.955	0.307	6.461	18.48	1.19	6%
Un 7 04693_1	1.049	64.662	0.234	0.458	20.936	0.518	0.000	0.145	0.017	88.019	0.314	7.228	16.85	1.21	7%
Un 5 19600_1	1.298	67.651	0.250	0.542	17.464	0.641	0.000	0.147	0.080	88.074	0.305	7.206	16.43	1.18	7%
Un 8 06460_1	1.154	64.673	0.857	1.130	18.636	0.806	0.000	0.175	0.682	88.113	0.313	6.093	20.37	1.24	6%
Un 26 19600_4	1.134	69.140	0.256	0.946	15.654	0.787	0.000	0.147	0.060	88.124	0.301	7.240	16.08	1.16	7%
Un 6 17900_1	1.374	67.166	0.756	0.391	17.122	0.649	0.000	0.196	0.474	88.129	0.306	5.428	21.94	1.19	5%
Un 18 04693_2	1.165	66.890	0.239	0.437	18.693	0.562	0.000	0.146	0.027	88.159	0.306	7.266	16.49	1.20	7%
Un 20 18700_3	1.198	66.952	0.167	1.698	17.374	0.580	0.000	0.161	0.030	88.161	0.307	6.568	18.18	1.19	7%
Un 27 18700_4	1.412	66.814	0.566	0.066	17.854	0.869	0.000	0.139	0.471	88.191	0.307	7.440	15.72	1.17	7%
Un 26 19600_4	1.143	67.925	0.200	0.823	17.356	0.614	0.000	0.149	0.051	88.261	0.304	7.211	16.54	1.19	7%
Un 26 19600_4	1.158	67.372	0.245	0.710	17.810	0.729	0.000	0.151	0.092	88.267	0.305	7.030	16.95	1.19	7%
Un 20 18700_3	1.175	68.629	0.279	0.878	16.283	0.804	0.000	0.156	0.066	88.269	0.302	6.903	17.08	1.18	7%
Un 5 19600_1	1.393	67.435	0.217	1.110	17.092	0.791	0.000	0.167	0.089	88.295	0.307	6.390	18.68	1.19	6%
Un 20 18700_3	1.297	66.974	0.199	2.154	16.563	0.887	0.000	0.179	0.054	88.308	0.306	5.954	20.16	1.20	6%
Un 6 17900_1	1.173	67.652	0.709	0.155	17.276	0.608	0.000	0.154	0.591	88.319	0.305	6.918	17.14	1.18	7%
Un 6 17900_1	1.137	67.235	0.801	0.113	17.453	0.629	0.004	0.152	0.800	88.324	0.306	7.005	17.00	1.19	7%
Un 9 19600_2	1.419	67.885	0.251	0.578	17.182	0.809	0.000	0.153	0.055	88.331	0.305	6.958	16.96	1.18	7%
Un 6 17900_1	1.219	67.755	0.706	0.198	17.014	0.673	0.000	0.147	0.626	88.337	0.305	7.268	16.32	1.18	7%
Un 26 19600_4	1.092	67.987	0.280	0.877	17.315	0.554	0.000	0.148	0.122	88.375	0.304	7.237	16.36	1.18	7%
Un 26 19600_4	1.252	68.991	0.187	0.353	16.619	0.792	0.000	0.154	0.054	88.401	0.301	6.962	16.80	1.17	7%
Un 9 19600_2	1.367	68.152	0.262	0.730	16.891	0.841	0.000	0.156	0.040	88.438	0.303	6.951	17.20	1.19	7%
Un 20 18700_3	1.292	68.098	0.275	0.906	16.881	0.833	0.000	0.144	0.039	88.469	0.304	7.375	15.95	1.17	7%
Un 26 19600_4	1.071	67.237	0.214	0.472	18.616	0.657	0.002	0.161	0.076	88.505	0.306	6.666	18.00	1.20	7%
Un 20 18700_3	1.639	67.651	0.223	0.550	17.564	0.707	0.000	0.147	0.029	88.510	0.305	7.068	16.39	1.16	7%
Un 20 18700_3	1.092	69.319	0.189	0.834	16.209	0.739	0.000	0.145	0.010	88.537	0.300	7.401	15.80	1.17	7%
Un 27 18700_4	1.204	66.780	0.615	0.500	17.774	0.953	0.010	0.143	0.595	88.572	0.308	7.238	16.10	1.16	7%
Un 7 04693_1	0.797	64.501	0.177	1.877	20.407	0.652	0.000	0.139	0.025	88.573	0.314	7.666	16.27	1.24	8%
Un 7 04693_1	1.062	66.865	0.250	1.302	18.279	0.641	0.000	0.154	0.026	88.579	0.307	7.010	17.31	1.21	7%
Un 9 19600_2	1.543	68.488	0.323	0.036	17.241	0.730	0.000	0.158	0.061	88.582	0.303	6.720	17.43	1.17	7%
Un 6 17900_1	1.173	67.160	0.693	1.045	17.374	0.567	0.000	0.154	0.468	88.635	0.307	6.959	17.26	1.20	7%
Un 20 18700_3	1.399	67.143	0.254	0.820	18.053	0.723	0.000	0.163	0.091	88.647	0.307	6.488	18.31	1.18	6%
Un 9 19600_2	1.526	68.884	0.189	0.447	16.663	0.748	0.000	0.159	0.037	88.653	0.302	6.722	17.40	1.17	7%
Un 20 18700_3	1.550	68.501	0.262	0.730	16.634	0.834	0.000	0.155	0.011	88.677	0.302	6.875	17.09	1.17	7%
Un 9 19600_2	1.438	68.599	0.201	0.492	16.945	0.826	0.000	0.172	0.011	88.684	0.303	6.222	18.87	1.17	6%
Un 6 17900_1	1.109	67.576	0.645	0.227	17.621	0.635	0.000	0.168	0.708	88.690	0.306	6.374	18.74	1.19	6%
Un 18 04693_2	1.137	66.829	0.276	0.494	19.236	0.597	0.000	0.124	0.017	88.711	0.308	8.594	13.99	1.20	9%
Un 5 19600_1	1.413	68.666	0.124	0.900	16.628	0.772	0.000	0.166	0.042	88.711	0.302	6.436	18.21	1.17	6%
Un 11 17900_2	1.128	68.232	0.568	0.537	17.232	0.605	0.003	0.173	0.234	88.713	0.303	6.101	19.16	1.17	6%

ELECTRONIC APPENDIX FOR CHAPTER 4 – CONTINUED

Un 5 19600_1	1.248	63.183	0.266	0.480	22.561	0.810	0.004	0.161	0.021	88.734	0.318	6.668	19.19	1.28	7%
Un 6 17900_1	1.142	67.281	0.746	0.597	17.436	0.578	0.015	0.151	0.822	88.769	0.306	7.127	16.89	1.20	7%
Un 26 19600_4	1.397	69.062	0.247	0.926	16.178	0.801	0.000	0.160	0.005	88.775	0.301	6.664	17.43	1.16	7%
Un 5 19600_1	1.508	68.644	0.291	0.601	16.760	0.710	0.000	0.156	0.113	88.784	0.303	6.845	17.15	1.17	7%
Un 26 19600_4	1.339	68.423	0.187	0.933	16.735	0.973	0.000	0.157	0.043	88.789	0.303	6.790	17.28	1.17	7%
Un 27 18700_4	1.529	68.584	0.454	0.552	16.727	0.687	0.000	0.150	0.118	88.800	0.302	6.956	16.48	1.14	7%
Un 9 19600_2	1.510	69.165	0.160	0.336	16.727	0.721	0.000	0.151	0.039	88.808	0.302	7.111	16.46	1.17	7%
Un 9 19600_2	1.417	68.108	0.304	0.573	17.455	0.672	0.000	0.159	0.130	88.819	0.304	6.749	17.63	1.19	7%
Un 6 17900_1	1.216	68.041	0.729	0.165	17.202	0.636	0.000	0.141	0.693	88.823	0.304	7.572	15.64	1.18	8%
Un 5 19600_1	1.265	69.078	0.220	1.083	16.257	0.693	0.000	0.178	0.061	88.834	0.301	6.015	19.45	1.17	6%
Un 6 17900_1	1.308	68.211	0.665	0.202	17.339	0.638	0.000	0.172	0.329	88.864	0.304	6.199	18.96	1.17	6%
Un 9 19600_2	1.362	68.088	0.201	1.042	17.087	0.816	0.000	0.142	0.132	88.869	0.304	7.495	15.72	1.18	7%
Un 5 19600_1	1.507	68.784	0.224	0.543	16.848	0.750	0.000	0.150	0.065	88.872	0.303	7.170	16.40	1.17	7%
Un 26 19600_4	1.460	68.375	0.158	0.929	16.946	0.839	0.000	0.135	0.035	88.875	0.303	7.932	14.84	1.17	8%
Un 26 19600_4	1.482	68.125	0.191	0.575	17.422	0.931	0.000	0.149	0.008	88.884	0.305	7.109	16.51	1.17	7%
Un 5 19600_1	1.413	68.851	0.183	0.940	16.523	0.776	0.000	0.159	0.045	88.889	0.302	6.777	17.37	1.17	7%
Un 5 19600_1	1.292	68.725	0.256	0.730	16.894	0.785	0.000	0.157	0.054	88.892	0.303	6.815	17.18	1.17	7%
Un 26 19600_4	1.168	68.372	0.158	0.860	17.497	0.665	0.000	0.136	0.050	88.906	0.303	7.588	15.03	1.14	8%
Un 20 18700_3	1.375	68.739	0.223	0.384	17.087	0.899	0.000	0.161	0.042	88.911	0.302	6.639	17.68	1.17	7%
Un 26 19600_4	1.584	68.341	0.151	1.254	16.562	0.865	0.000	0.153	0.013	88.922	0.303	6.994	16.82	1.17	7%
Un 26 19600_4	1.621	68.734	0.151	0.612	16.896	0.757	0.000	0.144	0.013	88.928	0.302	7.415	15.76	1.17	7%
Un 9 19600_2	1.521	69.204	0.221	0.272	16.793	0.734	0.000	0.153	0.051	88.948	0.301	6.940	16.72	1.16	7%
Un 5 19600_1	1.473	68.140	0.255	0.878	17.244	0.754	0.000	0.154	0.069	88.967	0.304	6.974	17.02	1.18	7%
Un 9 19600_2	1.346	67.795	0.268	1.161	17.436	0.790	0.000	0.162	0.047	89.004	0.305	6.635	17.98	1.19	7%
Un 9 19600_2	1.352	69.023	0.149	1.209	16.329	0.760	0.000	0.161	0.029	89.012	0.302	6.593	17.63	1.16	7%
Un 26 19600_4	1.416	68.852	0.347	0.455	16.935	0.796	0.000	0.142	0.087	89.030	0.301	7.494	15.58	1.17	7%
Un 26 19600_4	1.530	68.832	0.222	0.333	17.032	0.887	0.000	0.149	0.051	89.036	0.302	7.184	16.30	1.17	7%
Un 26 19600_4	1.517	68.665	0.252	0.631	16.919	0.814	0.000	0.172	0.068	89.038	0.302	6.234	18.87	1.17	6%
Un 6 17900_1	1.111	67.686	0.713	0.192	17.726	0.631	0.000	0.163	0.824	89.046	0.305	6.516	18.15	1.18	6%
Un 20 18700_3	1.634	68.614	0.262	0.386	17.213	0.740	0.000	0.143	0.055	89.048	0.303	7.463	15.69	1.17	7%
Un 26 19600_4	1.087	66.365	0.232	1.403	19.063	0.689	0.000	0.135	0.086	89.060	0.308	7.904	15.30	1.21	8%
Un 9 19600_2	1.561	68.549	0.206	0.739	17.005	0.817	0.000	0.153	0.032	89.062	0.303	6.999	16.78	1.17	7%
Un 26 19600_4	1.291	68.638	0.095	1.210	16.890	0.794	0.000	0.126	0.023	89.067	0.302	8.482	13.80	1.17	8%
Un 5 19600_1	1.605	67.571	0.192	0.492	18.146	0.863	0.000	0.154	0.047	89.069	0.306	6.967	17.18	1.19	7%
Un 9 19600_2	1.679	69.190	0.259	0.108	16.885	0.796	0.000	0.148	0.024	89.090	0.302	7.150	16.18	1.15	7%
Un 7 04693_1	1.151	67.281	0.253	1.067	18.687	0.510	0.000	0.145	0.026	89.120	0.306	7.370	16.19	1.19	7%
Un 11 17900_2	1.025	61.286	0.652	0.623	24.313	0.547	0.000	0.150	0.527	89.123	0.324	6.884	18.39	1.26	7%
Un 9 19600_2	0.987	65.940	0.299	3.692	17.235	0.663	0.000	0.160	0.155	89.131	0.310	6.723	18.24	1.22	7%
Un 9 19600_2	1.384	68.477	0.244	0.852	17.150	0.792	0.000	0.175	0.058	89.133	0.303	6.092	19.30	1.17	6%
Un 9 19600_2	1.488	68.942	0.205	0.675	16.872	0.781	0.000	0.149	0.028	89.139	0.302	7.113	16.29	1.16	7%
Un 26 19600_4	1.448	68.336	0.211	0.876	17.318	0.643	0.000	0.155	0.157	89.143	0.303	6.936	17.05	1.18	7%
Un 6 17900_1	1.191	67.936	0.746	0.477	17.341	0.604	0.000	0.157	0.741	89.193	0.304	6.793	17.40	1.18	7%
Un 26 19600_4	1.598	68.706	0.182	0.644	17.111	0.783	0.000	0.155	0.015	89.195	0.302	6.897	17.00	1.17	7%
Un 5 19600_1	1.474	69.302	0.215	0.267	17.003	0.766	0.000	0.159	0.042	89.227	0.301	6.702	17.29	1.16	7%
Un 20 18700_3	1.333	68.771	0.275	0.405	17.400	0.848	0.000	0.149	0.050	89.232	0.302	7.116	16.33	1.16	7%
Un 5 19600_1	1.436	68.208	0.302	0.555	17.809	0.661	0.000	0.139	0.135	89.245	0.304	7.684	15.39	1.18	8%
Un 9 19600_2	1.290	68.961	0.251	0.599	17.118	0.804	0.000	0.172	0.079	89.274	0.302	6.257	18.76	1.17	6%
Un 26 19600_4	1.368	68.766	0.233	0.652	17.206	0.886	0.000	0.149	0.023	89.283	0.302	7.147	16.38	1.17	7%
Un 26 19600_4	1.498	69.070	0.270	0.475	16.950	0.858	0.000	0.149	0.062	89.331	0.301	7.128	16.27	1.16	7%
Un 5 19600_1	1.678	68.837	0.200	0.893	16.755	0.787	0.000	0.165	0.031	89.347	0.302	6.465	18.05	1.16	6%
Un 26 19600_4	1.448	67.800	0.237	2.071	16.696	0.731	0.000	0.158	0.211	89.351	0.304	6.759	17.58	1.18	7%
Un 26 19600_4	1.354	69.692	0.136	0.476	16.774	0.717	0.000	0.154	0.049	89.352	0.299	6.940	16.69	1.16	7%
Un 20 18700_3	1.301	68.284	0.178	0.751	17.841	0.821	0.000	0.146	0.033	89.356	0.304	7.111	16.07	1.14	7%
Un 5 19600_1	2.087	68.015	0.211	1.121	16.921	0.835	0.000	0.155	0.027	89.372	0.304	6.815	17.20	1.17	7%
Un 9 19600_2	1.152	66.979	0.226	0.897	19.072	0.728	0.000	0.176	0.148	89.377	0.308	6.051	19.77	1.19	6%
Un 20 18700_3	1.680	68.857	0.165	0.462	17.311	0.757	0.000	0.165	0.006	89.404	0.302	6.246	18.11	1.13	6%
Un 27 18700_4	1.229	68.818	0.523	0.275	17.490	0.776	0.000	0.153	0.141	89.404	0.302	6.965	16.76	1.16	7%
Un 20 18700_3	1.622	69.080	0.335	0.070	17.270	0.792	0.000	0.153	0.094	89.415	0.302	6.989	16.68	1.16	7%
Un 5 19600_1	1.584	69.213	0.251	0.238	17.080	0.754	0.000	0.164	0.133	89.418	0.302	6.486	17.89	1.16	6%
Un 20 18700_3	1.583	69.095	0.256	1.277	16.162	0.838	0.000	0.163	0.066	89.440	0.301	6.543	17.77	1.16	7%
Un 5 19600_1	1.068	68.872	0.175	0.781	17.697	0.637	0.000	0.156	0.055	89.441	0.303	6.883	17.11	1.17	7%
Un 26 19600_4	1.244	69.481	0.204	0.948	16.565	0.840	0.000	0.166	0.001	89.449	0.300	6.432	18.00	1.15	6%
Un 9 19600_2	1.347	68.099	0.204	1.327	17.487	0.777	0.000	0.179	0.029	89.449	0.304	5.951	19.86	1.18	6%
Un 26 19600_4	1.466	68.660	0.211	0.711	17.406	0.809	0.001	0.123	0.081	89.468	0.302	8.690	13.50	1.17	9%
Un 20 18700_3	1.389	68.141	0.233	1.678	17.016	0.872	0.000	0.137	0.027	89.493	0.304	7.812	15.18	1.18	8%
Un 9 19600_2	1.337	68.108	0.256	0.886	17.887	0.767	0.000	0.154	0.139	89.535	0.305	7.044	17.01	1.20	7%
Un 20 18700_3	1.961	69.045	0.247	0.100	17.267	0.744	0.000	0.150	0.032	89.546	0.302	7.033	16.42	1.15	7%
Un 20 18700_3	1.242	69.132	0.189	0.987	17.028	0.808	0.000	0.150	0.024	89.559	0.301	7.103	16.36	1.16	7%
Un 5 19600_1	1.120	68.819	0.176	1.071	17.584	0.722	0.000	0.140	0.054	89.686	0.303	7.688	15.35	1.18	8%
Un 9 19600_2	1.887	69.123	0.244	0.513	17.032	0.768	0.000	0.165	0.064	89.796	0.302	6.480	18.03	1.17	6%
Un 20 18700_3	1.852	68.645	0.204	1.364	16.705	0.810	0.000	0.159	0.065	89.804	0.303	6.523	17.50	1.14	7%
Un 9 19600_2	1.266	69.071	0.358	0.738	17.176	0.714	0.000	0.162	0.325	89.811	0.302	6.599	17.72	1.17	7%
Un 9 19600_2	1.443	69.684	0.172	0.693	16.896	0.725	0.000	0.170	0.039	89.823	0.300	6.316	18.34	1.16	6%
Un 6 17900_1	1.265	68.319	0.635	0.399	18.122	0.467	0.000	0.174	0.503	89.884	0.304	6.150	19.19	1.18	6%
Un 6 17900_1	1.156	68.835	0.588	0.245	17.846	0.608	0.000	0.149	0.460	89.887	0.303	7.177	16.31	1.17	7%

ELECTRONIC APPENDIX FOR CHAPTER 4 – CONTINUED

Un 6 17900_1	1.141	67.715	0.594	0.840	18.168	0.613	0.000	0.154	0.670	89.893	0.306	6.973	17.10	1.19	7%
Un 20 18700_3	1.141	69.148	0.252	1.214	17.067	0.767	0.000	0.141	0.172	89.902	0.302	7.624	15.36	1.17	8%
Un 26 19600_4	1.433	69.228	0.211	0.880	17.159	0.881	0.000	0.133	0.020	89.946	0.301	8.018	14.47	1.16	8%
Un 9 19600_2	1.600	69.610	0.194	0.487	17.083	0.779	0.000	0.158	0.054	89.965	0.301	6.749	17.15	1.15	7%
Un 20 18700_3	1.144	69.585	0.167	0.511	17.689	0.700	0.000	0.162	0.023	89.980	0.300	6.604	17.56	1.16	7%
Un 20 18700_3	1.257	68.576	0.226	1.892	17.011	0.834	0.000	0.166	0.022	89.984	0.303	6.422	18.25	1.17	6%
Un 20 18700_3	1.205	68.736	0.167	1.118	17.843	0.700	0.000	0.145	0.083	89.996	0.303	7.363	15.89	1.17	7%
Un 9 19600_2	1.826	69.586	0.267	0.181	17.193	0.770	0.000	0.174	0.167	90.162	0.302	6.145	18.84	1.15	6%
Un 26 19600_4	1.368	69.209	0.103	1.690	16.809	0.846	0.000	0.172	0.012	90.209	0.303	6.233	18.71	1.16	6%
Un 20 18700_3	1.528	70.168	0.212	0.227	17.188	0.745	0.000	0.162	0.055	90.286	0.299	6.590	17.43	1.15	7%
Un 26 19600_4	1.437	69.931	0.269	0.436	17.102	0.829	0.000	0.154	0.139	90.298	0.299	6.943	16.65	1.15	7%
Un 26 19600_4	1.392	69.371	0.173	1.206	17.111	0.883	0.000	0.152	0.050	90.338	0.300	6.863	16.51	1.13	7%
Un 11 17900_2	1.163	65.762	0.708	0.766	20.589	0.614	0.000	0.140	0.606	90.347	0.310	7.588	16.10	1.22	8%
Un 20 18700_3	1.244	69.787	0.274	0.667	17.263	0.878	0.014	0.161	0.085	90.372	0.300	6.670	17.34	1.15	7%
Un 20 18700_3	1.482	69.910	0.255	0.577	17.182	0.760	0.000	0.164	0.043	90.374	0.300	6.553	17.69	1.16	7%
Un 7 04693_1	1.126	69.007	0.244	0.806	18.504	0.537	0.000	0.155	0.026	90.403	0.302	6.892	16.91	1.16	7%
Un 20 18700_3	1.332	69.921	0.231	0.438	17.480	0.860	0.000	0.171	0.023	90.456	0.300	6.288	18.39	1.15	6%
Un 20 18700_3	1.619	69.826	0.303	0.305	17.410	0.758	0.000	0.150	0.086	90.458	0.300	7.120	16.19	1.15	7%
Un 20 18700_3	1.453	70.012	0.238	0.284	17.313	0.794	0.000	0.155	0.232	90.481	0.300	6.922	16.65	1.15	7%
Un 20 18700_3	1.765	69.376	0.176	1.089	17.139	0.800	0.000	0.149	0.011	90.506	0.301	7.189	16.23	1.16	7%
Un 9 19600_2	1.691	70.233	0.232	0.053	17.215	0.829	0.000	0.162	0.097	90.512	0.300	6.637	17.35	1.15	7%
Un 26 19600_4	6.614	65.458	0.222	1.768	15.522	0.801	0.000	0.134	0.020	90.539	0.311	7.917	15.44	1.22	8%
Un 26 19600_4	1.632	69.202	0.184	1.274	17.248	0.803	0.000	0.156	0.058	90.557	0.302	6.905	17.02	1.17	7%
Un 20 18700_3	1.695	70.416	0.282	0.026	17.050	0.870	0.009	0.162	0.047	90.557	0.299	6.562	17.36	1.14	7%
Un 26 19600_4	1.499	69.725	0.186	0.492	17.640	0.874	0.000	0.136	0.024	90.575	0.301	7.865	14.71	1.15	8%
Un 11 17900_2	1.045	57.902	0.639	0.703	28.829	0.653	0.000	0.122	0.700	90.592	0.335	8.339	15.94	1.33	8%
Un 20 18700_3	1.407	69.953	0.204	0.739	17.356	0.784	0.000	0.146	0.019	90.608	0.300	7.317	15.74	1.15	7%
Un 5 19600_1	1.599	70.358	0.235	0.087	17.289	0.777	0.000	0.145	0.137	90.626	0.299	7.379	15.50	1.14	7%
Un 20 18700_3	1.278	68.721	0.263	1.978	17.338	0.841	0.000	0.151	0.060	90.631	0.303	7.082	16.60	1.17	7%
Un 20 18700_3	1.546	69.984	0.225	0.309	17.566	0.861	0.000	0.144	0.038	90.673	0.299	7.273	15.54	1.13	7%
Un 20 18700_3	1.156	69.243	0.222	1.589	17.398	0.871	0.000	0.171	0.037	90.686	0.301	6.314	18.57	1.17	6%
Un 5 19600_1	1.211	69.429	0.185	0.690	18.317	0.695	0.000	0.154	0.036	90.718	0.301	6.981	16.75	1.17	7%
Un 20 18700_3	1.364	69.421	0.231	1.468	17.287	0.816	0.000	0.136	0.028	90.750	0.301	7.842	14.82	1.16	8%
Un 5 19600_1	1.417	69.760	0.177	1.560	16.875	0.839	0.000	0.125	0.024	90.778	0.300	8.524	13.53	1.15	9%
Un 20 18700_3	1.768	70.371	0.249	0.077	17.369	0.787	0.000	0.151	0.052	90.825	0.299	7.164	16.14	1.15	7%
Un 20 18700_3	1.280	69.818	0.234	0.725	17.795	0.805	0.000	0.156	0.039	90.852	0.300	6.923	16.81	1.16	7%
Un 20 18700_3	1.509	69.203	0.164	1.951	17.060	0.846	0.000	0.168	0.000	90.901	0.302	6.423	18.31	1.17	6%
Un 26 19600_4	1.489	69.730	0.186	1.410	17.012	0.908	0.000	0.152	0.040	90.926	0.300	7.028	16.48	1.16	7%
Un 26 19600_4	1.158	64.121	0.210	0.514	23.963	0.766	0.000	0.154	0.052	90.938	0.316	6.806	18.13	1.23	7%
Un 26 19600_4	1.370	70.543	0.230	1.164	16.740	0.835	0.000	0.155	0.020	91.056	0.298	6.720	16.56	1.11	7%
Un 5 19600_1	1.448	69.800	0.323	0.549	17.932	0.681	0.000	0.167	0.164	91.064	0.300	6.426	18.04	1.16	6%
Un 20 18700_3	1.155	70.519	0.155	0.495	17.871	0.706	0.000	0.160	0.057	91.118	0.298	6.761	17.11	1.15	7%
Un 20 18700_3	1.235	69.922	0.228	0.655	18.249	0.801	0.000	0.117	0.080	91.287	0.300	9.124	12.59	1.15	9%
Un 26 19600_4	1.528	70.670	0.162	0.769	17.320	0.894	0.000	0.177	0.007	91.528	0.298	6.078	18.93	1.15	6%
Un 20 18700_3	1.407	70.472	0.154	0.634	17.944	0.773	0.000	0.171	0.024	91.579	0.299	6.288	18.27	1.15	6%
Un 5 19600_1	1.686	71.093	0.265	0.095	17.544	0.766	0.000	0.173	0.116	91.737	0.297	6.182	18.31	1.13	6%
Un 26 19600_4	1.525	71.995	0.176	0.540	18.100	0.891	0.000	0.159	0.039	93.426	0.295	6.744	16.68	1.12	7%
Uranothorite Saprolite															
Un 23 845_2_T	3.483	16.664	0.325	1.114	12.260	4.497	36.671	0.068	3.440	78.523	0.678	14.040	18.23	2.56	14%
Un 23 845_2_T	3.093	17.732	0.324	3.445	12.320	3.979	34.410	0.229	3.131	78.663	0.654	4.440	60.08	2.64	4%
Un 23 845_2_T	3.121	19.797	0.332	2.517	11.510	3.575	29.273	0.097	3.259	73.481	0.613	9.849	25.05	2.46	10%
Un 23 845_2_T	2.749	22.584	0.312	1.123	11.855	2.723	24.210	0.078	3.324	68.957	0.567	12.374	19.41	2.40	12%
Coffinite Saprolite															
Un 22 845_3_C	2.821	42.474	0.362	1.143	15.023	1.100	12.030	0.128	1.938	77.020	0.397	8.124	20.78	1.68	8%
Un 22 845_3_C	2.569	43.840	0.419	0.775	13.852	0.926	9.411	0.149	1.599	73.542	0.389	6.726	24.05	1.61	7%
Un 22 845_3_C	2.440	48.479	0.496	1.014	17.470	0.575	6.644	0.178	1.395	78.691	0.367	5.701	26.52	1.51	6%
Un 22 845_3_C	2.418	50.418	0.476	2.127	14.614	0.796	6.487	0.145	1.453	78.934	0.360	7.002	20.84	1.45	7%
Un 22 845_3_C	2.011	46.046	0.441	1.141	21.152	0.510	5.369	0.126	1.344	78.140	0.380	7.932	19.92	1.58	8%
Un 22 845_3_C	2.191	46.767	0.507	0.416	17.843	0.877	2.955	0.151	1.360	73.068	0.374	6.584	23.86	1.57	7%
Un 22 845_3_C	2.204	41.906	0.470	0.623	15.165	0.739	1.726	0.156	1.349	64.338	0.395	6.515	27.76	1.80	6%

ELECTRONIC APPENDIX FOR CHAPTER 4 – CONTINUED

Coffinite Vein															
Un 24 762_4_C	1.800	37.547	0.073	1.831	15.562	1.639	0.367	0.085	13.502	72.405	0.427	11.609	17.00	1.97	12%
Un 24 762_4_C	1.907	36.630	0.113	0.903	15.025	1.494	0.332	0.087	12.884	69.375	0.432	11.523	17.80	2.05	11%
Un 24 762_4_C	2.420	36.795	0.103	1.116	14.805	1.631	0.307	0.084	12.992	70.253	0.431	11.909	17.11	2.03	12%
Un 24 762_4_C	2.088	36.766	0.096	1.314	14.741	1.771	0.365	0.058	12.868	70.066	0.431	16.679	11.87	1.98	17%
Un 24 762_4_C	1.691	32.771	0.071	1.028	14.635	1.716	0.324	0.065	12.111	64.413	0.459	15.039	15.02	2.25	15%
Un 24 762_4_C	1.641	34.275	0.101	1.265	14.447	1.572	0.339	0.063	11.714	65.417	0.447	15.466	13.86	2.14	15%
Un 24 762_4_C	2.032	36.233	0.080	1.243	14.385	1.767	0.375	0.088	12.701	68.904	0.434	10.881	18.21	1.98	11%
Un 24 762_4_C	1.743	33.828	0.077	1.706	14.373	1.399	0.345	0.076	13.045	66.592	0.451	13.043	16.88	2.20	13%
Un 24 762_4_C	2.025	29.353	0.055	1.457	14.262	1.248	0.277	0.077	11.076	59.829	0.485	12.262	19.61	2.40	12%
Un 24 762_4_C	1.815	34.184	0.079	0.873	14.207	1.401	0.320	0.110	12.372	65.359	0.448	8.944	24.16	2.15	9%
Un 24 762_4_C	1.932	32.576	0.086	1.741	14.178	1.445	0.300	0.076	13.198	65.531	0.461	13.224	17.43	2.30	13%
Un 24 762_4_C	1.763	33.862	0.071	1.201	14.095	1.498	0.317	0.081	12.886	65.773	0.450	11.925	17.93	2.13	12%
Un 24 762_4_C	1.524	31.750	0.059	1.575	13.911	1.329	0.249	0.084	12.301	62.781	0.467	11.882	19.80	2.35	12%
Un 24 762_4_C	1.758	34.267	0.091	1.256	13.905	1.604	0.364	0.081	11.653	64.979	0.446	12.218	17.67	2.15	12%
Un 24 762_4_C	1.651	34.384	0.114	1.716	13.761	1.850	0.310	0.099	12.491	66.377	0.446	9.805	21.71	2.12	10%
Un 24 762_4_C	2.155	29.990	0.044	1.131	13.748	1.311	0.314	0.081	12.131	60.904	0.481	11.955	20.28	2.42	12%
Un 24 762_4_C	2.230	34.374	0.098	0.316	13.737	1.595	0.365	0.067	11.995	64.777	0.446	14.301	14.66	2.09	14%
Un 24 762_4_C	1.571	33.852	0.062	1.238	13.619	1.432	0.329	0.079	11.875	64.057	0.449	12.000	17.45	2.09	12%
Un 24 762_4_C	1.673	35.509	0.122	1.706	13.603	1.582	0.318	0.060	12.065	66.639	0.438	15.656	12.74	1.99	16%
Un 24 762_4_C	2.241	33.300	0.099	1.679	13.597	1.415	0.288	0.085	12.543	65.247	0.455	11.438	19.26	2.20	11%
Un 24 762_4_C	1.793	33.242	0.067	1.164	13.570	1.444	0.325	0.084	11.820	63.509	0.453	11.659	19.03	2.21	12%
Un 24 762_4_C	1.997	33.628	0.075	0.652	13.430	1.987	0.324	0.072	12.723	64.888	0.452	13.631	16.13	2.19	14%
Un 24 762_4_C	2.106	33.284	0.106	0.734	13.334	1.687	0.317	0.082	11.863	63.515	0.454	11.553	18.51	2.13	12%
Un 24 762_4_C	1.303	28.141	0.080	1.003	13.044	1.430	0.234	0.094	10.442	55.772	0.496	9.493	25.21	2.38	9%
Un 24 762_4_C	1.973	32.860	0.067	0.701	12.981	1.407	0.296	0.078	12.104	62.467	0.457	12.796	17.74	2.27	13%
Un 24 762_4_C	2.034	32.271	0.143	0.984	12.944	1.520	0.334	0.067	11.898	62.196	0.461	14.603	15.57	2.27	15%
Un 24 762_4_C	1.764	30.696	0.089	0.786	12.870	1.276	0.275	0.084	11.544	59.384	0.473	10.933	20.60	2.25	11%
Un 24 762_4_C	2.004	32.968	0.093	0.740	12.866	1.829	0.305	0.082	11.135	62.022	0.455	11.220	18.75	2.10	11%
Un 24 762_4_C	1.932	32.047	0.092	0.299	12.850	1.839	0.316	0.087	12.399	61.861	0.463	11.392	20.35	2.31	11%
Un 24 762_4_C	1.635	30.285	0.082	2.274	12.848	1.411	0.271	0.066	11.627	60.498	0.477	14.486	16.46	2.38	14%
Un 24 762_4_C	2.031	32.262	0.066	0.675	12.839	1.843	0.271	0.081	12.478	62.545	0.461	12.198	18.89	2.30	12%
Un 24 762_4_C	2.381	32.997	0.111	0.893	12.809	1.594	0.290	0.080	12.722	63.877	0.457	12.323	18.17	2.23	12%
Un 24 762_4_C	2.063	31.785	0.100	0.639	12.759	1.714	0.279	0.068	11.801	61.208	0.464	13.780	15.99	2.20	14%
Un 24 762_4_C	2.110	31.045	0.047	0.779	12.745	1.388	0.286	0.087	12.126	60.613	0.471	11.252	21.14	2.37	11%
Un 24 762_4_C	2.064	32.396	0.083	0.991	12.664	1.516	0.281	0.090	12.370	62.453	0.460	10.680	20.87	2.22	11%
Un 24 762_4_C	1.835	31.766	0.105	0.779	12.591	1.914	0.298	0.070	12.035	61.392	0.465	13.656	16.55	2.25	14%
Un 24 762_4_C	1.746	31.665	0.108	0.710	12.579	1.831	0.314	0.066	11.069	60.087	0.465	14.619	15.61	2.28	15%
Un 24 762_4_C	2.211	31.486	0.091	0.725	12.531	1.554	0.261	0.086	12.037	60.982	0.467	10.977	20.52	2.25	11%
Un 24 762_4_C	2.049	29.430	0.080	1.122	12.503	1.247	0.280	0.089	11.018	57.817	0.485	10.579	22.61	2.38	11%
Un 24 762_4_C	1.552	32.708	0.061	1.593	12.445	1.574	0.293	0.103	12.077	62.407	0.458	9.280	23.67	2.19	9%
Un 24 762_4_C	1.429	30.511	0.074	1.066	12.344	1.390	0.278	0.084	11.215	58.391	0.475	11.738	20.60	2.41	12%
Un 24 762_4_C	1.910	30.376	0.061	1.148	12.272	1.452	0.282	0.058	11.427	58.986	0.476	15.803	14.24	2.25	16%
Un 24 762_4_C	1.421	31.444	0.091	1.770	12.209	1.490	0.262	0.092	11.361	60.139	0.467	10.104	22.00	2.22	10%
Un 24 762_4_C	1.809	30.719	0.092	1.729	12.176	1.609	0.297	0.067	10.678	59.177	0.472	14.168	16.47	2.33	14%
Un 24 762_4_C	2.201	30.990	0.095	0.397	12.014	1.505	0.279	0.050	10.841	58.372	0.470	19.121	12.08	2.31	19%
Un 24 762_4_C	1.966	28.567	0.063	1.679	11.828	1.219	0.271	0.071	10.949	56.612	0.491	13.325	18.64	2.48	13%
Un 24 762_4_C	1.453	27.372	0.081	1.016	11.529	1.380	0.258	0.059	9.325	52.472	0.501	14.149	16.17	2.28	14%
Un 24 762_4_C	1.679	29.928	0.073	0.680	11.527	2.025	0.274	0.098	11.196	57.479	0.479	9.102	24.67	2.24	9%
Un 24 762_4_C	1.568	29.491	0.068	1.564	11.324	1.546	0.287	0.097	10.510	56.453	0.482	9.495	24.69	2.34	9%
Un 24 762_4_C	1.217	28.475	0.070	1.693	11.258	1.300	0.260	0.071	10.513	54.857	0.490	12.875	18.76	2.41	13%
Un 24 762_4_C	1.438	27.891	0.085	1.084	11.235	1.279	0.233	0.088	10.342	53.673	0.496	10.813	23.67	2.55	11%
Un 24 762_4_C	1.240	29.173	0.085	1.448	11.119	1.546	0.300	0.082	10.554	55.546	0.484	10.694	21.09	2.25	11%
Un 24 762_4_C	1.159	26.775	0.061	1.622	11.003	1.261	0.278	0.075	10.662	52.896	0.508	12.226	21.16	2.58	12%
Un 24 762_4_C	1.166	27.166	0.049	1.370	10.650	1.458	0.256	0.062	9.991	52.169	0.502	13.693	17.13	2.34	14%
Un 24 762_4_C	1.278	28.294	0.096	1.559	10.576	1.480	0.245	0.057	10.773	54.359	0.492	15.809	15.16	2.39	16%
Un 24 762_4_C	1.191	26.945	0.062	1.397	10.399	1.599	0.254	0.043	10.335	52.225	0.505	19.953	12.10	2.41	20%
Un 24 762_4_C	1.378	26.374	0.042	1.387	10.214	1.180	0.240	0.080	9.970	50.865	0.511	10.902	22.79	2.48	11%
Un 24 762_4_C	1.585	27.067	0.068	4.267	10.166	1.528	0.233	0.067	10.484	55.465	0.505	14.384	18.70	2.68	14%
Un 24 762_4_C	1.436	25.841	0.094	0.599	10.031	1.828	0.261	0.060	10.271	50.420	0.516	13.839	17.43	2.41	14%
Uraninite															
Un 25 762_4_U	1.772	66.820	0.605	3.306	6.251	0.000	0.024	0.352	1.416	80.546	0.304	3.248	39.57	1.27	3%
Un 25 762_4_U	1.576	61.843	0.614	4.418	9.611	0.000	0.000	0.340	1.243	79.645	0.318	3.323	41.37	1.36	3%
Un 25 762_4_U	1.561	61.150	0.547	4.167	8.918	0.000	0.000	0.310	1.232	77.885	0.319	3.479	38.12	1.32	3%
Un 25 762_4_U	1.498	59.439	0.515	1.451	15.525	0.000	0.000	0.321	1.166	79.915	0.327	3.488	40.65	1.41	3%
Un 25 762_4_U	1.532	57.514	0.487	5.043	9.493	0.000	0.007	0.324	1.164	75.564	0.330	3.436	42.32	1.44	3%
Un 25 762_4_U	1.545	57.214	0.506	4.886	10.265	0.000	0.000	0.305	1.164	75.885	0.332	3.593	40.08	1.43	4%
Un 25 762_4_U	1.439	57.076	0.513	2.871	11.700	0.000	0.000	0.297	1.151	75.047	0.333	3.573	39.18	1.39	4%
Un 25 762_4_U	1.231	48.886	0.415	4.650	16.196	0.000	0.000	0.269	0.844	72.492	0.364	3.895	41.43	1.60	4%

ELECTRONIC APPENDIX FOR CHAPTER 4 – CONTINUED

ADDITIONAL MATERIAL D

CO-AUTHORED ARTICLE ABSTRACT:

ZIRCON AT THE NANOSCALE RECORDS METASOMATIC PROCESSES LEADING TO LARGE MAGMATIC-HYDROTHERMAL ORE SYSTEMS

Liam Courtney-Davies[1], Cristiana L. Ciobanu[1], Max R. Verdugo-Ihl[1], Ashley Slattery[2], Nigel J. Cook[1], Marija Dmitrijeva[1], William M. Keyser[1], Benjamin P. Wade[2], **Urs I. Domnick[1]**, Kathy Ehrig[3], Jing Xu[1,4], Alkiviadis Kontonikas-Charos[1]

[1]*School of Chemical Engineering, The University of Adelaide, Adelaide, SA 5005, Australia*

[2]*Adelaide Microscopy, The University of Adelaide, Adelaide, SA 5005, Australia*

[3] *BHP Olympic Dam, Adelaide, SA 5000, Australia*

[4]*Key Laboratory of Mineral Resources, Institute of Geology and Geophysics, Chinese Academy of Sciences, Beijing 100029, China*

Article published in Minerals (2019) 9, 364.

minerals

MDPI

Article

Zircon at the Nanoscale Records Metasomatic Processes Leading to Large Magmatic–Hydrothermal Ore Systems

Liam Courtney-Davies [1,*], Cristiana L. Ciobanu [1], Max R. Verdugo-Ihl [1], Ashley Slattery [2], Nigel J. Cook [1], Marija Dmitrijeva [1], William Keyser [1], Benjamin P. Wade [2], Urs I. Domnick [1], Kathy Ehrig [3], Jing Xu [1,4] and Alkiviadis Kontonikas-Charos [1]

1 School of Chemical Engineering and Advanced Materials, The University of Adelaide, Adelaide, SA 5005, Australia; cristiana.ciobanu@adelaide.edu.au (C.L.C.); max.verdugoihl@adelaide.edu.au (M.R.V.-I.); nigel.cook@adelaide.edu.au (N.J.C.); marija.dmitrijeva@adelaide.edu.au (M.D.); william.keyser@adelaide.edu.au (W.K.); urs.domnick@adelaide.edu.au (U.I.D.); j.xu@adelaide.edu.au (J.X.); alkiviadis.kontonikas-charos@adelaide.edu.au (A.K.-C.)

2 Adelaide Microscopy, The University of Adelaide, Adelaide, SA 5005, Australia; ashley.slattery@adelaide.edu.au (A.S.); benjamin.wade@adelaide.edu.au (B.P.W.)

3 BHP Olympic Dam, Adelaide, SA 5000, Australia; kathy.ehrig@bhp.com

4 Key Laboratory of Mineral Resources, Institute of Geology and Geophysics, Chinese Academy of Sciences, Beijing 100029, China; xujing3800@126.com

* Correspondence: liam.courtney-davies@adelaide.edu.au

Received: 30 April 2019; Accepted: 13 June 2019; Published: 16 June 2019

check for updates

Abstract: The petrography and geochemistry of zircon offers an exciting opportunity to better understand the genesis of, as well as identify pathfinders for, large magmatic–hydrothermal ore systems. Electron probe microanalysis, laser ablation inductively coupled plasma mass spectrometry, high-angle annular dark-field scanning transmission electron microscopy (HAADF-STEM) imaging, and energy-dispersive X-ray spectrometry STEM mapping/spot analysis were combined to characterize Proterozoic granitic zircon in the eastern Gawler Craton, South Australia. Granites from the ~1.85 Ga Donington Suite and ~1.6 Ga Hiltaba Suite were selected from locations that are either mineralized or not, with the same style of iron-oxide copper gold (IOCG) mineralization. Although Donington Suite granites are host to mineralization in several prospects, only Hiltaba Suite granites are considered "fertile" in that their emplacement at ~1.6 Ga is associated with generation of one of the best metal-endowed IOCG provinces on Earth. Crystal oscillatory zoning with respect to non-formula elements, notably Fe and Cl, are textural and chemical features preserved in zircon, with no evidence for U or Pb accumulation relating to amorphization effects. Bands with Fe and Ca show mottling with respect to chloro–hydroxy–zircon nanoprecipitates. Lattice defects occur along fractures crosscutting such nanoprecipitates indicating fluid infiltration post-mottling. Lattice stretching and screw dislocations leading to expansion of the zircon structure are the only nanoscale structures attributable to self-induced irradiation damage. These features increase in abundance in zircons from granites hosting IOCG mineralization, including from the world-class Olympic Dam Cu–U–Au–Ag deposit. The nano- to micron-scale features documented reflect interaction between magmatic zircon and corrosive Fe–Cl-bearing fluids in an initial metasomatic event that follows magmatic crystallization and immediately precedes deposition of IOCG mineralization. Quantification of α-decay damage that could relate zircon alteration to the first percolation point in zircon gives ~100 Ma, a time interval that cannot be reconciled with the 2–4 Ma period between magmatic crystallization and onset of hydrothermal fluid flow. Crystal oscillatory zoning and nanoprecipitate mottling in zircon intensify with proximity to mineralization and represent a potential pathfinder to locate fertile granites associated with Cu–Au mineralization.

Keywords: zircon; IOCG deposits; Olympic Cu–Au Province; HAADF STEM; Fe–Cl-metasomatism; chloro–hydroxy–zircon nanoprecipitates; granite fertility

1. Introduction

Ore deposits falling within the broad iron-oxide-Cu–Au (IOCG) clan are a fascinating, and in some cases, poorly understood, family of magmatic–hydrothermal ore systems (References [1,2] and references therein). Debate on their genesis includes the relative timing and evolution of fluids during transition from the magmatic to hydrothermal stage. Detailed investigation of magmatic accessory minerals at appropriate scales of observation has enabled fluid–mineral interaction to be fingerprinted (e.g., using apatite [3,4]).

Zircon ($ZrSiO_4$) is a common accessory mineral and has been pivotal for the evolution of U–(Th)–Pb geochronology (References [5] and references therein). Aside from actinides, magmatic zircon will incorporate a range of trace elements (lanthanides, Y, Hf, and Ti) which are valuable tracers for mantle versus crustal origin of melts and for underpinning plate tectonic models during Earth cycles (e.g., [6–8]). Contemporary consensus views the incorporation of other, "non-formula" components in zircon, including Ca, Fe, Al, and H_2O, as being unrelated to primary magmatic processes (Reference [9], and references therein). These are most often measured within altered zircon (e.g., [10]) and are attributed to metamictization-related effects.

In this contribution, we bridge micron- to nanoscale observations to comprehensively characterize magmatic zircon from Proterozoic granites in the eastern Gawler Craton, South Australia (Figure 1A). Iron-oxide copper gold systems of various sizes are found within granites of different ages in the Olympic Cu–Au Province [11], for example, the Olympic Dam deposit [12] and Wirrda Well prospect, hosted by ~1.6 Ga (Hiltaba Suite) and ~1.85 Ga (Donington Suite) granitoids, respectively. The U–Pb age of hydrothermal hematite from Olympic Dam, a product of Fe-metasomatism, has been constrained by isotope dilution-thermal ionization mass spectrometry (ID-TIMS) to 1589.91 ± 0.94 Ma [13], crystallizing roughly 2–4 Ma after zircon within the granite hosting the deposit (chemical abrasion ID-TIMS; 1593.87 ± 0.21 Ma) [14].

The overarching aims of the present work were two-fold. Firstly, we aimed to document metasomatic, fluid-assisted alteration of zircon that occurs in a magmatic–hydrothermal environment prior to structural damage induced by alpha-decay. Secondly, we tested this hypothesis and its implications using samples from metallogenetically productive and unproductive granites of the same suites across the Gawler Craton. We set out to show that micron- to nanoscale observations of zircon geochemistry and crystal structure can, in combination, be used to trace early mineralizing fluids. Furthermore, we provide atomic-scale resolution images of zircon, offering insights into metasomatic processes and products, such as the formation of zircon nanoprecipitates and structural defects.

Such an approach provides potential qualitative indicators of magma fertility (the ability of a magma to generate hydrothermal fluids that are sufficiently well-endowed with Cu, etc., to form a sizable ore deposit). Such an idea is validated by geochemical analysis of known productive and unproductive granites, with a broad application in IOCG exploration across the Gawler Craton and elsewhere.

2. Background and Rationale

2.1. Zircon Chemistry and Structure

Magmatic zircon has a crystal structure resistant to physical and chemical degradation during secondary processes, properties which have motivated research into its usage as a durable host for nuclear waste storage [15]. However, zircon undergoes self-irradiation damage during U–(Th)–Pb decay, ultimately transitioning from crystalline to an amorphous (metamict) state [10], which can be

followed by partial to complete recrystallization. The amorphous domains begin to interconnect due to the radiation damage (α-decay), over a time period determined by U/Th concentrations and annealing rates [16]. The time dependency of structural damage is highly relevant for geochronology, as it can result in discordance of the U–Pb system, most commonly through Pb-loss. Disturbances to zircon U–Pb systematics via metamictization can, however, be selectively eliminated by chemical abrasion of damaged zones, prior to ID-TIMS, permitting high-precision geochronological constraints [17].

The secondary textures commonly observed to crosscut growth zones in magmatic zircon are attributed to re-equilibration of zircon in aqueous fluids and melts (Reference [18] and references therein). Primary oscillatory zoning in zircon can, however, be locally preserved, even in cases when the superimposed reaction temperature exceeds ~600 °C [19]. Structural damage can also create pathways for fluids to enter and precipitate minerals as inclusions within zircon displaying secondary microstructures. For example, Fe–Ti oxides and ZrO_2 observed along dislocation and pores in Hadean zircons (Jack Hills, Western Australia) are considered to postdate primary crystallization [20].

Elemental abundance and isotope ratios in zircon, including rare earth element (REE) fractionation patterns and Eu/Eu*, Sr/Y, and V/Sc anomalies, all readily determined by microbeam analysis, can be used to define magma fertility and track its evolution (Reference [21] and references therein). These geochemical pathfinders have been extensively applied to target metallogenically productive ("fertile") and non-productive ("infertile") granitic intrusions [22]. Despite the potential for identifying geochemical changes in zircon as a response to metasomatism, the commonly used microanalytical instrumentation, such as laser-ablation inductively-coupled plasma mass-spectrometry (LA-ICP-MS), cannot accurately spatially resolve compositions smaller than a few microns at best, a high threshold relative to typical internal textures and structures commonly found in zircon.

Z-contrast techniques such as high-angle annular dark-field scanning transmission electron microscopy (HAADF STEM; e.g., [23]) allows processes of metamictization and alteration to be addressed down to the nanoscale. For example, fission tracks relating to radiation damage, the nanoscale occurrence of Pb, and evidence for nanoscale U-mobility have been revealed by this technique [24–27]. Increasing levels of spatial resolution and analytical precision combined with in situ micro-sampling techniques have permitted HAADF STEM study of foils prepared by focused ion beam (FIB)-scanning electron microscopy (SEM) to visualize atomic structure and defects in minerals (e.g., [28,29]).

2.2. *The Olympic Cu–Au Province*

The Olympic Cu–Au Province, South Australia (Figure 1A) hosts IOCG-style mineralization attributed to hydrothermal activity associated with emplacement of the Gawler Silicic Large Igneous Province at ~1.6 Ga [11], accompanying the onset of Columbia/Nuna supercontinent breakup [30]. Magmatic activity is represented by the Hiltaba Suite and contemporaneous Gawler Range Volcanics [31]. The ~700 km long Olympic Cu–Au Province strikes roughly N–S along the eastern margin of the Gawler Craton from the Mount Woods Inlier in the north, which hosts the Prominent Hill deposit, through Olympic Dam and Carrapateena, to the Moonta and Hillside deposits in the south (Figure 1A). Each major deposit is surrounded by numerous smaller, less explored prospects. Host lithologies range from Gawler Range Volcanics (e.g., Acropolis prospect; Figure 1B), granites of Hiltaba Suite affiliation (e.g., Olympic Dam within Roxby Downs Granite; RDG), or older granitoids (e.g., ~1.85 Ga Donington Suite granites at Wirrda Well and Carrapateena; Figure 1A,B).

Several other styles of mineralization occur on the Eyre Peninsula to the immediate west of the Olympic Province. These include older banded iron formations [32] and younger U-mineralization within cover rocks suprajacent to granites belonging to the Samphire Pluton of Hiltaba Suite affiliation [33]. A further Hiltaba Suite granitoid is the Charleston Granite (Figure 1A). No IOCG-style mineralization has yet been discovered associated with either the Charleston Granite or the Samphire Pluton. Donington Suite granitoids are present throughout the Eyre Peninsula and outcrop as far south as Cape Donington, south of Port Lincoln. Although the potential for an extension of the Olympic Cu–Au Province westwards into the Eyre Peninsula remains largely untested, we note that

several of the aforementioned banded iron formation ores feature geochemical signatures suggestive of overprinting by hydrothermal fluids of granitic affiliation [32,34,35].

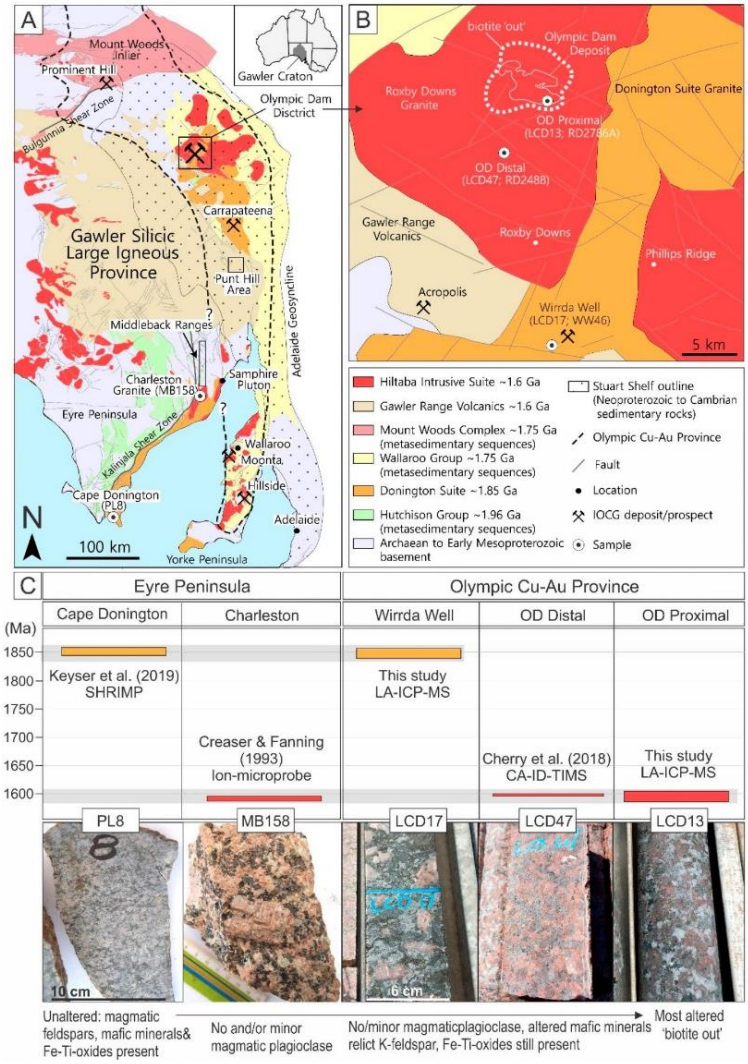

Figure 1. (**A**) Geological map of the eastern Gawler Craton and (**B**) the Olympic Dam district; data were taken from the Geological Survey of South Australia (https://map.sarig.sa.gov.au/). Locations of the five granite samples addressed in this study and the outline of the Olympic Cu–Au district are marked. (**C**) Table of ages and corresponding uncertainties (colored bars) for each granite sample studied here, with geochronology conducted either in this study (LA-ICP-MS) or in previous published work as indicated. The orange and red uncertainty bars represent the Donington Suite and Hiltaba Intrusive Suite, respectively, and their location within either the Eyre Peninsula or Olympic Cu–Au Province. Corresponding hand specimen photographs of each sample are shown below the age diagram, indicating degree of granite alteration. References: Keyser et al. (2019) [34]; Creaser and Fanning (1993) [36]; Cherry et al. (2018) [14].

Formation of IOCG deposits remains highly contested, particularly with respect to sources and timing of fluids and contained metals (References [1,2], and references therein). In the Gawler Craton,

lithospheric architecture, mantle metasomatism, and cratonic metallogeny [37,38] have been linked to generic models for IOCG genesis with global applicability [1]. The large volumes of Fe required to form IOCG deposits associated with granitoid-derived fluids or felsic magmatism have recently been proposed to be derived from underplating mafic magma in deeper reservoirs allowing for volatile- and metal-transfer via magma mingling and magnetite flotation [39]. If Fe is sourced from a deep magma reservoir, then zircon, as a ubiquitous magmatic accessory mineral, should record this, either in the magmatic growth stage or as an overprint following interaction with early, low pH hydrothermal fluids released from the locally Fe-enriched magma. Zircon from fertile and barren granitoids should, therefore, differ from one another, both in terms of their geochemical signatures and textures at the micron- to nanoscale.

3. Sample Suite

For this study, we used magmatic zircon from five granitoids of Donington- (~1.85 Ga) and Hiltaba-affiliation (~1.6 Ga) from within and outside the Olympic Cu–Au Province (Figure 1C; Table 1). Except for the example from Cape Donington, all granites considered here displayed macroscopic alteration, albeit to varying degrees, while still retaining granitoid textures and some relict magmatic minerals. The sample suite is summarized in Table 1 with respect to rock type, location, key features, and types of analysis reported in the present contribution.

Zircon from all five case studies were temporally well-constrained by U–Pb methods, either previously published, or given in this study (Figure 1C). We included zircon from RDG samples, collected at locations distal and proximal to the Olympic Dam deposit (Figure 1B), to evaluate whether metasomatic processes analogous to those reported for feldspars [40] and apatite [3] could be tracked. Secondly, we sought to identify whether such processes are recognizable in older zircon from Donington Suite granite hosting the Wirrda Well prospect [41], 25 km SSE of Olympic Dam. Zircon from the Charleston and Cape Donington granites are included to assess the potential of zircon as an indicator of the metallogenic fertility of plutons in the Eyre Peninsula bordering the Olympic Cu–Au Province, where IOCG-style mineralization has not thus far been discovered.

4. Methodology

Four granite samples (3 one-inch polished blocks and one thin-section) and one polished block containing separated zircon (sample PL8) were studied in backscattered electron (BSE) and secondary electron (SE) modes using an FEI Quanta 450 SEM. Cathodoluminescence imaging was undertaken using an FEI Quanta 600 SEM equipped with a tungsten filament electron source. The purpose was to identify zircon grains with representative characteristics, particularly primary growth with oscillatory zoning textures and overprinting thereof. Such grains were analyzed by electron probe microanalysis (EPMA; Cameca SX-Five) and LA-ICP-MS (RESOlution-LR excimer laser microprobe coupled to an Agilent 7900x Quadrupole ICP-MS) for minor to trace element and U–Pb compositions using both spot analysis and mapping. All instruments are housed at Adelaide Microscopy, University of Adelaide. Extended details of instrumentation and analytical parameters are provided in Supplementary Materials A. All geochemical data are tabulated in Supplementary Materials B.

For subsequent S/TEM study, seven foils (Table 1; Figure 2A–E, Figure 3B,C, and Supplementary Materials C, Figure S1) were extracted in-situ, thinned to <100 nm by ion beam (Ga^+) milling and attached to Cu grids on an FEI Helios Nanolab 600 FIB-SEM platform. Of the seven foils, five were cut across oscillatory zonation observed on grain surfaces in zircon to target their development at depth, allowing correlation between micron- and nanoscale characteristics. In the case of the Wirrda Well Donington sample (LCD17), foil preparation targeted areas that yielded concordant (Foil #5) and discordant (Foil #4) U/Pb data points. In the Olympic Dam (OD) distal sample (LCD47), two zircon grains were cut, one with primary oscillatory zoning (Foil #1) and a second grain (Foil #2) displaying secondary, highly altered domains lacking oscillatory zoning.

Table 1. Summary of the samples and foils investigated in this study.

Region	Sample ID	Granite Petrography and Age(s), References	Locality (Drill Hole)	Micron-scale Analysis				Nanoscale Analysis: HAADF STEM Imaging and EDS Spot/Mapping					Figures Showing Zircon Images and Maps
				Analytical Methods					Key Zircon Features				
				LA-ICP-MS			EPMA Map	Foil No. (#)	NF Element Zoning (STEM Maps)	Mottling/ CHZ-Nano-precipitates	Others	Main Zone Axes Imaged (See Figures 12 and 13)	
				U–Pb Dating	Spot Analysis	Map							
Olympic Cu–Au Province	LCD47	HS-Roxby Downs granite [14,40,42], this study	Distal from OD (RD2488)		x			#1	Fe, Ca, Cl	X	screw dislocation	$(1\bar{1}1]$)	Figures 2, 8, 10, 11, 14, 15, Supplementary C, Figures S1 and S3
								#2 *	Fe, Ca, Al, <Cl, Y	x	Xtm veinlet, pores	(001])	Figure 2, Supplementary Figure S3
	LCD13		Proximal to OD (RD2786A)	x	x		Fe, Cl	#3	Fe, Cl, <Ca	x	Hm inclusions	(001])	Figures 3, 5, 9, Supplementary Figure S3
	LCD17	DS granite [42,43], this study	Wirrda Well (WW46)	x	x		Fe, Cl	#4	Fe, Ca	x	Xtm veinlet, screw dislocation	(001])	Figures 3, 5, 6, 15, Supplementary Figure S3
								#5 **	Not mapped	x	Fe detected from spot analysis	[100]; $[1\bar{1}0]$	Figures 3 and 5
Eyre Peninsula	MB158	HS-Charleston granite [36,44]	South of Middleback Ranges					#6	Fe, Ca, Ti, Al, Y, Th		2-D screw dislocation, fracture U-NP	[001]	Figures 7, 15, Supplementary Figure S1
	PL8	DS granite [44]	Cape Donington		x	x		#7	None—primary magmatic		stretching defects	[100]; $[1\bar{1}0]$	Figures 2, 15, Supplementary Figure S2

All samples were characterized by EPMA spot analysis. Sample MB158 for Charleston granite was not analyzed by LA-ICP-MS due to the small size of zircon grains, and particularly the grain from which Foil #6 was extracted (see Figure S1). U–Pb dating was carried out for two samples (including the grains from which the foils were extracted) from locations that were not previously dated. * Foil #2 differs from Foil #1 in containing secondary rather than primary textures. ** Foils #4 and #5 were cut perpendicular and parallel to grain elongation (c-axis), respectively. Upper case X represents the most intense mottling/nanoprecipitates. Abbreviations: CHZ—chloro–hydroxy–zircon; NF—non-formula elements; Hm—hematite; Xtm—xenotime; OD—Olympic Dam; HS—Hiltaba Suite; DS—Donington Suite; U-NP—uranium-bearing nanoparticles.

Nanoscale study, HAADF STEM imaging, and EDS spot analysis/mapping were performed using an ultra-high-resolution, probe-corrected, FEI Titan Themis S/TEM operated at 200 kV. This instrument is equipped with the X-FEG Schottky source and Super-X EDS geometry. The Super-X EDS detector provides geometrically symmetric EDS detection with an effective solid angle of 0.8 Sr. Probe correction delivered sub-Ångstrom spatial resolution and an inner collection angle greater than 50 mrad was used for HAADF experiments using the Fischione HAADF detector.

Diffraction indexing was performed using Winwulff© 1.5.2 software and publicly available data from the American Mineralogist Crystal Structure Database. Crystal structure models were obtained using CrystalMaker®version 10.1.1 and STEM for xHREM^{TM} version 4.1 software.

5. Results

5.1. Zircon Petrography, U–Pb Dating, and Selection of Grains for Nanoscale Study

Screening of zircon populations in each sample shows a range of grain sizes from 30 to ~300 μm, displaying both primary and secondary overprinting textures (Figure 2A–D). Zircons in two samples of unknown age but with assumed affiliation were dated by LA-ICP-MS to confirm their Hiltaba and Donington Suite ages.

Uranium–Pb dating of Wirrda Well zircon (LCD17) produced an upper intercept age of 1848 ± 10 Ma with concordant and highly discordant data points (Figure 3A), corresponding to published Donington Suite ages [43,44]. Dating of the OD proximal zircon (LCD13) gives an upper intercept age of 1572 ± 37 Ma, with analyses displaying both a high degree of concordance and discordancy. Full U–Pb data for analyzed zircons and reference material is tabulated in Supplementary Materials B, Table S3.

Selection of grains for nanoscale study was based upon several criteria: (i) well-constrained U–Pb ages in which case the FIB cut was placed next to a LA-ICP-MS crater (Figure 3); (ii) euhedral morphology with elongation along the *c*-axis; and (iii) large, least-fractured, inclusion-free grains. Subhedral zircon with marginal dissolution was also included to assess the most intense alteration observed within the sample suite (e.g., OD distal zircon; Figure 2B,D). In all five samples, zircon displays crystal oscillatory zoning expressed as bright and dark bands on BSE images (Figures 2 and 3 and Supplementary Materials C, Figure S1A). The intensity contrast of the banding ranged from subtle in zircon in granites from the Eyre Peninsula (PL8 and Charleston; Figure 2E and Supplementary Materials C, Figure S1A) to strong in granites from the Olympic Cu–Au Province. Furthermore, the dark bands could display mottled textures with respect to what appears to be inclusions, varying from sub-micron (in the banding) to ~1–2 μm (in the domains obliterating the zoning) (Figure 2C,D).

Spot EDS-SEM analysis does not show any compositional difference between the "inclusions" and host band/domain suggesting these could instead be pores. However, secondary electron imaging only rarely shows the presence of pores, generally in the scalloped areas with coarser mottled textures. Otherwise, the nature of the sub-micron "inclusions" cannot be resolved with SEM imaging alone.

Except for the Cape Donington sample (PL8; Figure 2E), all grains were fractured to varying degrees and were associated with marginal corrosion and occurrence of darker still domains with irregular and/or scalloped morphologies superimposed on crystal zoning (Figure 2D). Radial fractures, typically interpreted as accompanying metamictization, were present in such cases, notably in the OD distal zircon (Figure 2B,D). Additionally, veinlets and overgrowths of xenotime (Figure 3B), as well as tiny U-bearing phases, were also present in the RDG samples.

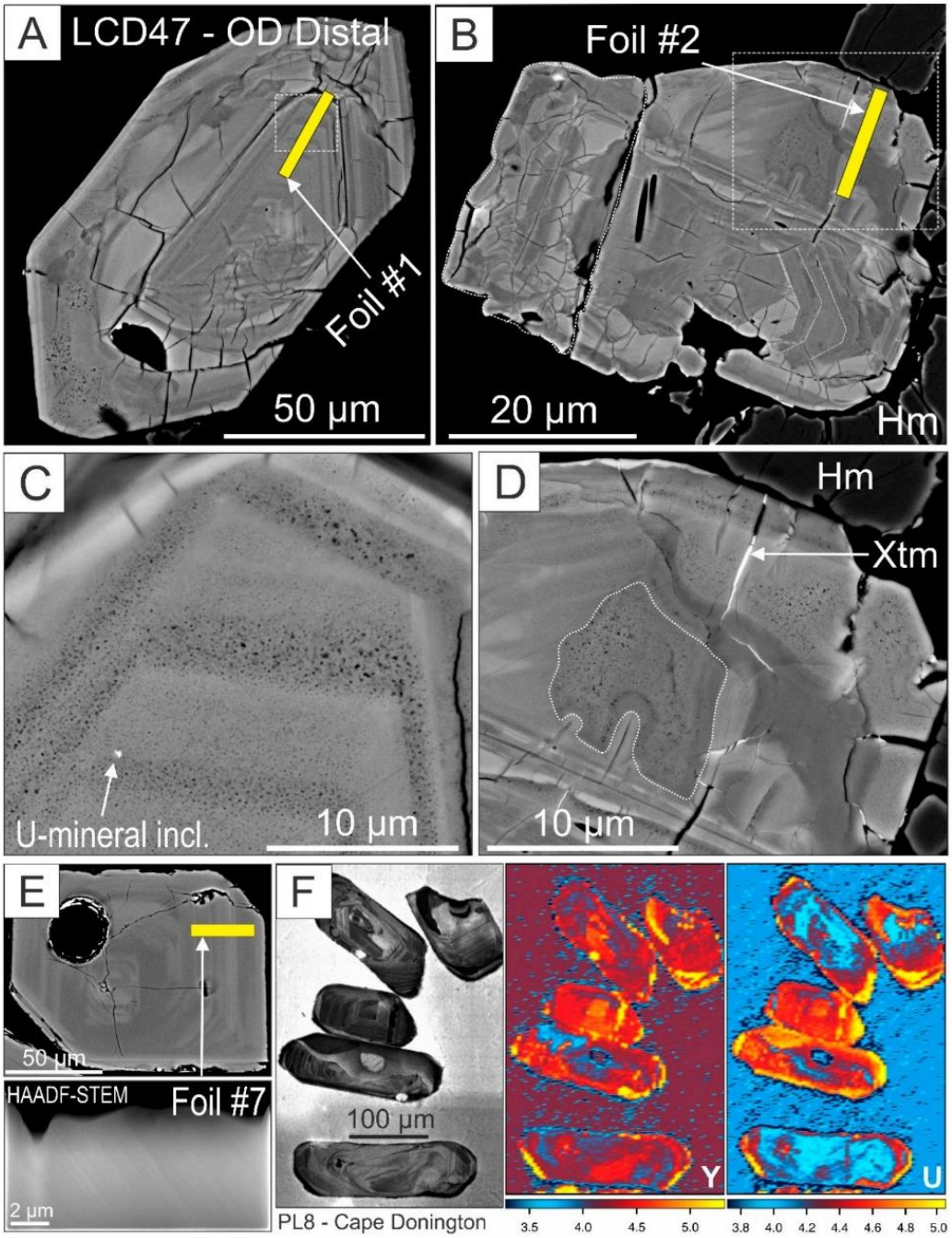

Figure 2. BSE images of grains #1 (**A** and **C**) and #2 (**B** and **D**) from OD distal zircon (sample LCD47). Note the mottled dark areas were either bands within crystal oscillatory zoning (**C**) or scalloped domains superimposed onto crystal zoning (**D**). (**E**) BSE (top) and HAADF STEM image (bottom) showing crystal oscillatory zoning for Cape Donington zircon (PL8). (**F**) Cathodoluminescence image (left) and LA-ICP-MS element maps (right) showing oscillatory zoned patterns for Y and U in coarser zircon grains from PL8. Scale in 10^n counts per second (extended maps are given in Supplementary Materials C, Figure S2).

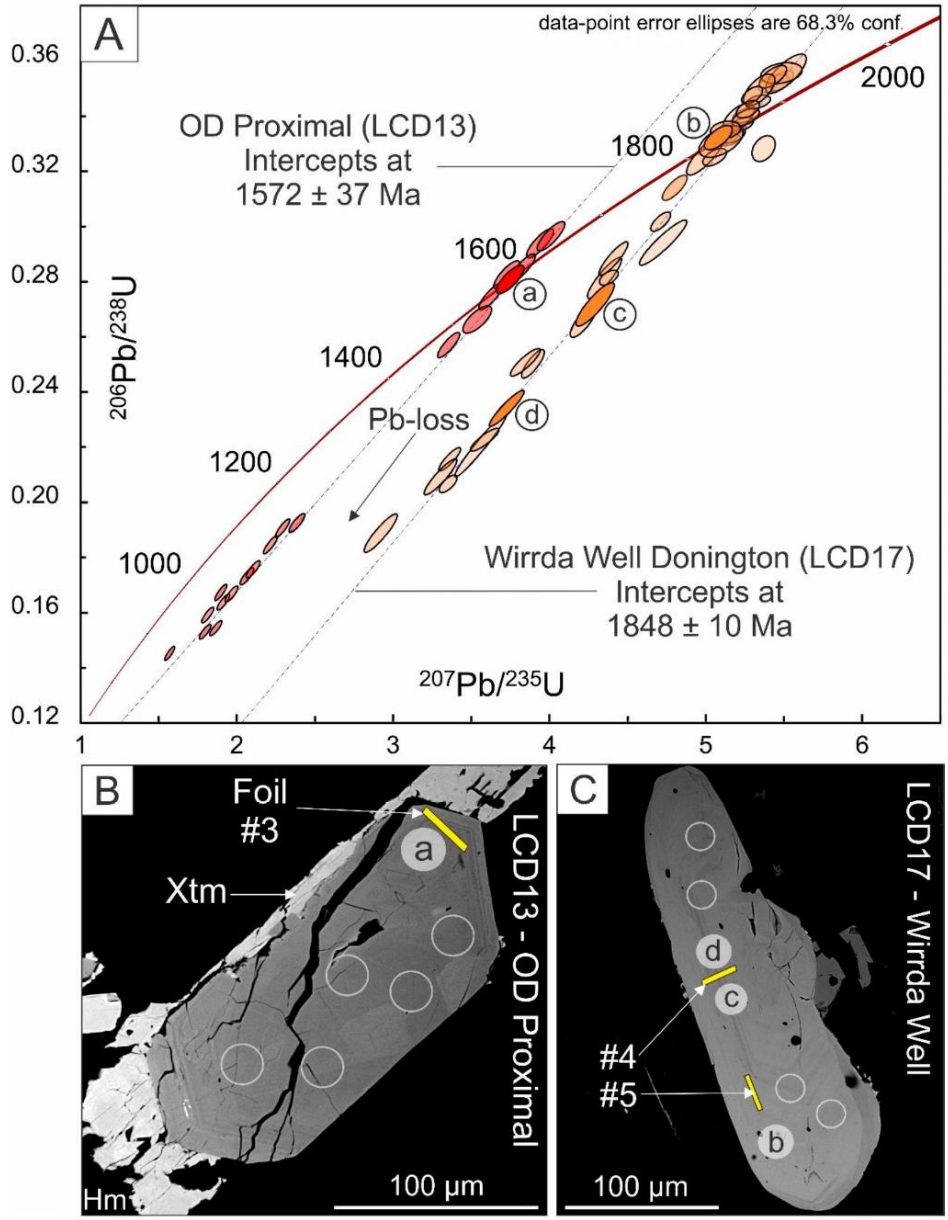

Figure 3. Concordia diagram (**A**) for OD proximal zircon (LCD13, red ellipses) and Wirrda Well zircon (LCD17, orange ellipses; U–Pb data are presented in Supplementary Materials B, Table S3). Circled letters correspond to LA-ICP-MS craters in BSE images of the dated grains (**B** and **C**).

5.2. *Trace and Minor Element Concentrations*

Electron microprobe datasets for analyzed zircon (Table 2 and Supplementary Materials B, Table S4) showed steady, consistent concentrations of HfO_2 (1.5–2.0 wt.%), Y_2O_3, $(HREE)_2O_3$ and P_2O_5, minor UO_2, PbO, and ThO_2 in most but not all analyses, and sporadic concentrations of Na_2O, K_2O, CaO, MgO, MnO, and Al_2O_3 above the minimum detection limit (mdl) values across the sample suite. TiO_2

was measured consistently (up to 0.06 wt.%) in the Charleston Granite sample only. Sc_2O_3 was below mdl in most analyses.

"Bright" and "dark" bands in zircon from Cape Donington zircon (PL8) were indistinguishable in terms of composition but the latter had lower analytical totals before recalculation. "Dark" bands in zircon from the Wirrda Well Donington Suite and Charleston Granite samples (LCD17 and MB158) also had totals ~1 wt.% lower than the "bright" bands, generally higher Fe_2O_3 and minor but measurable Cl. Analogous trends were seen in samples the two OD samples (LCD47 and LCD13), in which the "dark" bands contained 1.0–1.9 wt.% Fe_2O_3 and ~0.1 wt.% Cl. Analytical totals were 1–2 wt.% lower than for "bright" bands. Additionally, fluorine was measurable (up to 0.15 wt.%) in a minority of analytical spots from the "dark" bands. Variability of concentrations within each sample, and between "bright" and "dark" bands in the same zircon grain, was a feature of the dataset; the degree of intra-grain variability increased with the total of non-formula elements. Importantly, measured concentrations of Y_2O_3, $(HREE)_2O_3$, P_2O_5, UO_2, and ThO_2 were statistically identical in "bright" and "dark" bands across the dataset.

Laser ablation inductively coupled plasma mass spectrometry datasets (Supplementary Materials B, Table S5) corroborated and confirmed the accuracy and inherent variability of the EPMA data. Zircon from the Charleston granite was not considered due to the small grain sizes. Other elements (e.g., Sn, Nb, Ta) were not present at concentrations exceeding (at most) a few tens of ppm. Even using a small diameter spot (19 μm), the LA-ICP-MS method did not permit selective analysis of "bright" and "dark" bands.

Cape Donington zircon showed oscillatory patterns correlating with U, Pb, REE, and Y in LA-ICP-MS maps (Figure 2F; Supplementary Materials C, Figure S2). Chondrite-normalized fractionation trends constructed from LA-ICP-MS data (Figure 4A) showed reproducible patterns for zircon in each granite, although with systematic differences in the LREE portion between Donington and Hiltaba Suite samples.

Principal component analysis (PCA) applied to the centered logratio-transformed LA-ICP-MS dataset provided additional insights. A projection of PC1 versus PC2 (Figure 4B,C) showed two distinct groupings: (1) Y, REE (except Eu and Pr) and P; and (2) Hf, U, Pb, Th, Ti, Nb, Eu, and Pr. On both plots, these groupings are distinct from a third group comprising Fe, Mn, Al, and Ca. These patterns underscore interpretation of the EPMA data in which the geochemical signature associated with the metasomatic overprint was defined by Fe, Mn, Al, and Ca, and is independent of any magmatic signature or pattern of distribution at the grain-scale involving element groups (1) and (2). A ternary Fe–Al–Hf diagram (Figure 4D) allows a visual expression of chemical change from least-altered zircon (sample PL8), effectively without Fe or Al, through moderately altered zircon in sample LCD17, to the sub-populations of zircon in samples LCD13 and LCD17 from Olympic Dam, which contained the highest amounts of substituting non-formula (NF) elements.

5.3. Assessment of Zircon Stoichiometry and Substitution Model

Recalculation of EPMA data was undertaken following a template used for hydrogarnet and underlying assumptions/substitutions as provided by Supplementary Materials A. A key objective was an estimation of H_2O content based on allocation of all minor elements (Fe, Al, Mn, and Ca) to structural sites, bringing analytical totals close to 100 wt.% (from ~99.2). The data (Supplementary Materials B, Table S4) showed a correlation between atom per formula unit (apfu) values for $(REY + Sc)^{3+}$ and P^{5+} on the plot of these two variables (Figure 4E), albeit with a deficiency in the latter—a feature widely described in several publications (see Supplementary Materials A) and taken to indicate more complex substitution mechanisms. Electron microprobe datasets implicitly carry a margin of analytical error, which in the case of the zircon analyzed here were compounded by concentrations of many elements around or below mdl, and by assumptions in the formula calculation that were in turn based on equivocal evidence given in the literature (see Supplementary Materials A). As such, derived stoichiometries and calculated OH contents represent only a best-possible estimation based on the data available.

Nonetheless, using mean compositions and a simplified formulation in which Zr* + REE* + Fe + NF = 1, where Zr * = Zr + Hf + Th + U; REE* = Sc + Y + (La to Lu); NF = Mg + Ca + Mn + Nb + Pb + Al, B = Si + Al + P + Ti = 1, and I = Na + K (interstitial), mean compositions (Table 3) can be defined for zircon from the bright and dark bands within each sample.

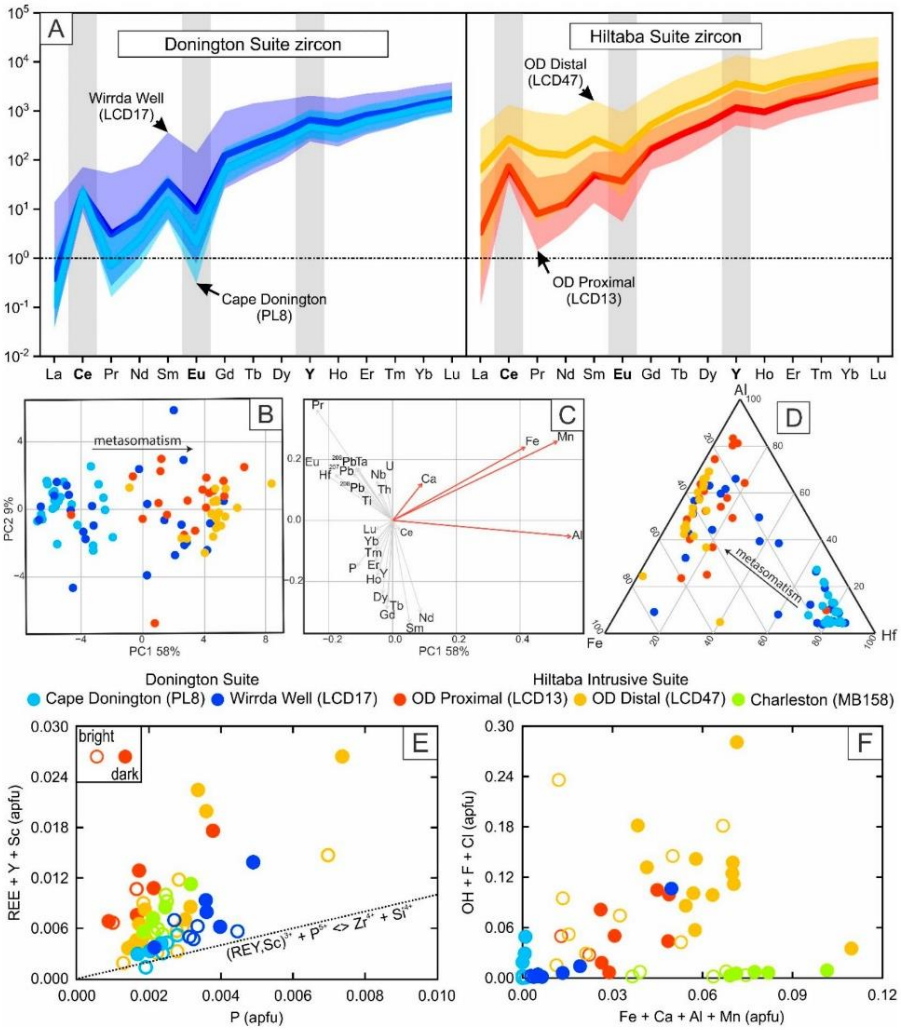

Figure 4. (**A**) LA-ICP-MS chondrite-normalized REY (REE + Y) fractionation trends for Donington Suite (light and dark blue) and Hiltaba Intrusive Suite (red and orange) samples. (**B** and **C**) PCA of LA-ICP-MS data, used to distinguish associated element signatures, and (**D**) a ternary Fe–Al–Hf diagram demonstrating the degree of zircon metasomatism (LA-ICP-MS data; Supplementary Materials B, Table S5). (**E**) Plot of $(REY+Sc)^{3+}$ versus P^{5+} (EPMA data). (**F**) Plot of "non-formula" components $\Sigma(Fe_2O_3 + Al_2O_3 + MnO + CaO)$ versus apfu $\Sigma(OH + Cl + F)$, respectively. The EPMA diagrams illustrate the relationship between substitution of both non-formulae elements and OH in zircon. Open and closed data points represent bright and dark bands in zircon, respectively; color codes correspond to samples in **A**–**D** (EPMA data; Supplementary Materials B, Table S4). See main text and Supplementary Materials A for additional explanation.

Table 2. EPMA zircon spot analyses. Gr1: grain 1; Gr2; grain2.

LCD13 (OD Proximal)		Na_2O	MgO	Al_2O_3	SiO_2	P_2O_5	K_2O	CaO	TiO_2	MnO	Fe_2O_3	Y_2O_3	ZrO_2	HfO_2	PbO	ThO_2	UO_2	Cl	Sum	H_2O *	Sum *
Bright		0.046	0.016	<mdl	32.57	0.039	0.011	0.076	0.01	0.035	0.822	0.023	63.834	2.355	0.036	<mdl	0.163	0.116	100.60	0.11	100.69
Bright		0.03	0.011	<mdl	32.165	0.064	<mdl	0.042	0.01	0.037	0.46	0.145	64.104	1.454	0.089	0.08	0.332	0.048	99.640	0.23	99.86
Mean	$n = 2$	0.038	0.014	<mdl	32.368	0.052	<mdl	0.059	0.01	0.036	0.641	0.084	63.969	1.905	0.063	<mdl	0.248	0.082	100.12	0.17	100.275
Dark		0.083	0.047	0.011	32.291	0.063	0.011	0.153	0.015	0.029	0.972	0.085	62.507	1.532	0.032	0.078	0.178	0.119	98.599	0.002	98.574
Dark		0.123	0.028	0.41	31.637	0.565	0.031	0.138	0.036	0.117	1.152	1.051	60.714	2.818	0.083	0.09	0.888	0.075	101.254	0.197	101.434
Dark		0.197	0.019	0.186	31.056	0.39	0.017	0.211	0.024	0.11	1.386	0.868	59.613	2.485	0.097	0.073	0.827	0.066	98.842	0.465	99.292
Dark		0.058	0.022	0.008	32.46	0.145	0.007	0.123	0.012	0.049	0.9	0.484	62.749	1.148	0.048	0.196	0.25	0.156	99.547	0.049	99.561
Dark		<mdl	0.021	0.021	32.218	0.082	0.011	0.185	0.008	0.071	0.956	0.12	63.205	1.385	0.048	0.122	0.21	0.379	99.705	0.149	99.769
Dark		0.067	0.013	0.007	31.601	0.034	0.016	0.085	0.008	0.068	0.912	0.029	62.204	2.855	0.048	<mdl	0.203	0.163	98.780	0.353	99.096
Dark		0.064	0.021	0.056	31.239	0.066	0.01	0.381	0.007	0.114	1.161	0.166	60.557	2.049	0.07	0.092	0.742	0.086	97.675	0.438	98.052
Mean	$n = 7$	0.099	0.024	0.1	31.786	0.192	0.015	0.182	0.016	0.08	1.063	0.4	61.65	2.039	0.061	0.109	0.471	0.149	99.20	0.236	99.397
LCD47 (OD Distal)		**Na_2O**	**MgO**	**Al_2O_3**	**SiO_2**	**P_2O_5**	**K_2O**	**CaO**	**TiO_2**	**MnO**	**Fe_2O_3**	**Y_2O_3**	**ZrO_2**	**HfO_2**	**PbO**	**ThO_2**	**UO_2**	**Cl**	**Sum**	**H_2O ***	**Sum ***
Bright (Gr2)		<mdl	0.017	0.132	31.645	0.113	0.006	0.032	0.043	0.059	0.227	0.317	67.091	1.379	0.03	0.103	0.145	0.008	101.963	1.194	103.156
Bright (Gr2)		0.074	0.023	0.122	31.294	0.072	0.008	0.535	0.024	0.153	1.807	0.211	61.755	1.399	0.042	0.117	0.219	0.076	98.399	0.877	99.259
Mean	$n = 2$	<mdl	0.02	0.127	31.47	0.093	0.007	0.284	0.034	0.106	1.017	0.264	64.423	1.389	0.036	0.11	0.182	0.042	100.181	1.036	101.208
Dark (Gr2)		0.036	0.027	0.18	30.965	0.115	0.006	0.427	0.009	0.143	1.44	0.167	61.61	1.402	0.03	0.051	0.111	0.147	97.233	0.651	97.851
Dark (Gr2)		0.046	0.03	0.196	31.273	0.054	0.006	0.435	0.038	0.174	1.333	0.043	61.692	1.736	0.037	0.023	0.12	0.089	97.565	0.467	98.012
Dark (Gr2)		0.059	0.033	0.838	30.827	0.136	0.012	0.792	0.018	0.262	1.948	0.553	58.456	1.225	<mdl	0.089	0.125	0.111	96.520	0.086	96.532
Mean	$n = 3$	0.047	0.03	0.405	31.022	0.102	0.008	0.551	0.022	0.193	1.574	0.254	60.586	1.454	0.034	0.054	0.119	0.116	97.106	0.401	97.465
Bright (Gr1)		<mdl	0.011	0.009	33.017	0.11	<mdl	0.01	0.011	<mdl	0.91	0.116	65.951	1.263	0.036	0.036	0.048	0.008	101.641	0.143	101.783
Bright (Gr1)		0.053	0.023	0.09	30.846	0.073	0.006	0.47	<mdl	0.138	1.177	0.113	61.442	1.618	0.04	0.058	0.188	0.099	96.740	0.645	97.335
Bright (Gr1)		0.111	0.032	0.143	31.561	0.266	0.011	0.329	0.007	0.202	1.348	0.486	60.903	1.602	0.042	0.042	0.286	0.066	98.095	0.149	98.193
Bright (Gr1)		<mdl	0.016	0.034	31.791	0.05	0.006	0.015	0.037	0.012	0.496	0.017	65.21	1.247	0.03	0.017	0.051	<mdl	99.214	0.465	99.679
Bright (Gr1)		<mdl	0.012	0.035	32.376	0.086	<mdl	0.024	0.007	0.019	0.381	0.057	65.094	1.416	0.025	0.024	0.037	0.009	99.780	0.072	99.850
Bright (Gr1)		<mdl	0.4	0.447	32.714	0.118	0.006	0.03	0.035	0.03	0.69	0.165	65.902	1.477	0.041	0.027	0.061	0.012	102.467	0.375	102.839
Bright (Gr1)		<mdl	0.02	0.1	32.199	0.108	<mdl	0.033	0.017	0.06	0.4	0.15	65.179	1.394	0.029	0.041	0.052	0.012	100.099	0.253	100.349
Mean	$n = 5$	<mdl	0.073	0.123	32.072	0.116	0.007	0.13	0.019	0.077	0.772	0.158	64.24	1.431	0.035	0.035	0.103	0.034	99.719	0.3	100.004
Dark (Gr1)		0.034	0.029	0.467	30.897	0.129	0.014	0.429	0.013	0.214	1.45	0.764	60.699	1.358	0.037	0.074	0.147	0.09	97.673	0.648	98.301
Dark (Gr1)		0.038	0.019	0.027	31.119	0.071	0.007	0.244	0.021	0.132	1.239	0.06	62.206	1.414	0.023	0.035	0.082	0.098	97.233	0.613	97.823
Dark (Gr1)		0.023	0.027	0.214	31.359	0.072	0.006	0.455	0.048	0.163	1.175	0.159	61.716	1.448	0.029	0.053	0.116	0.122	97.660	0.386	98.018
Dark (Gr1)		0.028	0.02	0.228	31.43	0.067	0.008	0.434	0.01	0.145	1.909	0.138	61.736	1.232	0.019	0.055	0.094	0.125	98.030	0.58	98.582
Dark (Gr1)		0.032	0.03	0.216	31.454	0.064	0.008	0.374	0.077	0.186	1.666	0.081	61.894	1.405	0.017	0.035	0.105	0.085	98.014	0.462	98.457
Dark (Gr1)		0.067	0.021	0.159	31.781	0.069	<mdl	0.442	0.006	0.171	1.413	0.087	62.024	1.258	0.025	0.042	0.085	0.065	98.042	0.232	98.233
Dark (Gr1)		0.098	0.028	0.262	31.635	0.288	0.014	0.512	0.029	0.189	1.74	0.937	60.734	1.349	0.032	0.101	0.276	0.067	99.357	0.468	99.748
Dark (Gr1)		0.06	0.039	0.335	30.747	0.061	0.009	0.478	0.083	0.191	1.774	0.094	63.446	1.476	0.038	0.03	0.134	0.069	99.311	1.397	100.692
Dark (Gr1)		0.094	0.023	0.073	30.481	0.12	<mdl	0.28	0.008	0.143	0.968	0.252	62.081	1.27	0.035	0.059	0.082	0.124	96.452	0.843	97.267
Mean	$n = 9$	0.053	0.026	0.22	31.211	0.105	0.009	0.405	0.033	0.17	1.482	0.286	61.837	1.357	0.028	0.054	0.125	0.094	97.975	0.625	98.569

Table 2. *Cont.*

MB158 (Charleston)		Na_2O	MgO	Al_2O_3	SiO_2	P_2O_5	K_2O	CaO	TiO_2	MnO	Fe_2O_3	Y_2O_3	ZrO_2	HfO_2	PbO	ThO_2	UO_2	Cl	Sum	H_2O	Sum *
Bright		<mdl	<mdl	0.036	33.001	0.099	0.008	0.175	0.04	0.129	1.292	0.224	65.185	1.353	0.051	0.148	0.13	0.016	102.381	0.032	102.41
Bright		0.032	0.016	<mdl	31.708	0.092	<mdl	0.674	0.052	0.188	2.082	0.147	63.283	1.32	0.049	0.081	0.12	0.046	100.153	0.005	100.147
Bright		0.058	0.007	0.02	31.93	0.087	0.007	0.66	0.06	0.087	1.704	0.108	63.229	1.393	0.046	0.042	0.107	0.034	99.980	0	99.973
Bright		0.048	0.053	0.164	32.152	0.096	0.005	0.933	0.031	0.144	1.224	0.273	62.378	1.536	0.038	0.038	0.154	0.063	99.842	0.022	99.85
Bright		0.033	0.012	0.013	32.399	0.083	0.007	0.253	0.027	0.175	1.02	0.114	64.156	1.524	0.036	0.038	0.148	0.016	100.366	0.005	100.368
Mean	$n = 5$	0.043	0.022	0.058	32.238	0.091	0.007	0.539	0.042	0.145	1.464	0.173	63.646	1.425	0.044	0.069	0.132	0.035	100.544	0.013	100.55
Dark		0.044	0.019	0.035	31.646	0.095	0.007	1.115	0.029	0.133	1.784	0.206	62.498	1.21	0.057	0.124	0.143	0.06	99.657	0.016	99.659
Dark		0.04	0.016	0.073	32.077	0.124	<mdl	1.399	0.055	0.153	2.203	0.355	61.528	1.16	0.045	0.232	0.147	0.064	100.175	0.029	100.189
Dark		<mdl	0.016	0.013	31.92	0.082	<mdl	0.677	0.064	0.176	2.211	0.19	62.89	1.375	0.032	0.121	0.16	0.047	100.293	0.024	100.306
Dark		0.062	0.012	0.01	31.372	0.07	<mdl	0.981	0.014	0.219	1.306	0.102	61.879	1.397	0.036	0.046	0.15	0.052	98.0480	0	98.037
Dark		0.033	0.017	0.083	31.403	0.081	0.007	1.033	0.014	0.163	1.281	0.113	61.841	1.523	<mdl	0.084	0.154	0.049	98.317	0.014	98.32
Mean	$n = 5$	0.045	0.016	0.043	31.684	0.09	<mdl	1.041	0.035	0.169	1.757	0.193	62.127	1.333	0.043	0.121	0.151	0.054	99.298	0.017	99.302
PL8 (Cape. Don)		Na_2O	MgO	Al_2O_3	SiO_2	P_2O_5	K_2O	CaO	TiO_2	MnO	Fe_2O_3	Y_2O_3	ZrO_2	HfO_2	PbO	ThO_2	UO_2	Cl	Sum	H_2O *	Sum *
Bright		<mdl	0.008	<mdl	32.518	0.107	<mdl	<mdl	0.005	<mdl	<mdl	0.15	65.716	1.233	0.023	0.027	0.035	<mdl	100.06	0.012	100.071
Bright		<mdl	0.01	0.008	32.801	0.092	<mdl	<mdl	0.007	0.012	0.026	0.039	65.94	1.392	0.019	0.015	0.021	<mdl	100.589	0.003	100.592
Bright		<mdl	<mdl	<mdl	32.646	0.097	<mdl	0.01	<mdl	<mdl	<mdl	0.075	65.891	1.275	0.038	0.03	0.064	<mdl	100.396	0.009	100.405
Bright		<mdl	<mdl	<mdl	32.759	0.074	<mdl	<mdl	0.012	<mdl	<mdl	0.034	65.863	1.334	0.026	0.02	0.045	<mdl	100.249	0	100.249
Mean	$n = 4$	<mdl	<mdl	<mdl	32.681	0.093	<mdl	<mdl	0.008	<mdl	<mdl	0.075	65.853	1.309	0.027	0.023	0.041	<mdl	100.324	0.006	100.329
Dark		<mdl	0.009	<mdl	31.997	0.077	<mdl	<mdl	0.01	<mdl	0.032	0.028	65.14	1.326	0.03	<mdl	0.012	<mdl	98.907	0.142	99.049
Dark		<mdl	0.008	<mdl	32.423	0.09	<mdl	<mdl	0.006	<mdl	<mdl	0.038	65.806	1.41	<mdl	<mdl	0.016	<mdl	100.114	0.092	100.206
Dark		<mdl	<mdl	<mdl	32.005	0.065	<mdl	<mdl	0.008	<mdl	0.041	0.025	65.502	1.326	0.023	<mdl	0.015	<mdl	99.233	0.239	99.472
Mean	$n = 3$	<mdl	0.009	<mdl	32.142	0.077	<mdl	<mdl	0.008	<mdl	0.037	0.03	65.483	1.354	0.027	<mdl	0.014	<mdl	99.418	0.158	99.576
LCD17 (Wirrda Well)		Na_2O	MgO	Al_2O_3	SiO_2	P_2O_5	K_2O	CaO	TiO_2	MnO	Fe_2O_3	Y_2O_3	ZrO_2	HfO_2	PbO	ThO_2	UO_2	Cl	Sum	H_2O *	Sum *
Bright		<mdl	0.011	<mdl	32.758	0.104	<mdl	0.018	0.006	<mdl	0.197	0.093	64.529	1.288	0.031	0.026	0.051	<mdl	99.548	0.021	99.568
Bright		<mdl	0.013	<mdl	32.77	0.172	<mdl	<mdl	0.009	<mdl	0.161	0.108	64.598	1.265	0.028	0.027	0.048	<mdl	99.515	0.006	99.521
Bright		<mdl	0.012	<mdl	32.874	0.125	<mdl	<mdl	0.008	<mdl	0.128	0.092	65.057	1.343	0.034	0.027	0.045	0.009	99.970	0.007	99.975
Bright		<mdl	<mdl	<mdl	32.789	0.121	<mdl	<mdl	0.01	<mdl	0.236	0.083	65.159	1.389	0.034	0.025	0.047	<mdl	100.179	0.009	100.188
Bright		<mdl	0.015	<mdl	32.735	0.129	0.007	0.012	0.006	<mdl	0.105	0.089	65.159	1.31	0.019	0.031	0.059	<mdl	100.028	0.013	100.041
Mean	$n = 5$	<mdl	0.013	<mdl	32.785	0.13	<mdl	<mdl	0.008	<mdl	0.165	0.093	64.9	1.319	0.029	0.027	0.05	<mdl	99.848	0.011	99.859
Dark		0.027	0.031	0.22	31.317	0.188	0.008	0.26	0.014	0.085	1.338	0.368	62.109	1.282	0.038	0.066	0.108	0.081	98.193	0.498	98.673
Dark		0.036	0.017	<mdl	32.724	0.138	0.006	0.046	0.006	0.038	0.471	0.202	63.7	1.383	<mdl	0.05	0.077	0.052	99.383	0.016	99.388
Dark		0.035	0.013	<mdl	32.421	0.139	0.007	0.029	0.008	0.042	0.743	0.112	64.242	1.334	0.03	0.033	0.081	0.027	99.775	0.062	99.831
Dark		<mdl	0.010	<mdl	33.089	0.084	0.007	0.01	0.009	<mdl	0.272	0.053	65.846	1.245	0.026	<mdl	0.037	<mdl	100.893	0.006	100.9
Dark		<mdl	0.008	<mdl	32.259	0.152	<mdl	0.011	0.006	0.012	0.162	0.116	64.684	1.204	0.034	0.016	0.054	<mdl	99.062	0.011	99.072
Mean	$n = 5$	0.033	0.016	<mdl	32.362	0.140	0.007	0.071	0.009	0.044	0.597	0.17	64.116	1.29	0.032	0.041	0.071	0.053	99.461	0.119	99.573
average mdl		0.023	0.007	0.006	0.021	0.010	0.005	0.009	0.004	0.011	0.024	0.008	0.049	0.101	0.014	0.010	0.011	0.007			

Sum *: Sum of element totals including calculated H_2O (H_2O*) and corrected for F and Cl. Sc, Nb, and F were measured but are generally below the mdl. Full values for these elements and REY elements are included in Supplementary Materials B, Table S4. Formulae calculation values and α-decays/mg values are in Supplementary Materials B, Table S4.

Table 3. Mean zircon compositions in bright and dark bands in each studied sample.

Lithology and Location	Sample ID	Zircon Composition
Cape Donington, Donington Suite	PL8	Bright: $(Zr^*_{0.994}REE^*_{0.001})_{\sum=0.995}(Si_{1.002}P_{0.002}O_4)$;
		Dark: $(Zr^*_{0.996}Fe_{0.001}REE^*_{0.003})_{\sum=1}(Si_{0.986}P_{0.002}O_{3.95})(OH)_{0.049}$.
Wirrda Well, Donington Suite	LCD17	Bright: $Zr^*_{0.979}Fe_{0.004}REE^*_{0.006}NF_{0.001})_{\sum=0.989}(Si_{1.006}P_{0.005}O_{3.966})(OH)_{0.001}$;
		Dark: $i_{0.002}(Zr^*_{0.943}Fe_{0.031}REE^*_{0.014}NF_{0.013})_{\sum=1}(Si_{0.962}Al_{0.008}P_{0.005}O_{3.862})(OH,Cl)_{0.106}$.
OD-distal Hiltaba Suite	LCD47	Bright: $(Zr^*_{0.986}Fe_{0.009}REE^*_{0.003}NF_{0.002})_{\sum=1}(Si_{0.993}Al_{0.001}P_{0.002}O_{3.978})(OH,Cl)_{0.015}$;
		Dark: $i_{0.004}(Zr^*_{0.934}Fe_{0.04}REE^*_{0.004}NF_{0.022})_{\sum=1}(Si_{0.915}Al_{0.012}P_{0.002}Ti_{0.002}O_{3.672})(OH,Cl)_{0.281}$.
OD-proximal Hiltaba Suite	LCD13	Bright: $i_{0.003}(Zr^*_{0.97}Fe_{0.019}REE^*_{0.007}NF_{0.004})_{\sum=1}(Si_{0.993}P_{0.001}O_{3.959})(OH,Cl)_{0.028}$;
		Dark: $i_{0.004}(Zr^*_{0.942}Fe_{0.027}REE^*_{0.013}NF_{0.018})_{\sum=1}(Si_{0.972}Al_{0.002}P_{0.002}O_{3.864})(OH,F,Cl)_{0.105}$.
Charleston Granite, Hiltaba Suite	MB158	Bright:$(Zr^*_{0.962}Fe_{0.019}REE^*_{0.009}NF_{0.009})_{\sum=0.999}(Si_{0.985}Al_{0.001}P_{0.003}Ti_{0.001}Fe_{0.01}O_{3.969})(OH,Cl)_{0.007}$;
		Dark: $i_{0.003}(Zr^*_{0.941}Fe_{0.009}REE^*_{0.009}NF_{0.041})_{\sum=1}(Si_{0.964}Al_{0.001}P_{0.003}Fe_{0.031}O_{3.933})(OH,Cl)_{0.006}$.

Note: All granite samples, with the exception of PL8, show various degrees of alteration (see above). The presented compositions are for grains that were micro-sampled for S/TEM analysis. * To obtain a good stoichiometry between the A and B sites, we used a slightly modified procedure for calculating the formulae of the Charleston zircon, in which Fe was allocated in both A and B sites.

The lack of Fe or other non-formula elements and Cl is of note in the Cape Donington zircon, implying these elements were not of magmatic origin. The relatively high OH content in these otherwise less altered zircons may be an artefact of the calculation rather than real and lies within analytical precision of the EPMA method. Critical for the narrative of this contribution, zircon from all three altered granites from the Olympic Cu–Au Province (two of Hiltaba age, one of Donington age) display concomitant enrichment in Fe and other NF elements and in (OH, Cl, F) in the darker bands and over those in unaltered zircon (PL8), in full agreement with the nanoscale observations. Concentrations of other minor (magmatic) elements remain unchanged (within analytical error).

A plot of the main "non-formula" components, and Fe versus OH + Cl + F (Figure 4F) showed a strong correlation for all altered zircon, except Charleston. Mean compositions and empirical formulae for each sub-population are given in Supplementary Materials B, Table S4.

5.4. Distribution of Minor Elements: Micron- to Nanoscale Patterns

The presence of Fe and Cl in zircon was also assessed by EPMA mapping of zircon in two samples: Wirrda Well (LCD17) and OD-proximal (LCD 13). The maps show excellent positive correlation between the two elements in the crystal zoning of Wirrda Well zircon (Figure 5A,B) but antipathetic patterns for OD proximal zircon (Figure 5C,D). The OD proximal zircon displays a combination of primary and overprinting textures in which the oscillatory zoning is only preserved on the rims, whereas the middle part of the grain is affected by fractures and re-crystallization obliterating primary zoning (Figures 3B and 5C,D).

Imaging in HAADF STEM mode depicts oscillatory zoning as bright and dark bands relating to non-formula elements in all foils shown in this study (Table 1), except the Cape Donington zircon (Foil #6). Superimposed mottled textures in the darker bands were only observed in zircon from the Olympic Cu–Au Province. Mapping using STEM EDS showed Fe banding in all zircons except Cape Donington. In the latter, the oscillatory zoning was related to trace elements typical of magmatic zircon (REY, actinides), the concentrations of which were below the detection limits of the EDS STEM method but readily mappable by LA-ICP-MS (Figure 2F; Supplementary Materials C, Figure S2). In contrast, the Wirrda Well–Donington zircon displayed an excellent correlation between micron and nanoscale oscillatory zoning patterns with respect to Fe, as shown by both EPMA and STEM EDS mapping (Figure 5A,B and Figure 6). The Fe distribution, however, did not reveal the mottled texture in the darker Fe-rich bands or veinlets crosscutting the brighter bands, as observed in the HAADF STEM images (Figure 6C).

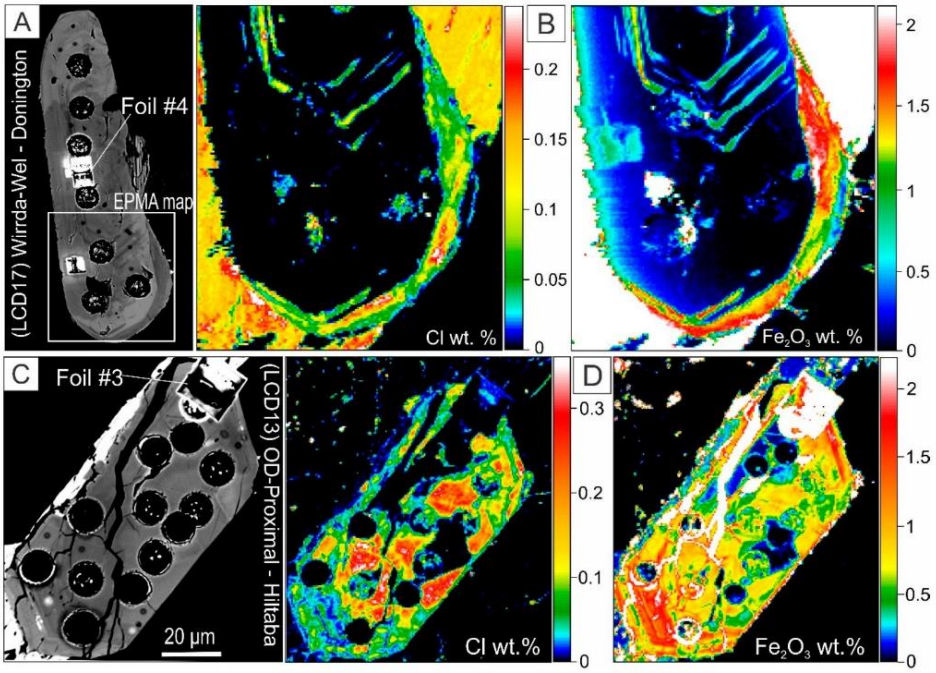

Figure 5. (**A**) BSE image of oscillatory-zoned Wirrda Well–Donington Suite zircon (sample LCD17) that was dated (LA-ICP-MS craters) and used for nanoscale study (foil location as marked). (**B**). EPMA maps for Cl and Fe_2O_3 (in wt.%), showing that both elements appear homogeneously enriched and positively correlated with one another within oscillatory bands. (**C**,**D**) BSE image and EPMA maps for Cl and Fe_2O_3 (wt.%) of OD proximal zircon (sample LCD 13; foil marked at the top). Note the high concentrations of both elements within the middle part which was affected by fractures and re-crystallization. In contrast, crystal zoning on the rim shows inverse correlation between the two elements (e.g., banding intersecting the FIB cut).

The most varied chemistry mapped at the nanoscale was observed in zircon from the Charleston Granite (Figure 7A). Banding with respect to Fe, Ca, Ti, Al, Y, and Th was recorded outside of a magmatic domain, itself defined by faint oscillatory banding expressed by variation in major element concentration as shown by O, Si, and Zr maps. No mottled textures were present throughout such chemically complex bands. The EDS STEM maps also showed that Fe displayed a sharp boundary against the magmatic domain, contrasting with the diffuse boundaries shown by the other trace elements. All these elements, including U (but not Pb), were enriched within a fracture around the magmatic domain, and within a fine particle inclusion hosted at the diffuse boundary (Figure 7A). The fracture, leading towards this U-bearing fine particle, was represented by a rectangular network of dark nanodomains that hosted pores (Figure 7B–D). These domains were nonetheless crystalline, albeit disordered and with slightly different orientation relative to one another and to host zircon.

The best example of mottled textures throughout oscillatory banding with respect to Fe (Ca, Cl) was shown by the least altered grain in OD distal zircon (Foil #1; Figure 8A). The HAADF STEM image of the foil mimics the BSE image (Figure 2A,C) with respect to the mottled textures throughout the banding. Relative to the generally homogenous distribution of Fe and Ca throughout a given band, the Cl map shows distinct spots of higher concentration. This was exemplified by the signals for Ca and Cl along a profile (Figure 8B). Likewise, variable correlations were seen between the high Cl areas and concentration of major elements, O and Zr, as shown on the EDS STEM maps obtained from mottled areas (Figure 8C). The highly altered zircon grain (Foil #2) showed two distinct domains:

(i) weakly-banded and mottled and (ii) cleaner domains that were strongly enriched in Ca, Fe, and Al. The latter surrounds veinlets of xenotime displaying enrichment in HREE and U (Supplementary Materials C, Figure S3).

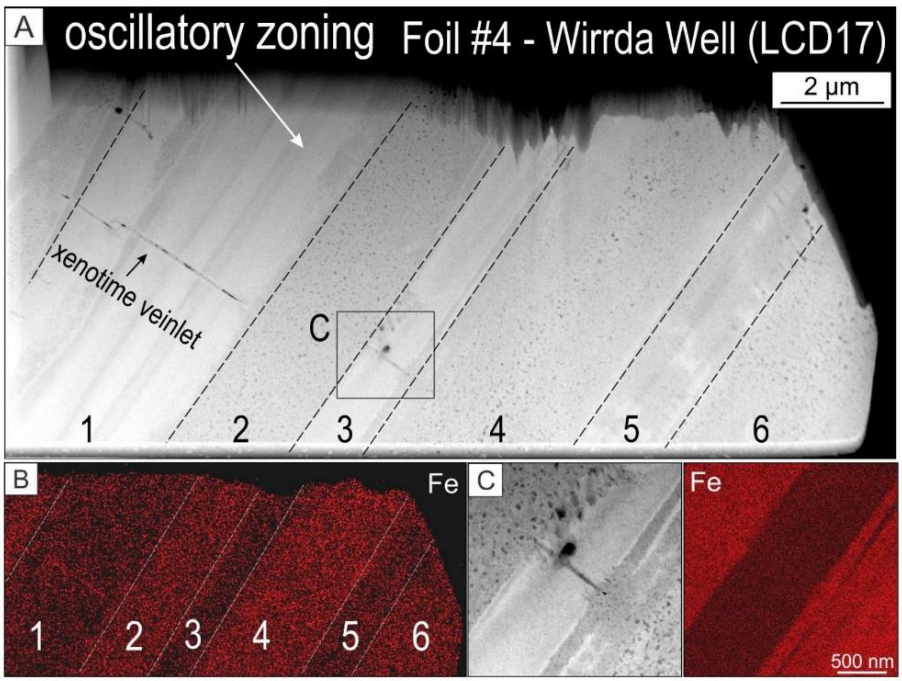

Figure 6. (**A**) HAADF STEM images (**A** and **C**) and EDS STEM maps for Fe (**B** and **D**) for Wirrda Well-Donington zircon showing crystal oscillatory zoning (**A** and **B**). The dark bands (even numbers) were enriched in Fe and show mottled texture in the image, but not on the Fe map (**B**). Note that the oscillatory banding was crosscut by a xenotime-bearing veinlet (extended map shown in Supplementary Materials C, Figure S3). (**C**,**D**) Higher resolution maps showing the interface between light and dark bands confirmed that the mottled texture (**C**) was not reflected in the Fe distribution (**D**).

Olympic Dam proximal zircon (Foil #3) displayed a combination of primary and overprinting textures correlating with minor trace element patterns (Figure 9). In depth, the foil revealed a subsurface 5 µm-diameter inclusion of hematite (Figure 9B–D), as well as oscillatory banding with mottled textures of variable density. As in the OD distal zircon, Fe was evenly distributed throughout the bands, whereas Cl appeared more heterogeneous (Figure 9E,F). In detail, the Fe-poor bands were crosscut by Fe-rich veinlets (Figure 9F). The largest areas of Cl-enrichment were observed in parts of the Fe-rich bands but typically did not correspond to the crosscutting Fe-rich trails. Such patterns of Fe and Cl explain the inverse trends mapped at the micron-scale in the same grain (Figure 5C,D).

5.5. Mottled Areas: Nanoparticles to Fine Particles of Chloro–Hydroxy–Zircon

The nature of the mottled areas (identified in foils as listed in Table 1) relative to Cl-enrichment and substitution mechanisms for zircon was addressed by EDS spot analysis and mapping at various resolutions (Figures 10 and 11). Higher resolution maps of one Cl-rich area selected from Figure 8C reproduced the same variability between major elements and Cl (and remarkably little variation in terms of minor elements) in the particles observed as dark nanodomains on HAADF STEM image (Figure 10A). An inverse correlation between O and Zr corresponded to either diffuse or stronger Cl concentration, whereas the strongest Cl concentrations were not reflected by major element variation.

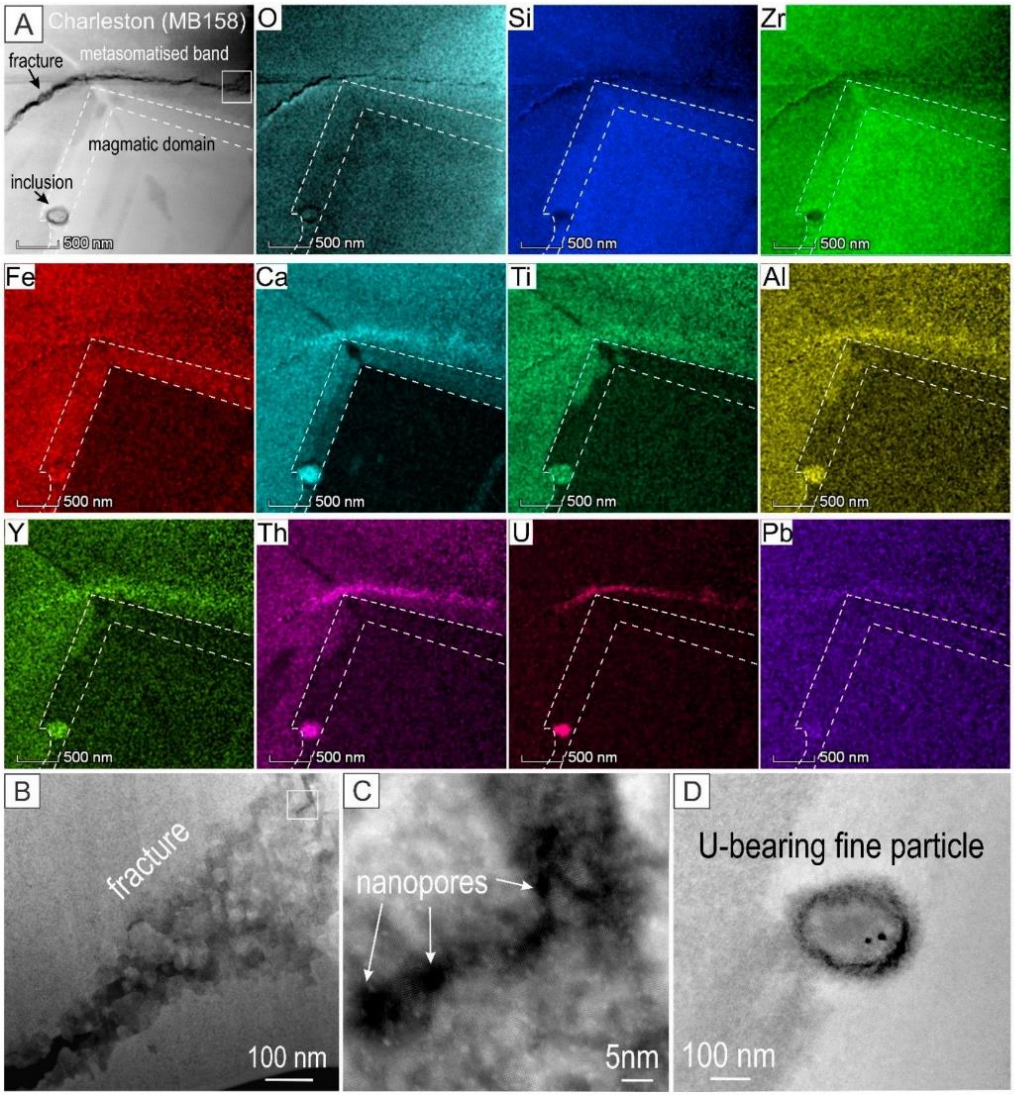

Figure 7. (**A**) HAADF STEM image and EDS STEM element maps of Charleston zircon (Foil #6) showing enrichment in trace elements outside of a magmatic domain as marked. Note the sharp boundary (dashed lines) for Fe but not the other elements, which instead display a diffuse boundary. Trace element (re)mobilization (all elements except Fe) along this boundary was observed along the adjacent fracture and the U-bearing fine particle. (**B**–**D**) HAADF STEM images showing zircon details along the fracture as marked. The U-bearing fine particle (**D**) displayed a dark rim and was beam-sensitive, indicating that it was most likely amorphous (it could not be imaged at high-resolution due to the thickness of the foil at this location). The image in (**B**) is the inset box indicated on (**A**), and image (**C**) shows the inset box indicated on (**B**). Image (**D**) shows detail of the inclusion from image (**A**).

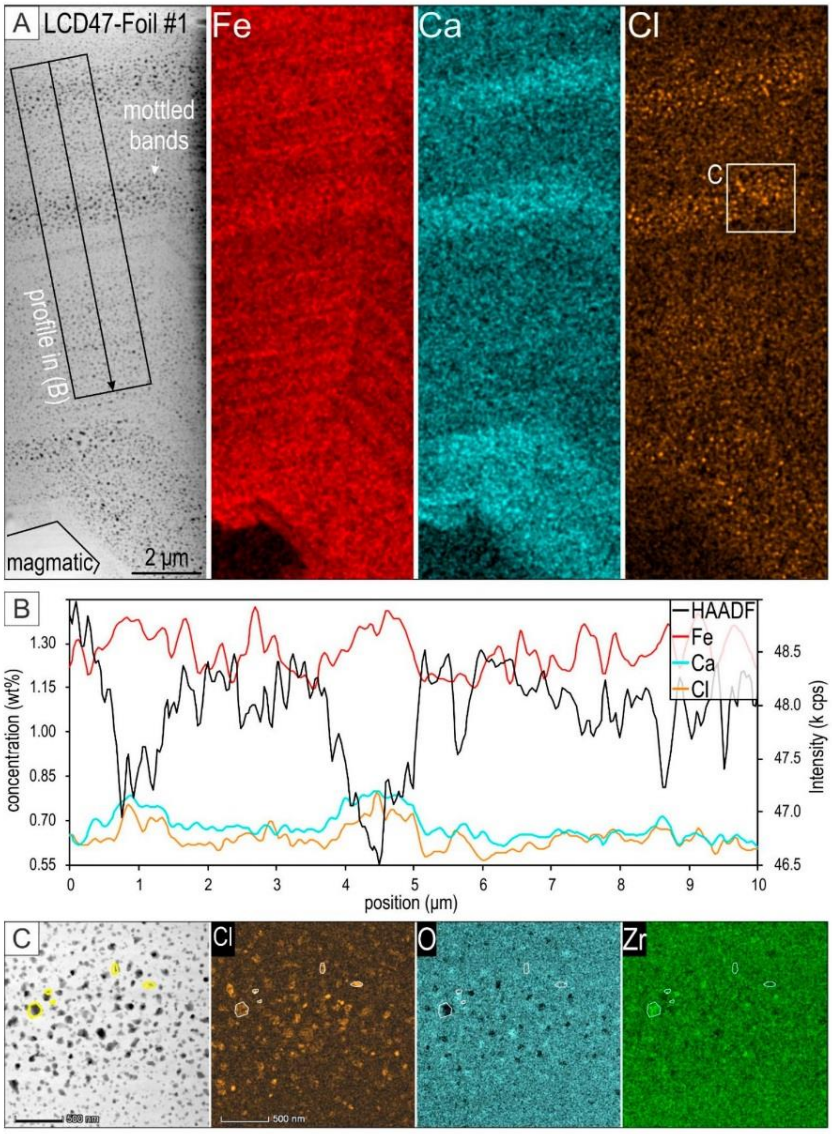

Figure 8. Trace element distributions in OD distal zircon from Foil #1. (**A**) HAADF STEM image and EDS STEM maps for Fe, Ca, and Cl showing oscillatory zoning and mottled textures. Enrichment in Ca and Cl occurred throughout the mottled bands. (**B**) Profile across the oscillatory zoning displayed positive correlation between Ca and Cl across the most intensively mottled bands. Iron distributions broadly correlated with Ca and Cl across the same bands but showed small-amplitude variation reflecting the finest-scale oscillatory banding. The HAADF intensity signal showed a negative correlation with the Ca- and Cl-enriched bands. (**C**) Image and EDS STEM maps (extended maps in Supplementary Materials C, Figure S3) of a Cl-rich area as marked in (**A**). Note the inconsistency in correlation between Cl with O and Zr (compare the areas outlined on the figure), e.g., high Zr and low-O where Cl-enrichment is moderate, but no changes for O and Zr for nanodomains with the highest Cl content.

The highest Cl concentration was recorded from the smallest particles (10–30 nm-diameter) of grey color, (Foil #1; Figure 10B). A profile across one of the darker particles shows that Cl was concentrated

at the edge of the particle (Figure 10C). The HAADF signal intensity and O decreased across the boundary of the particle, whereas major and minor elements displayed a slight increase. These results can also be associated with variable particle thickness, their position relative to the plane of imaging, or the presence of voids/pores, particularly for the coarser and darkest domains. Comparative imaging of the same area in both HAADF and bright-field STEM modes illustrates these features (Supplementary Materials C, Figure S1). Such voids could, however, also have been produced via the plucking out of coarser particles during ion milling.

The morphology and size of the particles throughout samples with mottled textures (Foils #1–5) varies from several nm up to 100 nm (nanoparticles) to hundreds of nm (fine particles) (Figure 11A). The largest particles, with well-defined geometrical shapes, can include pores, whereas cross-cutting darker veins will show numerous defects when imaged at high resolution (see below). Energy-dispersive X-ray maps of one medium-sized particle showed strong (lower and higher) variation in O and Zr concentrations relative to host zircon; no variation in Si was recorded (Foil #1; Figure 11B). Weak enrichment in Cl and U was present whereas Ca-rich nanoparticles occurred just outside, along the edge of the mapped particle. Overall, these results suggest that the main substitution involved replacement of O by OH^- and/or Cl leading to chloro–hydroxy–zircon formation. Although substitution of $(SiO_4)^{4-}$ tetrahedra by $4(OH,Cl)^-$ can also be invoked, such a relationship is not obvious from the EDS mapping.

5.6. Atomic-Scale HAADF STEM Imaging—Zircon Crystallinity and Lattice-Scale Defects

Four main zone axes in zircon were imaged throughout the seven foils (Table 1; Figure 12A–D). In each case, imaging showed the same overall orientation across zircon in any given foil, indicating that the chemically heterogenous domains were an integral part of the same single crystal. Despite observing evidence of lattice disorder, zircon in all samples was found to be crystalline with no amorphous areas identified. This absence of amorphous domains was observed in both the brighter bands of magmatic zircon from Cape Donington, throughout the darker or mottled bands in all other samples, and in the proximity of fractures containing newly formed phases such as xenotime.

Atomic arrangements on HAADF STEM images for the four zone axes shown in Figure 12 were interpreted using crystal structure models obtained after indexing of the Fast Fourier Transform (FFT) obtained for each image and also STEM simulations (Figure 13). These show that the brightest spots represent an overlap between Zr and Si atoms on (001) and $(1\bar{1}0)$ zone axes (Figure 13A,B), whereas both Zr (brightest, with dumbbell arrangement) and Si (darker) atoms can be resolved on the (100) and $(1\bar{1}1)$ zone axes (Figure 13C,D). There was a relatively good fit between the HAADF STEM images and simulations in each case. Such image assessment of individual zone axes by HAADF STEM was necessary to identify the presence of lattice-scale defects.

Lattice-scale defects on $(1\bar{1}1)$ zone axis in zircon were observed along a veinlet crosscutting a fine particle in Foil #1 (darker color on HAADF STEM images; Figure 14A–D). One of the defects had a hexagonal shape (Figure 14D) and showed clear modifications in both size and intensity of individual atoms relative to "normal" zircon on this zone axis (Figures 12D and 13D). An intensity profile showed changes across this defect which were interpretable as substitutions of individual Zr and Si atoms along the (011) direction (Figure 14E). Signals for Zr decrease within the defect suggesting substitution by lighter cations (e.g., Ca, Al) in variable proportions. One of the Si sites in the defect showed a higher signal relatively to host zircon, whereas the other was barely visible (correlating with darkest areas on the image). Substitution within the $(SiO_4)^{4-}$ tetrahedra can be invoked in which Me^{5+} (e.g., P^{5+}) replaces Si^{4+}, necessitating charge balance via substitution of $(OH,Cl)^-$ for O^{2-}.

Lattice-scale defects were imaged on all zone axes in zircon except $(1\bar{1}0)$ (Figure 15). In magmatic zircon from Cape Donington (Foil #7), lattice disorder was found in the brighter U-richer bands (Supplementary Materials B, Table S4; Figure 2F). Square-shaped defects on the $(100)_{zircon}$ zone axis appear darker and showed arrays of single Zr (and Si—although these were less well resolved on the image) columns along the c-axis, which were doubled in the b direction leading to a smaller, squarish arrangement (outlined in Figure 15A).

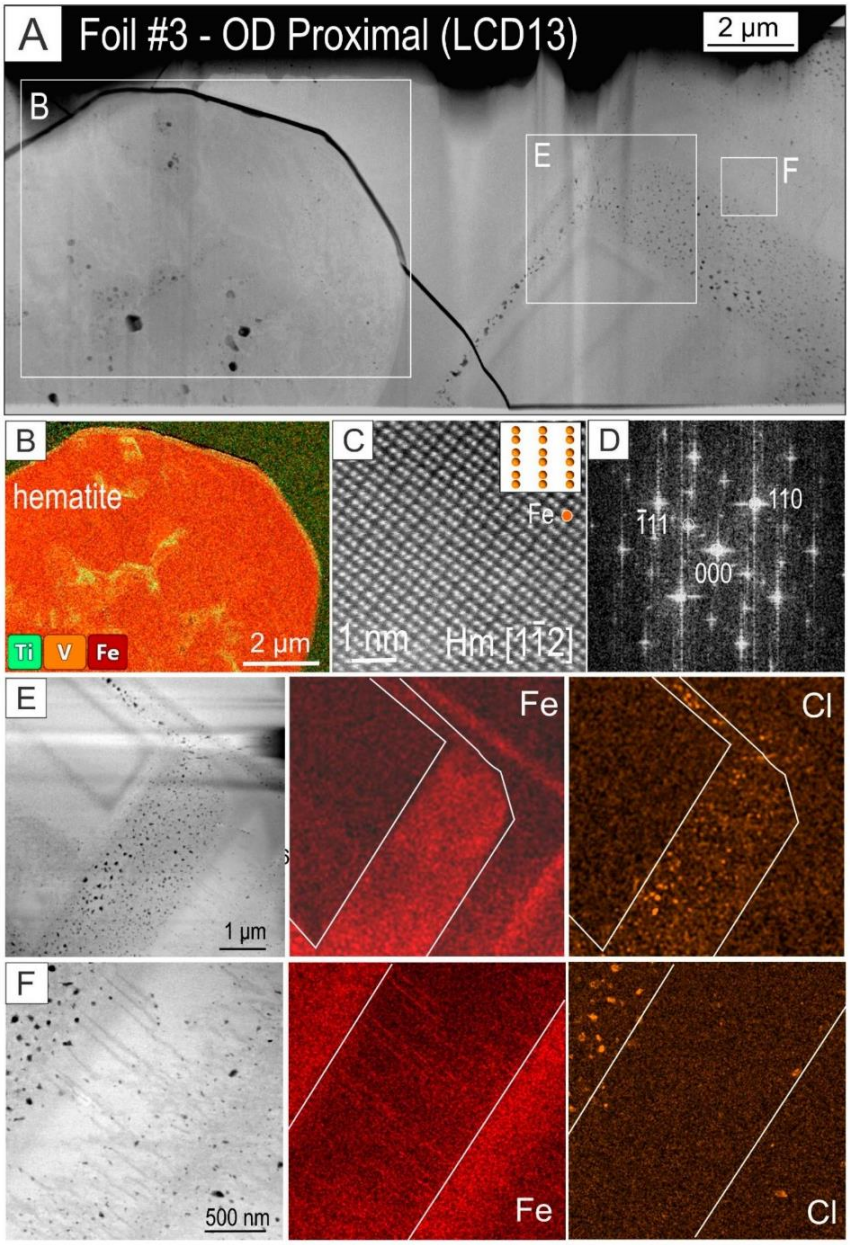

Figure 9. Trace element distributions in OD proximal zircon (Foil #3). (**A**) HAADF STEM image showing oscillatory banding, mottled textures, and an inclusion of hematite in zircon. High field strength element (HFSE) enrichment in hematite shown on the EDS STEM map in (**B**). Identification of hematite from the atomic-scale resolution image in (**C**) and Fast Fourier Transform (FFT) in (**D**) as marked. (**E**,**F**) HAADF STEM images and EDS STEM maps obtained from areas as marked on (**A**) (rotated 90 degrees clockwise) showing Fe and Cl enrichment throughout the mottled bands. Note the irregular distribution of Cl relative to Fe in both (**E**) and (**F**). Importantly, the Fe map in (**F**) shows Fe-rich veinlets crosscutting brighter bands.

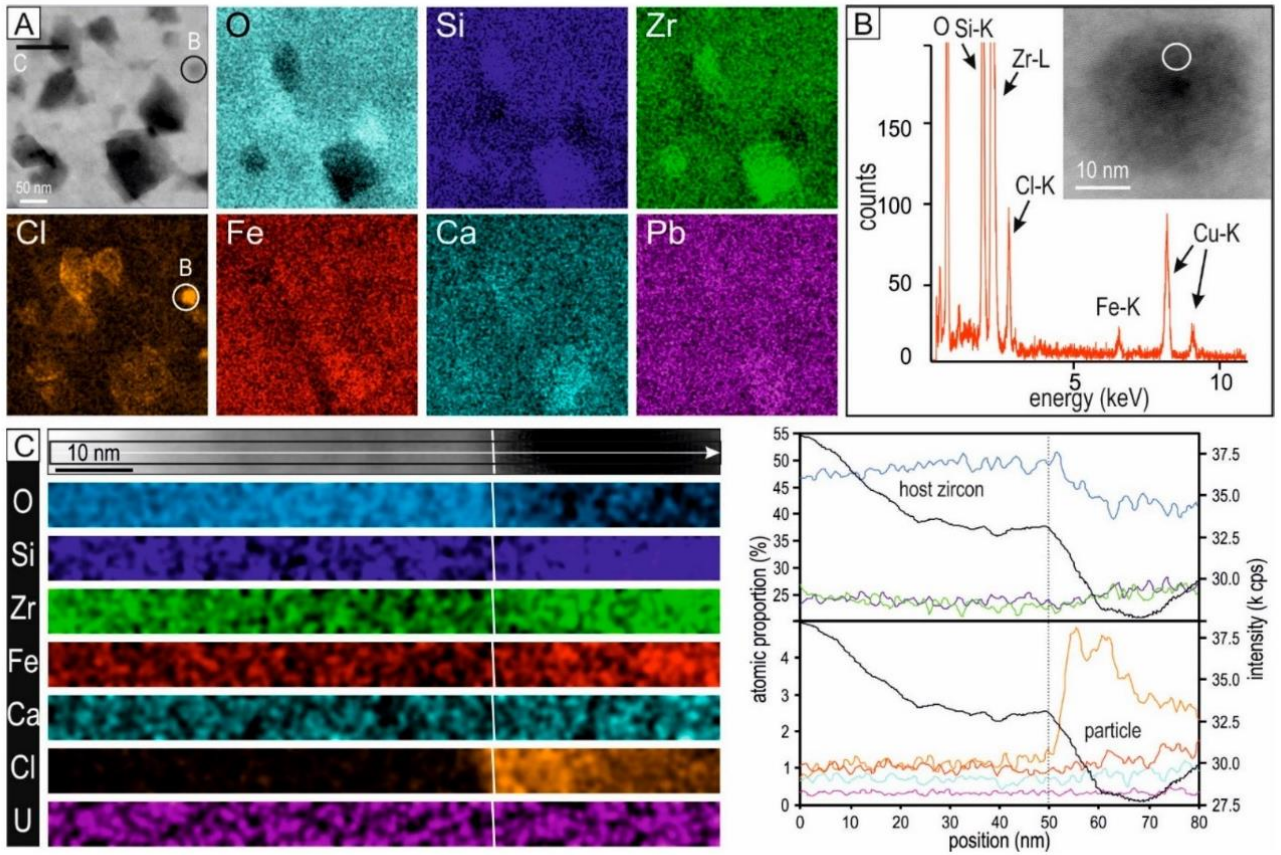

Figure 10. Aspects of nanoscale inclusions + pores throughout the mottled bands in the OD distal zircon (Foil #1). (**A**) Image and EDS STEM maps for a Cl-rich area selected from Figure 8C showing that the highest Cl was recorded in the smallest particles with no differences on the major or trace elements maps. Inverse correlation between O and Zr was recorded for the coarser, darkest inclusions with moderate enrichment in Cl. Note the weak variation in Fe and Ca, but not in Pb. (**B**) EDS spectrum for Cl-richest nanoparticle circled in (**A**). (**C**) EDS STEM maps (left) and profiles (right) across a particle with medium Cl-enrichment in (**A**). Profiles show high concentrations of Cl at the particle margin with increases in both major and minor elements but a strong HAADF signal decrease.

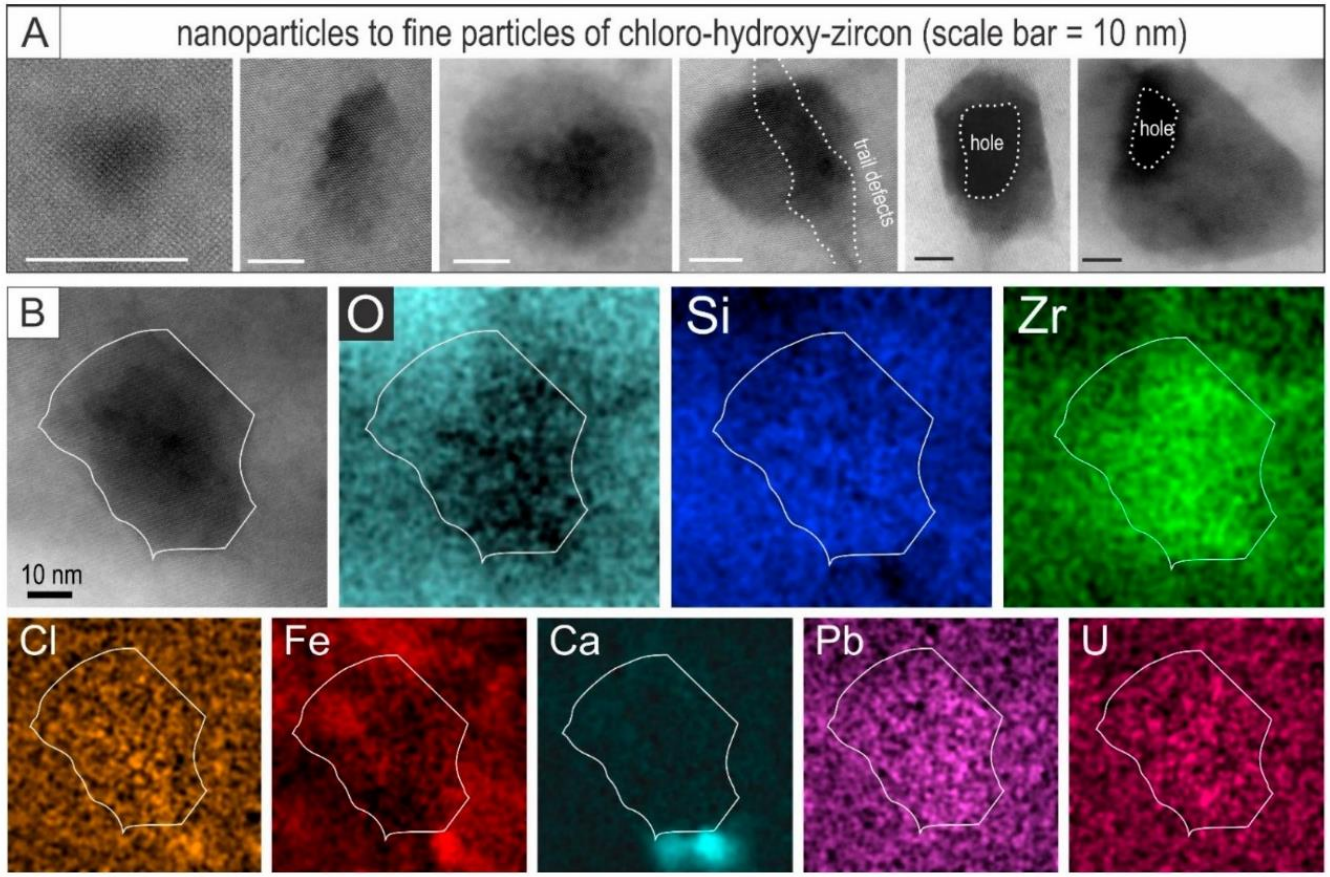

Figure 11. (**A**) HAADF STEM images of inclusions representative of all samples with mottled textures showing their variation in size and morphology as marked. Note the presence of rounded pores in the coarsest particles. (**B**) Image and EDS STEM maps of a single particle from the OD distal zircon (Foil #1). Note the strong variation in O and Zr concentration but not Si relative to host zircon and the weak relative enrichment in Cl, U, and Pb. Ca-rich nanoparticles occur just outside, at the lower edge of the mapped particle.

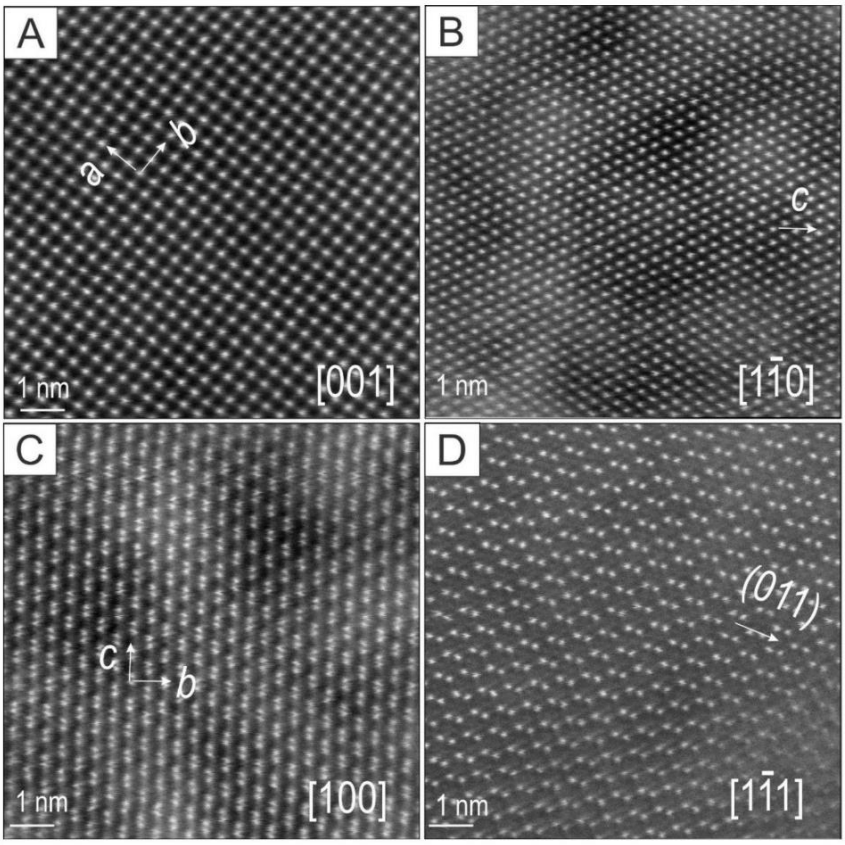

Figure 12. (**A**–**D**) High-resolution HAADF STEM images of zircon on four main zone axes as marked.

Linear defects were observed along the edge of xenotime veinlets (e.g., Wirrda Well–Donington zircon; Figure 15B). Atom displacement across the two sides of the defect can be interpreted as resulting from a simple screw dislocation considering the "atom loop" observed on the defect plane. The "loop" is illustrated by the atoms placed between the two planes with different heights relative to one another across the defect (smaller size atoms highlighted in Figure 15B). Linear defects along kink faults were imaged on (001) zone axis in Charleston zircon (Figure 15C). In this case, the fault steps/widths changed irregularly, as shown by the presence or absence of "atom loops" on the defect plane (overlays on Figure 15C). Wider planar defects, tens of nm in width, also occurred in the Charleston zircon (Figure 15D). This image can also be interpreted as a simple screw dislocation (yellow lines in Figure 15D). Interstitial atoms were inferred within the defect area only. Their size and brightness changed relative to the Zr and Si atoms on the (001) zone axis in zircon outside the defect area. Such changes could reflect differences in atom heights between the two planes on either side of the defect, or more speculatively, could be attributed to the presence of foreign atoms occurring interstitially in the zircon lattice (mixed site Ti, Ca, Th, Y, etc.). The latter supposition can be correlated with the presence of mixed sites of Ti, Ca, Th, Y, etc., as is known from zirconolite ($CaZrTi_2O_7$).

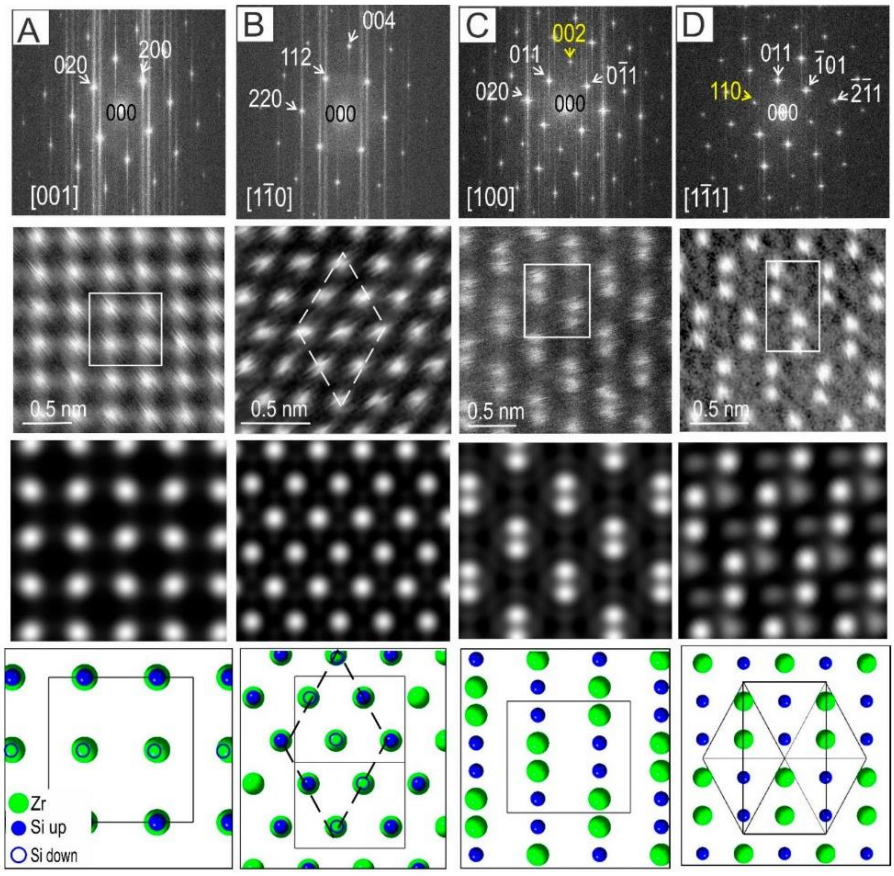

Figure 13. From top to bottom, FFT, HAADF image, STEM simulation, and crystal structure model for each of the main zone axes (**A–D**, as marked) imaged in zircon (Figure 12). The images and simulations were interpreted in agreement with crystal structure models on zone axes as obtained from indexing FFTs obtained from images in Figure 11. The two zone axes with dumbbell atomic arrangements (**C**,**D**) cannot be resolved using the ideal space group for zircon, $I4_1/amd$, due to the presence of forbidden reflections ($00l$; $l \neq 4n$ and $hh0$; $l \neq 4n$; marked in yellow). Indexing, crystal models, and STEM simulations were obtained using the $I2_12_12_1$ space group. The models and simulations did not change when using the $I4_1/amd$ space group.

The most complex defects were imaged in Fe-rich bands from OD distal zircon in the $[1\bar{1}1]$ zone axis (Foil #1; Figure 15E). In this case, changes in the atomic arrangement along the (011) can be interpreted as displacements with anti-phase modulation along fault planes (yellow lines in Figure 15E. In contrast, the defect within the fine particle described above (Figures 14D and 15F) can be interpreted as the result of local fluid–mineral interaction leading to an increase in OH/halogen content in the nanoparticles/fine particles.

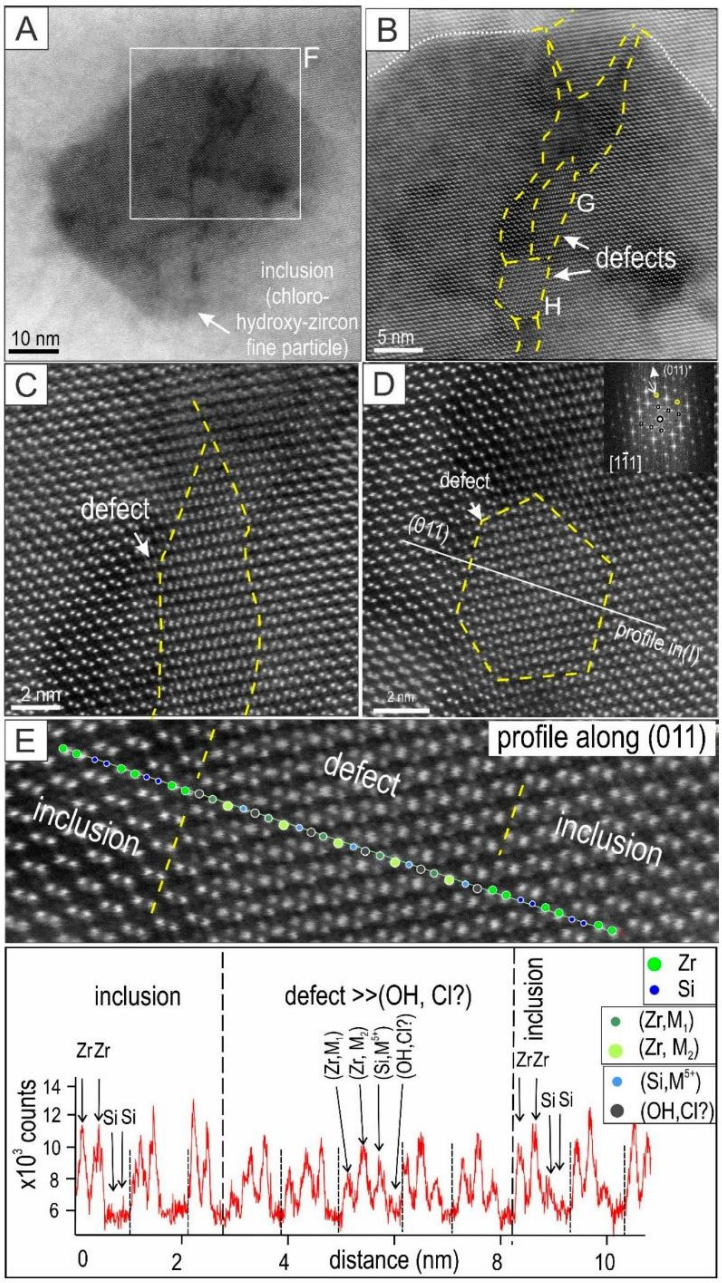

Figure 14. (**A**–**D**) Images showing defects along a fracture crosscutting one of the fine particles (Foil #1). The FFT pattern obtained from the image (inset **D**) shows a square sub-pattern with weaker reflections superimposed onto the main reflections. Yellow, dashed lines mark the defect shape. (**E**) Intensity profile across the defect in (**D**) showing modifications in the Zr and Si signals as marked.

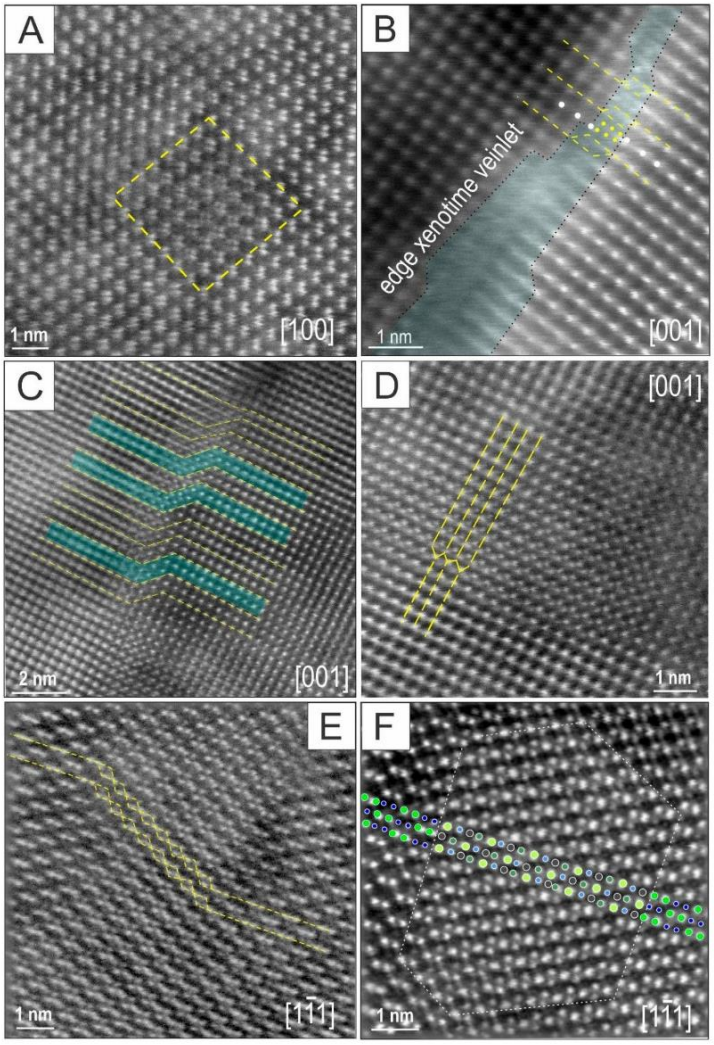

Figure 15. Atomic-scale resolution HAADF STEM images of defects in zircon. (**A**) Square-shaped defect (yellow outline) in U-richer bands from Cape Donington (Foil #7), tilted on the (100) zone axis. The doubling of Zr atoms observed along the *c*-axis suggests atom "stretching) along b induced by strain, attributable to α-recoil damage during U-decay. (**B**) Simple linear defect in Wirrda Well–Donington zircon (Foil #4) observed at the edge of a xenotime veinlet (blue overlay); sample tilted on the (001) zone axis in zircon. Screw dislocations (dashed lines) are marked by atom loops in the defect plane (yellow dots) relative to Zr atoms (white dots) outside the defect. (**C**–**D**) Screw dislocations (dashed lines) along a fault or at the edge of a planar defect on the (001) zone axis in Charleston zircon (Foil #6). Note irregular atom loops along the fault plane (blue overlays). (**E**–**F**) Defects in the Fe-rich, mottled bands from OD distal zircon (Foil #1) with sample tilted on the $[1\bar{1}1]$ zone axis in zircon. Antiphase atom displacement (dashed line) suggesting lattice stretching along (011) directions in (**E**). (**F**) Details of the defect (dotted line) in Figure 14D showing the size and intensity modifications in Zr and Si atoms along the (011) direction (colors as in Figure 14E). The image shows the inferred missing Si atoms as dark, regular spots along this direction.

6. Discussion

6.1. Zircon Metasomatism Down to the Nanoscale: Are Iron and Chlorine of Magmatic or Hydrothermal Origin?

It is difficult to unequivocally distinguish magmatic (primary) from secondary patterns in zircon displaying crystal oscillatory zoning with respect to Fe and Cl due to the lack of crosscutting textures and because such elements could also have been components in either granitic melts or hydrothermal fluids. For example, a magmatic origin for divalent Fe was suggested by Reference [45] based on observed substitutions. In the present study, we were able to rule out a magmatic origin by analysis of zircon from a granite belonging to the same ~1.85 Ga Donington Suite which showed the presence of Fe and Cl only in parts of the craton where they are associated with or host younger (~1.6 Ga) IOCG-type mineralization (Wirrda Well). Moreover, the concentrations of Fe and Cl in the Hiltaba Suite zircons increased with proximity to more intense mineralization. Oscillatory zoning patterns can be produced via metasomatism (ion exchange between a mineral and a percolating fluid moving though pores in a rock) in the absence of open fractures. Therefore, we stipulate that Fe–Cl zoning represents a first stage of zircon alteration via metasomatism that is quite distinct from late-stage fracture-infill or textures superimposed onto the zoning (xenotime veinlets, U-bearing nanoparticles; Figures 6–8).

Metasomatism allows partial or complete pseudomorphic replacement of one mineral by another. In some cases, the new mineral may be the same species but differs from the parent in terms of minor/trace elements, as was shown for hematite from Olympic Dam [46]. Such processes are "metasomatic" in a broader sense and occur when replacement reactions couple dissolution with (re)precipitation rates (CDRR). This interpretation concurs with empirical evidence from other studies of Hiltaba Suite granites [47], showing local alteration of magmatic feldspars or accessories via CDRR. Variation among the geochemical patterns recorded by zircon (e.g., Ca and Cl, as well as Ti, Al, Th, and Y in Charleston zircon) can be attributed to local mineralogical changes in the granite during early alkali–calcic alteration, e.g., release of cations during replacement of magmatic plagioclase by sericite or biotite by chlorite [42,47].

Metasomatism was accompanied by development of nanoscale structures, such as formation of chloro–hydroxy–zircon nanoprecipitates in all samples from the Olympic Dam district, but significantly, not in those from the Eyre Peninsula (Table 1).

Defects were observed throughout the Fe-rich bands, as well as in magmatic zircon from Cape Donington, but none show amorphization. Linear defects associated with fracture opening can be attributed to structure swelling along fission tracks (Figure 15B). This allows trace element remobilization, in turn leading to formation of U-nanoparticles or xenotime like those shown in zircon in Archean granites from Jack Hills [24,25]. Likewise, lattice expansion via stretching or screw-dislocation defects (Figure 16) can be considered part of the "swelling" induced by radiation damage.

The substitution model for metasomatized zircon shows cation exchange in which loss of 0.4–2 wt.% Si can be compensated by incorporation of OH– and halogens without significant removal of primary magmatic trace elements (Supplementary Materials A). Zirconium can, however, be replaced by Fe and other non-formulae cations. Chemical changes, affecting both Zr and Si, observed in defects along fractures crosscutting fine particles (Figure 14) were concordant with chloro–hydroxy–zircon of variable chemistry, as assessed by EPMA data. However, heterogeneity was observed at the nanoscale, including localized concentrations of other elements, e.g., Ca or Cl-bearing nanoparticles (Figures 10 and 11), thus explaining much of the scatter in the geochemical data obtained at the EPMA-scale.

6.2. Timing of Zircon Alteration: Is Metasomatism Pre- or Post-Metamictization?

The incorporation of Fe and associated non-formula elements relating to metasomatism as introduced above, has been extensively discussed in terms of zircon alteration linked to self-irradiation. The overarching idea is that zircon should not be able to incorporate such elements at wt.% concentration unless it accumulates radiation damage, a process resulting in swelling and amorphization, and thus, creating pathways for fluid percolation (Reference [18] and references therein).

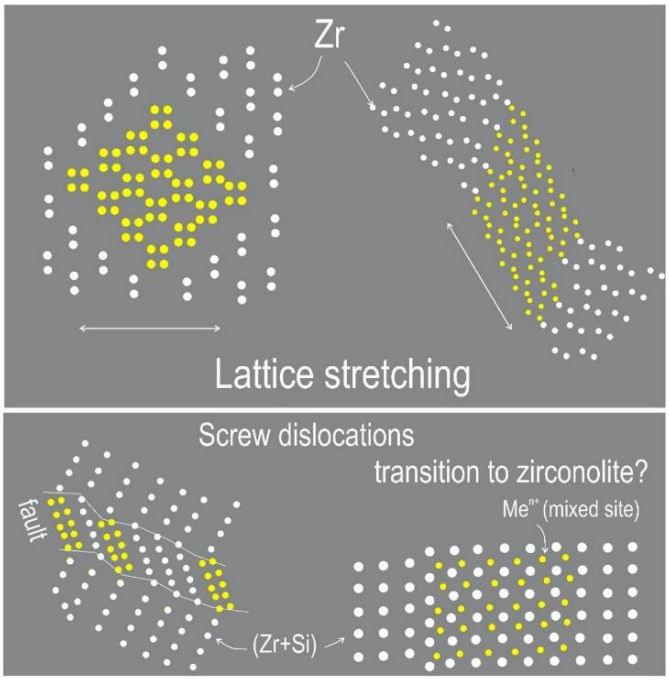

Figure 16. Schematic representation of atom arrangements in defects indicating lattice stretching and screw dislocations leading to expansion of the zircon structure. Such aspects are attributable to self-induced irradiation damage effects.

Quantification of the radiation damage necessary to facilitate major element substitution (the "First Percolation Point") was defined as a dose of ~2×10^{18} α-decays/g (hereafter, D_c), and representing ~30–40% amorphization as a network of interconnected aperiodic domains within the crystal structure [48,49]. The link between the first percolation point and a sudden increase in non-formula elements, particularly Ca, was shown for altered zircon exhibiting U–Pb discordancy [18,19]. A high-porosity-to-spongy appearance is commonly reported, leading to deficient EPMA totals and darkening on BSE images [50]. The latter authors also contend that H_2O incorporation is promoted by pores. Nanoscale Fe- or Pb-bearing inclusions were shown in Archean zircon [24], while pores with Ca- and U-rich margins have been documented from a pegmatite zircon [26].

Using molecular dynamic simulations of alpha-recoil cascades produced via actinide decay, models of self-irradiation damage in zircon show domains of disordered material as small as a few nm [18]. However, imaging of zircon in this study (Figure 12, Figure 14, and Figure 15) did not unequivocally support this model, even for samples within the D_c range required for the crystalline-to-amorphous transition. This may relate to thermal annealing following metasomatism, e.g., associated with emplacement of the Gairdner dyke swarm at ~820 Ma, the most recent major tectono-thermal event recognized throughout the Gawler Craton [51].

Nevertheless, the D_c accumulation since ~820 Ma should have produced recognizable disorder at the nanoscale. The range of defects discussed here (Figures 14–16) are the closest expression of lattice disorder, although not truly amorphization. The positive correlation reported in other studies between high non-formula elements and D_c (e.g., [19]) is not as well-defined in this dataset. Sigmoidal trendlines shown in previous studies are comparable to that shown here, although there is a large spread in the data here, with points displaying high D_c and low Fe, and vice versa (Figure 17A). Therefore, the correlation between increasing non-formula elements and D_c may not necessarily be the result of high-U zircon creating their own pathways for increased fluid interaction. Furthermore,

high-U zircon from this study indicate the D_c required to reach the first percolation point would not have been met until ~100 Ma after zircon crystallization. This postdates the measured timing of hematite crystallization, itself a result of Fe-metasomatism [13]. The presence of hematite inclusions with an HFSE signature within Olympic Dam zircon, is further evidence of Fe–Cl-metasomatism impacting on zircon (Figure 9B) occurring in the early, magmatic-to-hydrothermal transition stage [52], rather than post-metamictization. As highlighted by trace element analysis (Figure 4; Supplementary Materials Table S4), Donington Suite data plots at lower D_c and Fe_2O_3 values than Hiltaba Suite zircon (Figure 17A) reflect the lower U-contents and lesser alteration of zircon. Even in the case of zircon in Donington Suite granite from Wirrda Well, superimposed Fe–Cl-metasomatism is recognized due to the presence of adjacent Hiltaba Suite granites linked to the same batholith that generated the RDG, host to mineralization at Olympic Dam.

The D_c can affect U–Pb systematics in zircon and be manifest as discordance of data points via Pb loss (Figure 3). Accurate (CA)-ID-TIMS ages for magmatic crystallization can, nevertheless, be obtained [14], despite the presence of micron- to nanoscale domains, which in the present dataset do not appear to concentrate remobilized U or Pb. Such phenomena have been shown in previous studies [24,27], where they relate to alteration associated with highly metamict zircons.

6.3. Zircon Alteration Model and Magma "Fertility"

Concentrations of Cl within zircon containing Fe and other non-formula elements was measured and imaged for the first time in natural zircon. Electron microprobe maps show consistent distributions of Cl correlating with Fe in micron-scale banding (Figure 5). At the nanoscale, however, Cl was present as nanoparticles within Fe–Ca-metasomatized mottled bands (Figures 8–11). Such an association between Fe and Cl would be expected in early IOCG fluids exsolved after granite crystallization [52]. Cl-rich nanoparticles became volumetrically more significant in samples from the vicinity of the Olympic Dam deposit, while smaller amounts of Cl were also measured in the nearby Wirrda Well Donington zircon as well as Charleston zircon. In contrast, the Cape Donington zircon displayed a complete absence of Cl. Therefore, we concluded that Cl was inherent to hydrothermal fluids derived from the Hiltaba Suite granites. Moreover, such Fe–Cl-bearing fluids also affected nearby older granites (Donington Suite), host to ~1.6 Ga IOCG mineralization at Wirrda Well.

Zircon metasomatism can be attributed to a low-fluid, mineral-buffered diffusion-reaction process in the beginning (only crystal zoning), followed by formation of chloro–hydroxy–zircon nanoprecipitates when fluids become highly focused (Figure 17B). Iron-rich nano-veinlets begin to interconnect across crystal zones previously metasomatized during increase in the flux of Fe-rich fluids (formation of hematite inclusions; Figure 9). Comparable phenomena in which a mineral can host nanoscale inclusions of the same mineral but with subtle yet distinct chemical differences, are known from Fe oxides, notably Si–Fe nanoprecipitates within silician magnetite. These are documented both from banded iron formation deposits [53] and the Olympic Dam deposit [54].

The preservation of pre-existing crystal orientation in zircon nanoprecipitates and host zircon is characteristic of reactions via a sharp interface, typical of CDRR replacement. Moreover, transient porosity developed during CDRR progression provides sites for deposition of nanoprecipitates, as suggested here and elsewhere (e.g., [55–57]). Hydrothermal fluids interacting with zircon can be considered acidic based on the hydrated-substitution model for zircon (Supplementary Materials A and B, Table S4). Fluid transport of Fe, from the granite-derived fluid and Ca + Al from breakdown of minerals in the granite via alkali–calcic alteration is likely to occur as chloride complexes and can lead to Si and/or Zr loss, according to the reactions:

$$ZrSiO_4 + 4xH^+ \leftrightarrow Zr(SiO_4)_{1-x}(OH)_{4x} + xSi^{4+} \quad (1)$$

$$ZrSiO_4 + x\left(Fe^{n+} + nCl^-\right) \leftrightarrow Fe_xZr_{1-x}SiO_{4-xn}Cl_{xn} + xZrO_2 + x(n-2)O^{2-}, \quad (2)$$

where n = 2 or 3, and x = 0 to 1.

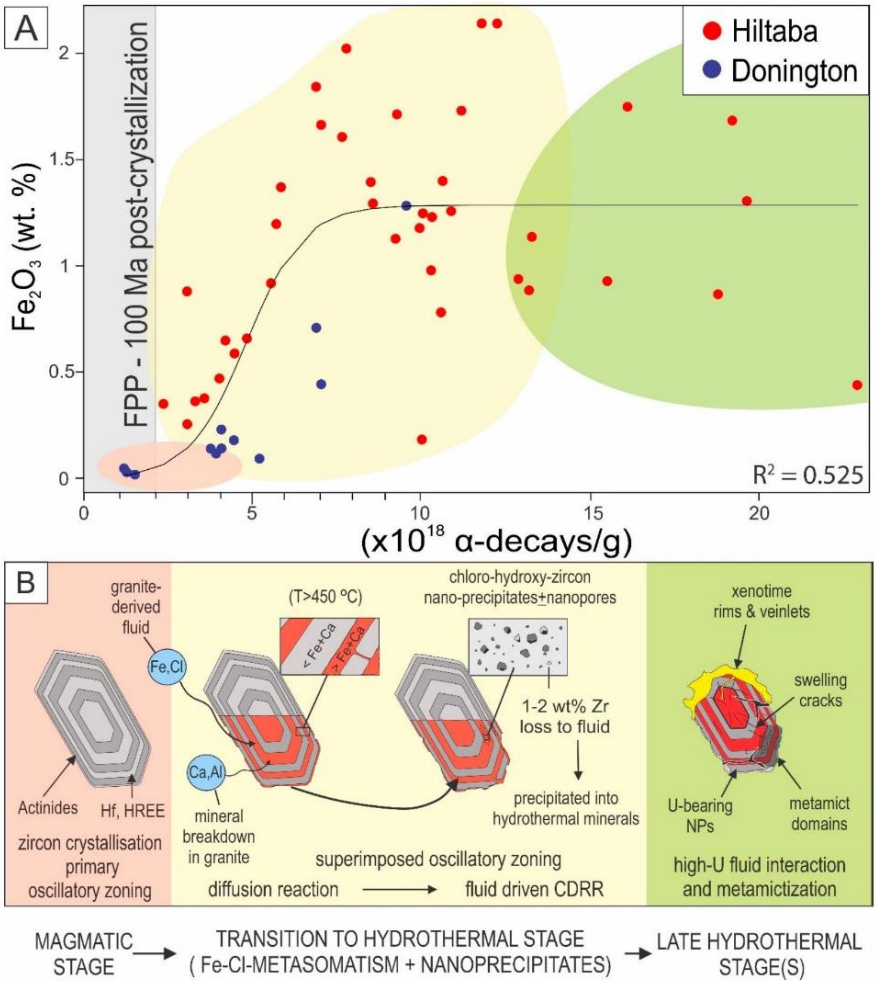

Figure 17. (**A**) Plot of Fe_2O_3 (wt.%) versus D_c (×10^{18} α-decays/g) for all zircon samples as marked and using EPMA data from Supplementary Materials B, Table S4 (four analyses with D_c > 25 were excluded). A sigmoid through the data was fit by non-linear least squares regression using the software "R". Although the first percolation point (FPP) for zircon was marked at D_c = 2 (as defined by Salje et al. [48]), a sharp increase in wt.% Fe_2O_3 was seen only at D_c = ~3. The FPP in Olympic Dam zircon was only reached at least 100 Ma after crystallization, using the dose concentration calculation of Meldrum et al. [58]. Also, note the scatter in the dataset concordant with the weak correlation between the highest measured non-formula element (Fe) and D_c. (**B**) Schematic diagram illustrating evolution of magmatic zircon from granites in the Olympic Cu–Au Province. Colored areas in (**A**) correspond to the main evolutionary stages in (**B**). Note that Cape Donington zircon, with the lowest non-formula elements, plots in a magmatic domain that straddles the FPP line. In contrast, analyses with high U concentration corresponded to intensively altered stages (green), featuring superimposed textures with all the characteristic of metamict zircon, possibly resulting from interaction with late-stage, U-rich hydrothermal fluids. Metasomatic textures and association with abundant, Cl-rich nanoprecipitates are typical features of fertile granites. The association between Fe and Cl recorded in metasomatized zircon during magmatic-to-hydrothermal transition is a diagnostic signature of fertile IOCG systems.

The Fe–Cl-rich signature of post-magmatic fluids is recorded within the mottled textures of zircon and represents the onset of IOCG mineralization during the magmatic-to-hydrothermal transition. From ID-TIMS dating of hematite, iron metasomatism is known to have occurred at Olympic Dam shortly after granite crystallization (~2–4 Ma later) [13]. The present data support early, as well as prolonged, zircon alteration, illustrated here from areas that are overprinting primary growth (Figure 2B,D). The Fe–Cl-rich metasomatized zones within zircon were also imaged directly adjacent to magmatic relict domains (Figure 8A). Recrystallization of zircon surrounding xenotime veinlets was observed down to the nanoscale (Supplementary Materials C, Figure S3). Whereas zircon metasomatism overprinting primary growth zoning can be related to the earliest hydrothermal fluids exsolved at the depth of granite emplacement, later cycles of zircon alteration could happen during and/or after granite uplift as the IOCG mineralizing system evolved.

Overall, the increase in Cl associated with abundant chloro–hydroxy–zircon nanoprecipitates correlates with proximity to the Olympic Dam orebody. Such features can, thus, be considered a direct indicator of magma "fertility" (the ability of a magma to generate hydrothermal fluids that are sufficiently well-endowed with Cu, U, etc., to form a sizable ore deposit) in Hiltaba Suite granites. Furthermore, the presence of Cl in zircon from other Hiltaba Suite granites such as Charleston, indicates potential undiscovered IOCG mineralization using the zircon pathfinder.

7. Conclusions and Implications

1. From the case studies presented and comparison between them, zircon may be substituted with non-formula elements, notably Fe and Cl, released ~2–4 Ma after magmatic crystallization, during a widespread metasomatic event, prior to fluid pathway development during metamictization.

2. Chloro–hydroxy–zircon nanoprecipitates record the Fe–Cl-signature of fluids released during the magmatic-to-hydrothermal transition in IOCG systems, which volumetrically increase in granites of different age with proximity to Olympic Dam. Such nanoprecipitates represent a potential pathfinder to mineralization associated with fertile granites. Although we recommend that the data should initially be tested in other IOCG terranes, there exists potential for similar features to be identified within zircon from other deposit types involving penetrative metasomatic alteration.

3. Relationships between micron- and nanoscale observations in zircon are a largely untapped research field. With ever increasing instrumental resolution and analytical precision, nanoscale studies can provide new insights into processes carrying implications for geochronology, ore deposit genesis and mineral exploration.

4. In summary, this study has shown that early metasomatic alteration can be recorded in magmatic zircon and that these patterns can be preserved over geological time, even when superimposed by the effects of metamictization. This implies that nanoscale studies of magmatic zircon, when coupled with careful micron-scale characterization of textures and compositions, could represent a valuable new tool in mineral exploration.

Supplementary Materials: The following are available online at http://www.mdpi.com/2075-163X/9/6/364/s1, Supplementary Materials A: Extended details of methodology (Tables S1 and S2); Supplementary Materials B: Expanded data tables (Tables S3–S5); Supplementary Materials C: Additional figures (Figures S1, S2, and S3A–S3E).

Author Contributions: L.C.-D. and C.L.C. conceived this contribution. Analytical work was conducted L.C-.D., C.L.C., M.R.V.-I., M.D., W.K., J.X. and U.I.D., with A.S. operating the Titan Themis instrument and B.P.W. assisting with EPMA set-up. The manuscript was written by L.C.-D., C.L.C., M.R.V.-I. and N.J.C., with contributions from K.E., A.K.-C. and B.P.W.

Funding: This research was funded from the project "Trace elements in iron-oxides: deportment, distribution and application in ore genesis, geochronology, exploration and mineral processing", supported by BHP Olympic Dam and the South Australian Government Mining and Petroleum Services Centre of Excellence. N.J.C. and K.E. acknowledge funding from the ARC Research Hub for Australian Copper–Uranium (Grant IH130200033).

Acknowledgments: We acknowledge the AMMRF for instrument access. Sarah Gilbert assisted with LA-ICP-MS analysis and Animesh Basak assisted with FIB-SEM operation. Chris Kalnins is thanked for preparing two of the TEM foils presented. We kindly thank two anonymous reviewers for comments that helped improve this manuscript.

Conflicts of Interest: The authors declare no conflicts of interest.

References

1. Groves, D.I.; Bierlein, F.P.; Meinert, L.D.; Hitzman, M.W. Iron oxide copper-gold (IOCG) deposits through Earth history: Implications for origin, lithospheric setting, and distinction from other epigenetic iron oxide deposits. *Econ. Geol.* **2010**, *105*, 641–654. [CrossRef]
2. Barton, M.D. Iron oxide (-Cu-Au-REE-P-Ag-U-Co) systems. In *Treatise on Geochemistry*, 2nd ed.; Elsevier: Amsterdam, The Netherlands, 2014; Volume 13, pp. 515–541.
3. Krneta, S.; Ciobanu, C.L.; Cook, N.J.; Ehrig, K.; Kontonikas-Charos, A. Apatite at Olympic Dam, South Australia: A petrogenetic tool. *Lithos* **2016**, *262*, 470–485. [CrossRef]
4. Krneta, S.; Ciobanu, C.L.; Cook, N.J.; Ehrig, K.J. Numerical modeling of REE fractionation patterns in fluorapatite from the Olympic Dam deposit (South Australia). *Minerals* **2018**, *8*, 342. [CrossRef]
5. Condon, D.J.; Schmitz, M.D. One hundred years of geochronology. *Elements* **2013**, *9*, 3–80. [CrossRef]
6. Harley, S.L.; Kelly, N.M. Zircon Tiny but Timely. *Elements* **2007**, *3*, 13–18. [CrossRef]
7. Rubatto, D.; Hermann, J. Zircon behaviour in deeply subducted rocks. *Elements* **2007**, *3*, 31–35. [CrossRef]
8. Scherer, E.E.; Whitehouse, M.J.; Munker, C. Zircon as a Monitor of Crustal Growth. *Elements* **2007**, *3*, 19–24. [CrossRef]
9. Hoskin, P.W.O.; Schaltegger, U. The composition of zircon and igneous and metamorphic petrogenesis. *Rev. Mineral. Geochem.* **2003**, *53*, 27–62. [CrossRef]
10. Ewing, R.C.; Meldrum, A.; Wang, L.M.; Weber, W.J.; Corrales, L.R. Radiation damage in zircon. *Rev. Mineral. Geochem.* **2003**, *53*, 387–425. [CrossRef]
11. Skirrow, R.G.; Bastrakov, E.N.; Barovich, K.; Fraser, G.L.; Creaser, R.A.; Fanning, C.M. Timing of iron oxide Cu-Au-(U) hydrothermal activity and Nd isotope constraints on metal sources in the Gawler craton, South Australia. *Econ Geol.* **2007**, *102*, 1441–1470. [CrossRef]
12. Ehrig, K.; McPhie, J.; Kamenetsky, V. Geology and Mineralogical Zonation of the Olympic Dam Iron Oxide Cu-U-Au-Ag Deposit, South Australia. In *Geology and Genesis of Major Copper Deposits and Districts of the World: A Tribute to Richard H. Sillitoe*; Hedenquist, J.W., Harris, M., Camus, F., Eds.; Society of Economic Geologists Special Publication 16; Society of Economic Geologists: Littleton, CO, USA, 2012; pp. 237–267.
13. Courtney-Davies, L.; Tapster, S.; Ciobanu, C.; Cook, N.J.; Verdugo-Ihl, M.R.; Ehrig, K.J.; Kennedy, A.K.; Gilbert, S.E.; Condon, D.J.; Wade, B.P. A multi-technique evaluation of hydrothermal hematite U-Pb isotope systematics: Implications for ore deposit geochronology. *Chem. Geol.* **2019**, *513*, 54–72. [CrossRef]
14. Cherry, A.R.; Ehrig, K.; Kamenetsky, V.S.; McPhie, J.; Crowley, J.L.; Kamenetsky, M.B. Precise geochronological constraints on the origin, setting and incorporation of ca. 1.59 Ga surficial facies into the Olympic Dam Breccia Complex, South Australia. *Precambr. Res.* **2018**, *315*, 162–178. [CrossRef]
15. Ewing, R.C.; Lutze, W.; Weber, W.J. Zircon—A Host-Phase for the Disposal of Weapons Plutonium. *J. Mater. Res.* **1995**, *10*, 243–246. [CrossRef]
16. Holland, H.D.; Gottfried, D. The effect of nuclear radiation on the structure of zircon. *Acta Cryst.* **1955**, *8*, 291–300. [CrossRef]
17. Mattinson, J. Zircon U–Pb chemical abrasion ("CA-TIMS") method: Combined annealing and multi-step partial dissolution analysis for improved precision and accuracy of zircon ages. *Chem. Geol.* **2005**, *220*, 47–66. [CrossRef]
18. Geisler, T.; Schaltegger, U.; Tomaschek, F. Re-equilibration of zircon in aqueous fluids and melts. *Elements* **2007**, *3*, 43–50. [CrossRef]
19. Geisler, T.; Rashwan, A.A.; Rahn, M.K.W.; Poller, U.; Zwingmann, H.; Pidgeon, R.T.; Schleicher, H.; Tomaschek, F. Low temperature hydrothermal alteration of natural metamict zircons from the Eastern Desert, Egypt. *Mineral. Mag.* **2003**, *67*, 485–508. [CrossRef]
20. Tang, F.; Taylor, J.M.; Einsle, J.F.; Borlina, C.S.; Fu, R.R.; Weiss, B.P.; Williams, H.M.; Williams, W.; Nagy, L.; Midgley, P.; et al. Secondary magnetite in ancient zircon precludes analysis of a Hadean geodynamo. *Proc. Natl. Acad. Sci. USA* **2019**, *116*, 407–412. [CrossRef]
21. Lu, Y.J.; Loucks, R.R.; Fiorentini, M.L.; McCuaig, T.C.; Evans, N.J.; Yang, Z.M.; Hou, Z.Q.; Kirkland, C.L.; Parra-Avila, L.A.; Kobussen, A. Zircon compositions as a pathfinder for porphyry Cu ± Mo ± Au deposits. *Econ. Geol.* **2016**, *19*, 329–347.

22. Belousova, E.A.; Griffin, W.L.; O'Reilly, S.Y.; Fisher, N.I. Igneous zircon: Trace element composition as an indicator of source rock type. *Contrib. Mineral. Petrol.* **2002**, *143*, 602–622. [CrossRef]
23. Utsunomiya, S.; Ewing, R.C. Application of high-angle annular dark field scanning transmission electron microscopy—Energy dispersive X-ray spectrometry, and energy-filtered transmission electron microscopy to the characterization of nanoparticles in the environment. *Environ. Sci. Technol.* **2003**, *37*, 786–791. [CrossRef]
24. Utsunomiya, S.; Palenik, C.S.; Valley, J.W.; Cavosie, A.J.; Wilde, S.A.; Ewing, R.C. Nanoscale occurrence of Pb in an Archean zircon. *Geochim. Cosmochim. Acta* **2004**, *68*, 4679–4686. [CrossRef]
25. Utsunomiya, S.; Valley, J.W.; Cavosie, A.J.; Wilde, S.A.; Ewing, R.C. Radiation damage and alteration of zircon from a 3.3 Ga porphyritic granite from the Jack Hills, Western Australia. *Chem. Geol.* **2007**, *236*, 92–111. [CrossRef]
26. Seydoux-Guillaume, A.M.; Bingen, B.; Paquette, J.L.; Bosse, V. Nanoscale evidence for uranium mobility in zircon and the discordance of U-Pb chronometers. *Earth Plan. Sci. Lett.* **2015**, *409*, 43–48. [CrossRef]
27. Kusiak, M.A.; Dunkley, D.J.; Wirth, R.; Whitehouse, M.J.; Wilde, S.A.; Marquardtd, K. Metallic lead nanospheres discovered in ancient zircons. *Proc. Natl. Acad. Sci. USA* **2015**, *112*, 4958–4963. [CrossRef]
28. Ciobanu, C.L.; Cook, N.J.; Maunders, C.; Wade, B.P.; Ehrig, K. Focused Ion Beam and Advanced Electron Microscopy for Minerals: Insights and Outlook from Bismuth Sulphosalts. *Minerals* **2016**, *6*, 112. [CrossRef]
29. Cook, N.J.; Ciobanu, C.L.; Ehrig, K.; Slattery, A.; Verdugo-Ihl, M.R.; Courtney-Davies, L.; Gao, W. Advances and opportunities in ore mineralogy. *Minerals* **2017**, *7*, 233. [CrossRef]
30. Goldfarb, R.J.; Bradley, D.; Leach, D.L. Secular variation in economic geology. *Econ. Geol.* **2010**, *105*, 459–465. [CrossRef]
31. Allen, S.R.; McPhie, J.; Ferris, G.; Simpson, C. Evolution and architecture of a large felsic igneous province in western Laurentia: The 1.6 Ga Gawler Range Volcanics, South Australia. *J. Volcanol. Geotherm. Res.* **2008**, *172*, 132–147. [CrossRef]
32. Keyser, W.M.; Ciobanu, C.L.; Cook, N.J.; Johnson, G.; Feltus, F.; Johnson, S.; Dmitrijeva, M.; Ehrig, K.; Nguyen, P. Petrography and trace element signatures of iron-oxides in deposits from the Middleback Ranges, South Australia: From banded iron formation to ore. *Ore Geol. Rev.* **2018**, *93*, 337–360. [CrossRef]
33. Domnick, U.; Cook, N.J.; Bluck, R.; Brown, C.; Ciobanu, C.L. Petrography of granitoids from the Samphire Pluton, South Australia: Implications for uranium mineralization in overlying sediments. *Lithos* **2018**, *300–301*, 1–19. [CrossRef]
34. Keyser, W.; Ciobanu, C.L.; Cook, N.J.; Dmitrijeva, M.; Courtney-Davies, L.; Feltus, H.; Gilbert, S.; Johnson, G.; Ehrig, K. Iron-oxides constrain BIF evolution in terranes with protracted geological histories: The Iron Count prospect, Middleback Ranges, South Australia. *Lithos* **2019**, *324*, 20–38. [CrossRef]
35. Dmitrijeva, M.; Metcalfe, A.V.; Ciobanu, C.L.; Cook, N.J.; Frenzel, M.; Keyser, W.M.; Johnson, G.; Ehrig, K. Discrimination and variance structure of trace element signatures in hematite: A case study of BIF-mineralization from the Middleback Ranges, South Australia. *Math. Geosci.* **2018**, *50*, 381–415. [CrossRef]
36. Creaser, R.A.; Fanning, C.M. A U-Pb zircon study of the Mesoproterozoic Charleston Granite, Gawler Craton, South Australia. *Aust. J. Earth Sci.* **1993**, *40*, 519–526. [CrossRef]
37. Skirrow, R.G.; van der Wielen, S.E.; Champion, D.C.; Czarnota, K.; Thiel, S. Lithospheric architecture and mantle metasomatism linked to iron oxide Cu-Au ore formation: Multidisciplinary evidence from the Olympic Dam Region, South Australia. *Geochem. Geophys. Geosyst.* **2018**, *19*, 2673–2705. [CrossRef]
38. Wade, C.E.; Payne, J.L.; Barovich, K.M.; Reid, A.J. Heterogeneity of the sub-continental lithospheric mantle and 'non-juvenile' mantle additions to a Proterozoic silicic large igneous province. *Lithos* **2019**, *340–341*, 87–107. [CrossRef]
39. Ovalle, J.T.; La Cruz, N.L.; Reich, M.; Barra, F.; Simon, A.C.; Konecke, B.A.; Rodriguez-Mustafa, M.A.; Deditius, A.P.; Childress, T.M.; Morata, D. Formation of massive iron deposits linked to explosive volcanic eruptions. *Sci. Rep.* **2018**, *8*, 14855. [CrossRef]
40. Kontonikas-Charos, A.; Ciobanu, C.L.; Cook, N.J.; Ehrig, K.; Krneta, S.; Kamenetsky, V.S. Feldspar evolution in the Roxby Downs Granite, host to Fe-oxide Cu-Au-(U) mineralisation at Olympic Dam, South Australia. *Ore Geol. Rev.* **2017**, *80*, 838–859. [CrossRef]
41. Krneta, S.; Cook, N.J.; Ciobanu, C.L.; Ehrig, K.; Kontonikas-Charos, A. The Wirrda Well and Acropolis prospects Gawler Craton, South Australia: Insights into evolving fluid conditions through apatite chemistry. *J. Geochem. Explor.* **2017**, *181*, 276–291. [CrossRef]

42. Kontonikas-Charos, A.; Ciobanu, C.L.; Cook, N.J.; Ehrig, K.; Krneta, S.; Kamenetsky, V.S. Rare earth element geochemistry of feldspars: Examples from Fe-oxide Cu-Au systems in the Olympic Cu-Au Province, South Australia. *Mineral. Petrol.* **2018**, *112*, 145–172. [CrossRef]
43. Jagodzinski, E.A. Compilation of SHRIMP U-Pb geochronological data Olympic Domain, Gawler Craton, South Australia, 2001–2003. *Geosci. Aust. Rec.* **2005**, *20*, 2005.
44. Keyser, W.; Ciobanu, C.L.; Cook, N.J.; Courtney-Davies, L.; Kennedy, A.; Wade, B.P.; Ehrig, K.; Dmitrijeva, M.; Kontonikas-Charos, A.; Feltus, H.; et al. Petrographic and geochronological constraints on the granitic basement to the Middleback Ranges, South Australia. *Precambr. Res.* **2019**, *324*, 170–193. [CrossRef]
45. Pérez-Soba, C.; Villaseca, C.; Gonzáles del Tánago, J.; Nasdala, L. The composition of zircon in the peraluminous Hercynian granites of the Spanish Central System batholith. *Can. Mineral.* **2007**, *45*, 509–527. [CrossRef]
46. Verdugo-Ihl, M.R.; Ciobanu, C.L.; Cook, N.J.; Ehrig, K.; Courtney-Davies, L.; Gilbert, S. Textures and U-W-Sn-Mo signatures in hematite from the Cu-U-Au-Ag orebody at Olympic Dam, South Australia: Defining the archetype for IOCG deposits. *Ore Geol. Rev.* **2017**, *91*, 173–195. [CrossRef]
47. Kontonikas-Charos, A.; Ciobanu, C.L.; Cook, N.J.; Ehrig, K.; Ismail, R.; Krneta, S.; Basak, A. Feldspar mineralogy and rare earth element (re)mobilization in iron-oxide copper gold systems from South Australia: A nanoscale study. *Mineral. Mag.* **2018**, *82*, S173–S197. [CrossRef]
48. Salje, E.K.H.; Chrosch, J.; Ewing, R.C. Is "metamictization" of zircon a phase transition? *Am. Mineral.* **1999**, *84*, 1107–1116. [CrossRef]
49. Ríos, S.; Malcherek, T.; Salje, E.K.H.; Domeneghetti, C. Localized defects in radiation-damaged zircon. *Acta Cryst.* **2000**, *56*, 947–952. [CrossRef]
50. Nasdala, L.; Kronz, A.; Wirth, R.; Váczi, T.; Pérez-Soba, C.; Willner, A.; Kennedy, A.K. Alteration of radiation-damaged zircon and the related phenomenon of deficient electron microprobe totals. *Geochim. Cosmochim. Acta* **2009**, *73*, 1637–1650. [CrossRef]
51. Wingate, M.T.D.; Campbell, I.H.; Compston, W.; Gibson, G.M. Ion microprobe U–Pb ages for Neoproterozoic basaltic magmatism in south-central Australia and implications for the breakup of Rodinia. *Precambr. Res.* **1998**, *87*, 135–159. [CrossRef]
52. Verdugo-Ihl, M.R.; Ciobanu, C.L.; Cook, N.J.; Ehrig, K.; Courtney-Davies, L. Defining early stages of IOCG systems: Evidence from iron-oxides in the outer shell of the Olympic Dam deposit, South Australia. *Mineral. Depos.* **2019**. [CrossRef]
53. Xu, H.; Shen, Z.; Konishi, H. Si-magnetite nano-precipitates in silician magnetite from banded iron formation: Z-contrast imaging and ab initio study. *Am. Mineral.* **2014**, *99*, 2196–2202. [CrossRef]
54. Ciobanu, C.L.; Verdugo-Ihl, M.R.; Slattery, A.; Cook, N.J.; Ehrig, K.; Courtney-Davies, L.; Wade, B.P. Silician magnetite: Si-Fe-nanoprecipitates and other mineral inclusions in magnetite from the Olympic Dam deposit, South Australia. *Minerals* **2019**, *9*, 311. [CrossRef]
55. Tooth, B.; Ciobanu, C.L.; Green, L.; O'Neill, B.; Brugger, J. Bi-melt formation and gold scavenging from hydrothermal fluids: An experimental study. *Geochim. Cosmochim. Acta* **2011**, *75*, 5423–5443. [CrossRef]
56. Verdugo-Ihl, M.R.; Ciobanu, C.L.; Cook, N.J.; Slattery, A.; Ehrig, K. Copper nanoparticles along fluid inclusion trails in hematite. In Proceedings of the Goldschmidt 2018, Boston, MA, USA, 12–17 August 2018.
57. Owen, N.D.; Ciobanu, C.L.; Cook, N.J.; Slattery, A.; Basak, A. Nanoscale study of clausthalite-bearing symplectites in Cu-Au-(U) ores: Implications for ore genesis. *Minerals* **2018**, *8*, 67. [CrossRef]
58. Meldrum, A.; Boatner, L.A.; Weber, W.J.; Ewing, R.C. Radiation damage in zircon and monazite. *Geochim. Cosmochim. Acta* **1988**, *62*, 2509–2520. [CrossRef]

ADDITIONAL MATERIAL E

CONFERENCE ABSTRACT:

PETROGRAPHY AND HYDROTHERMAL ALTERATION OF GRANITOIDS FROM THE SAMPHIRE MAGMATIC COMPLEX, SOUTH AUSTRALIA, AND IMPLICATIONS FOR URANIUM MINERALISATION IN OVERLYING SEDIMENTS

Urs Domnick[1], Nigel J. Cook[1], Russel Bluck[2], Callan Brown[2], Cristiana L. Ciobanu[1],

[1]*School of Chemical Engineering and Advanced Materials, The University of Adelaide, Adelaide, SA 5005, Australia*

[2]*Samphire Uranium, 28 Greenhill Road, Wayville, SA 5034, Australia*

Conference abstract, AusIMM Uranium Conference 2017, Adelaide, Australia, June 6th-7th.

Petrography and hydrothermal alteration of granitoids from the Samphire Magmatic Complex, South Australia, and implications for uranium mineralisation in overlying sediments

U. Domnick[1], N.J. Cook[1], R. Bluck[2], C. Brown[2], C.L. Ciobanu[1]

1.
School of Chemical Engineering, The University of Adelaide, Adelaide, SA 5005,
urs.domnick@adelaide.edu.au

2.
Samphire Uranium, 28 Greenhill Road, Wayville, SA 5034

ABSTRACT

In 2007, UraniumSA discovered the Blackbush deposit (inferred resource: 14,850t U) on the northern Eyre Peninsula, South Australia (UraniumSA, 2007). Uranium is hosted in Eocene sandstone of the Kanaka Beds, overlying likely Hiltaba-aged granites - the most probable source rocks. This deposit is currently the only sediment-hosted U deposit investigated in detail in the Gawler Craton. By constraining the petrography and mineralogy of the granites, insights into the post-emplacement evolution can be gained, which may provide an exploration indicator for other sediment-hosted uranium systems.

Three geochemically distinct granite types were identified within a magmatic complex ('Samphire'), which correspond to domains interpreted from geophysical data. Minor aplites and micropegmatites are also part of the complex. All granites show complex alteration overprints and textures with increasing intensity closer to the deposit, as well as crosscutting veining. Alkali feldspar has been replaced by porous K-feldspar and albite, and plagioclase is overprinted by an assemblage of porous albite + sericite ± calc-silicates (prehnite, pumpellyite, epidote). This style of feldspar alteration is regionally widespread and known from Hiltaba granites around Olympic Dam and in the Moonta-Wallaroo region (Kontonikas-Charos et al. 2014; 2017). In two granite types biotite is replaced by calcic garnet. Calc-silicates are indicative of Ca-metasomatism (endoskarn), sourced from the anorthite component of altered plagioclase. Minor clay alteration of feldspars is present in all samples. Mineral assemblages in veins include quartz+hematite, hematite+coffinite, fluorite+quartz, and clay minerals. Minor chlorite and sericite are found in all vein types.

All granite types are anomalously rich in U (concentrations between 10 and 81 ppm). Highly variable Th/U ratios, as well as hydrothermal U minerals (mostly *uranothorite*) in granites and veins, are clear evidence for U mobility. Acidic and oxidising deuteric fluids may have concentrated U in the upper parts of the granite. Porosity, resulting from feldspar alteration, was a vital prerequisite for leaching U.

Kontonikas-Charos A et al. (2014) *Lithos 208-209*, 178-201.
Kontonikas-Charos A et al. (2017) *Ore Geol Rev 80*, 838-859.
UraniumSA (2007) *ASX RELEASE 12 December 2007*, 4 pp

ADDITIONAL MATERIAL F

CONFERENCE ABSTRACT:

COFFINITE AGES IN THE BLACKBUSH URANIUM DEPOSIT, SOUTH AUSTRALIA: URANIUM TRANSPORT INDUCED BY TECTONIC EVENTS

Urs Domnick[1], Nigel J. Cook[1], Russel Bluck[2], C Brown[2], Cristiana L. Ciobanu[1], Benjamin P. Wade[3]

[1]*School of Chemical Engineering and Advanced Materials, The University of Adelaide, Adelaide, SA 5005, Australia*

[2]*Samphire Uranium, 28 Greenhill Road, Wayville, SA 5034, Australia*

[3]*Adelaide Microscopy, The University of Adelaide, Adelaide, SA 5005, Australia*

Conference abstract, AusIMM Uranium Conference 2018, Adelaide, Australia, June 5th-6th.

Coffinite ages in the Blackbush uranium deposit, South Australia: uranium transport induced by tectonic events

U. Domnick[1], N.J. Cook[1], R. Bluck[2], C. Brown[2], C.L. Ciobanu[1], B. Wade[3]

1.
School of Chemical Engineering, The University of Adelaide, Adelaide, SA 5005, urs.domnick@adelaide.edu.au

2.
Samphire Uranium, 28 Greenhill Road, Wayville, SA 5034

3.
Adelaide Microscopy, The University of Adelaide, Adelaide, SA 5005

ABSTRACT

In 2007, UraniumSA discovered the Blackbush deposit (inferred resource: 14,850t U) on the northern Eyre Peninsula, South Australia (UraniumSA, 2007). This deposit is currently the only sediment-hosted U deposit that has been investigated in any detail in the Gawler Craton.

Eocene sandstone of the Kanaka Beds overlies a massive saprolite derived from the subjacent Hiltaba-aged (~1585 Ma) granites. These granites are considered as the most probable source rocks for the uranium. (Domnick et al., 2017). In the deposit, uranium is present as coffinite ($U(SiO_4)_{1-x}(OH)_{4x}$) and is hosted mainly in the sandstone, along the unconformity, as well as a roll front downstream, and to a minor degree in the saprolite. Coffinite and traces of uraninite can also be found in hematite-coffinite bearing veins in the underlying granite.

The coffinite in the sandstone and saprolite mainly occurs intergrown with framboidal Fe-sulphides and lignite grains, as well as coatings around grains of quartz. It is poor in trace elements such as REE or Th. In contrast, vein-hosted coffinite contains a significant amount of Y (11 wt.%) and HREE.

Chemical U-Pb dating (582 spot analyses) of coffinite in all three occurrences (sandstone, saprolite and veins) gives a normal distribution with a mean age of17±1.6 Ma for the whole population. This is interpreted as valuable evidence for a single coffinite-forming event at that time, which affected all parts of the deposit. Such an event likely coincided with tectonic movement, indicated by horst and graben structures in the early Miocene Melton limestone. This unit is overlying the Eocene sandstone, and, in turn, is overlain by Pliocene Gibbon Beds that show no evidence of tectonism.

Uraninite in the granite-hosted vein yielded a significantly older age of 41±2 Ma. This predates sedimentation of the Eocene Kanaka Beds, and likely indicates transport and redeposition of uranium by oxidising fluids within the exposed granite.

These two ages obtained indicate that uraninite formed in granite veins and was subsequently dissolved and reprecipitated as coffinite in younger sediments during tectonic events in the Tertiary.

Domnick, U., Cook, N.J., Bluck, R., Brown, C., Ciobanu, C.L. (2017) Petrography and geochemistry of granitoids from the Samphire Pluton, South Australia: Implications for uranium mineralisation in overlying sediments.Lithos 300, 1-19.
UraniumSA (2007) *ASX RELEASE 12 December 2007*, 4 pp.

ADDITIONAL MATERIAL G

CONFERENCE ABSTRACT AND POSTER:

URANIUM TRANSPORT FROM MESOPROTEROZOIC BEDROCK GRANITE INDUCED TECTONISM: THE BLACKBUSH URANIUM DEPOSIT, SOUTH AUSTRALIA

Urs Domnick[1], Nigel J. Cook[1], Cristiana L. Ciobanu[1], Benjamin P. Wade[2]

Russel Bluck[3], Allen K. Kennedy[4]

[1]*School of Chemical Engineering and Advanced Materials, The University of Adelaide, Adelaide, SA 5005, Australia*

[2]*Adelaide Microscopy, The University of Adelaide, Adelaide, SA 5005, Australia*

[2]*Samphire Uranium, 28 Greenhill Road, Wayville, SA 5034, Australia*

[4]*John de Laeter Centre, Curtin University of Technology, Bentley, WA 6102, Australia*

Conference abstract and poster, 15th Quadrennial IAGOD Symposium, Salta, Argentina, August 28th-31st. Symposium Volume, SEGEMAR, A99.

15th Quadrennial IAGOD International Association on the Genesis of Ore Deposits Symposium, Salta, Argentina.

URANIUM TRANSPORT FROM MESOPROTEROZOIC BEDROCK GRANITE INDUCED BY TECTONISM: THE BLACKBUSH URANIUM DEPOSIT, SOUTH AUSTRALIA

Urs Domnick[1], Nigel J. Cook, Cristiana L. Ciobanu, Benjamin P. Wade, Russel Bluck, Allen Kennedy

[1]*School of Chemical Engineering, The University of Adelaide, Australia - urs.domnick@adelaide.edu.au*

BACKGROUND

The Blackbush deposit, northern Eyre Peninsula, South Australia, (inferred resource 12,580 tonnes U (UraniumSA, 2007)) is currently the only sediment-hosted U deposit in the Gawler Craton that has been investigated in any detail. Uranium is mainly hosted at the unconformity between Eocene sandstone of the Kanaka Beds and a massive saprolite derived from the subjacent Hiltaba-aged (~1585 Ma) granites, affiliated with the Samphire Pluton (Figure 1).

Basement geology of the Gawler Craton remains poorly constrained. Beneath the Blackbush deposit, three distinct granitoids are recognised (Domnick *et al.*, 2018). The southern part of the pluton features a characteristic green granite (B) whereas the northern part, immediately underlying the Blackbush deposit, is comprised by granite C, characterised by reddened feldspars. These two granites are separated by an arcuate domain of a yellow granite (A), which is significantly less evolved than the other two, as indicated by higher Ca, and lower U. All three granites show complex alteration overprints and textures, as well as crosscutting veins. Alkali feldspar has been replaced by porous K-feldspar and albite, and plagioclase is overprinted by an assemblage of porous albite + sericite ± calc-silicates. In granites A and B, igneous biotite is replaced by calcic garnet. Calc-silicates are indicative of Ca-metasomatism, sourced from the anorthite component of altered plagioclase. Clay alteration of feldspars is present in all samples. Mineral assemblages in veins include quartz+ hematite, hematite + coffinite, fluorite + quartz, and clay minerals. Chlorite and sericite are found in all vein types and overprint other minerals.

Previously published geochronological constraints on the Samphire Pluton are 1584±4 Ma, and 1586±6 Ma for granite B and granite C, respectively (Jagodzinski and Reid, 2017). Here we present new geochronological data for zircon from the underlying granites and for U-minerals in veins within granite, saprolite and overlying sandstone.

METHODS

Sensitive high-resolution ion microprobe (SHRIMP) U-Pb data was obtained for zircons separated and concentrated from the three granites using a SHRIMP II at the John De Laeter Centre, (Perth, Western Australia). Chemical U-Pb ages for coffinite and uraninite were obtained by electron probe microanalysis.

RESULTS

New SHRIMP U-Pb zircon data for all three granites confirms previously published ages (Jagodzinski and Reid, 2017) albeit with minor differences. Granite B yielded an age of 1585±9 Ma, Granite C 1579±9 Ma, and Granite A 1588±9 Ma. The age overlap for granites of distinct appearance and geochemistry indicates either short-lived magmatic activity and/or differences in fractionation due to differences in crustal assimilation. The anomalously high U contents between 10 and 81 ppm in Granite C under the deposit, as well as highly variable Th/U ratios, and the presence of hydrothermal U minerals, like uranothorite and coffinite are clear evidence for mobility of U, which was facilitated by the porosity created during feldspar alteration, and strongly indicate that the granite is the most probable source rock for the uranium (Domnick *et al.*, 2018).

In the deposit, uranium is present as coffinite, $[U(SiO_4)_{1-x}(OH)_{4x}]$, and is hosted mainly in the sandstone, along the unconformity, as well as within a roll front downstream, and to a minor degree also in saprolite (Figure 1). Coffinite and traces of uraninite can also be found in hematite-coffinite-bearing veins that crosscut the underlying granite.

The coffinite in the sandstone and saprolite occurs intergrown with framboidal Fe-sulphides and lignite grains, as well as coatings around grains of quartz. It is poor in trace elements such as REE or Th. In contrast, coffinite within the granite-hosted veins contains a significant amount of Y (11 wt.%) and HREE. Minor uranium also occurs absorbed in lignite, presumably as U^{6+}. Chemical U-Pb dating (582 spot analyses) of coffinite in all three occurrences (sandstone, saprolite and veins) gives a normal distribution with a mean age of 17±1.6 Ma for the whole population. Uraninite in the granite-hosted vein yielded a significantly older age (41±2 Ma).

DISCUSSION AND CONCLUSIONS

Coffinite ages are interpreted as valuable evidence for a single coffinite-forming event during the Miocene. Such an event likely coincided with tectonic movement, indicated by horst and graben structures in the early

Miocene Melton limestone. The latter unit overlies the Eocene sandstone, and, in turn, is overlain by Pliocene Gibbon Beds that show no evidence of tectonism. The significantly older age of granite-vein uraninite indicates this predates sedimentation of the Eocene Kanaka Beds, and likely indicates transport and redeposition of uranium by oxidising fluids within the exposed granite. The ages obtained here on hydrothermal minerals indicate that uraninite formed in granite veins and was subsequently dissolved and reprecipitated as coffinite in younger sediments during tectonic events in the Tertiary. Such data allow interpretation of U-mineralization in the deposit as resulting from U transport out of Mesoproterozoic bedrock granite during tectonic activity.

REFERENCES

Domnick, U, Cook, N.J., Bluck, R., Brown, C., Ciobanu, C.L., 2018. Petrography of granitoids from the Samphire Pluton, South Australia: implications for uranium mineralization in overlying sediments. Lithos 300–301: 1–19.

Jagodzinski, E.A., Reid, A.J. (2017) Project PGC03-01: Geochronology from the Samphire uranium project. PACE Geochronology: Results of Collaborative Geochronology Projects 2013–2015, Report Book 2015/00003, p. 10–28. Department of the Premier and Cabinet, South Australia, Adelaide.

UraniumSA (2007), ASX Release, 12 December 2007, 4 pp.

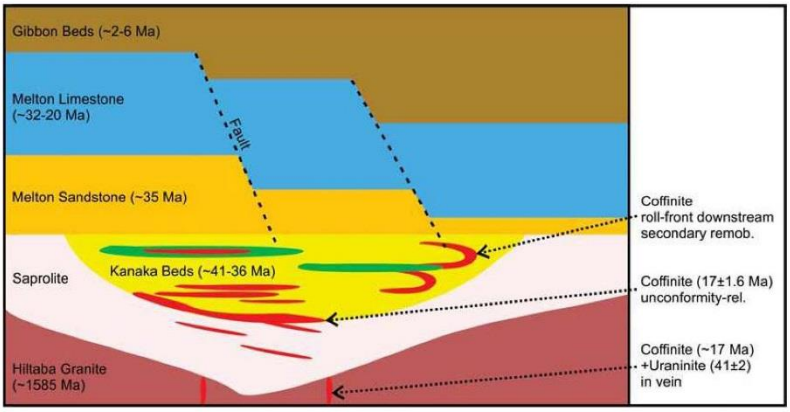

Fig. 1. Schematic cross-section through the Samphire deposit and new chemical ages for U- minerals.

Uranium transport from Mesoproterozoic bedrock granite induced by tectonism: The Blackbush Uranium Deposit, South Australia

Urs Domnick[1], Nigel J. Cook[1*], Cristiana L. Ciobanu[1], Benjamin P. Wade[2], Russel Bluck[3], Allen Kennedy[4]

THE UNIVERSITY of ADELAIDE

1 School of Chemical Engineering, The University of Adelaide, SA 5005, Australia
2 Adelaide Microscopy, The University of Adelaide, SA 5005, Australia
3 Samphire Uranium, 28 Greenhill Road, Wayville, Australia
4 John de Laeter Centre, Curtain University of Technology, Bentley, WA 6102, Australia

Summary

The Blackbush Uranium Deposit is an unconformity-related uranium deposit (~12,500 tonnes U at 100 ppm cut-off) on Eyre Peninsula, South Australia (Figure 1), discovered in 2007 [1]. It is currently the only sediment-hosted uranium deposit investigated in any detail in the Gawler Craton, which is well known for its IOCG(+U) deposits like Olympic Dam. These deposits are associated with ~1590 Ma Hiltaba suite granites, which also form the granitic bedrock of the Blackbush deposit. Three different granitic phases were identified around the deposit and subsequently dated via SHRIMP giving an age of ~1585 Ma for all phases. They show high U contents and disturbed Th/U ratios, as well as coffinite bearing veins, proving mobility of U and reaffirming that the granites are the source rock of the U in the deposit [2]. The U in the deposit itself is mainly present as coffinite in different lithologies, mineralisation styles and mineral associations. Chemical U-Pb dating of coffinite via microprobe across different styles and lithologies yielded a tight age range of 17±1.6 Ma, strongly indicating a single coffinite-forming event at that time. This roughly coincides with tectonic movement as indicated in horst and graben structures in older, but not younger sediment covering the deposit.

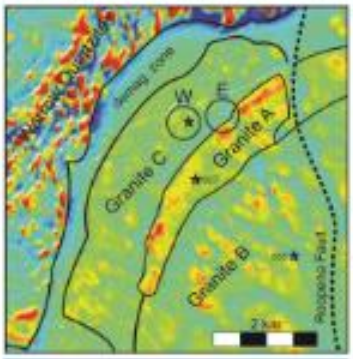

Fig. 2
Total magnetic intensity, first derivative (TMI) Map of the area around the deposit.
stars = SHRIMP samples.
W = western mineralized zone (unconformity); E = eastern mineralized zone (roll-front downstream)
TMI data by SARIG, interpretation by Samphire Uranium

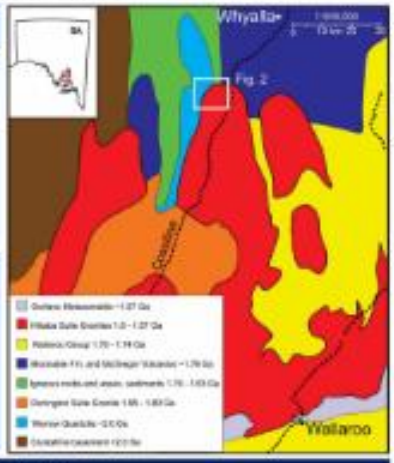

Fig. 1
Map of eastern Eyre and western Yorke Peninsula, South Australia.
Based on material provided by SARIG and Samphire Uran

Methodology

Sensitive high-resolution ion microprobe (SHRIMP) U-Pb data was obtained for zircons separated and concentrated from the three granites using a SHRIMP II at the John De Laeter Centre (Perth, WA). Chemical U-Pb ages for coffinite and uraninite were obtained by electron probe microanalysis.

Results

New SHRIMP U-Pb zircon data for all three granites confirms previously published ages [3] albeit with minor differences. Granite B yielded an age of 1585±9 Ma, Granite C 1570±9 Ma, and Granite A 1588±6 Ma. The age overlap for granites of distinct appearance and geochemistry indicates either short-lived magmatic activity and/or differences in fractionation due to differences in crustal assimilation. In the deposit, uranium is present as coffinite, $[U(SiO_4)_{1-x}(OH)_{4x}]$, and is hosted mainly in the sandstone, along the unconformity, as well as within a roll front downstream, and to a minor degree also in saprolite (Figure 3). Coffinite and traces of uraninite can also be found in hematite-coffinite-bearing veins that crosscut the underlying granite.

The coffinite in the sandstone and saprolite occurs intergrown with framboidal Fe-sulphides and lignite grains, as well as coatings around grains of quartz. It is poor in trace elements such as REE or Th. In contrast, coffinite within the granite-hosted veins contains a significant amount of Y (11 wt.%) and HREE. Minor uranium also occurs absorbed in lignite, presumably as U^{6+}. Chemical U-Pb dating (582 spot analyses) of coffinite in all three occurrences (sandstone, saprolite and veins) gives a normal distribution with a mean age of 17±1.6 Ma for the whole population. Uraninite in the granite-hosted vein yielded a significantly older age (41±2 Ma) (Figure 4).

Acknowledgements
U.D. acknowledges receipt of a Ph.D. scholarship from the Cathlow Family Trust. The assistance of staff at Adelaide Microscopy with microanalytical work is gratefully acknowledged. N.J.C. received support from the ARC Research Hub for Australian Copper-Uranium.

References
[1] UraniumSA (2007) ASX Release, 12 December 2007, 4 pp.
[2] Domnick, U. et al. (2017) Lithos 300, 1-19.
[3] Jagodzinski, E.A., Reid, A.J. (2017) In: PACE Geochronology Report Book 2015/00803, p. 19-28. DPC, S.A.

Background

Uranium is mainly hosted at the unconformity between Eocene sandstone of the Kanaka Beds and a saprolite derived from the subjacent Hiltaba-aged (~1585 Ma) granites, affiliated with the Samphire Pluton (Figure 2).

Beneath the Blackbush deposit, three distinct granitoids are recognised [2]. The southern part of the pluton features a characteristic green granite (B) whereas the northern part, immediately underlying the Blackbush deposit, is comprised by granite C, characterised by reddened feldspars. These two granites are separated by an arcuate domain of a yellow granite (A), which is significantly less evolved than the other two, as indicated by higher Ca- and lower U. All three granites show complex alteration overprints and textures, as well as crosscutting veins. Alkali feldspar has been replaced by porous K-feldspar and albite, and plagioclase is overprinted by an assemblage of porous albite + sericite ± calc-silicates. In granites A and B, igneous biotite is replaced by calcic garnet. Calc-silicates are indicative of Ca-metasomatism, sourced from the anorthite component of altered plagioclase. Clay alteration of feldspars is present in all samples. Mineral assemblages in veins include quartz + hematite, hematite + coffinite, fluorite + quartz, and clay minerals. Chlorite and sericite are found in all vein types and overprint other minerals.

Discussion

Coffinite ages are interpreted as valuable evidence for a single coffinite-forming event during the Miocene. Such an event likely coincided with tectonic movement, indicated by horst and graben structures in the early Miocene Melton limestone. The latter unit overlies the Eocene sandstone, and, in turn, is overlain by Pliocene Gibbon Beds that show no evidence of tectonism. The significantly older age of granite-vein uraninite indicates this predates sedimentation of the Eocene Kanaka Beds, and likely indicates transport and redeposition of uranium by oxidising fluids within the exposed granite. The ages obtained here on hydrothermal minerals indicate that uraninite formed in granite veins and was subsequently dissolved and reprecipitated as coffinite in younger sediments during tectonic events in the Tertiary. Such data allow interpretation of U-mineralisation in the deposit as resulting from U transport out of Mesoproterozoic bedrock granite during tectonic activity.

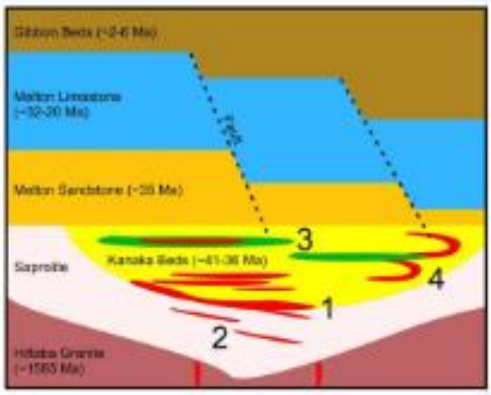

↑ **Fig. 3**
Schematic representation of the deposit and its stratigraphy
Mineralization styles
1 = unconformity-related
2 = tabular saprolite-hosted
3 = tabular sandstone + lignite hosted
4 = roll-front downstream
Based on material by Samphire Uranium

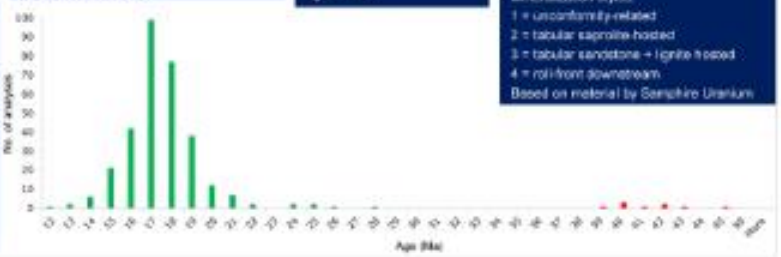

↓ **Fig. 4**
Histogram of the coffinite (green) and uraninite (red) ages in Ma

REFERENCES

Allen, S.R., McPhie, J., Ferris, G., Simpson, C., 2008. Evolution and architecture of a large felsic Igneous Province in western Laurentia: The 1.6 Ga Gawler Range Volcanics, South Australia. Journal of Volcanology and Geothermal Research 172, 132–147.

Allen, S.R., Simpson, C.J., McPhie, J., Daly, S.J., 2003. Stratigraphy, distribution and geochemistry of widespread felsic volcanic units in the Mesoproterozoic Gawler Range Volcanics, South Australia. Australian Journal of Earth Sciences 50, 97–112.

Alley, N.F., Clarke, J.D.A., MacPhail, M., Truswell, E.M., 1999. Sedimentary infillings and development of major Tertiary palaeodrainage systems of south-central Australia. In: Thiry, M., Simon-Coinçon, R. (Eds), Palaeoweathering, Palaeosurface and Related Continental Deposits, Special Publication No. 27, International Association of Sedimentologists, Blackwell Science, 337-367.

Apukhtina, O.B., Kamenetsky, V.S., Ehrig, K., Kamenetsky, M.B., Maas, R., Thompson, J., McPhie, J., Ciobanu, C.L., Cook, N.J., 2017. Early, deep magnetite-fluorapatite mineralization at the Olympic Dam Cu-U-Au-Ag deposit, South Australia. Economic Geology 112, 1531-1542.

Armstrong, J.T., 1988. Quantitative analysis of silicate and oxide minerals: Comparison of Monte Carlo, ZAF, and φ(ρz) procedures. Microbeam Analysis, 239-246.

Bailie, R.H., Robb, L.J., 2004. Polymetallic mineralization in the granites of the Bushveld Complex - examples from the central southeastern lobe. South African Journal of Geology 107, 633–652.

Barker, F., 1979. Trondhjemite: definition, environment and hypotheses of origin. In: Developments in petrology Vol. 6, Elsevier, 1-12.

BHP, 1982. Open File Envelope No. 4124, EL 766 Mullaquana, Progress and final reports for the period 8/12/80 to 7/12/82.

Bluck, R., Brown, C., 2017. Characterisation of the Samphire granite, Hiltaba Suite, northeastern Eyre Peninsula. MESA Journal 85, 31-40.

Bowles, J.F.W., 1990. Age dating of individual grains of uraninite in rocks from electron microprobe analyses. Chem. Geol. 83, 47-53.

Braun, J.-J., Pagel, M., Muller, J.-P., Bilong, P., Michard, A., Guillet, B., 1990. Cerium anomalies in lateritic profiles. Geochimica et Cosmochimica Acta 54, 781-795.

Budd, A.R., 2006. A- and I-type subdivision of the Gawler Ranges-Hiltaba Volcano-Plutonic Association. Presentation at Goldschmidt Conference 2006.

Budd, A.R., Skirrow, R.G., 2007. The nature and origin of gold deposits of the Tarcoola goldfield and

implications for the central Gawler gold province, South Australia. Economic Geology 102, 1541–1563.

Budd, A.R., Wyborn, L., Bastrakova, I., 1998. Exploration significance of the Hiltaba Suite, South Australia. AGSO Research Newsletter 29, 1-4.

Budd, A.R., Wyborn, L.A.I., Bastrakova, I.V., 2002. The metallogenic potential of Australian proterozoic granites. Geoscience Australia Record 2001/12.

Cerny, P., Blevin, P.L., Cuney, M., London, D., 2005. Granite-related ore deposits. Economic Geology 100th Anniversary Volume, 337-370.

Cherry, A., Ehrig, K., Kamenetsky, V., McPhie, J., Crowley, J., Kamenetsky, M., 2018. Precise geochronological constraints on the origin, setting and incorporation of ca. 1.59 Ga surficial facies into the Olympic Dam Breccia Complex, South Australia. Precambrian Research 315, 162-178.

Ciobanu, C.L., Cook, N.J., Utsunomiya, S., Pring, A., Green, L., 2011. Focussed ion beam - transmission electron microscopy applications in ore mineralogy: bridging micron- and nanoscale observations. Ore Geology Reviews 42, 6-31.

Ciobanu, C.L., Wade, B.P., Cook, N.J., Schmidt Mumm, A., Giles, D., 2013. Uranium-bearing hematite from the Olympic Dam Cu-U-Au deposit, South Australia: a geochemical tracer and reconnaissance Pb-Pb geochronometer. Precambrian Research 238, 129-147.

Claoué-Long, J.C., Compston, W., Roberts, J., Fanning, C.M., 1995. Two Carboniferous ages: a comparison of SHRIMP zircon dating with conventional zircon ages and $^{40}Ar/^{39}Ar$ analysis. Geochronology time scales and global stratigraphic correlation. SEPM Special Publication 54, 3-21.

Compston, W., Williams, I.S., Meyer, C.E., 1984. U-Pb geochronology of zircons from lunar breccia 73217 using a sensitive high-mass resolution ion microprobe. Journal of Geophysical Research: Solid Earth 89(S02), B525-B534.

Courtney-Davies, L., Ciobanu, C.L., Tapster, S.R., Cook, N.J., Ehrig, K., Crowley, J.L., Verdugo-Ihl, M.R., Wade, B.P., Condon, D.J., in review. Opening the Magmatic-Hydrothermal Window: High-Precision U-Pb Geochronology of the Mesoproterozoic Olympic Dam Cu-U-Au-Ag Deposit, South Australia. Economic Geology.

Courtney-Davies, L., Ciobanu, C.L., Verdugo-Ihl, M.R., Slattery, A., Cook, N.J., Dmitrijeva, M., Keyser, W., Wade, B.P., Domnick, U., Ehrig, K., Xu, J., Kontonikas-Charos, A., 2019. Zircon at the nanoscale records metasomatic processes leading to large magmatic-hydrothermal ore systems. Minerals 2019, 9, 364.

Coyner, S.J., Kamenov, G.D., Mueller, P.A., Rao, V., Foster, D.A., 2004. FC-1: a Zircon Reference Standard for the Determination of Hf Isotopic Compositions via Laser Ablation ICP-MS. American Geophysical Union, Fall Meeting 2004, abstract V51C-0584

Creaser, R.A., 1989. The geology and petrology of Middle Proterozoic felsic magmatism of the Stuart Shelf, South Australia. PhD thesis, La Trobe University, Melbourne, unpublished.

Creaser, R.A., Fanning, C.M., 1993. A U-Pb zircon study of the Mesoproterozoic Charleston Granite, Gawler Craton, South Australia. Australian Journal of Earth Sciences 40, 519-526.

Cuney, M., 2005. World-class unconformity-related uranium deposits: Key factors for their genesis. In: Mao J., Bierlein F.P. (Eds), Mineral Deposit Research: Meeting the Global Challenge. Springer, Berlin, Heidelberg.

Cuney, M., 2009. The extreme diversity of uranium deposits. Mineralium Deposita 44, 3-9

Cuney, M., 2010. Evolution of uranium fractionation processes through time: driving the secular variation of uranium deposit types. Economic Geology 105, 553-569

Cuney, M., 2014. Felsic magmatism and uranium deposits. Bulletin de la Société Géologique de France 185, 75-92.

Cuney, M., Friedrich, M., 1987. Physicochemical and crystal-chemical controls on accessory mineral paragenesis in granitoids. Implications on uranium metallogenesis. Bulletin de mineralogie 110, 235-247.

Curtis, S., Thiel. S., 2019. Identifying lithospheric boundaries using magnetotellurics and Nd isotope geochemistry: An example from the Gawler Craton, Australia. Precambrian Research 320, 403-423.

Dahlkamp, F.J., 1993. Uranium Ore Deposits. Springer.

Daly, S.J., Fanning, C.M., Fairclough, M.C., 1998. Tectonic evolution and exploration potential for the Gawler Craton, South Australia. AGSO Journal of Australian Geology and Geophysics 17, 145–168.

Debon, F., Le Fort, P., 1983. A chemical–mineralogical classification of common plutonic rocks and associations. Earth and Environmental Science, Transactions of The Royal Society of Edinburgh 73, 135–149.

Domnick, U, Cook, N.J., Bluck, R., Brown, C., Ciobanu, C.L., 2018. Petrography of granitoids from the Samphire Pluton, South Australia: implications for uranium mineralisation in overlying sediments. Lithos 300–301, 1–19.

Domnick, U., Cook, N.J., Ciobanu, C.L., Courtney-Davies, L., Dmitrijeva, M., Verdugo-Ihl, M.R., Xu, J., Keyser, W., Slattery, A., Kennedy, A.K., Bluck, R., in review, a. Micron- to nanoscale

characterisation and U-Pb geochronology of zircon from granites of the Samphire Pluton, South Australia. Precambrian Research.

Domnick, U., Cook, N.J., Ciobanu, C.L., Wade, B.P., Bluck, R., 2020. A Mineralisation Age for the Sediment-Hosted Blackbush uranium Prospect, North-Eastern Eyre Peninsula, South Australia. Minerals, 10, 191.

Donovan, J.J., Singer, J.W., Armstrong, J.T., 2016. A new EPMA method for fast trace element analysis in simple matrices. Am. Mineral. 101, 1839-1853.

Donovan, J.J., Tingle, T.N., 1996. An Improved Mean Atomic Number Background Correction for Quantitative Microanalysis. Microscopy and Microanalysis 1, 1-7.

Douglas, G.B., Butt, C.R.M., Gray, D.J., 2011. Geology, geochemistry and mineralogy of the lignite-hosted Ambassador palaeochannel uranium and multi-element deposit, Gunbarrel Basin, Western Australia. Mineral. Deposita 46, 761-787.

Eby, G.N., 1992.Chemical subdivision of the A-type granitoids: petrogenetic and tectonic implications. Geology 20, 641–644.

Ehrig, K., Kamenetsky, V., Mc`Phie, J., Cook, N.J., Ciobanu, C.L., 2017. Olympic Dam iron-oxide Cu-U-Au-Ag deposit. In: Phillips, G.N. (Ed), Australian Ore Deposits. AusIMM, Melbourne, 601-610.

Ehrig, K., McPhie, J., Kamenetsky, V., 2012. Geology and mineralogical zonation of the Olympic Dam iron oxide Cu-U-Au-Ag deposit, South Australia. In: Hedenquist, J.W., Harris, M., Camus, F. (Eds), Geology and Genesis of Major Copper Deposits and Districts of the World, a Tribute to Richard Sillitoe. SEG Special Publication 16, 237-268.

Engvik, A.K., Putnis, A., Fitz Gerald, J.D., Austrheim, H., 2008. Albitization of granitic rocks: the mechanism of replacement of oligoclase by albite. The Canadian Mineralogist 46, 1401–1415.

Fanning, C.M., Reid, A.J., Teale, G.S., 2007. A geochronological framework for the Gawler Craton, South Australia, South Australia Geological Survey Bulletin 55, 258.

Ferris, G., Schwarz, M., Heithersay, P., 2002. The geological framework, distribution and controls of Fe-oxide Cu-Au mineralisation in the Gawler Craton, South Australia: part 1: geological and tectonic framework. In: Porter, T.M. (Ed), Hydrothermal Iron Oxide Copper-Gold Related Deposits: A Global Perspective. 2. Adelaide, PGC Publishing, 9–31.

Finch, R.J., Hanchar, J.M., 2003. Structure and chemistry of zircon and zircon-group minerals. Reviews in Mineralogy and Geochemistry 53, 1–25.

Fraser, G.L., McAvaney, S., Neumann, N., Szpunar, M., Reid, A., 2010. Discovery of early Mesoarchean crust in the eastern Gawler Craton, South Australia. Precambrian Research 179, 1–21.

Fraser, G.L., Neumann, N.L., 2010. New SHRIMP U-Pb zircon ages from the Gawler Craton and

Curnamona Province, South Australia, 2008–2010. Geoscience Australia, Record, 2010/16.

Gaspar, M., Knaack, C., Meinert, L.D., Moretti, R., 2008. REE in skarn systems: a LA-ICP-MS study of garnets from the Crown Jewel gold deposit. Geochimica et Cosmochimica Acta 72, 185–205.

George, E., 1985. Les mineralisations uraniferes jurassiques liees spatialement a une discordance hercynienne. Petrographie, mineralogie, et geochimie des gisements du Rouergue (Aveyron, France). Geol. Geochim. Uranium 9, 219.

Goldsmith, S.D., 2014. The Samphire Project: A distal IOCG and evidence for Mesoarchean crust in the Gawler Craton. Honours thesis, The University of Adelaide, unpublished.

Goodwin, S., 2010. Geochemical and isotopic investigation into the tectonic setting of Mesoarchean and Paleoproterozoic granitoid suites within the eastern Gawler Craton, South Australia. Honours thesis. The University of Adelaide, unpublished.

Government of South Australia (Department for Energy and Mining), 2019. Uranium. http://www.energymining.sa.gov.au/minerals/invest/mineral_commodities/uranium

Guo, X.F., Szenknect, S., Mesbah, A., Labs, S., Clavier, N., Poinssot, C., Ushakov, S.V., Curtius, H., Bosbach, D., Ewing, R.C., Burns, P.C., Dacheux, N., Navrotsky, A., 2015. Thermodynamics of formation of coffinite, $USiO_4$. PNAS 112, 6551-6555.

Guzman, E.R., Solache, M., Iturbe-García, J.L., Ordonez-Regil, E., 1995. Uranium in phosphate rock and derivates. Journal of Radioanalytical and Nuclear Chemistry 189, 301-306.

Hand, M., Reid, A., Jagodzinski, L., 2007. Tectonic Framework and Evolution of the Gawler Craton, Southern Australia. Economic Geology 102, 1377–1395.

Hastie, A.R., Kerr, A.C., Pearce, J.A., Mitchell, S.F., 2007.Classification of altered volcanic island arc rocks using immobile trace elements: development of the Th–Co discrimination diagram. Journal of Petrology 48, 2341–2357.

Herold, N., Huber, M., Greenwood, D.R., Müller, R.D., Seton, M., 2011. Early to Middle Miocene monsoon climate in Australia. Geology 39, 3–6.

Hitzman, M.W., Valenta, R.K., 2005. Uranium in iron oxide-copper-gold (IOCG) systems. Economic Geology 100, 1657–1660.

Hou, B., Fabris, A.J., Keeling, J.L., Fairclough, M.C., 2007. Cainozoic palaeochannel-hosted uranium and current exploration methods, South Australia. MESA Journal 46, 34–39.

Hou, B., Fabris, A.J., Michaelsen, B.H., Katona, L.F., Keeling, J.L., Stoian, L., Wilson, T.C., Fairclough, M.C., Cowley, W.M., 2012. Paleodrainage and Cenozoic costal barriers of South Australia: a new map and GIS dataset. MESA Journal 66, 26–32.

Hou, B., Keeling, J., Li, Z., 2017. Paleovalley-related uranium deposits in Australia and China: a review of geological and exploration models and methods. Ore Geology Reviews 88, 201–234.

Hövelmann, J., Putnis, A., Geisler, T., Schmidt, B.C., Golla-Schindler, U., 2010. The replacement of plagioclase feldspars by albite: observations from hydrothermal experiments. Contributions to Mineralogy and Petrology 159, 43–59.

Howard, K.E., Reid, A., Hand, M., Barovich, K., Belousova, E., 2006. Does the Kalinjala Shear Zone represent a palaeosuture zone? MESA Journal 43, 16–20.

Hu, R., Bi, X., Zhou, M., Peng, J., Su, W., Liu, S., Qi, H., 2017. Uranium metallogenesis in South China and its relationship to crustal extension during the Cretaceous to Tertiary. Economic Geology 103, 583–598.

IAEA, 2018. Geological Classification of Uranium Deposits and Description of Selected Examples. IAEA TECDOC No. 1842. Vienna: International Atomic Energy Agency, 2018.

IAEA, 2019. PRIS Power Reactor Information System. https://pris.iaea.org/pris/, accessed 11/11/19.

Ingham, E.S., Cook, N.J., Cliff, J., Ciobanu, C.L., Huddleston, A., 2014. A combined chemical, isotopic and microstructural study of pyrite from roll-front uranium deposits, Lake Eyre Basin, South Australia. Geochimica et Cosmochimica Acta 125, 440-465.

IUPAC, 1998. Isotopic compositions of the elements 1997. Pure & Appl. Chem 70, 1, 217-235.

Keyser, W., Ciobanu, C.L., Cook, N.J., Courtney-Davies, L., Kennedy, A., Wade, B.P., Ehrig, K., Dmitrijeva, M., Kontonikas-Charos, A., Feltus, H., Johnson, G., 2019. Petrographic and geochronological constraints on the granitic basement to the Middleback Ranges, South Australia. Precambrian Research 324, 170-193.

King, D., Woodmansee, W.C., 1956. Port Lincoln Uranium Exploration - Diamond drilling at the Hospital Prospect. Mining Review, South Australia Department of Mines, 101, 32-41.

Kontonikas-Charos, A., Ciobanu, C.L., Cook, N.J., 2014. Albitization and redistribution of REE and Y in IOCG systems: insights from Moonta-Wallaroo, Yorke Peninsula, South Australia. Lithos 208-209, 178–201.

Kontonikas-Charos, A., Ciobanu, C.L., Cook, N.J., Ehrig, K., Krneta, S., Kamenetsky, V.S., 2017. Feldspar evolution in the Roxby Downs Granite, host to Fe-oxide Cu-Au-(U)mineralisation at Olympic Dam, South Australia. Ore Geology Reviews 80, 838–859.

Kontonikas-Charos, A., Ciobanu, C.L., Cook, N.J., Ehrig, K., Krneta, S., Kamenetsky, V.S., 2018. Rare earth element geochemistry of feldspars: examples from Fe-oxide Cu-Au systems in the Olympic Cu-Au Province, South Australia. Mineralogy and Petrology, in press.

Kristensen, H.M., Korda, M., 2019. Tactical Nuclear Weapons 2019. Bulletin of the Atomic Scientists

75:5, 252-261.

Liang, R., Chi, G., Ashton, K., Blamey, N., Fayek, M., 2017. Fluid compositions and P-T conditions of vein-type uranium mineralization in the Beaverlodge uranium district, northern Saskatchewan, Canada. Ore Geology Reviews 80, 460–483.

Ludwig, K.R.A., 2009. SQUID 2.50: A User's manual: Berkeley Geochronology Center, Special Publication No. 5, 110, Berkeley, California.

Ludwig, K.R.A., 2012. Isoplot/Ex rev. 4.1: A Geochronological Toolkit for Microsoft Excel; Berkeley Geochronology Centre Special Publication No. 5, 75, Berkeley, California.

Macmillan, E., Cook, N.J., Ehrig, K., Ciobanu, C.L., Pring, A., 2016. Uraninite from the Olympic Dam IOCG-U-Ag deposit: linking textural and compositional variation to temporal evolution. American Mineralogist 101, 1295–1320.

Mathian, M., Aufort, J., Braun, J., Riotte, J., Selo, M., Balan, E., Allard, T., 2019. Unraveling weathering episodes in Tertiary regoliths by kaolinite dating (Western Ghats, India). Gondwana Research 69, 89–105.

McAvaney, S.O., Thiel, S., Wade, C.E., 2016. The Kalinjala Shear Zone - intracontinental shear zone or palaeosuture? Paper Presented at the Australian Earth Science Convention, Adelaide.

McAvaney, S.O., Wade, C.E., 2015. Stratigraphy of the lower Gawler Range Volcanics in the Roopena area, northeastern Eyre Peninsula, Geological Survey of South Australia. Report Book 2015/00021, 420 pp.

McAvaney, S.O.; Wade, C.E.; Krapf, C.B.E., 2014. Geology of the CULTANA 1:100 000 map sheet (6432), Report Book 2014/00006, Department for Manufacturing, Innovation, Trade, Resources and Energy, South Australia, Adelaide.

McGowran, B., Hill, R.S., 2015. Cenozoic climatic shifts in southern Australia. Transactions of the Royal Society of South Australia 139, 1, 19-37.

Montel, J.M., Foret, S., Veschambre, M., Nicollet, C., Provost, A., 1996. Electron microprobe dating of monazite. Chemical Geology 131, 37-53.

Murphy, W.M., Shock, E.L., 1999. Environmental aqueous geochemistry of actinides. In: Burns, P.C., Finch, R. (Eds), Uranium: Mineralogy, Geochemistry and the Environment. Reviews in Mineralogy and Geochemistry 38, 221–254.

Neumann, N., Sandiford, M., Foden, J., 2000. Regional geochemistry and continental heat flow: Implications for the origin of the South Australian heat flow anomaly. Earth and Planetary Science Letters 183, 107-120.

Parker, A.J., 1980. The Kalinjala Mylonite Zone, Eastern Eyre Peninsula. Quarterly Geological Notes - Geological Survey of South Australia 76, 6–11.

Parker, A.J., 1993. Kimban orogeny. In: Drexel, J.F., Preiss, W.V., Parker, A.J. (Eds), The Geology of South Australia: The Precambrian (Vol. 1). Geological Survey of South Australia, Adelaide.

Parker, A.J., Fanning, C.M., 1998. Whyalla, South Australia. Explanatory Notes 1:250 000 Geological Series Sheet SI53-8, Geological Survey of South Australia.

Peiffert, C., Nguyen-Trung, C., Cuney, M., 1996. Uranium in granitic magmas. Part 2: Experimental determination of uranium solubility and fluid-melt partition coefficients in the uranium oxide-haplogranite-H_2O-NaX (X=Cl,F) system at 770°C 2 kbar. Geochimica et Cosmochimica Acta 60, 1515-1529.

Plümper, O., Putnis, A., 2009. The complex hydrothermal history of granitic rocks: multiple feldspar replacement reactions under subsolidus conditions. Journal of Petrology 50, 967–987.

Reid, A., 2019. The Olympic Cu-Au Province, Gawler Craton: A Review of the Lithospheric Architecture, Geodynamic Setting, Alteration Systems, Cover Successions and Prospectivity. Minerals 9(6), 371.

Reid, A., Hand, M., 2012. Mesoarchean to Mesoproterozoic evolution of the southern Gawler Craton, South Australia. Episodes 35, 216–225.

Reid, A., Jagodzinski, E., Gerhard, F., 2017. Project PGC03-01: Geochronology from the Samphire Uranium Project. In: Jagodzinski, E.A., Reid, A.J. (Eds), PACE Geochronology: Results of collaborative geochronology projects 2013–2015, Report Book 2015/00003. Department of the Premier and Cabinet, South Australia, Adelaide, 10–28.

Reid, A.J., 2017. Geology and metallogeny of the Gawler Craton. In: Phillips, G.N. (Ed), Australian Ore Deposits. The Australasian Institute of Mining and Metallurgy, Melbourne, 589-594.

Rudnick, R.L., Gao, S., 2003. 3.01 - composition of the continental crust. In: Holland, H.D., Turekian, K.K. (Eds), Treatise on Geochemistry (Vol. 3: The Crust), Oxford. 1-64.

Ruzicka, V., 1993.Vein uranium deposits. Ore Geology Reviews 8, 247–276.

Samphire Uranium, 2019. www.samphireuranium.com.au

Schofield, A., 2011. Uranium systems processes in the Crocker Well Suite, South Australia. Geoscience Australia. Record 2011/45.

Shand, S.J., 1943. Eruptive rocks. Their genesis, composition, classification, and their relation to ore-deposits with a chapter on meteorite. John Wiley & Sons, New York.

Skirrow, R., Bastrakov, E.N., Barovich, K., Fraser, G.L., Creaser, R.A., Fanning, C.M., Raymond, O.L. & Davidson, G.J., 2007. Timing of Iron Oxide Copper-Gold Hydrothermal Activity and Nd Isotope Constraints on Metal Sources in the Gawler Craton, South Australia. Economic Geology 102, 1441–1470.

Skirrow, R.G. (Ed), 2009. Uranium ore-forming systems of the Lake Frome region, South Australia: Regional spatial controls and exploration criteria. Geoscience Australia Record 2009/40.

Skirrow, R.G., Bastrakov, E.N., Davidson, G., Raymond, O.L., Heithersay, P., 2002. The geological framework, distribution and controls of Fe-oxide Cu-Au mineralisation in the Gawler Craton, South Australia: part II - alteration and mineralisation. In: Porter, T.M. (Ed), Hydrothermal Iron Oxide Copper-Gold & Related Deposits: A Global Perspective. 2. Adelaide, PGC Publishing, 33–47.

Steiger, R.H., Jäger, E., 1977. Subcommission on geochronology: Convention on the use of decay constants in geo- and cosmochronology. Earth and Planetary Science Letters 36, 359-362.

Stewart, K.P., Foden, J., 2003. Mesoproterozoic granites of South Australia. South Australia. Department of Primary Industries and Resources. Report Book 2003/15.

Stoian, L.M., 2009. Palynological analysis of samples 53448, 2490100, and 2490112. South Australian Resources Information Gateway. minerals.sarig.sa.gov.au, accessed 05/11/19.

Streckeisen, A., 1974. Classification and nomenclature of plutonic rocks. Geologische Rundschau 63, 773–786.

Szpunar, M., Hand, M., Barovich, K., Jagodzinski, E., Belousova, E., 2011. Isotopic and geochemical constraints on the Paleoproterozoic Hutchison Group, southern Australia: implications for Paleoproterozoic continental reconstructions. Precambrian Research 187, 99–126.

Taylor, S.R., 1964. Abundance of chemical elements in the continental crust; a new table. Geochimica et Cosmochimica Acta 28, 1273-1285.

UraniumSA, 2007. Uranium discovery. ASX RELEASE 12 December 2007. 1–4 pp, http://www.asx.com.au/asx/statistics/displayAnnouncement.do?display=pdf&idsId=00794394.

UraniumSA, 2010. The Mullaquana Uranium Project. South Australian Explorers' Conference, 26 November 2010.

UraniumSA, 2013. SAMPHIRE PROJECT UPDATE. ASX RELEASE 27 September 2013. 1–27 pp. http://www.asx.com.au/asx/statistics/displayAnnouncement.do?display=pdf&idsId=01448164.

UraniumSA, 2014. Significant upside targeting high grade unconformity uranium mineralisation Blackbush deposit, Samphire Project. ASX RELEASE 25 July 2014. 1–8 pp. http://www.asx.com.au/asx/statistics/displayAnnouncement.do?display=pdf&idsId=01536222.

UraniumSA, 2015. Samphire Uranium Project – April 2015. Presentation at South Australian Resources and Energy Investment Conference 2015.

Verdugo-Ihl, M.R., Ciobanu, C.L., Cook, N.J., Ehrig, K., Courtney-Davies, L., 2019. Defining early stages of IOCG systems: Evidence from iron oxides in the outer shell of the Olympic Dam deposit, South Australia. Mineralium Deposita, 1-24.

Wade, C.E., 2011. Definition of the Mesoproterozoic Ninnerie Supersuite, Curnamona Province, South Australia. MESA Journal 62, 25-42.

Wade, C.E., Reid, A.J., Wingate, M.T.D., Jagodzinski, E.A., Barovich, K., 2012. Geochemistry and geochronology of the c. 1585 Ma Benagerie Volcanic Suite, southern Australia: Relationship to the Gawler Range Volcanics and implications for the petrogenesis of a Mesoproterozoic silicic large igneous province. Precambrian Research 206, 17–35.

Whalen, J.B., Currie, K.L., Chappell, B.W., 1987. A-type granites: geochemical characteristics, discrimination and petrogenesis. Contributions to Mineralogy and Petrology 95, 407–419.

Williams, I.S., 1998. U-Th-Pb geochronology by ion microprobe. Applications of microanalytical techniques to understanding mineralizing processes. Reviews in Economic Geology 7, 1-35.

Wilson, T., 2015. Uranium and uranium mineral systems in South Australia, 3rd edition. Report Book 2015/00011, Geological Survey of South Australia, Mineral and Energy Resources Group.

Wingate, M.T.D., Campbell, I.H., Compston, W., Gibson, G.M., 1998. Ion microprobe U–Pb ages for Neoproterozoic basaltic magmatism in south-central Australia and implications for the breakup of Rodinia. Precambrian Research 87, 135–159.

Wise, T., 2019. Prospectivity modelling of the Olympic Cu–Au Province. MESA Journal 90, 36-41.

Wülser, P.-A., 2009. Uranium metallogeny in the North Flinders Ranges region of South Australia. PhD thesis, The University of Adelaide, unpublished.

Wülser, P.A., Brugger, J., Foden, J., Pfeifer, H.R., 2011. The sandstone-hosted Beverley uranium deposit, Lake Frome Basin, South Australia: mineralogy, geochemistry, and a time constrained model for its genesis. Economic Geology 106, 835–867.

Yeates, G., 1990. Middleback Range iron ore deposits. In: Hughes, F.E. (Ed), Geology of the Mineral Deposits of Australia & Papua New Guinea. 2. The AusIMM, Melbourne, 1045–1048.

Zalensky, V., 2019. Characterization of fluorite using laser ablation inductively coupled plasma mass spectrometry. Honours thesis, School of Chemical Engineering and Advanced Materials, The University of Adelaide, unpublished.